Implementation of an advanced algorithm for enhanced signal analysis in electrical resistance tomography using the EIDORS toolbox

A thesis submitted to the University of Cape Town in fulfilment of the
requirements for degree of Master of Science in Engineering

by

Olubode Caleb Adetunji

BSc.(Physics), PGD (Mathematical sciences)

Department of Chemical Engineering

University of Cape Town

March 2011

Abstract

Electrical resistance tomography (ERT) is a technology for producing images of internal body structures from the analysis of the electrical measurements made from the rings of electrode system fitted on the body surface. Producing an image from measurements in ERT is broadly classified into a forward and inverse problem. In the forward modelling of the problem computing the boundary voltages from a model of the electric flux given the resistivity distribution within the domain of the vessel is required. The technique requires an iterative processes in order to address the ill-posed and non-linear mathematical inverse problem associated with ERT, i.e. to progressively improve on a calculated resistivity distribution to match the simulated forward solution with the measured data. To achieve these calculations, the use of a public domain library of MATLAB functions, EIDORS, was explored. The forward solver function in the library is based on the finite element method (FEM), which is robust at handling complicated geometries, complete electrode modelling and the spatially variable or non-linear material properties.

A study of the current stimulation and voltage measurement codes in the library lead to the development of six 3-D measurement sequence tables for collecting data over two, three and four rings of sixteen equally spaced electrodes system in a ring, with consideration to a sequence of current stimulation through both opposite and adjacent electrode pairs. With the voltage measured using these tables, the inverse solver code included in the library was explored in solving the inverse problem based on the regularisation technique.

The modification and customisation of the open-source library of functions for analysis of measured voltage signals from the UCT vessel lead to the development of an image reconstruction procedure which was coded in MATLAB for each of the six 3-D measurement strategies.

The primary objectives of this research include an implementation of a 3-D algorithm in visualising the movement of solid suspended objects through image reconstruction and assessment of the quality of these images as well as validation of the application of the 3-D algorithm in visualising the movement of conductive solution.

Implementation of the 3-D algorithm was demonstrated in an applied context with the use of the six programs to visualise the position of a suspended solid object along the diameter of the vessel. A comparative study of the volume and centre of gravity of the suspended solid objects and reconstructed images using the six reconstruction codes enables the determination of the optimal measurement strategy.

Although there was improvement in the resolution of the reconstructed images with the stimulation of current through opposite electrode pairs instead of adjacent pairs, analysis of tomogram of the variation of position and volume of suspended phantom along the diameter of the vessel indicate the resolution of the images decreases towards the centre of the vessel. Three major sources of error that account for this observation are (1) the use of first order FEM in the explored libraries instead of higher order FEM, (2) the variation of the mesh density from fine mesh near the boundary to coarse mesh towards the centre in explored 3-D mesh generator, (3) the inaccuracy in reproducing the tank phantom measurements due to limitation in the memory space and processing power of the computer used for the 3-D imaging.

The 3-D reconstruction software developed using the optimal measurement strategy was further applied to visualise the movement of more conductive solution relative to the less conductive bulk solution in some experimental work. The analysis of the reconstructed images provided a means of ascertaining the physical phenomenon influencing the movement of the fluid.

Declaration

I declared that dissertation is my own work, unaided work. Every received support has been referenced. It is being submitted for the degree of Masters of Science in Engineering in the University of Cape Town. It has not been submitted before for any degree or examination in any other university

Signature of Author...

Cape Town

24 March 2011

Acknowledgements

The contribution of the following people was immense and cannot be overemphasised.

My heartfelt gratitude goes to my supervisor, Dr Jochen Petersen, for granting me the opportunity to undertake studies under your exemplary and scholarly supervisory role. I may not have had the opportunity to express my skills in applied mathematics if you had not brought me on the image reconstruction research.

The funding for this project has been through a joint donation by African Institute for Mathematical Sciences (AIMS), Centre for Bioprocess and Engineering Research (CeBER) and the International scholarship award granted to me in 2010 and 2011 by the University of Cape Town (UCT). Your donation is appreciated and I am very grateful.

The pieces of advice provided by Bill Randall, the electrical engineer at the Department of Chemical Engineering(Chem Eng.), UCT, is equally worthy of note. When the going became though and the hope of getting to the destination dwindle, your suggestions and encouragement will perpetually be remembered. Graham Inggs, the IT officer in Chem Eng., helped consistently in properly installing some of the libraries in the explored open source software for this research.

The milestone progress made in the course of this research may not have been except for the kind and generous tutoring provided by Timothy Long. 'Tim', you are great!

The involvement of Professor Nicolas Florsch of the University of Paris in this work is significant and worthy of commendation. The pace at which I acquire the fundamental principle of electrical resistance tomography might not have been, but for his dedicated support shown in the way he made himself available for my questions.

My special thanks and appreciation goes to Naadia for facilitating the flawless write-up as well as Andrew Mcbride and Andrew McMahoon suggestions when the numerical approach to be used in this work had not been decided. Much support was equally provided by Granville of Chem Eng. electronic workshop in learning the short-cut method of operating the UCT tomography hardware.

The quick and helpful responses of the authors of EIDORS, Andy Adler and Bill Lionheart, to complains about identified bugs in their code is appreciated.

On the final note, my profound gratitude goes to my parents and sibling for their unfading love and support over years. I dedicate this piece to you.

Table of Contents

Chapter 1: Introduction

Chapter 2: Literature Review

Chapter 3: Mathematical Development

Chapter 4: Experimental Design and Analysis Tools

Chapter 5: Results and Discussion

Chapter 6: Conclusion and Recommendations

Appendices

Appendix H: MATLAB Functions for Loading Data to the Reconstruction Codes of the Two, Three and Four Rings Electrodes System

List of Figures

Chapter 2: Literature Review

Chapter 3: Mathematical Development

Chapter 4: Experimental Design and Analysis Tools

Chapter 5: Results and Discussion

List of Tables

Chapter 2: Literature Review

Chapter 3: Mathematical Development

Chapter 4: Experimental Design and Analysis Tools

Chapter 5: Results and Discussion

NOMENCLATURE

ρ	Resistivity distribution
$U(\rho)$	Resistivity to potential mapping
V	The measured potential
L	The regularisation matrix
α	The regularisation parameter
Ŋ(L)	A null space
S_w	A subspace where a true solution is assumed to lie
ρ_n	N dimensional resistivity distribution vector
Γ	The covariant matrix
P	The number of discretised element in the finite element mesh
M	Dimension of a subspace lower than N
w_m	Dimensional orthonormal eigenvector of Γ
WW^T	Orthogonal projection onto S_w
I	An identity matrix or current distribution over boundary electrodes
W	The matrix having the vectors w_m or a discrete differential operator
J	The jacobian of the mapping of $U(\rho_i)$
$diag(.)$	The diagonal matrix
Ω	Three dimensional domain of resistivity distribution
ξ	Admittivity distribution – reciprocal of impedivity
u	Electrical potential or displacement distribution in a mechanical system
I_l	Injected current into i_{th} electrode E_i
z_i	Constant impedance
n	The outward unit normal vector
ϕ_i	Shape function of a finite element
$\lvert E_l \rvert$	Area of the surface of the l_{th} electrode
λ	A positive scalar parameter

e	Norm of the additive noise
μ	Mean expected value of statistical variable
∇	Del operator represented by nabla symbol
$C^k(\Omega)$	Sets of all real-valued function of u.
v	Test function
δ	Radius of a sphere
f	Boundary force distribution
k	Stiffness of solid material or constant parameter
g	locally integrable function
R	Set of real numbers
$H'(\Omega)$	Sobolev space
σ_o	Background conductivity around which small changes are assumed to occur
$\theta^e(x)$	Trial solution expressed in terms of the shape function and nodal voltages

GLOSSARY

PCA	principal component analysis
PAS	Position of axis of symmetry
EIDORS	Electrical Impedance and Diffuse Optical Reconstruction software
NETGEN	Automatic mesh generation tool for two or three dimensions
FEM	Finite element method
ERT	Electrical resistance tomography
2-D	Two dimensional cartesian coordinate space
3-D	Three dimensional cartesian coordinate space
UCT	University of CapeTown
TS	Industrial tomography systems
MRI	Magnetic resonance imaging
PET	positron emission tomography
APT	Applied potential tomography
CT	Computed tomography
FFT	Fast fourier transform
Fps	Frames per second
UMIST	University of Manchester institute of science and technology
BCM	Basis contrained method
SSRM	Subspace regularisation method
STRM	Standard Tikhonov regularisation method
PC	personal computer
RAM	Random access memory
DISTMESH	A simple mesh generator in MATLAB
CSG	Constructive solid geometry
Pdf	Probability density function
PVC	polyvinylchloride

Isopotential	A line or surface connecting point of equal potential values in an electric field region
In-vivo	Occurring or made to occur within a living organism or natural setting
Peristaltic pump	A positive displacement pump used for pumping a variety of fluids
Frame	Two hundred and fifty-six (256) measured voltage data set due to sixteen (16) sequence of current stimulation in a ring. It is the minimum data set required to reconstruct an image.

CHAPTER 1

INTRODUCTION

1.1 Background

Gaining a better understanding of the internal composition of pipelines, vessels, reactors and separators is supported with a technology that enables the visualisation of the interior of the vessel. Delineation of the interior of the process vessels or pipelines containing multiphase mixtures with the help of an imaging technique will enhance investigation and optimisation of the processes within the vessel through an online control system aiming at reducing energy consumption, increasing product yield and monitoring the performance of the processes.

An appropriate imaging technique is sought to visualise complex processes within process vessels. For example, the measurement of formation of a vortex and its maintenance to achieve separation of solid/liquid mixture in a hydrocyclone process requires a non-invasive process measurement technique from outside the hydrocyclone so as not to disturb the vortex.

Similarly, fluidised beds are employed in reactions where the solid is a catalyst or a heat transfer medium by passing a gas or liquid up through a bed of solid material at sufficient velocity to maintain fluid behaviour. When this process is optimised, excellent mixing is obtained. To achieve an optimised reaction, during operation, a process measurement is sought to measure the homogeneity of the fluidised beds and the presence of any contaminants that may need removing from outside the vessel as any measurement within the process vessel will potentially disturb the fluidity of the system.

A further example is a filtration processes, where the filter medium is replaced after a fixed time due to drop in performance and then cleaned before being returned to operation in batch and continuous filtration, respectively. As filtration occurs within the filtered medium, especially a filtration process that involves solids, a process measurement technique is needed to measure what is actually happening within the filter medium, owing to the difficulty of determining this with any conventional instrument.

Also, measuring the flow of each phase in the pipe during multiphase flow (flow of two or more phases such as liquid, gas and solid along a closed or open pipe) will provide information on the mass, volume and degree of mixing within the pipe. Multiphase flow can only be measured by a measurement technique that is non-intrusive, otherwise, the flow will be disturbed.

Similarly, although the behaviour of fluids could be modelled and described using computational fluid dynamics techniques, obtaining an "on-line" data sets from an experimental rig during chemical processes such as batch mixing, polymerisation reactions, polymer extrusion and crystallisation in order to validate the model is a challenge. Data sets acquired by process measurement help developers to optimise their models, as the measured data is used to validate the reliability of the model. More importantly, a process measurement technique that provides visualisation of the measurement variable (concentration and turbulence) is being sought by many oil and gas companies in order to identify flow regimes that are operational during a certain time of the flow and mixing process. A process measurement of this kind will enhance investigation into oil sand research, where visibility is reduced owing to stainless steel equipment and opaque fluid (sand in heavy oil). Likewise, the opaque medium presented by the heap of ores in heap leaching processes disallows the visualisation of the flow of the leach solution through the heap of mined ores. A process measurement technique that enables the visualisation of the flow of the leach solution from analysis of the measured data sets taken during an "on-line" flow will enhance investigation into an improved form of recovery of the leachate. Thus, a process measurement technique aiding the visualisation of the flow of the leach solution without disturbing heap leaching processes is called for in heap leaching research.

Electrical Resistance Tomography (ERT) is an imaging technique of choice due to its effectiveness in aiding the visualisation of interior of process vessels in a non-intrusive, non-destructive, non-radioactive manner and at a low cost. ERT enables the visualisation of resistance or conductance distribution within a less resistant or conductive homogeneous medium, respectively, from voltage measurement made on multiple electrodes fitted on the periphery of the process vessel due to sequence of current stimulation through array of electrode. ERT could be used to model any higher resistive materials such as Perspex or Polyvinyl chloride (PVC) materials relative to the bulk solution by suspending these into the bulk homogeneous solution. Modelling the specific geometry of region of resistivity or conductance distribution using the ERT technique in 3-D will require mesh density of order of 10^5, which is only obtainable using computing system of much bigger memory and higher processing power.

The peripheral electrodes are fitted so as to ensure contact with the process fluid without disturbing the process flow pattern.

In general, an electrical resistance image reconstruction technique used for ERT involves computing the solution of a non-linear and ill-posed inverse problem. Non-linearity in image reconstruction arises due to isopotential lines curving in a way which depends on the spatial conductivity distribution (Pinheiro *et al*. 1998). Non-linearity is reduced to an iterative procedure using Newton's method, as it exhibits quadratic convergence for a non-singular derivative (Pinheiro *et al*. 1998).

The ERT technique has been applied for the analysis of a number of chemical processes using two-dimensional (2-D) image reconstruction code developed in the Department of Chemical Engineering, University of Cape Town. Stevenson (2006) carried out an analysis of particle suspension and mixing in biological systems using the ERT technique developed from 2-D algorithm. An on-line velocity flow profiling system using electrical resistance tomography was made by Long (2006) with a view to visualising the flow of slurries in 2-D. Recently, an application of ERT in evaluating the influence of nozzle design on the gas hold-up distribution in boiling bubble column reactors formed the scope of work of Sudhakaran (2010).

However, the conclusions and recommendations from the analysis of the results from these applications were based on 2-D reconstructed images using 2-D voltage measurement strategies which inherently contains the following errors: (a) the assumption that isopotential regions are curves and not surfaces and (b), that the effect of objects or zones of higher or lower conductivity outside the plane of electrodes has no effect on the voltage pattern on the plane.

1.2 ERT Basic Principles

Electrical resistance tomography in general involves the computation of: (1) the electric field in the interior, in order to compute the Jacobian (sensitivity matrix), (2) solving the forward problem of calculating predicted voltage measurements at the boundary from a given interior material properties, and (3) finding the solution of a non-linear and an ill-posed inverse problem by iteratively matching the predicted with the measured voltages. For complex geometries and inhomogeneous material medium, the finite element method (FEM) is required for addressing the aforementioned mathematical problems.

Pinheiro (2002) stated that a restraint to the development of 3-D algorithm was related to the isopotentials that were assumed to be curves rather than surfaces. This erroneous assumption lead to the modelling of the electric field lines in 2-D and an implementation of measurement strategy in a ring of electrodes (2-D data collection strategy). However, the development of 3-D algorithms in ERT has been promoted following the precise modelling of the electric flux distribution within the domain of any geometry and availability of computer systems with larger memory and high processing power.

1.3 Thesis objectives

A motivation for this research that spans the scope of developing a three-dimensional (3-D) image reconstruction algorithm springs from the acknowledgement of Pinheiro's assertion (2002) and the discovery made by Jossinet *et al* (1987) who showed from their multi-electrode study that the sensitivity outside of the plane containing the injection electrode is far from being negligible.

The central focus of this research is to implement an advanced algorithm for the analysis of voltage signals in electrical resistance tomography. Specifically, an enhanced signal analysis of measured voltage distribution on the boundary of process vessel resulting from perturbation of a homogeneous conductivity distribution inside the vessel is required for reconstructing images of region of lower or higher conductivity (inhomogeneity) in three-dimensions (3-D). The written reconstruction codes from the implemented algorithm will be tested by visualising the displacement of an object of low conductivity along the diameter of the vessel, and the flow of a highly conductive solution through a bulk solution, of lower conductivity. The need to unravel the dilemma of ascertaining the resolution of the reconstructed image is carried out through a comparative study of the volume and the centre of gravity of the reconstructed image and suspended phantom. These objectives are conceived to demonstrate an implementation of the 3-D algorithm in the applied context, which has not yet been demonstrated as summarised in the problem statement in the next section.

1.4 Problem Statement

A demonstration of an implementation of 3-D algorithm in visualising the movement of solid suspended objects is undertaken in the work. This will enable the determination of the best measurement strategy for the UCT ERT rig designed with various measurement strategies.

Furthermore, in view of lack of any attempt to assessing image quality from previous implementation of 3-D algorithm, this work intends to address the dilemma through a comparative study of the volume and centre of mass of the suspended systems and reconstructed image.

The work will also validate the use of the 3-D algorithm in visualising the movement of conductive solution injected into a mildly saline bulk solution using the obtained best measurement strategy for the UCT ERT rig.

1.5 Thesis outline

- The review of literature documented in chapter 2 begins with an overview of various imaging techniques. Following this, basic principle of ERT, ERT measurement principle and image reconstruction principle in relation to 2-D and 3-D algorithm were considered. Subsequently, an account of diverse applications of ERT from medical to industrial purposes, such as visualisation of solid/liquid or liquid/gas or liquid/liquid as well as processes in fluidised beds, are given. Thereafter, a record of background studies into ERT hardware, background knowledge of UCT hardware and implemented measurement sequences in ERT was made so as to lay a foundation for the comparative evaluation of various ERT devices considered. Succeeding this section of the review is an examination of applicable software in ERT, which paves the way for the history of EIDORS that is reported. The chapter concludes with problem statement being re-iterated.

- In chapter 3, detailed mathematical methods involved in both the forward and the inverse problem of image reconstruction using ERT is documented. A flow chart describing the sequence of operation in image reconstruction is also provided. The exploration of an open source software lead to identification of MATLAB functions that implement the mathematical formulations needed for the forward and the inverse problems. This library of functions is then described with a view to explaining the numerical operations to be computed for the forward and the inverse problem. The diverse measurement strategies implemented in order to obtain the optimum strategy with regards to the UCT tomography set-up are illustrated in the concluding section of this chapter.
- An account of the experimental design and the physical properties of the suspended solid objects chosen as an analysis tools are given in chapter 4. The chapter is introduced with a description of the hardware material for the experimental set-up. Thereafter, the explored open source software such as EIDORS for addressing the forward and the inverse problem and NETGEN for modelling the UCT tomography vessel in ERT are discussed. The concept of probability required in addressing the inverse problem is then explained. This is followed by the description of experimental work for imaging the movement of solid objects suspended in mildly saline solution and the movement of conductive fluid in the same solution.

- The results and discussion of this research is presented in chapter 5. The section describing the developed reconstruction code for 3-D imaging of suspended solid objects from data sets collected following the implementation of diverse measurement strategies is used to introduce this chapter. With due consideration to a few reconstructed images, major sources of error blurring the precise resolution of the images are, then, highlighted. Six measurement sequences consisting of voltage measurement over two, three and four rings due to a sequence of current stimulations through opposite and adjacent electrode pairs respectively are implemented. For each measurement strategy, the volume and position of an axis parallel to the vertical axis and passing through the centre of gravity is computed for each reconstructed image. The absolute value of the difference in volume and position of the centre of image between the reconstructed image and suspended phantom is also computed for each image. A comparative study of the these physical properties of the image and actual suspended objects is used in determining the best measurement strategy for the UCT tomography hardware. The application of the 3-D reconstruction code in visualising the movement of conductive solution within a bulk mildly saline homogeneous solution will be considered subsequently. The application is directed as ascertaining the phenomena influencing the movement of the conductive solution within free solution and in a saturated sponge. Similarly, the 3-D image reconstruction code is employed in visualising the movement of the conductive fluids through a packed bed medium. This is followed by an analysis of the movement of the conductive fluid through various media.

- The conclusions and recommendations of this work are reported in chapter 6.

CHAPTER 2

LITERATURE REVIEW

2.1 Overview of Imaging Techniques

In order to visualise the interior of an opaque body or medium, a number of imaging techniques with regards to the field of application yield remarkable results. In medical practise, magnetic resonance imaging (MRI) is often employed to create images of the inside of opaque organs in living organisms as well as detecting the amount of bound water in geological structures. To carry out a MRI scan, the living organism is placed in a magnetic field so as to align the spins of the atomic nuclei of the tissue molecules. The position of alignment of the proton is then caused to change due to resonance between atomic nuclei and radio waves by applying oscillating magnetic field pulses at radio wave frequency in a plane perpendicular to the magnetic field lines. The spinning of protons produces a faint signal that is detected by the receiver of the MRI scanner. Images are created from a computer processing the received information. With this technique, it is obvious that the principle for creating images involves a form of invasion of the internal constituent of the organs being imaged since the protons of the atomic nuclei are required to be aligned initially.

An alternative imaging technique in the field of medicine is positron emission tomography (PET). It is a nuclear medicine imaging technique which produces a three-dimensional (3-D) image of functional processes in the body. In applying the method, a positron emitting radionuclide (tracer) is introduced into the body on a biological active molecule. The PET system then detects the pairs of opposing gamma rays emitted indirectly by the tracer. Computer analysis of the detected pairs of gamma rays is used to reconstruct images of tracer concentration in 3-D or 4-D (the fourth dimension being time). Considering the injection of tracer in to the body to be imaged, the technique may not be appropriate for imaging industrial processes sensitive to the radioactive tracers, in which the normal function of the process is to be preserved.

Another imaging technique that has found applications in both medicine and industry for diagnosis of ailment and non destructive testing of product for defects, respectively, is X-ray scan. X-rays are produced in a highly evacuated glass bulb (X-ray tube) when streams of high energy and accelerating electrons (cathode rays) released from the cathode strike the anode (heavy metal of high melting point such as tungsten). A high voltage is applied between the two electrodes placed at the ends of the tube to ensure the streams have sufficient energy to knock off the electrons from the anode or to emit radiation when stopped by the anode. Imaging an interior body or objects using the X-ray technique

requires passing the decelerated streams of electrons or emitted radiation through the body or objects and focussing the emitted radiation on a photographic plate or a fluorescent screen. The relative opacity of different parts of the body is determined from the darkness of the shadows produced on the plates or screen.

A multidimensional view of the body's interior with more detail and additional view capabilities than the regular X-ray imaging is achieved with X-ray computed tomography (CT) scanning. Using the CT technique, the amount of radiation being absorbed throughout the body or object is measured by rotating a numerous X-ray beams and a set of electronic X-ray detectors around the body or object. At the same time, the examination table should be moving through the scanner so that the X-ray beam follows a spiral path. The large data of measured radiation is then processed by a computer program to create 2-D cross sectional images of the body. The image slices may be reassembled by a computer software to obtain a 3-D view of the body's interior.

Studies that seek to identify subsurface soil structure benefit from the induced polarisation imaging technique (IP) often applied in geophysical exploration. IP operates by inducing an electric current into the subsurface through two electrodes and measurement of voltage is made through two other electrodes. The IP measuring technique requires the use of non-polarisable potential electrodes and special wire layout. Besides, IP relies on Alternating current signals which need to be resolved mathematically.

Unlike the MRI, X-rays, CT and PET imaging technique that are more cumbersome and more complex, more risky, certain process tomography techniques provide means of visualising the interior of process vessels and pipelines containing multiphase mixtures without disturbing the flow of normal function of the process in a less dangerous and portable manner. An example of process tomography that is non-invasive, non-radioactive and low cost is electrical resistance tomography (ERT). From the listed imaging techniques, thus, ERT is explored in this work to image inhomogeneity of conductivity distribution within a process vessel.

2.2 ERT Measurement Principle and Algorithm

An account of measurement principle governing ERT as well as diverse algorithm that had been explored in ERT are given in this section.

2.2.1 ERT Measurement Principle

Practically, measurement vessels, usually cylindrical, are fitted with an electrode system, typically arranged in rings (of 16-64 electrodes) around the circumference. Current is injected into an electrode pair (typically adjacent or opposite) and the resultant peripheral voltages between other electrodes are recorded. The conductivity distribution (image) is reconstructed from this data using a finite element technique. In other words, the data sets may be post-processed to achieve a higher quality image, either by Electrical Impedance and Diffuse Optical Reconstruction Software (EIDORS) or user written software (Randall *et al*. 2007).

At present, the Department of Chemical Engineering, University of Cape Town, has a C++ program which controls the data acquisition system from the UCT tomography hardware measurement system, provides real-time visualisation and can record data for offline analysis by EIDORS open source software (Randall *et al*. 2007). A comparative evaluation of the UCT instrument and two AC excitation instruments (University of Manchester and Industrial Tomography System, ITS) has been performed, and UCT instrument compared favourably with these systems (Stephenson *et al.* 2007).

Figure 2.1a shows a two-dimensional circular object, the resistivity distribution of which is to be determined, and to the surface of which 16 electrodes have been connected. Suppose current is passed between two of these electrodes (say numbers 8 and 16), and the electrical potential at the other electrodes measured. The values of these potentials must reflect the distribution of current within the object, and hence the distribution of resistance (Barber *et al*. 1983). When a voltage is applied between electrodes 8 and 16, $V_{56}$is the voltage difference between electrodes 5 and 6 while current is flowing. The sets of potential measured at all the electrodes for a single injection is a frame from which an image can be reconstructed. For better images, potentials are measured at all the electrodes for all possible pairs of electrodes through which current is applied. However, these measurements are not all independent; using N electrodes it is only possible to produce $N - 1$ independent current distributions (Barber *et al*. 1983). Because of the voltage drop across the contact resistance, adjacent voltage difference measurement involving an electrode through which current is injected is not measured. In other words, for N electrodes, $N - 3$ measurements of voltage difference can be obtained for each pair of adjacent current electrodes. There is also reciprocity between the electrode pairs of current application, and of voltage measurement, such measurement of V_{56} and V_{65}, yielding same magnitude with only a change of sign, and hence it can be shown that the number of independent measurements is $N(N - 3)/2$. Accordingly, a sixteen electrodes ring will yield 104 independent voltage difference measurements for all possible pairs of current application. All possible current injections are considered in order to average the data and so improve the signal/noise ratio.

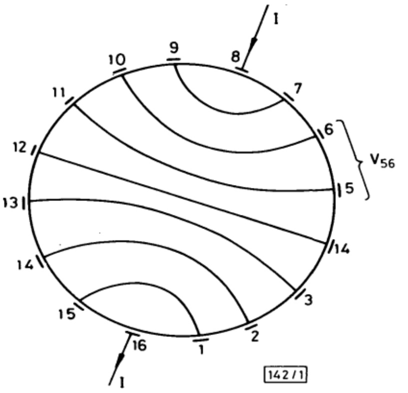

(a)

Figure 2.1(a). Electrode positions and isopotentials for a circular region of uniform resistivity (Barber *et al*. 1983).

Figure 2.1a shows these lines of constant potential (here called isopotentials) which end on electrodes for this particular electrode configuration, and for a medium of uniform resistivity. Considering the voltage difference between electrodes 5 and 6, if the measured voltage difference is different from the calculated voltage difference, the resistivity in all of the region between the isopotentials which end on electrodes 5 and 6 is altered to a certain value in order to produce the measured potential difference. Keeping the current between the drive electrodes constant, the resistivity will be altered in proportion to the voltage difference. The resulting image formed by backprojecting the profile measurements, normalised to the case of uniform resistivity, into the regions between the isopotential lines is the simplest image consistent with this profile of measurements. The images so produced by each current injection are then summed. This summed image is then filtered, by analogy with CT imaging, to reduce the blurring inherent in backprojection (Barber *et al*. 1983).

It is noteworthy that the voltage measurement strategies and current injection between adjacent electrodes are essentially two-dimensional data collection schemes, and results have been obtained by this method for two-dimensional distributions of resistivity. In reality, however, the distributions of resistivity of clinical and industrial interest are three-dimensional, and this poses some extra problems for the reconstruction, because current will flow out of the plane of the electrodes. In fact, a multi-electrode phantom study by Jossinet and Kardous confirmed that sensitivity out of the plane containing the injection electrode is far from being negligible (Pinheiro *et al*. 1998). A restraint to the development of three-dimensional measurement systems is related to the back-projection image reconstruction algorithm method employed by Barber and Brown, who in early days of electrical imaging research assumed isopotentials being curves rather than surfaces (Adler *et al*. 2006). Obtaining an optimal measurement scheme in the early days of three-dimensional tomography imaging was an issue of much concern. Contrary to reconstructed three-dimensional X-ray images that were obtained from a set of independent two-dimensional images, three-dimensional electrical resistance tomography cannot be reconstructed from a set of two-dimensional images owing to three-dimensional objects that cannot be decomposed, and taking into account the distribution of the current lines which do not remain localised in a plane. In other words, It is of paramount importance to reconstruct a full three-dimensional image from data collected over the whole surface of the body, as the current flux spreads out in all directions (Pinheiro *et al.* 1998).

Given the poorer signal-to-noise ratio obtained from diagonal current injection (i.e between layers of electrodes) and diagonal voltage measurement, and the fact that ERT data from 3D objects cannot be decomposed considering the current lines which do not remain localised in a plane, it was suggested by Pinheiro *et al*. (1998) that 3D image reconstruction requires 3D current injection patterns and measurement over the whole surface of the body. This is because current flux spreads out in all direction. Additionally, Paivii *et al*.(1999) stated that the more independent data are obtained the better spatial resolution can be achieved.

2.2.2 Image Reconstruction Principle Relating 2D Algorithm to 3D Algorithm

In the 1980s, medical electrical imaging was based on the assumption that the body under consideration was two-dimensional (Adler *et al*. 2006). This assumption was considered necessary owing to the limit of computational power of desktop computers, the limited number of drives and measurement channels employed. Before the discovery of the applied potential tomography (APT) technique, reconstructed images using resistivity had been obtained only from computer simulation or on laboratory phantoms, but not from *in-vivo* measurements. A practical difficulty of *in-vivo* measurements arises from the contact resistance between the electrode and the skin of the patient. This resistance is in series with the resistance to be measured, and is of the same order of magnitude (Barber *et al*. 1983). Applied Potential Tomography circumvents the difficulty of measuring potential values of the electrodes in contact with the body to be imaged by using a voltmeter of sufficiently high input impedance.

A number of research groups have presented accounts of initial studies on 3-D reconstruction algorithms. Goble *et al.* (1992) implemented an algorithm in which the region of interest is discretised into voxels whose sensitivity is computed using an analytical solution for the potential distribution for the homogeneous conductivity case (Pinheiro *et al.* 1998). In ERT, the Jacobian matrix is the matrix of the partial derivative of the measured voltages with respect to conductivity distribution over an element of a discretised domain. It is also an operator that maps the conductivity distribution of a domain to the measured voltage distribution. Paulson (1992) developed an algorithm in which trigonometric currents patterns are used and the image is reconstructed using a fast reconstruction algorithm whose Jacobian matrix is undetermined . In the development of a 3D algorithm by Metherall *et al.(*1996), a normalised sensitivity matrix was computed by assuming that the potential distribution is that of a point current source on the surface of a homogeneous, isotropic semi-infinite medium and then the matrix is inverted using customised techniques such as the fast Fourier transform (FFT) (Pinheiro *et al*. 1998).

However, the work of Pinheiro *et al*. (1998) differs from the work of Paulson presented above and Metherall *et al.*(1996) in the reconstruction procedure. Pinheiro employs a 3-D reconstruction algorithm, based on 3-D forward modelling and 3-D data collection over the entire surface, which iteratively uses a linear conductivity updates in conjunction with a general forward solver. The algorithms by Paulson (1992) and Metherall *et al*.(1996) algorithm involves a linearization around a homogeneous conductivity distribution and have no general forward solver. Furthermore, a ‘fast’ reconstruction algorithm was implemented in the work by Pinheiro *et al.* (1998) yielding a reduced set of equations, which has the advantage of no longer being ill-conditioned, but at the expense of a loss in image resolution. Pinheiro *et al.* (1998) circumvented the nonlinear nature of the inverse problem by reducing the problem into an iterative procedure using the Newton's method due to its quadratic convergence for a non-singular derivative.

2.2.3 Applications of ERT for Medical and Industrial Purposes Using 2D and 3D Algorithms

Figure 2.2b is a reconstruction of human forearm of Figure 2.1b based on the described two-dimensional algorithm, which reveals that in-vivo data can be collected and used to obtain an image. The image will be contaminated by structures above and below the plane of the electrodes, and because the isopotentials extend into the third dimension, the image is distorted in a way which decreases image resolution towards the centre (Barber *et al*. 1983). Although a simple geometric correction process was applied to the reconstructed image to produce that of figure 2.2b*,* one can still observe that basic structures, including the two bones, the muscular tissue, and possibly the two major blood vessels have been imaged in figure 2.2b when one compares figure 2.2a with figure 2.2b.

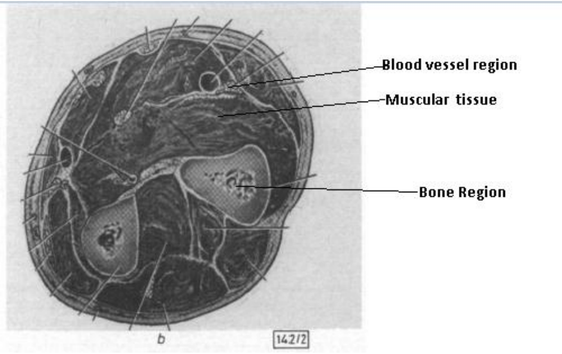

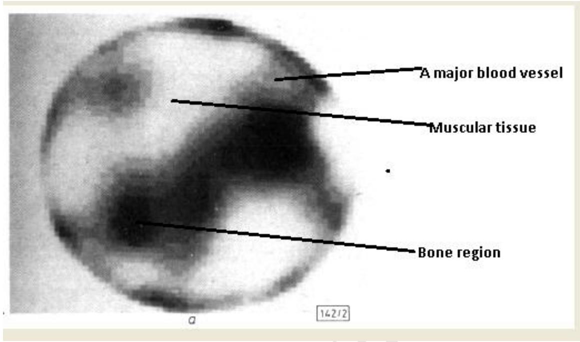

Figure 2.2(a). Diagrammatic cross-section of the human forearm at the level imaged (Barber *et al*. 1983).
Figure 2.2(b). Resistance image of a normal human forearm. Increasing blackness denotes increasing resistivity (Barber *et al*. 1983).

In the field of industrial process tomography, progress in research to obtaining a three-dimensional (3-D) reconstruction algorithm has been slower due to lack of an efficient way of computing the Jacobian matrix and in appropriate modelling of the electrode in three-dimensions that require access to a low level programming language. However, early 3-D reconstruction algorithms were from the medical Electrical Impedance Tomography (EIT) group, which included works of Goble *et al.*(1992) and Metherall *et al.*(1996) An early three-dimensional study of industrial process tomography was done by Pinheiro *et al* (1998).

In industry, process tomography is employed for the delineation of internal composition of pipelines and mixing vessels. Electrical resistance tomography (ERT) offers a relatively low-cost routine to determining in a non-destructive manner dynamics of states of chemical processes (Pinheiro *et al*. 1998). ERT allows a better understanding of the process kinetics (Pinheiro *et al*. 1998). Additionally, it does not only provide for online control of chemical processes to reduce energy consumption and increase product yields, but also enables the validation of existing computational fluid dynamics models (Pinheiro *et al*. 1998). In the work of Kim *et al.*(2005), particle concentration profiles for solid-liquid suspensions under shear driven flow was obtained using the ERT technique. A good qualitative comparison with the existing diffusion model was noticed from this result with respect to the particle concentration.

Williams *et al*. (1996) gave an account of the application of the ERT technique in studying solid suspension in aqueous media. Their results were used to investigate effects associated with impeller speed and solids volume fraction in a 30 litre vessel (Williams *et al.* 1996). Their work, which was one of the first recorded applications of ERT, was accredited to have provided a wealth of data to allow process model development, thus improving the overall understanding of the process in question (Steven *et al*. 2008).

Electrical resistance tomography was applied to pressure filtration, which required images at intervals of minutes since the dynamics of the process were relatively modest. It is equally applied for fluid mixing processes requiring images at 10-100ms intervals (Figure 2.3a), i.e. 10-100 frames per second (fps), as well as monitoring of highly dynamic multiphase flows in pipelines, Powder flow, Pneumatic Conveying, Hydraulic Conveying and Slurries (Figure 2.3f), which require images at 1ms intervals (1000 fps) for cross correlation techniques (Stephenson *et al.* 2007).

2.2.3.1 ERT Application for Solid/Liquid or Liquid/Gas or Liquid/Liquid Mixing

Specific applications where ERT has been successfully exploited, include solid/liquid mixing (Figure 2.2d), and liquid/gas mixing (Figure 2.2b), liquid/liquid mixing (Figure 2.2c). Wang *et al.*(2000) applied electrical resistance tomography technique to pseudo-stationary imaging of gas hold-up in 3-D for typical stirred vessel gas-liquid mixing. Holden *et al.*(1998) carried out imaging of homogeneous single phase mixing created by different impeller types and Stanley *et al.*(2005) applies the technique to the semi-batch feed addition of strong brine, mimicking the semi-batch addition of a feed reactant. Electrical Tomography has been applied to measure the depth of different components in a vessel in real time (Figure 2.2e). In the same vein, an alternative approach for defining mixing indices of solid-liquid mixtures and a suitable image reconstruction strategies for solid-liquid mixing were derived from ERT data measurement made by West *et al.* (1998). Their work employed a dual modality approach involving positron emission and ERT (Steven *et al.* 2008).

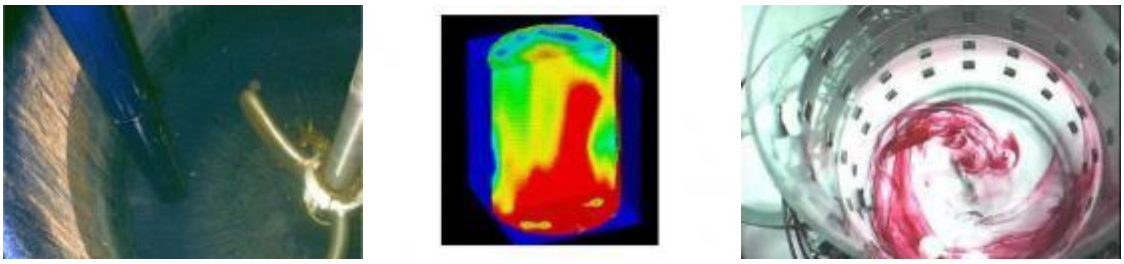

(a) Complete mixing with impellers (b) Gas-Liquid Mixing (c) Liquid –Liquid Mixing

(d) Solid-liquid Mixing (e) Interface detection (f) Monitoring flow of slurries

Figure 2.3. ERT is applied in delineation of chemical processes (Drupal 2010).

ERT also enables the imaging of a solid/liquid mixture pumped tangentially into a conical vessel, i.e. hydrocyclones. In hydrocyclones, the resulting centrifugal forces cause a vortex (the motion of the fluid swirling rapidly around a center) to form which encourages the solids to swirl to the bottom of the cone while the liquids exit at the top. In the course of the process, the challenge is to ensure that the vortex is formed and maintained to achieve the separation. Without the vortex the operation fails. The measurement challenge, which is to characterise the vortex from outside the hydrocyclone, is overcome with the application tomographic imaging, as any internal measurement would disturb the vortex (figure 2.4(a – b)).

Williams *et al*. (1998) studied the solid liquid suspensions by applying the ERT technique to image solid liquid suspension in three dimensions for varying agitation rates. The results which gave account of the extent of mixing within the system, were presented in form of voxel-resistivity distributions (Steven *et al*. 2008). Furthermore, a highly sensitive detection of solid accumulation on an impeller disc and settled solids build up on the vessel base itself was made by Holden *et al*. (1999) with the help of ERT on a 1.5 m diameter pilot scale vessel. To build up on the Holden *et al*. (1999) work, Mann *et al.* (2001) successfully imaged the pseudo-stationary solid-liquid suspension of plastic pellets for an agitated (75, 90 and 105 rpm) and non-agitated system in three dimensions using the ERT technique on the same pilot scale vessel as in figure 2.5 (Steven *et al.* 2008) .

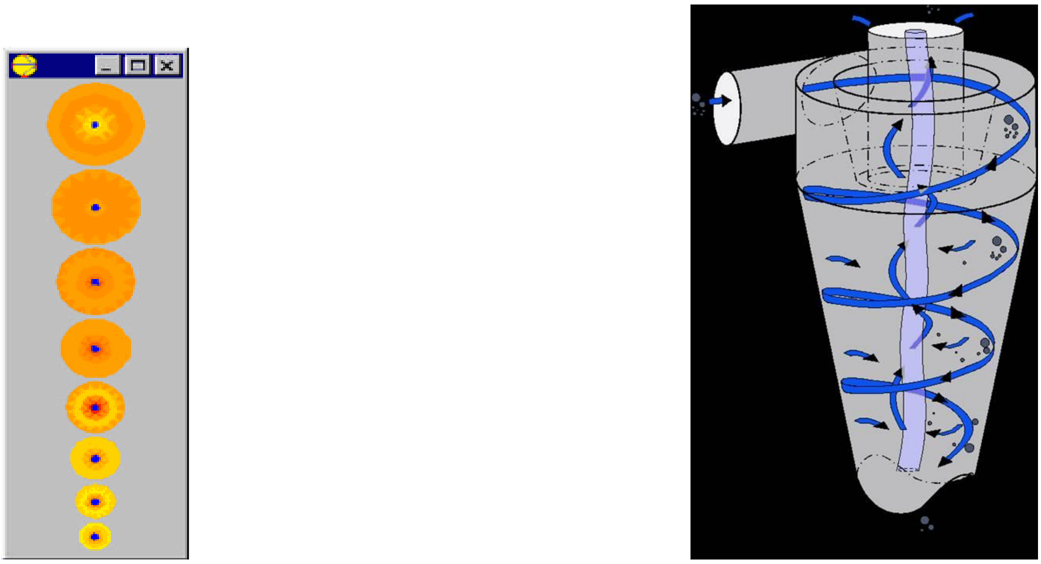

(a) (b)

(a) Tomography of a hydrocyclone reconstructed using parametric modelling (Ronson 2010).

(b) Measurement of the vortex from outside the hydrocyclone (Drupal 2010).

Figure 2.4. Measurement of Vortex in hydrocyclones using tomographic Images.

It can be observed from the ERT results that there was an increase in the extent of solids suspension as the agitation rate increases.

An application of the linear ERT system in monitoring the just-suspension speed for two impeller geometries (Table 2.1) and a number of sand concentrations, ranging from 1 to 10% by weight, was implemented in the work by Ricard *et al.*(2005). It was observed in all experimental runs that the visual estimates for the just suspended speed corresponded to the ERT predictions (Steven *et al.* 2008). Using the linear ERT system, Ricard *et al*.(2005) were able to track the extent of solid suspension for increasing agitation rate allowing real time process evaluation and optimisation (Steven *et al.* 2008)(figure 2.6).

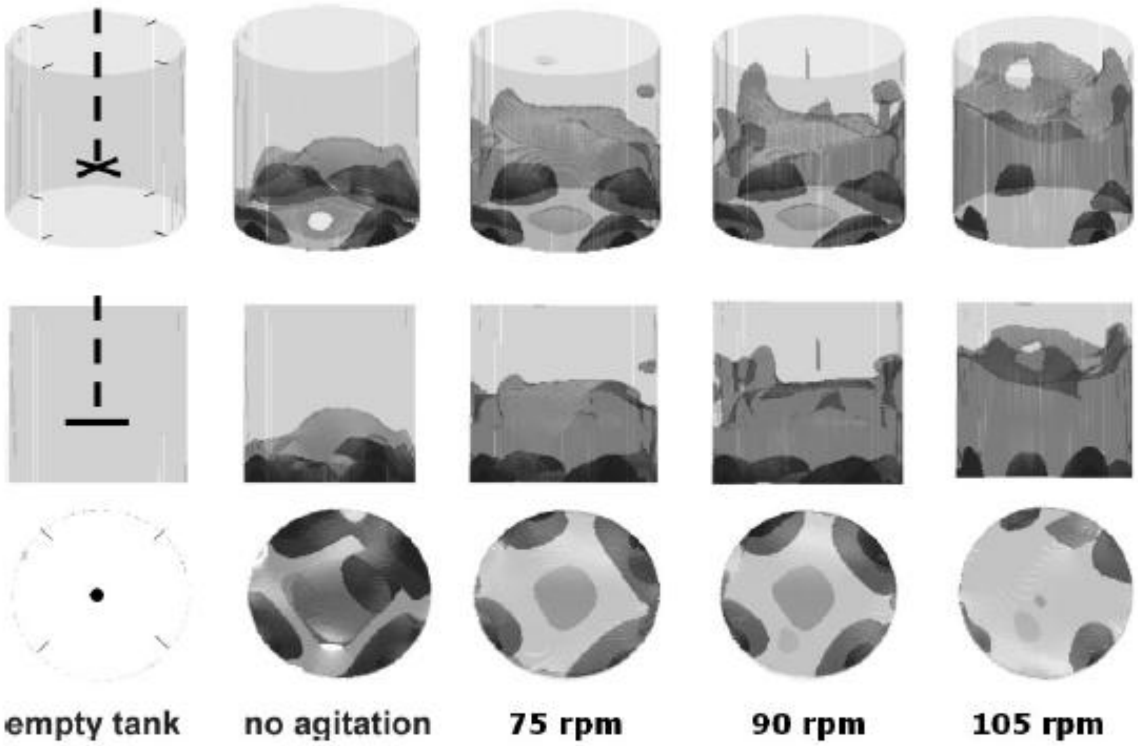

Figure 2.5. Pseudo-stationary solids mixing, agitation of 80 kg plastic pellets in a pilot plant vessel (from Mann *et al.* 2001).

Table 2.1. Summary of geometries and dimensions of the mixing configurations (Ricard *et al.* 2005).

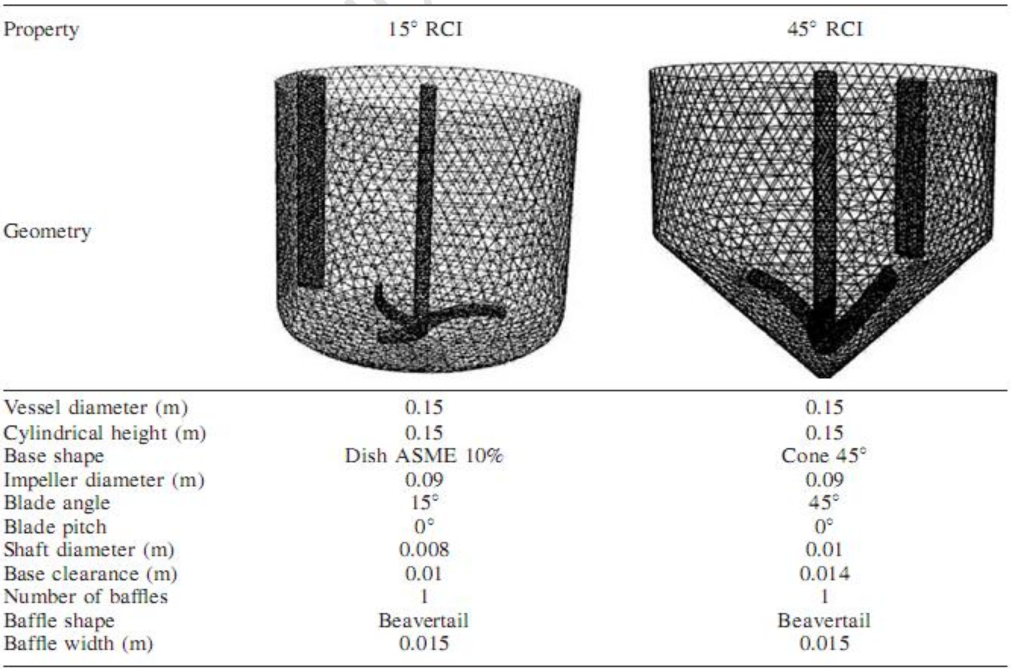

Property	15° RCI	45° RCI
Geometry		
Vessel diameter (m)	0.15	0.15
Cylindrical height (m)	0.15	0.15
Base shape	Dish ASME 10%	Cone 45°
Impeller diameter (m)	0.09	0.09
Blade angle	15°	45°
Blade pitch	0°	0°
Shaft diameter (m)	0.008	0.01
Base clearance (m)	0.01	0.014
Number of baffles	1	1
Baffle shape	Beavertail	Beavertail
Baffle width (m)	0.015	0.015

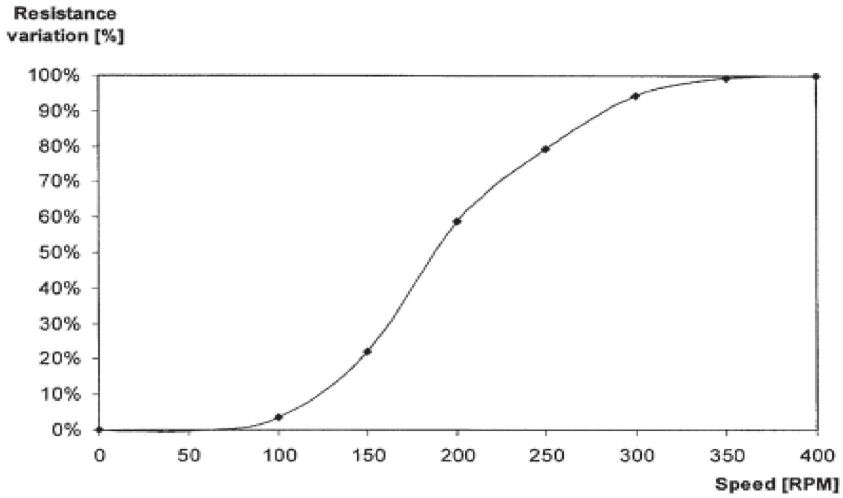

Figure 2.6. Variation of average bulk resistance with impeller speed in the 15^0 RCT system (Ricard *et al.* 2005) .

In principle, ERT can be used to investigate and monitor any process where the main continuous phase is at least slightly conducting and the other phases and components have differing values of conductivity (Drupal 2010).

2.2.3.2 Imaging Fluidised beds Using ERT technique

In a fluidised bed, a bed of solid particle is maintained in a fluid like state by passing a gas or liquid up through the bed at sufficient velocity to maintain fluid behaviour. Measurement of flow velocities to identify areas of good and poor contact in fluidized beds (Figure 2.7a) are obtained from analysis of process tomography images. One of the challenges is the measurement of the homogeneity of the fluidised bed and the presence of any waste products that may need removing, without disturbing the fluidity state of the system by inserting physical probes. ERT has been applied to image a sliding bed of sand particles in a pseudo-plastic fluid and the resulting concentration maps (Figure 2.7d) were compared with that Magnetic Resonance Imaging (MRI) (Figure 2.7b) of the same process together with a photograph of the actual transparent pipe (Figure 2.7a) within which the process took place by Graham *et al*.(2002). The ERT measurement of the process took a fraction of the time taken for MRI to do the same. Although the real time reconstructed image (figure 2.7c) is not in good agreement with the photograph as does the MRI, the image produced after an offline processing of the real time measurement compares favourably with the photograph (Steven *et al*. 2008).

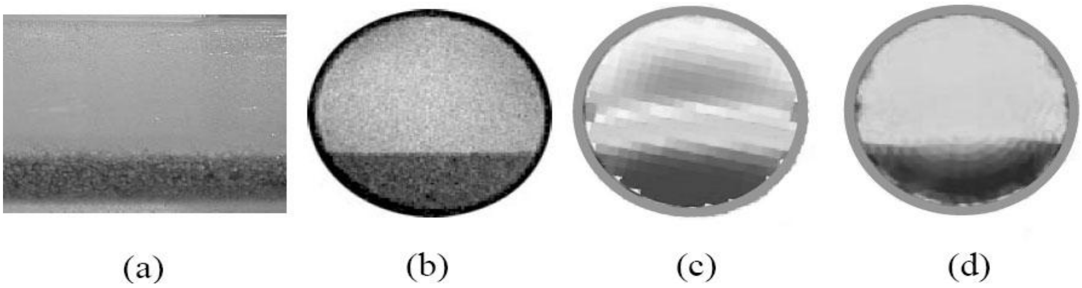

Figure 2.7. Comparison between MRI and ERT concentration profiles (a) photograph of sliding bed of sand particles in CMC (Carboxy Methyl Cellulose) taken during concentration data acquisition, (b) concentration map obtained with MRI, (c) real time concentration map obtained using ERT and (d) concentration map using ERT data and post-processing software (Steven *et al*. 2008).

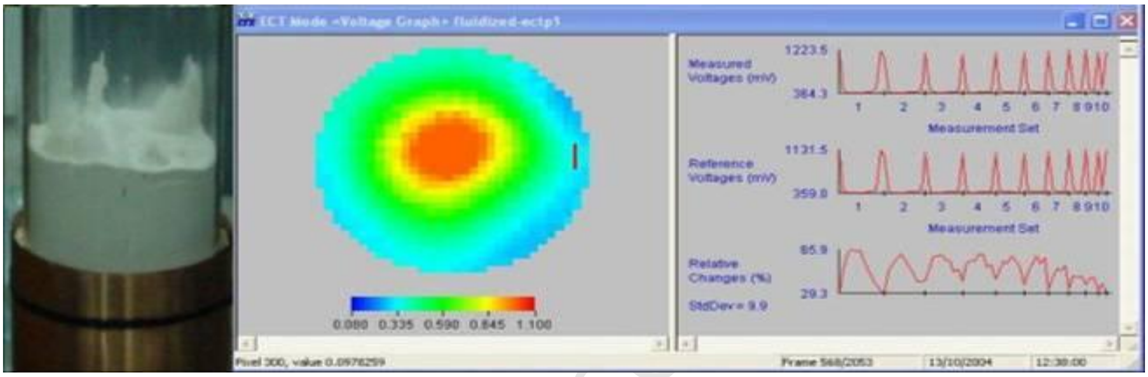

Figure 2.8(a). Fluidized beds (Drupal 2010).

Packing of catalyst, sand or some other solids which has been distributed into a vessel to form a surface is referred to as Packed beds. The packed bed provides lengthy and complex route for a gas or liquid to pass through. In the water industry, liquids may be pumped through the bed as a means of filtrations (Figure 2.8b). The central idea of packing is to encourage intimate contact of a large solid surface and a relatively small fluid volume. It is generally impossible to see what is happening inside the bed, considering the opaque nature of a packed bed, yet it is critical to ensure intimate contact of the fluids within the bed. Another requirement is to monitor for blockages within the beds or "channelling" which change the flow patterns of the fluids and reduce the effectiveness, which in turn reduces performance, decreases yield and increases costs (Figure 2.8a).

Figure 2.8(b). Packed beds (Drupal 2010).

Characterization of hydrodynamic processes in a bubble column based on superficial velocity of the gas, properties of the liquid phase , column diameter, sparger design and height of dispersion can be obtained by observing various flow patterns through the use of ERT (Figure 2.8c).

Figure 2.8(c). Bubble Columns (Drupal 2010).

2.3 ERT Hardware

A review of ERT hardware device is considered in this section. Both the conventional hardware set-up and new designs are examined with a description of the implemented measurement sequences.

2.3.1 Background Studies into ERT Hardware

Historically, practitioners of ERT have had two options, namely the development of in-house ERT instruments (figure 2.9) or the purchasing of commercially available instruments. ERT hardware components consist of process vessel or tomography rig fitted with planes of 8 or 16 electrode ring, data acquisition system and computer system. Both the computer system (PC) and the process vessel are connected to the data acquisition system in a bi-directional manner. The data acquisition system communicate with the process vessel by controlling the sequence of current stimulation and voltage measurement using the measurement sequence table downloaded into the computer system. It also communicates with the vessel by transferring the injected current and storing the measured voltage data from the vessel. The PC communicates with the data acquisition system in a two-way approach by relaying the measurement sequence table and extracting the stored measured voltage data in order to display reconstructed images, using the reconstruction code stored in the hardware of the PC as in figure 2.9.

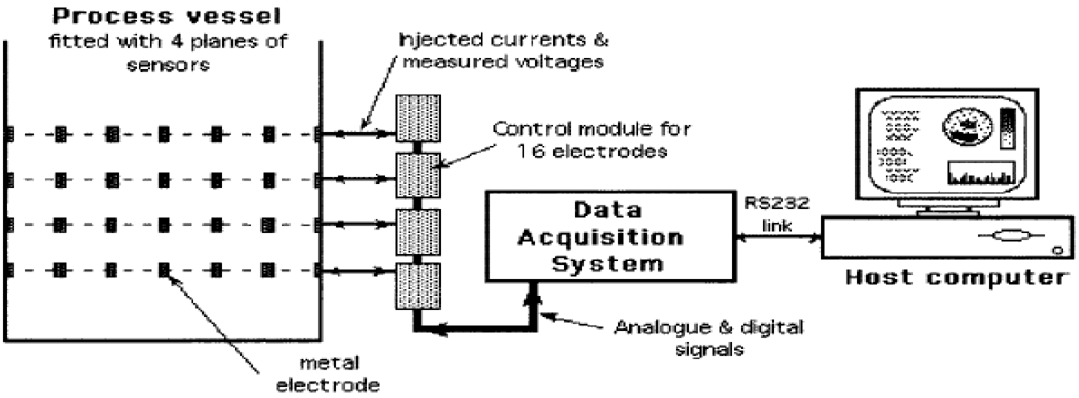

Figure 2.9. The structure of a typical electrical resistance tomography system (Fraser 1996).

A deviation from the conventional measurement strategy, involving an array of electrodes being fitted around the periphery of a multiple plane geometry in a ring-like form, was adopted by Bolton *et al.*(2002). A linear electrode array consisting of a dip stick type probe with a number of discrete electrodes equally and axially spaced was used in their work to detect and measure phases in solid-liquid suspensions. Although the underlying principle of linear electrode array design of was informed by Qiu *et al*.(1994), in which the novel technique enabled the simulation of seabed environment for laboratory experiments, it was noticed in the work of Bolton *et al*.(2002) that the linear electrode array suffers from more severe sensitivity non-uniformity compared to the circular array. During the experimental set-up, the laboratory scale linear probe (Figure 2.10b) was scaled up to incorporate the technology onto a glass lined baffle for use in an environment where the electrode material can react with the chemical compounds as in Figure 2.10(a). The measurement strategy for the linear probe was informed from the modelling of the three dimensional induced electric field carried out in the work of Bolton *et al*.(2002).

(a)

(b)

Figure. 2.10(a). Glass lined ‘Linear’ sensor for pilot reactor (Bolton *et al.* 2002).

Figure. 2.10(b). Laboratory-scale probe.

2.3.2 Background Knowledge of UCT ERT Hardware

The department of Chemical Engineering, University of Cape Town, has developed a current pulse measuring technique, simpler to implement than the conventional alternating current (AC) excited system and it is capable of high speed operation, enabling dynamic systems to be investigated (Randall *et al*. 2007). The UCT hardware allows a capture rate of up to 1000 frames/ seconds for a single 16 electrodes system and displays images at 20 fps (Randall *et al*. 2007). It has been applied for a fast approximation of the conductivity distribution in the plane of measurement in real–time by a 2D reconstruction algorithm embedded in the "on-line" control and data capture software (Randall *et al*. 2007). The C++ program which controls the system hardware provides real-time visualization and can record data for off-line analysis (Randall *et al*. 2007). According to Stephenson *et al*. (2007), using adjacent injection strategy, a frame rate range of 0.5 to 285 fps is achievable with the UCT tomography hardware.

In terms of strategy flexibility, UCT hardware has four configurations of measurement strategy, allowing current injection between any pair of electrodes on different planes and voltage measurement between either horizontally or vertically adjacent electrodes, but not opposite electrode pairs. The voltage measurement made on the peripheral electrodes are values of the isopotential lines perpendicular to the electric field, which are constituent of the isopotential surfaces (a map of points of equal potential from the reference point - earth). Thus, the isopotential surface due to a homogeneous solution will vary from that due to an inhomogeneous solution and this perturbation to the isopotential lines or surface due to inhomogeneity of the solution will take place in three dimensions.

More so, a signal-to-noise ratio range of 65 db at 1 frame per second through 45 db at 285 frames per second is achievable with the UCT hardware set-up. When the UCT tomography hardware is in operation, a range of fluid conductivity is obtained by adding incremental quantities of sodium chloride to deionised water. It has a conductivity range of 0.04mS/cm at 41 db to 60mS/cm at 37db (Stephenson *et al.* 2007). The excitation of the conductive solution contained in the UCT rig is done through a constant current driven into the electrode system (typically from 2mA to 2.5mA) via multiplexers. The total impedance presented to the constant current source and sink that pushes and pull the current from the selected electrode pair via four way multiplexers, is due to the sum of all the multiplexer resistances connected in series, plus the electrode impedance. The value of the total impedance may vary between 100Ω and 1Ω depending on the electrode size and solution conductivity. In order to maximize the current that the constant current source delivers to the electrode system, it is recommended that the total impedance, "on resistances", should be low so as to reduce the voltage drop due to the multiplexers module and the electrode in contact with the solution. This is achieved with the inclusion of high input differential amplifiers in the current pulse ERT system.

2.3.3 Implemented Measurement Sequences In ERT

In respect of the linear probe ERT hardware, an adjacent measurement strategy was implemented with the injection of constant amplitude current in the top and bottom electrodes on the sensor. The induced voltage differences due to the injection were measured between the neighbouring electrode pairs, leaving out the pair through which current was injected. Subsequently, the same magnitude of current amplitude was injected between the first pair of neighbouring electrodes, for example, electrode 1 and electrode 2, with the resulting voltage difference measured between the remaining electrodes. This scheme of current injection and voltage measurement was repeated for every other pair of electrode combinations. In other words, there were $n(n-3)/2$ possible independent measurements for n electrodes in an adjacent array. Bolton *et al*.(2002) used data sets recovered from the linear electrode probe to reconstruct tomography images using a sensitivity coefficient back-projection algorithm to better understand the change in conductivity from a previously acquired 'homogeneous' situation.

The UCT tomography system set-up includes a measuring rig consisting of a non-conducting cylindrical vessel container, fitted with 8 rings of 16 equally spaced copper electrodes in a ring. The tomography hardware distinguishes itself from that developed elsewhere in that it has an in-built multiplexing system which allows capture from 128 electrodes. Programming of the measuring sequences with which a full 3D data sets can be recorded, as well as its high speed capability was developed by Wilkinson *et al.* (2003).

The architecture of a basic ERT system (figure 2.12) is such that a current source and sink are applied to adjacent pairs of electrodes via the current multiplexers and the induced outer boundary voltages, determined simultaneously by 16 differential amplifiers which are hard wired to adjacent electrode pairs, are recorded (Randall. 2007). For each current injection on an adjacent pair in a plane, sixteen (16) measurement sequences were made on all the electrodes in the same plane (figure 2.13). The measured data set for an adjacent measurement scheme is in form of a "U curve" as shown in figure 2.13. Each "U curve " is a frame from which a single image may be reconstructed. In its full operational mode, the UCT ERT set produces data rates of 1000 frames/second from a single ring of 16 electrodes. At present, images are reconstructed from these data sets in less that 1ms and are being updated on the computer system at 20 frames/second (Randall. 2007).

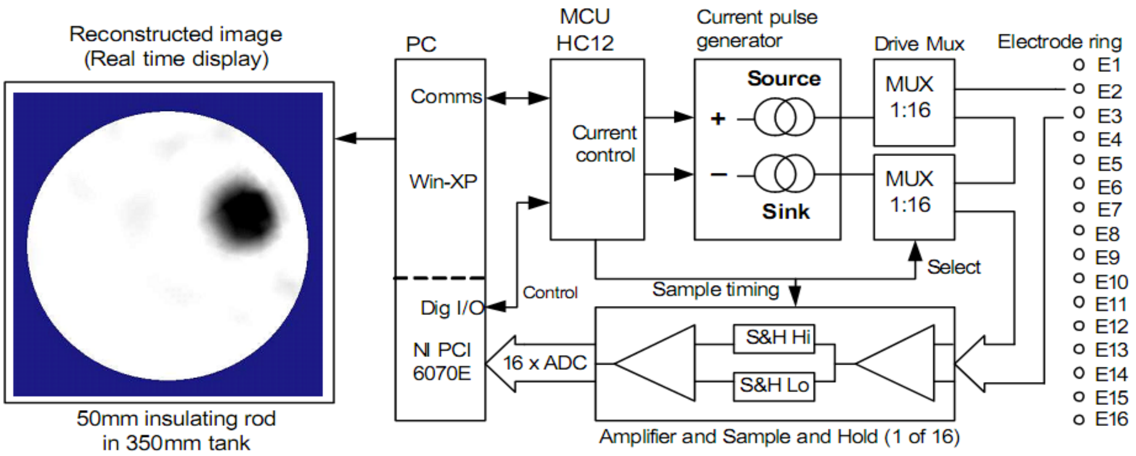

Figure 2.12. Basic current pulse ERT system for single ring of 16 electrodes (Randall. 2007)

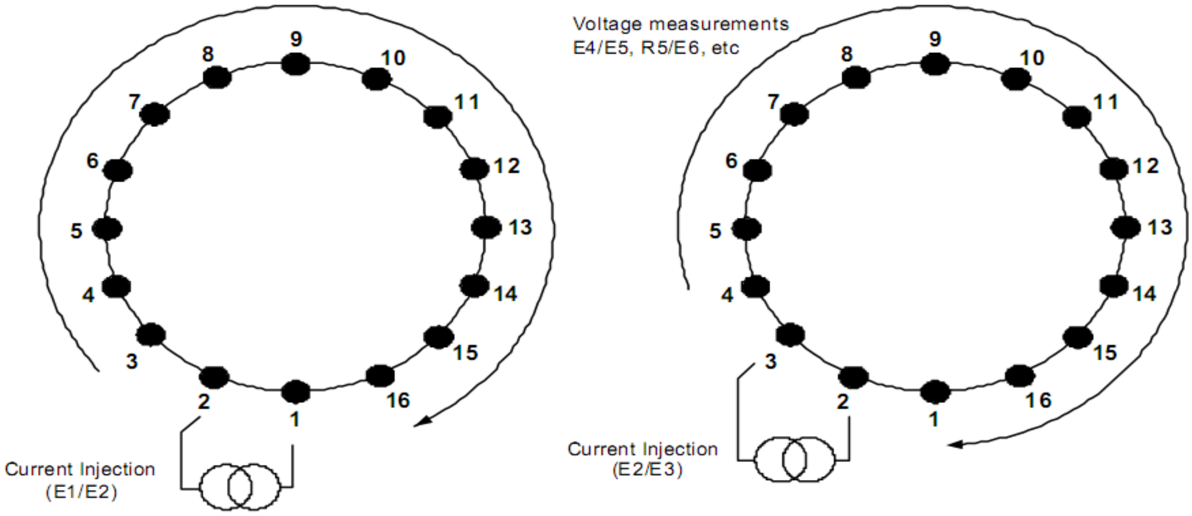

Figure 2.13. Adjacent pairs measuring sequence for a 16 electrode system.
The figures show the first two positions of the current injection sequence.
Output from the 16 amplifiers is recorded for each of the 16 current injection positions (Randall. 2007)

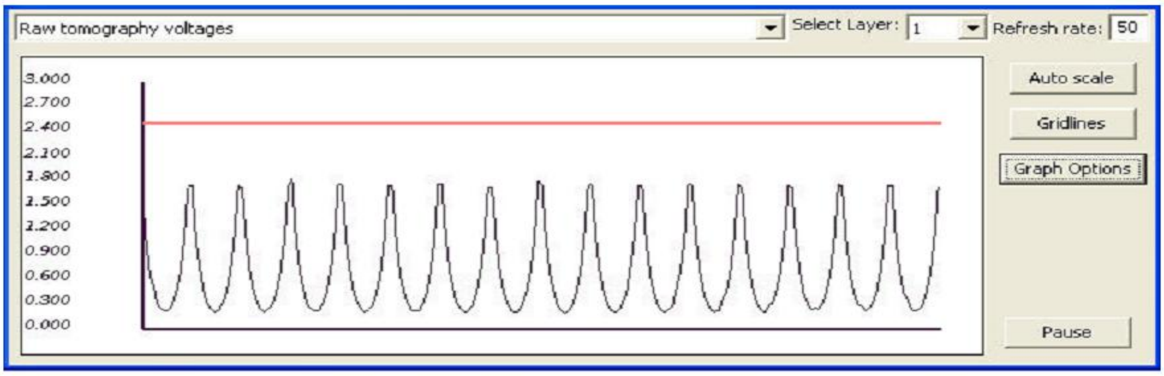
Raw tomography voltages
Select Layer: 1
Refresh rate: 50

Figure 2.14. Data set for single frame as displayed by the real time software. Data is for homogeneous system and therefore symmetrical. Each “U curve” is data recorded during single current injection cycle (Randall. 2007).

An improvised version of the basic ERT architecture of figure 2.12 was improved upon in terms of capability of the device to implement an alternative current injection and measuring sequences other than the single plane measurements by connecting in parallel a flexible and extendable multiplexing system to the electrode array, as shown in figure 2.15. With the addition of a single multiplexer (figure 2.15), the instrument allows simultaneous (2-D) data acquisition from up to eight rings of 16 electrodes and as such the device can be used in pipe-line flow measurements (Randall. 2007). On the other hand, when four multiplexers modules are connected in parallel to the electrode array, the current pulse may be applied between any of the 128 (8 x rings of 16) electrodes and measurements made between either adjacent electrodes on the same layer, or “vertically adjacent” electrodes on different layers (figure 2.16)(Randall. 2007). To obtaining an alternative set of current injection pairs or alternative voltage measurement scheme on the peripheral electrode, such as opposite pairs of electrode measurement, the "key-card" in the current pulse device needs to be replaced. Depending on the spatial geometry of the measuring vessel and the disturbance under investigation, suitable injection and measurement sequences are defined by sequencing tables, downloaded to the instrument from a PC.

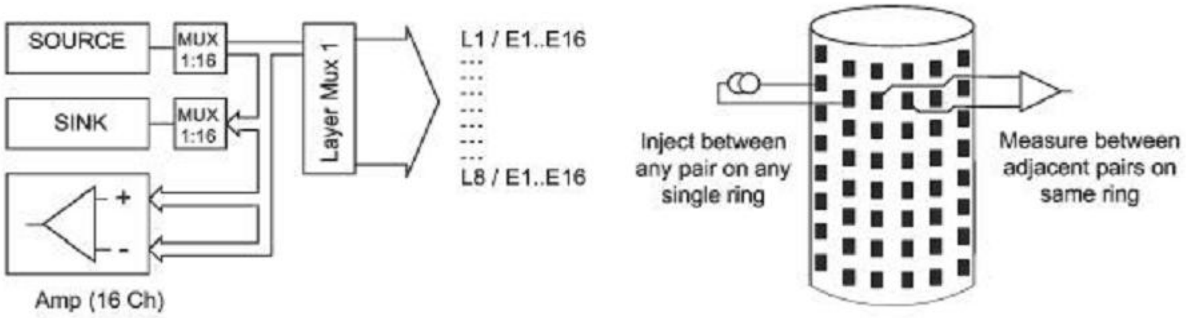

Figure 2.15. Multiplexer enabling data capture from 8 independent rings of 16 electrodes(Randall. 2007).

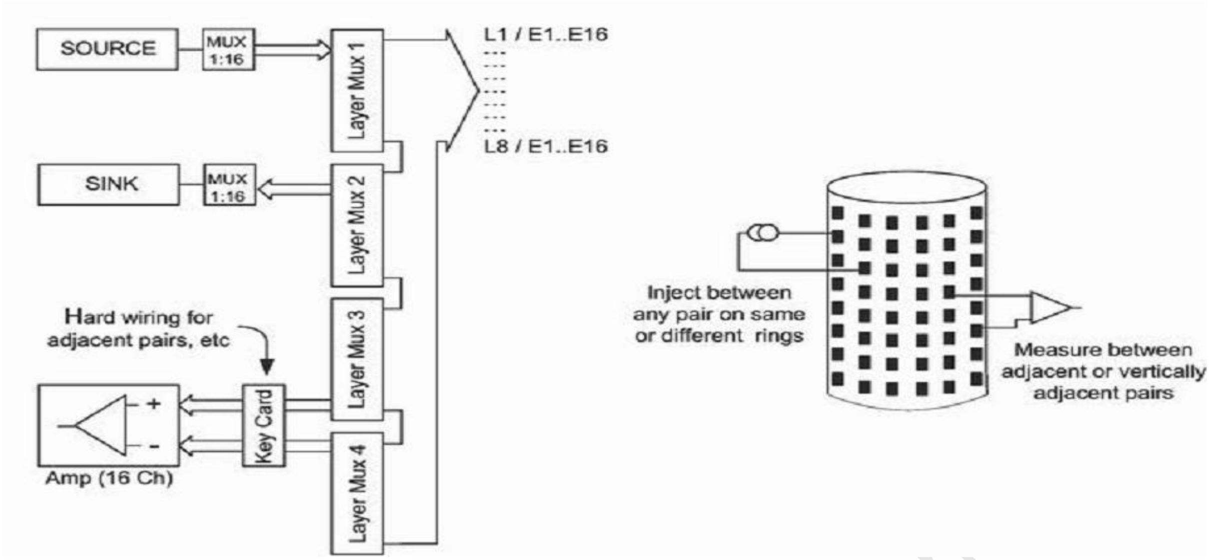

Figure 2.16. Full implementation of the multiplexing system which enabled programmed data capture sequences for full 3D image reconstruction(Randall. 2007).

2.3.4 Comparative Evaluation of Various ERT Devices

The performance requirement of three readily available ERT instruments has been carried out by Stephenson (2007) in order to outline future requirements of process ERT systems. The ERT systems are the Industrial Tomography Systems (ITS) P2000 from the University of Manchester Institute of Science and Technology (UMIST), the LCT instrument from the University of Manchester/Syngenta and the University of Cape Town tomography systems. The LCT instrument is the most flexible of the three instruments; users have total flexibility to create custom measurement strategies where both current injection and voltage measurements may be made between any of the 64 electrodes available, in either regular or irregular geometries.

From the comparison, it was clear that both the ITS P2000 and the UCT instruments do not display a linear response over the conductivity range studied. The linear instrumentation response is measured by the degree at which the voltage data presented to the algorithm maintains the same qualitative shape at various conductivities when there has been a step change in homogeneous conductivity for a difference based reconstructed image. The LCT study was particularly linear with the voltage curves overlying virtually perfectly. The mean percentage error of linearity of measurement was found to be 29.6% for the UCT instrument, 22.2% for the ITS P2000 instrument and 1.7% for the LCT instrument. The features of the instruments are the reasons for their respective preferred applications. The LCT instrument is suitable for slowly varying processes that require an indication of homogeneity. A fast process not requiring homogeneity such as flow regime identification and cross correlation technique might be best suited to the UCT instrument, while a mixing studies that require a relatively high frame rate but also the identification of homogeneity should perhaps employ ITS P2000 (Stephenson *et al.* 2007).

2.4 ERT Software

Image reconstruction technique of ERT is based on solving an inverse mathematical problem using numerical tools such as finite difference or finite volume or finite elements. Suitable numerical tools for ERT is expected to model the complex geometries used in many ERT analysis given the degrees of freedom associated with each nodal point. An overview of various open source applicable code with a description of the architecture of these codes are given in this section.

2.4.1 Applicable Software In Electrical Resistance Tomography

The EIDORS (Electrical Impedance and Diffuse Optical Reconstruction Software) is an open source software suite for image reconstruction in electrical impedance tomography and diffuse optical tomography, designed to facilitate collaboration, testing and new research in this field (Adler *et al*. 2005). MATLAB is a software that is used in the EIDORS project for rapid prototyping, graphical user interface construction and image display (Marko *et al*. 2000). EIDORS utilises MATLAB, installed on either Windows or Unix/Linux operating system, for two-dimensional mesh generation, solving of the forward problem, reconstruction and display of the images (Adler *et al*. 2005). An improved version of EIDORS with the capability to solve 3D reconstruction models is EIDORS3D. It is a software that facilitates research in the field of image reconstruction by providing a reference implementation, against which new developments can be compared, and by providing a functional software base onto which new ideas may be built and tested (Adler *et al*. 2005). The current version of EIDORS3D works with Octave (www.octave.org, version≥ 2.9.3) and Matlab (version ≥ 6.0) (Adler *et al*. 2005).

Modelling the resistivity distribution in the interior of a process vessel will require discretising the domain of interest into discrete elements. While there are many two-dimensional mesh generators written by various authors, such as Mitchell and Vavasis (2000), three-dimesional mesh generators are few, which include Distmesh and NETGEN, to which EIDORS version 3.3 has interfaces to. These mesh generators enable the export of the meshes in a format that can be easily imported in MATLAB. In most two-dimensional mesh generators, a tree data structure, quadtree, is used to partition a two dimensional space by recursively subdividing it into four regions or quadrant mesh generators are utilized. These make constrained meshes which are useful if one has some a priori known internal structures, such as human skull layer (Marko *et al.* 2000). A demerit in the use of the quadtree approach instead of the popular Delaunay triangulation is that the element quality in the

Delaunay meshes is superior compared to the quadtree meshes. However, the properties of Delaunay meshes cannot be extended to 3-D which makes it difficult to apply Delaunay approach in 3-D (Marko *et al.* 2000). In some cases, mesh smoothing have been used to produce better quality meshes (Field 1988). An automatic 3-D mesh generator such as NETGEN discretises a cylindrical domain of into a finite number of tetrahedra of varying sizes. The density of the mesh vary from a fine mesh near the boundary of the vessel to a coarse mesh towards the centre. In modelling the initial resistivity distribution, each tetrahedron is given a fixed value and the inverse problem is solved over the tetrahedra elements. The resistivity difference relative to the initial distribution based on the optimisation of the measured voltage with the simulated voltage is computed for each tetrahedron.

2.4.2 History of EIDORS

An Electrical Resistance and Diffuse Optical Reconstruction software, EIDORS (version 1), which implements MATLAB code library, was released in 1999, from the thesis of Vaukhonen in 1997 (Adler 2008). It has a capability of 2D mesh generation, solving the forward problem, inverse problem (image reconstruction) and displaying images (Adler 2006). The need for a 3D image reconstruction software motivated more research. EIDORS 3D (version 2) was released in 2002 from the thesis of Polydorides (Adler 2006). However, EIDORS 3D (version 2) lacks modular software structure so that researchers have to make changes to the original code itself (Adler 2006). This shortcoming was improved upon in EIDORS 3D (version 3) released in 2005 (Adler 2006). It included the following features: a provision of modular components which could be ``plugged'' into a selection of reconstruction algorithms, multiple algorithm support, and generalised mode format and interface software for common EIT systems (Adler 2005). Additionally, it included usage examples, test suites, open source license and language independence (i.e. From MATLAB only to octave (version ≥ 2.9.4) and MATLAB (version ≥ 6.0)) . Also, it has a pluggable code base which enables use of function pointers to allow adding new modules and controlling which parts of the function are executed and an automatic matrix caching. It also allows saving and reusing values of computationally expensive variables, such as the Jacobian and image priors (Adler 2005).

EIDORS 3D (version 3.3), released in 2008, contains the following high-level features: Interface to FEM generation tools (NETGEN and DISTMESH), a support for dual model solvers, new reconstruction algorithms (total variation, electrode movement solver, temporal solvers), data repository (with several contributed models, clinical and experimental data sets, faster algorithms (Jacobian computation, better caching, an iterative forward solver) as well as improved graphics and extensive tutorials (Adler 2008).

2.4.3 EIDORS' Architecture

EIDORS has two software architectures. Namely, object structure and software structure. The object structure consists of four primary objects: data, image, fwd_model and inv_model with properties $name$ and $type$. The $name$ is used to distinguish an object in a function, while the $type$ is used to identify object type (i.e. data or image). For example, the structures of the EIDORS fwd_model, inv_model, data and image objects are Figures 2.17 - 2.20 respectively.

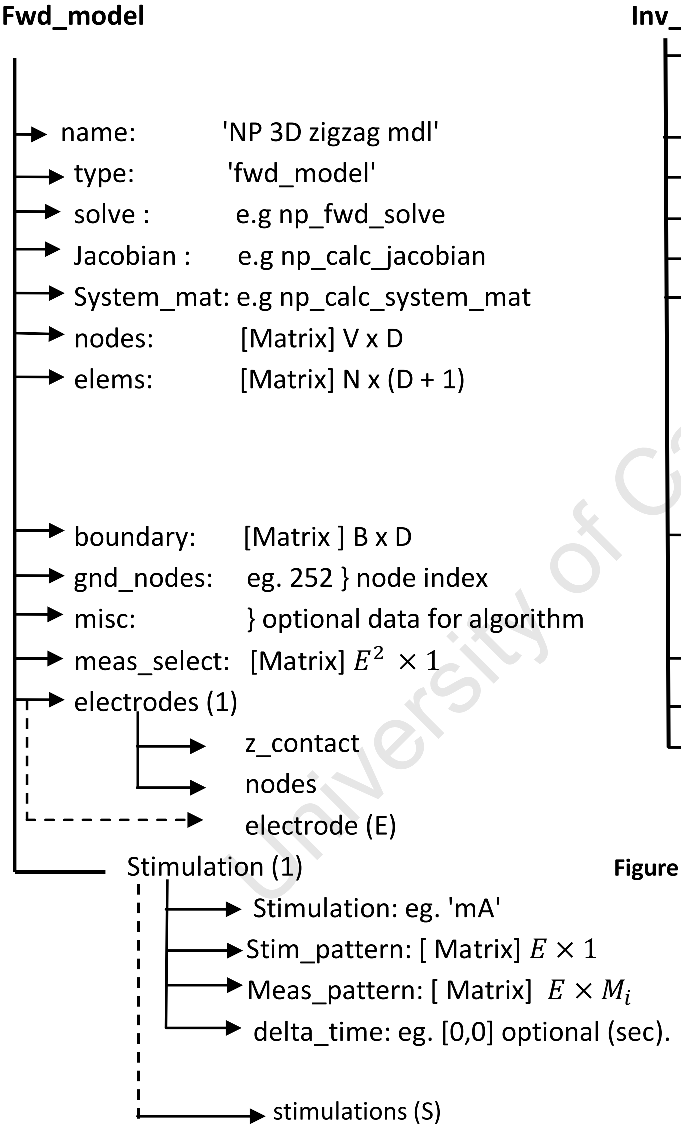

Figure 2.17. Structure of EIDORS forward problem solver

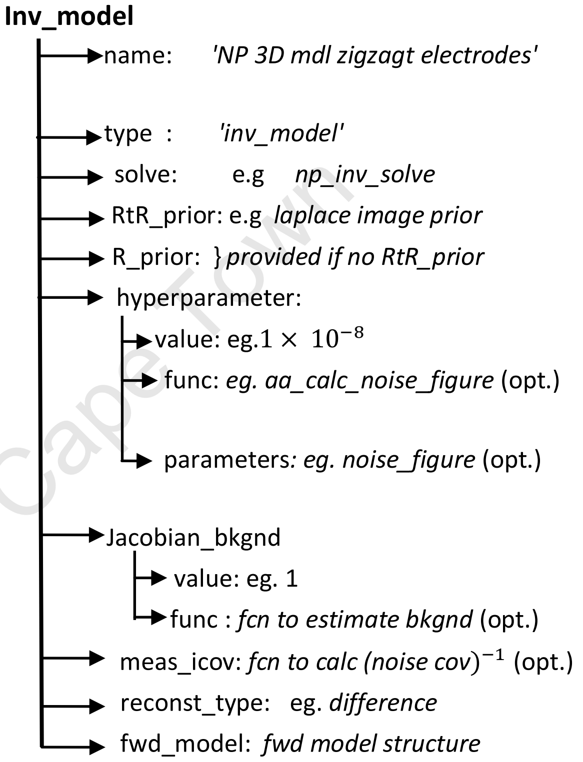

Figure 2.18. Structure of EIDORS inverse problem solver

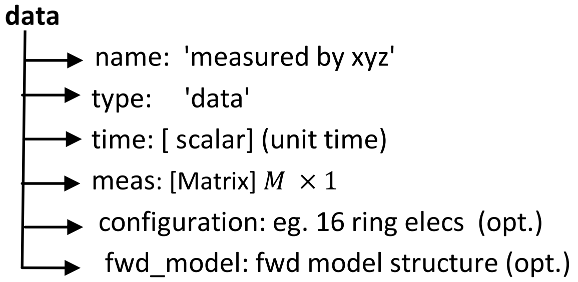

Figure 2.19. Structure of EIDORS data object

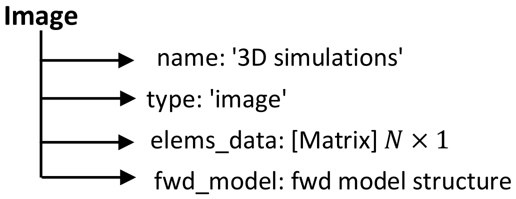

Figure 2.20. Structure of EIDORS image object

Since the Jacobian matrix, a forward model operator, relates the forward problem to the inverse problem, it is required that we consider how the Jacobian matrix is computed in EIDORS. In EIDORS, Jacobian or sensitivity matrix, J, is computed as follows. Given a FEM model of an EIT medium, F, we calculate the vector of voltages, v, for each FEM degree of freedom (mainly, degree of freedom are nodes, but in complete electrode model, electrodes are also associated with a degree of freedom) (Adler 2006). That is v = $F(\sigma, q)$, where σ is the vector of element conductivities and q is the current stimulation pattern, a vector of current inputs of each degree of FEM degree of freedom. The measured electrode voltage can be represented as a linear combination of voltages,V_{toE}. For each stimulation pattern, q_i, a vector of measurements m_i are required, each of which consist of a linear combination of electrode measurement represented by M_i. Thus,

$$m_i = M_i V_{toE}(\sigma, q_i) \tag{2.63}$$

Based on this model, J is calculated as :

$$J_{ij} = \frac{M_i\, V_{toE}\, \partial F(\sigma,q_i)}{\partial \sigma_j} |_{\sigma=\sigma_o} \tag{2.64}$$

where σ_o is the *background* conductivity around which small changes are assumed to occur (Adler 2006). To represent J as a matrix, measurements for all stimulation patterns, i , are flattened into column vectors which are concatenated for each finite element j. In EIDORS, the Jacobian is calculated using the function calc_jacobian which takes as parameters the FEM model (type fwd _model) and the image of *(type* image) (Adler 2006). Considering the object structure of EIDORS, the eidors_obj () function in used to create an object, which fill in default attributes and keeps track of cached properties. For instance, a homogeneous background image of conductivity one named *img_bkgnd*, may be computed given the *fem_model* as *fem* as follow:

img_bkgnd= eidors_obj('image', 'homo bkgnd');
img_bkgnd. elem_data = ones(length (fem. elems), 1);
img_bkgnd. fwd_model = fem;

The above expression specifies that the $type$ field is assigned to $image$ and the name is assigned (arbitrarily) to $homo\,bkgnd$. Calculating the Jacobian will require the calling of the function $calc\_jacobian$ as in

$$J = calc\_\ jacobian\ (\ fem, img\_bkgnd\ ).$$

The function first tests to check if J has been previously calculated for fem and img_bkgnd. If it has, the cached value is returned; otherwise , it loads and call the function in $fem.jacobian$, which may be $np\_calc\_jacobian$.. $np\_calc\_jacobian$ in turn calls the function from the software of Nick Polydorides (2002) (Adler 2006).

As illustrated in the aforementioned ERT measurement principle of section 2.2.1 and the implemented measurement sequences in ERT of section 2.3.3, 2-D measurement strategy with respect to modelling of the electric flux as a curve instead of surface has been obtained. Similarly, analysis of the 2-D imaging has enhanced further researches as stated in section 1.1 in the Department of Chemical Engineering, UCT. In reality, however, of much interest to the medical and industrial application is 3-D imaging since current flow out of the planes of electrodes in 3-D as confirmed by Jossinet and Kardous in their multi-electrode phantom study. More so, following the suggestion by Pinheiro (1998) that a 3-D data collection should be taken over the whole periphery of the domain in an independent manner for qualitative imaging, obtaining such a 3-D measurement scheme is paramount in this work.

Furthermore, although reconstructed images based on 2-D algorithm have been applied in diverse chemical processes as described in section 2.2.3, 3-D reconstructed images have not found many applications other than that recorded by Mann (2001), section 2.2.3.1. The few applications of the 3-D algorithm for visualising the interior conductivity distribution is related to the resolution of the images that are yet to be quantified. This is addressed in this research with a view to ascertaining the optimal 3-D measurement scheme for the UCT ERT vessel.

CHAPTER 3

MATHEMATICAL DEVELOPMENT

3.1 Description of Sequence of Operations in Image Reconstruction

It is necessary to give a brief description of each stage in the flow of processing and computation involved in solving the non-linear and ill-posed inverse problem of image reconstruction through an iterative technique, as illustrated in the flow chart of figure 3.1.

3.1.1 Electric stimulus (current injection)

The electric stimulus suggests the application of the current pulse measuring technique on the surface of the measurement vessels through the injection of current on pairs positioned within a ring or planar rings that are held firmly on the exterior body of the measurement vessels. From a list of various measurement schemes based on the electrode definition such as adjacent injection, opposite injection or planar injection, a specified value of miliamperes of current will be applied between electrode pairs.

3.1.2 Regularization Matrices and Prior Information

The second stage in the flow of computation is setting up the prior information. The inverse problem is posed in the form of an examination of the effects recorded at the boundary of a domain due to perturbation of the homogenous state of the medium within the domain in order to resolve the cause of the perturbation . In a well posed problem for any set of rational observation, the solution should have the following properties:

(1) A solution consistent with the observations exists.

(2) The solution is unique.

(3) The solution depends continuously on the observations (Polydorides 2002).

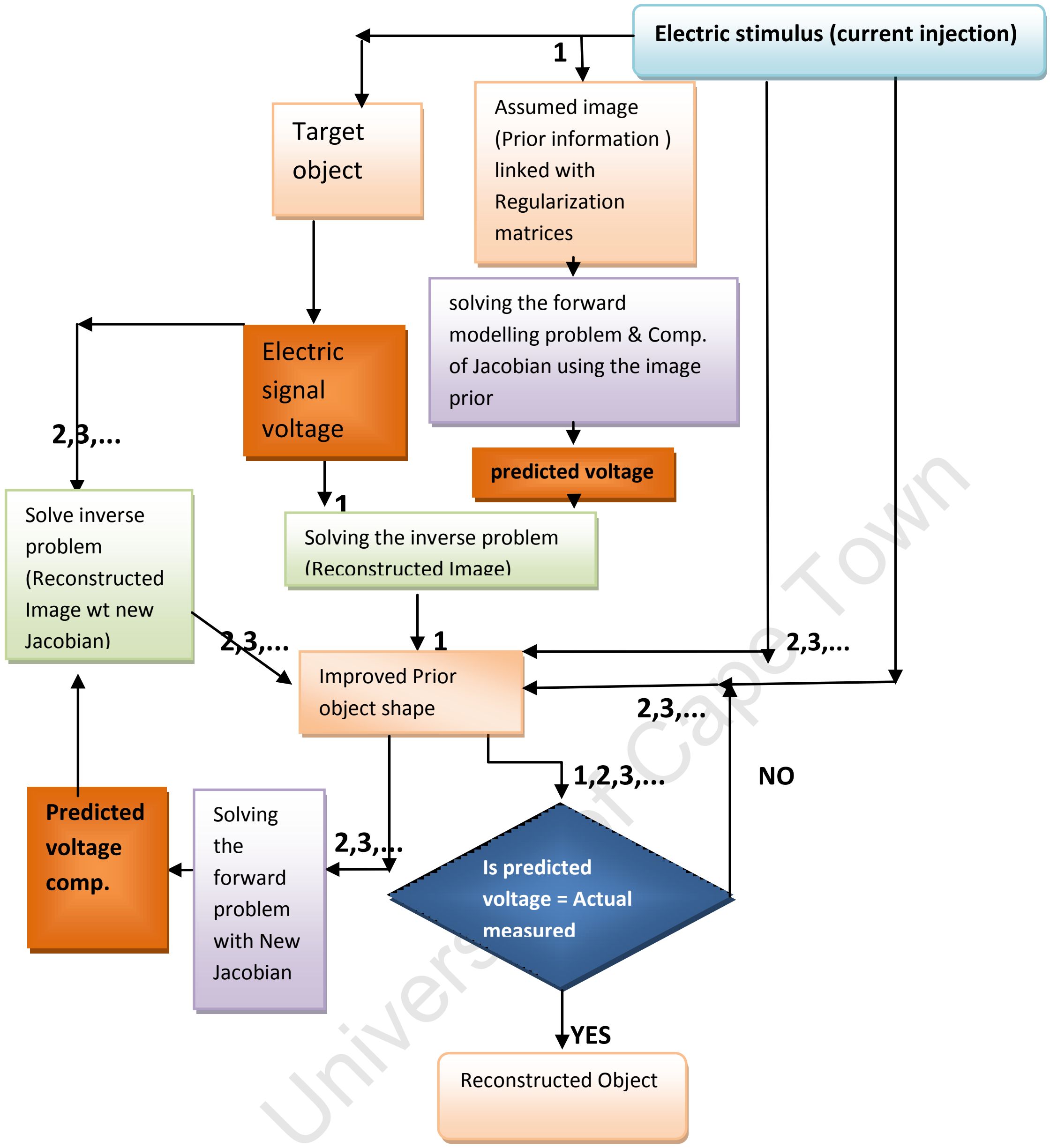

Figure 3.1. Flow chart for image reconstruction

Note: 1,2,3,... specifies the indices of the iterations.

Although some naturally imposed constraints may somehow ensure the validity of the first two criteria, it certainly fails the third one because even small perturbations in the measurements can lead to wild oscillations in the solution. Thus, the inverse conductivity problem is ill-posed.

Ill-posed problems are often addressed by replacing them with one which is somewhat different but less ill-posed. It contains more information than the ill-posed problem. Regularisation is a mathematical method for opting to address the ill-posed inverse problem by solving a similar one that is less demanding due to sufficient information. The prior information about the solution is provided to the inverse problem through the regularisation technique. The concept of regularisation acts as a constraint preserving the existence and the uniqueness but also the stability of the solution (Polydorides 2002).

In forming regularization matrices, the first or the second difference matrices can be used as such that the first difference matrices draws the solution of the Tikhonov regularized version of the EIT inverse problem towards a uniform distribution and the second difference draws the solution towards the combination of a uniform and a planar distribution. The Tikhonov regularized versions of the EIT inverse problem can be written in the form

$$\min_{\rho}\{|| V - U(\rho)||^2 + \alpha||L\rho||^2 \} \qquad (3.1)$$

where ρ is the resistivity distribution , $U(\rho)$ is the resistivity to potential mapping , that is, the potential obtained from the model with known ρ, V are the measured potentials, L is a so-called regularization matrix, and α is a regularization parameter (Vauhkonen 1998). In other words, the Tikhonov regularization method draws the solution toward the null space $\mathcal{N}(L)$ of the regularization matrix L. In this sense, the uniform distribution and the combination of a uniform and a planar distribution form the basis for the null spaces of first and second difference matrices respectively.

Similarly, the regularization matrix can constructed from a prior information of the true resistivity distribution in a way that the solution is drawn towards the known distribution by the regularization .

3.1.2.1 Basis Constrained Method (BCM)

In BCM the subspace S_w needs to be constructed, near which the true solution is assumed to lie. A more detailed description of how this is done can be found in Vauhkonen (1998). Data acquired from other sources, such as Magnetic Resonance Imaging (MRI) experiments or from earlier measured resistivity values are used to form a set of expectable resistivity distributions (vectors) ρ_n,$n = 1, \ldots, N$, near which the true resistivity distribution is assumed to be (Vauhkonen 1998). This type of a set of distribution is sometimes called the learning set. We assume that this set is comprehensive in the sense that any expectable impedance distribution is very near (in the Euclidean metric) to either one of the members ρ_n, or some linear combination of these members (Vauhkonen *et al.* 1998). Accordingly, the set can also be said to define a prior model. In BCM a low-dimensional subspace (with a predetermined dimension M) in which the set $\{\rho_n\}$ can be approximated with smallest two-norm is determined (Vauhkonen *et al.* 1998). For the set $\{\rho_n\}$, we calculate the covariance matrix Γ

$$\Gamma = N^{-1}\hat{\rho}\hat{\rho}^{T} \qquad (3.2)$$

where the matrix $\hat{\rho} = [\rho_1 \ , \ldots , \rho_N \ ] \in R^{P \times N}$ (3.3)

where P refers to the number of discretized elements in the finite element mesh (Vauhkonen 1998). One needs to calculate the M largest eigenvalues and the corresponding orthonormal eigenvector $w_m, m = 1, \ldots, M$ of Γ in order to find the $\mathrm{M} << N$-dimensional subspace in which the learning set can be approximated with the smallest mean square error. This can be done using the orthogonal iteration method (Golub, 1989). The implementation of the orthogonal iteration method has the advantage that one does not have to evaluate Γ or the calculation of all the eigenvectors and the eigenvalues associated with Γ. These M eigenvectors span the subspace S_w (Vauhkonen, 1998). This kind of a procedure is widely known as Principal Component Analysis (PCA) (Jolliffe 1986). The selection of the subspace dimension M is a compromise between good approximation properties (large M) and a good regularization properties (small M) (Vauhkonen 1998).

3.1.2.2 Subspace Regularization Method (SSRM)

Subspace regularization method requires the minimization of the functional, statement of the inverse problem, with respect to ρ and the use of the regularization matrix L whose null space is S_w. The orthogonal projector onto S_w is (due to the orthonormality of $\{w_m\}$) WW^T and the orthogonal projector onto the orthogonal complement is, thus

$$L = 1 - WW^T \qquad (3.4)$$

where I is the identity matrix and W is the matrix having the vector $w_m, m = 1, \ldots, M$ as its columns (Vauhkonen 1998). Constructing the vectors, $\rho \approx WW^T\rho$, that conform to the prior model approximately, for such ρ we have $(I - WW^T)\rho = \rho - WW^T\rho \approx 0$ and such ρ "are favoured." On the other hand, we have $\rho = WW^T\rho + (I - WW^T)\rho$

where the two projectors are orthogonal and, thus

$||\rho||^2 = ||WW^T\rho||^2 + ||(I - WW^T)\rho||^2$ (Vauhkonen *et al.* 1998). (3.5)

This informs that the smaller the value of the norm $||(I - WW^T)\rho||$, the greater the fraction of ρ is "explained " by the subspace associated with W and the smaller is the resulting penalty. In the limit α → ∞ we have then for the estimate

$$WW^T \rho^{e}_{\propto} = \rho^{e}_{\propto} \qquad (3.6)$$

so that we force the estimate into the subspace that is spanned by the column vectors of w (here e refers to the norm of the additive noise) (Vauhkonen *et al.* 1998). In this way, the idea of using

$L = 1 - WW^T$ for the regularization matrix is equivalent to using the distance of the solution ρ from the subspace S_w as a penalty.

3.1.2.3 Standard Tikhonov Regularization Method (STRM)

The regularization matrix is a diagonal weighting for J^TJ and the equation for the increment $\Delta\rho_i$ is

$$\Delta\rho_i = (J^T\ J + \propto diag(J^TJ))^{-1}[J^T\ (V - U(\ \rho_i)\ )\ ]$$

in STRM where J is the Jacobian of the mapping $U(\ \rho_i)$ and $diag(.)$ denotes the diagonal matrix. In this case diagonal matrix can be thought of as representing an approximation for the missing part of the second derivative of the mapping $U(\rho)$ (Vauhkonen *et al.* 1998).

3.1.3 Forward Modelling and Computation of the Jacobian

In addressing the forward problem in ERT that requires the computation of voltages on peripheral electrodes, one needs to construct the global admittance or system matrix, a function setting up the current patterns and solving the forward model at a certain level of tolerance, eventually extracting the array of boundary measurements (Polydorides 2002). The interior electric fields are also required in the calculation of the Jacobian, which is needed for reconstruction. Marko *et al.* (2000), Paivi *et al.* (1999) and Blue *et al.* (2000) stated that in order to solve the forward problem in a domain with a resistivity distribution, the potential distribution should satisfy the elliptic partial differential Poisson equation with the Dirichlet and Newmann boundary conditions, using a gap-electrode model approximation instead of the continuum electrode model approximation. In a domain Ω with an admittivity distribution $\xi \epsilon C^k$, the electric potential, *u*, satisfies the elliptic partial differential equation

$$\nabla \cdot \xi \nabla u = 0, \qquad (3.7)$$

If I_l is the current injected into the l_{th} electrode E_i which has a constant impedance z_l, the complete electrode boundary conditions are

$$V_l = u + Z_l \xi \frac{\delta u}{\delta n} \qquad (3.8)$$

$$I_l = \int_{E_l} \xi \frac{\delta u}{\delta n} ds \qquad (3.9)$$

where V_l is the constant voltage on electrode, E_l, n is the outward unit normal vector and

$$\xi \frac{\delta u}{\delta n} = 0 \qquad (3.10)$$

the current density on the boundary inter-electrode gap (Polydorides, 2002). Equation (3.8) and (3.9) are the Dirichlet boundary conditions while equation (3.11) specifies the Newmann boundary condition. In order to solve equation (3.7) using the finite element method (FEM) over the entire domain, it has to be transformed to the weak form.

Firstly, let consider the weak form for the Dirichlet problem. For a Dirichlet problem

$$-\nabla\cdot(k\nabla u) = f \quad \text{in} \quad \Omega \qquad (3.11a)$$

$$u = 0 \quad \text{on} \quad \delta\Omega \qquad (3.11b)$$

If f is continuous and u is a solution of (3.11), then it is natural to expect that the u and its partial derivatives of orders one and two are all continuous on Ω and of course, u is zero on $\delta\Omega$. The space $C^k(\Omega)$ is defined to be the sets of all real-valued functions u defined on $\bar{\Omega}$ with the property that u and its partial derivatives up to order k are all continuous on $\bar{\Omega}$. A solution to (3.11) is sought in the subspace

$$C_D{}^2(\bar{\Omega}) = \{u\epsilon C^2(\bar{\Omega}) : u = 0 \text{ on } \delta\Omega\} \text{ and } C_D{}^2(\bar{\Omega}) \subseteq C^k(\bar{\Omega})$$

where D stands for Dirichlet (Gockenbac 2006). If u is a solution to (3.11), then for any function v defined on Ω, multiplying both sides of the PDE by v yields

$$-\nabla\cdot(K\cdot\nabla u)v = fv \quad in\ \Omega$$

Since the two functions $-\nabla\cdot(K\cdot\nabla u)v$ and fv are equal on Ω, their integral over Ω must agree (Gockenbac 2006):

$$-\int_\Omega \nabla\cdot(K\cdot\nabla u)v = \int_\Omega fv\,. \qquad (3.12)$$

In this context, v is called test function. The idea is to check whether the PDE holds in the weighted average sense over Ω, using the test function v to define the weights in the average. Obviously, just because equation (3.12) holds for a particular test function v there is no reason to think that the PDE (equation (3.11)) holds. However, if equation (3.12) holds for all test functions v from a sufficiently large set, then equation (3.11) must hold. The sphere of radius δ centered at (x_o, y_o) is denoted by

$B_\delta\,(x_o, y_o)$:

$$B_\delta\,(x_o, y_o) = \{(x,y) \in R^2 : \|(x,y) - (x_o, y_o)\| < \delta\}.$$

Suppose $(x_o, y_o) \in \Omega$ and $\delta > 0$ is small enough that $B_\delta\,(x_o, y_o)$ is contained entirely in Ω. Consider any function $v \in C_D{}^2(\bar{\Omega})$ with the following properties:

1. $v(x,y) > 0$ for all $(x,y) \in B_\delta(x_o, y_o)$
2. $v(x,y) = 0$ for all $(x,y) \notin B_\delta(x_o, y_o)$
3. v has a total weight 1.

$$\int_{\Omega} v = \int_{B_{\delta(x_o,y_o)}} v = 1 \text{ (Gockenbac, 2006).} \tag{3.13}$$

Many such functions v exist as constructed in equation (3.22). But then $\int_{\Omega} fv = \int_{B_{\delta(x_o,y_o)}} fv$ is just a weighted average of f over the disk $B_{\delta}(x_o,y_o)$, and similarly

$$-\int_{\Omega} \nabla \cdot (K\nabla u)v = \int_{B_{\delta}(x_o,y_o)} \nabla \cdot (K\nabla u)v\,. \tag{3.14}$$

Applying Green's identity to the left – hand side of equation (3.14),

$$-\int_{\Omega} \nabla \cdot (K\nabla u)v = \int_{\Omega} k\nabla u \cdot \nabla v - \int_{\delta\Omega} kv\frac{\delta u}{\delta n}. \tag{3.15}$$

$$= \int_{\Omega} k\nabla u \cdot \nabla v \tag{3.16}$$

the boundary integral vanishes because v is zero on δΩ. This leads to weak form of Boundary Value Problem. That is to find $u \in C_D{}^2(\bar{\Omega})$ such that $\int_{\Omega} k\nabla u \cdot \nabla v = \int_{\Omega} fv$ for all $v \in C_D{}^2(\bar{\Omega})$, (3.17)

called variational form or weak form .

The elliptic (PDE) of equation (3.7) relating conductivity distribution, ξ, potential distribution, u, and current distribution, I, is similar to an elliptic (PDE) of such in a mechanical system that involves the stiffness distribution, k, the displacement distribution, u, and the boundary force distribution, f, in the FEM analysis. Following this, it is important to show that u that solves equation (3.17) is the same u that minimises, J, the potential energy of the system. When a partial differential equation (PDE) models a mechanical system in which u is the displacement and f is an external body force for u, the total potential energy of the system is

$$j(u) = \frac{1}{2}\int_{\Omega} k\nabla u \cdot \nabla u - \int_{\Omega} fu + \xi_o \tag{3.18}$$

where ξ_o is some constant (Gockenbac 2006). The state of equilibrium of the system corresponds to the displacement u that minimises the potential energy.

If $u, w \in C_D{}^2(\bar{\Omega})$; $v = w - u$, so that ($w = u + v$) then v is also in $C_D{}^2(\bar{\Omega})$. Mathematically, $C_D{}^2(\bar{\Omega})$ is a vector space and

$$j(w) = j(u+v) = j(u) + \int_{\Omega} k\nabla u \cdot \nabla v - \int_{\Omega} fv + \frac{1}{2}\int_{\Omega} k\nabla v \cdot \nabla v \tag{3.19}$$

The parameter k is positive and $v \cdot \nabla v = ||\nabla v||^2 > 0$, provided v is a nonconstant function (Gockenbac 2006). Because of the boundary condition, the only constant function in $C_D{}^2(\bar{\Omega})$ is the zero function, so if v is a nonzero displacement (that is, if $w \ddagger u$), then

$$\frac{1}{2}\int_{\Omega} k\nabla v \cdot \nabla v > 0$$

Therefore,

$$j(w) > j(u) \quad \text{for all } w \ddagger u. \tag{3.20a}$$

If and only if

$$\int_{\Omega} k\nabla u \cdot \nabla v - \int_{\Omega} fv = 0 \tag{3.20b}$$

For all $v \in C_D{}^2(\bar{\Omega})$. This shows that u minimises j over $C_D{}^2(\bar{\Omega})$ if and only if u satisfies equation (3.15). To explain other definition of partial derivatives, we introduce some new concepts. First of all, if u is a function, its support is the closure of the set on which u is nonzero;

Supp $(u) = (\{(x,y) \in R^2 : u(x,y) \ddagger 0\})$ (Gockenbac 2006). If u is defined on Ω and Supp (u) is a compact subset (that is, a closed and bounded subset) on Ω, then u is said to be compactly supported in Ω. A function compactly supported in Ω is zero on and near the boundary Ω. The space $C_o{}^{\infty}(\bar{\Omega})$ is defined to be the set of all functions that are infinitely differentiable on Ω and compactly supported in Ω. The condition that $u \in C_o{}^{\infty}(\bar{\Omega})$ is quite strong from equation (3.11). Such a function must have the property that it and all of its partial derivatives go to zero as (x, y) approaches the boundary of supp (u). To settle this question, it is important to show how to construct a family of functions in $C_o{}^{\infty}(\bar{\Omega})$. Let $(x_o, y_o) \in \Omega$ and δ > 0 be sufficient small that $B_\delta(x_o, y_o) \subset \Omega$, and define

Φ : Ω → **R** by

$$\Phi(x,y) = \begin{cases} \frac{e^{-1}}{(\delta^2 - \|(x,y)-(x_0,y_0)\|^2)} & ,(x,y) \epsilon B_\delta(x_o,y_o) \\ 0 \quad , & otherwise \end{cases} \tag{3.21}$$

Then, since $\frac{1}{(\delta^2 - \|(x,y)-(x_0,y_0)\|^2)} \to -\infty$ as $(x, y) \to \delta B_\delta(x_o, y_o)$.

It follows that $\Phi(x,y) \to 0$ as $(x,y) \to \delta B_\delta(x_o, y_o)$.

Moreover, each partial derivative of Φ, inside $B_\delta(x_o, y_o)$, consists of a rational function times the same exponential, which is enough to show that each partial derivative converges to zero as $(x,y) \to \delta B_\delta(x_o, y_o)$. Thus, $\Phi \in C_o{}^{\infty}(\bar{\Omega})$.

In fact, defining

$$v(x,y) = \frac{1}{\int_{B_{\delta(x_0,y_0)}} \Phi} \Phi(x,y), \tag{3.22}$$

it follows that $\int_{\Omega} v = 1$ and thus, v is a test function of the special type described in equation (3.13) (Gockenbac 2006). The arbitrariness of v is crucial, as otherwise a weak form is not equivalent to the strong from. Weight function is thought of as an enforcer, whatever it multiplies is enforced to be zero by its arbitrariness. The key to making the proof of a solution of the weak form to be a solution of the strong form possible is the arbitrariness of v. It can be assumed to be anything we need in order to prove the equivalence (Fish and Betytschko 2007).

Suppose u is a real-valued function defined on a domain Ω in R^2, and that u is integrable over every compact subset of Ω, (in this case, u is called locally integrable). If there exists another locally integrable function g defined on Ω such that

$$\int_{\Omega} gv = -\int_{\Omega} u\frac{\delta v}{\delta x} \quad \text{for all } v \in C_o{}^{\infty}(\bar{\Omega}) \tag{3.23}$$

holds, then u is said to be weakly differentiable with respect to x, and g is called the weak partial derivative with respect to x of u . The weak partial derivatives with respect to y are defined similarly. Weak partial derivatives are denoted by $\frac{\delta u}{\delta x}$ and $\frac{\delta u}{\delta y}$ just as are strong derivatives.

There is one restriction, however, that is necessary. The definition of weak derivatives requires only that $\frac{\delta u}{\delta x}$ and $\frac{\delta u}{\delta y}$ be locally integrable. In the variation equation (3.14) though, it must be possible to integrate the products

$$\frac{\delta u}{\delta x}\frac{\delta v}{\delta x} \text{ and } \frac{\delta u}{\delta y}\frac{\delta v}{\delta y}.$$

In particular, $v = u$ must be allowed, which shows that $\frac{\delta u}{\delta x}$ and $\frac{\delta u}{\delta y}$ must be square integrable:

$$\int_{\Omega} \left(\frac{\delta u}{\delta x}\right)^2 < \infty \, . \int_{\Omega} \left(\frac{\delta u}{\delta y}\right)^2 < \infty$$

In this way, $\int_{\Omega} fv$ must be finite, which also suggest that f and v should be square - integrable (if $f = v$, for example). It is therefore convenient to define the space

$$L^2(\Omega) = \{ : \Omega \rightarrow R : \int_{\Omega} v^2 < \infty \}.$$

It will be required that f, the right hand side of the PDE belongs to $L^2(\Omega)$. The solution u of equation (16) must satisfy $u, \frac{\delta u}{\delta x}, \frac{\delta u}{\delta y} \epsilon\, L^2(\Omega)$ (Gockenbac 2006).

The test function must satisfy the same conditions. These conditions are defined as the *Sobolev* Space $\mathbf{H}^1(\Omega)$:

$$\mathbf{H}^1(\Omega) = \{ v \epsilon L^2(\Omega) : \frac{\delta v}{\delta x}, \frac{\delta v}{\delta y}\, \epsilon L^2(\Omega)\}.$$

Finally, it is necessary that both the solution u and all the test function v satisfy the Dirichlet boundary condition. For this reason, it is necessary to introduce the following space:

$$H_o{}^1(\Omega) = \{ v \epsilon H^1(\Omega) : v = 0 \text{ on } \delta\Omega \}.$$

The space $H_o{}^1(\Omega)$ is another example of the sobolev space. The variational form of equation (3.12) can now be defined in terms of the Sobolev space $H_o{}^1(\Omega)$:

$$\text{Find } \quad u \epsilon H_o{}^1(\Omega), \ \int_{\Omega} k\nabla u \cdot \nabla v = \int_{\Omega} fv \quad \text{for all } \ v \epsilon H_o{}^1(\Omega) . \tag{3.24}$$

The right hand side (r.h.s) f is assumed to belong to $L^2(\Omega)$. It should be clear why the variational form is called weak-form, the requirements of the r.h.s of f and the solution u have been considerably weakened over the classical strong form of equation (3.11) (Gockenbac 2006).

We need derive the weak form of the Newmann problem. Let consider a Newmann problem of the form

$$-\nabla \cdot (K\nabla u) = f \quad in \;\; \Omega \tag{3.25a}$$

$$k\,\frac{\delta u}{\delta n} = 0 \qquad on \quad \delta n. \tag{3.25b}$$

The Dirichlet condition appears explicitly in the weak form as in equation (3.24) (in the definition of the space $H_o{}^1(\Omega)$), but as it will be shown below, the Neumann condition does not appear explicitly in the weak form of equation (3.25). Let assume that u satisfies equation (3.25). This presupposes that u has some extra smoothness beyond the requirement that $u \epsilon\, H^1(\Omega)$, both because the left hand side of equation (3.25) involves second derivatives of u and because $\frac{\delta u}{\delta n}$ is not well defined for an arbitrary $H^1(\Omega)$ function (Gockenbac 2006). Then

$$-\nabla \cdot (K\nabla u)v = fv \quad in \;\; \Omega \qquad \text{for all } \; v\epsilon H^1(\Omega) \tag{3.26a}$$

$$\Rightarrow \qquad -\int_\Omega \nabla \cdot (K\nabla u)v \;=\; \int_\Omega fv \;\; \text{for all } v\epsilon H^1(\Omega) \tag{3.26b}$$

$$\Rightarrow \qquad \int_\Omega k\nabla u \cdot \nabla v \;-\; \int_{\delta n} kv\frac{\delta u}{\delta n} = \int_\Omega fv \quad \text{for all } v\epsilon H^1(\Omega) \tag{3.26c}$$

$$\Rightarrow \qquad \int_\Omega k\nabla u \cdot \nabla v \;=\int_\Omega fv \quad \text{for all } v\epsilon H^1(\Omega) \tag{3.26d}$$

the boundary integral vanishes because of the Newmann boundary condition is satisfied by the solution u. In the Dirichlet case, it was the boundary condition on the test function v that caused the boundary integral to vanish . The weak form of equation (3.25) is thus defined to be the following problem:

Find $u \in H^1(\Omega)$ such that $\int_\Omega k\nabla u \cdot \nabla v = \int_\Omega fv$ for all $v \in H^1(\Omega)$. (3.27)

Any solution of equation (3.25) is also a solution of equation (3.27). But, one needs to check if the converse is true. After all equation (3.27) does not mention the Newmann boundary condition, and so it is not obvious that a solution of equation (3.27) will necessarily satisfy the Newmann condition. It does though, provided the solution u is smooth enough that Green's identity applies, and ∇u can be restricted to $\delta\Omega$ (Gockenbac 2006).

Suppose that $u\epsilon H^1(\Omega)$ is a solution of equation (3.24). Then since $H_o{}^1(\Omega) \subset H^1(\Omega)$,

$$\int_\Omega k\nabla u \cdot \nabla v = \int_\Omega fv \quad \text{for all } \; v\epsilon H_o{}^1(\Omega). \tag{3.28}$$

Applying Green's identity to the left side yields

$$-\int_{\Omega} \nabla \cdot (K\nabla u)v + \int_{\delta n} kv\frac{\delta u}{\delta n} = \int_{\Omega} fv \text{ for all } v \epsilon H_o{}^{1}(\Omega). \tag{3.29}$$

Since $v \epsilon H_o{}^{1}(\Omega)$, the boundary integral vanishes, yielding

$$-\int_{\Omega} \nabla \cdot (K\nabla u)v = \int_{\Omega} fv \text{ for all } v \epsilon H_o{}^{1}(\Omega) \tag{3.30}$$

It follows that the PDE of equation (3.25) must hold (considering the type of test function discussed in equation (3.22), whose support is a disk $B_{\delta}(x_o, y_o)$ – belongs to the space $H_o{}^{1}(\Omega)$).

To show that the Newmann condition (3.25b) also holds, we consider equation (3.27) and apply Green's function once again to obtain

$$-\int_{\Omega} \nabla \cdot (K\nabla u)v + \int_{\delta n} kv\frac{\delta u}{\delta n} = \int_{\Omega} fv \text{ for all } v \in H^{1}(\Omega), \tag{3.31}$$

but now we know that

$$-\int_{\Omega} \nabla \cdot (K\nabla u)v = \int_{\Omega} fv \text{ for all } v \in H^{1}(\Omega),$$

(since - $\nabla \cdot (K\nabla u)$ and f are equal on Ω).

Therefore $\int_{\delta n} kv\frac{\delta u}{\delta n}=0$ for all $v \epsilon H^{1}(\Omega)$ must hold. (3.32)

Although the precise argument is rather technical, it should be believable that equation (3.32) can hold for all $v \epsilon H^{1}(\Omega)$ only if $\frac{\delta u}{\delta n}$ is zero on δΩ (i.e. k is strictly positive) (Gockenbac 2006).

Since Dirichlet conditions must be explicitly imposed in the weak form, while Newmann conditions are implied even though not explicitly imposed, Dirichlet conditions are often called *essential boundary conditions*, while Newmann conditions are called *natural boundary conditions* .

Using the finite elements and according to the complete electrode model, the global admittance matrix A in a system with n nodes, k elements and l boundary electrodes is assembled as

$$A = \begin{bmatrix} A_c & A_e \\ A_e{}^{*} & A_d \end{bmatrix} \tag{3.33}$$

where

$$A_{c(i,j)} = A_{c1(i,j)} + A_{c2(i,j)} = \int_{\Omega} \xi \nabla \Phi_{\mathrm{i}} \cdot \nabla \Phi_{\mathrm{j}} dxdydz + \sum_{l=1}^{L} \frac{1}{Z_l} \int_{E_l} \Phi_l \Phi_j ds$$

(similar to equation (3.27))

for i, j=1,...,n, and Φ_i and Φ_j are the corresponding shape functions. The other two compartments of the matrix A have the form of

$$A_e(i,j) = -\frac{1}{(Z_l)_j} \int_{E_l} \Phi_l \, ds \tag{3.34}$$

for i =1,..., n and l=1,...,L;

$$A_d(i,l) = \begin{cases} |E_l| Z^{-1}{}_l & for\ i = l \\ 0 & otherwise \end{cases} \tag{3.35}$$

for i, j =1,...L. Here, $|E_l|$ is the area of the surface of the lth electrode (Polydorides 2002). The construction of the full-rank admittance matrix is done in three stages. At first, the A_c block of the matrix is assembled as though we were solving with only natural boundary conditions (such as the 'gap-shunt' electrode model and then augmented by the complete electrode blocks A_e and A_d (Polydorides 2002) . The calculation of the electrode blocks requires the integrals of products of shape functions over the elements under the electrodes. As we are using linear elements, these are integrals of quadratics which can be performed analytically (Polydorides 2002).

From equation (3.33), the forward computations are applied to the system

$$\begin{bmatrix} A_c & A_e \\ A^*{}_e & A_d \end{bmatrix} \begin{bmatrix} U_n \\ V_L \end{bmatrix} = \begin{bmatrix} 0 \\ I_b \end{bmatrix}, \tag{3.36}$$

solving for the nodal potential distribution U_n and the electrode potential V_L, and the right-hand side current vectors are denoted as I and their nonzero compartments as I_b (Polydorides 2002).

The system of equations highlighted in equation 3.36 can be solved numerically for the voltage distribution,V, on the boundary by a software code written in any high-level programming language that solves the product of the inverse of the system matrix, A, with the current distribution vector, I, injected through periphery electrodes. Being a 3-D problem, the need for a computer with much larger memory and high processing power make the use of FEM for online image reconstruction in 3-D a challenge. An alternative means to analysing the conductivity distribution within a 3-D domain through an offline image reconstruction is the exploration of suites of open source software, such as Free FEM, DEAL II, EIDORS, e.t.c. Among the enumerated public domain libraries of functions in various programming language, EIDORS was explored in this research due to its dedicated use for analysis of electrical and optical properties through reconstructed images in 3-D using the FEM approach.

Using the Electrical Impedance and Diffuse Optical Reconstruction Software (EIDORS), the forward calculations are mainly performed by the forward_solver function which, depending on the admittivity vector ξ, either opts for the Cholesky method or preconditioned conjugate gradients if $ξ \in \mathbf{R}^n$ or alternatively the **LU** method or biconjugate gradients in the case where $ξ \in \mathbf{C}^n$ (Polydorides 2002).

In the case where the admittivity ξ is complex, the Jacobian is calculated through the function that calculates four matrices which resemble the sensitivity of the real and imaginary parts of the measurement with respect to real or imaginary admittivity perturbations, i.e. $\mathbf{J}_{rr} = \delta \mathbf{V}_r / \delta ξ_r$, $\mathbf{J}_{ri} = \delta \mathbf{V}_r / \delta ξ_i$

, $\mathbf{J}_{ir} = \delta \mathbf{V}_i/\delta\xi_r$ and $\mathbf{J}_{ii} = \delta \mathbf{V}_i/\delta\xi_i$ where V_r and $\boldsymbol{V_i}$ are the real and imaginary parts of the measurements while $\xi_r = \sigma$ and $\xi_i = \omega\varepsilon$ the conductivity and permittivity vectors. The complex formulation of the forward problem is therefore

$$\begin{bmatrix} J_{rr} & J_{ri} \\ j_{ir} & J_{ii} \end{bmatrix} \begin{bmatrix} \xi_r \\ \xi_i \end{bmatrix} = \begin{bmatrix} V_r \\ V_i \end{bmatrix} \tag{3.37}$$

The Jacobian or sensitivity matrix, ***J***, is computed as follows in EIDORS. Given a FEM model of an EIT medium, ***F***, we calculate the vector of voltages, ***v***, for each FEM degree of freedom (mainly, degree of freedom are nodes, but in the complete electrode model, electrodes are also associated with a degree of freedom) (Adler *et al.* 2008). That is ***v*** = ***F*** (σ, q_i), where σ is the vector of element conductivities and q_i is the current stimulation pattern, a vector of current inputs of each degree of FEM degree of freedom. The measured electrode voltage can be represented as a linear combination of voltages, V_{toE}. For each stimulation pattern, q_i, a vector of measurements, m_i, are required, each of which consist of a linear combination of electrode measurements represented by M_i. Thus,

$$m_i = \; M_i \, V_{toE} \mathrm{F}\,(\sigma, q_i). \tag{3.38}$$

Based on this model, j, is calculated as:

$$J_{i,j} = \frac{M_i \, V_{toE} \delta\mathrm{F}\,(\sigma, q_i),}{\delta\sigma_j} \Big|_{\sigma=\sigma_0} \tag{3.39}$$

where σ_0 is the ``background'' conductivity around which small changes are assumed to occur. To represent j as a matrix, measurements for all stimulation patterns, i , are flattened into column vectors which are concatenated for each finite element j. In EIDORS, the Jacobian is calculated using the function calc_jacobian which takes as parameters the FEM model (type fwd_model) and the image of σ_o *(type* image) (Adler *et al*. 2006).

3.1.4 Solving the inverse problem (Inverse Modelling with EIDORS)

In addressing the inverse problem, Polydorides *et al.(*2002) eliminated the second-derivative terms from the Taylor expansion of the nonlinear forward problem, which makes it possible to construct a generalised inverse of the Jacobian, and inversion of the modified problem (well-posed) using the Newton-Raphson method - Gauss-Newton method. On the other hand, Polydorides *et al*.(2002) showed that one may opt for a linearized form of the inverse problem and then adopt some Tikhonov type regularization to obtain a step solution within the Newton-Raphson algorithm using Levenberg and Marquardt method where a variable regularisation parameter was employed. In principle, for the inverse admittivity problem the aim is to obtain a stable solution ξ^* which minimizes the residual error

$$f(\xi) = \tfrac{1}{2}(F(\xi) - V)^*(F(\xi) - V) = \tfrac{1}{2}\,\|F(\xi) - V\|_2{}^2 \qquad (3.40)$$

where $F(\xi)$: $\mathbf{C}^n \rightarrow \mathbf{C}^m$ is the nonlinear forward operator in a problem with n parameters (voxels) and m measurements, and $\mathbf{V}\in\mathbf{C}^m$ is the vector of voltages measurements for a fixed set of current patterns (Polydorides 2002). For clarity in the following, let $D(\xi) = F(\xi) - V$. As $F(\xi)$ is analytic, a Taylor expansion of $D(\xi)$ is

$$D(\xi + h) = D(\xi) + D'(\xi)h + \tfrac{1}{2}D''(\xi)h^2 + O(h^3) \qquad (3.41)$$

In an initial simplistic attempt to minimize $f(\xi)$ one can follow a linear least squares approach from which the Newton-Raphson iteration for well posed problems is derived by seeking a step h for which $D(\xi + h) \approx 0$.

Neglecting second-order term and above

$$D(\xi) = -D'(\xi)h \qquad (3.42)$$

$$h_{NR} = -\big(D'(\xi)\big)^{-1} D(\xi) = \big(F'(\xi)\big)^{-1}\big(V - F(\xi)\big) \qquad (3.43)$$

Finally arriving at the Newton-Raphson iterative solution

$$\xi_{k+1} \;=\; \xi_k + \big(F'(\xi_k)\big)^{-1}\big(V - F(\xi)\big), \qquad (3.44)$$

where $F'(\xi_k)$ is the Jacobian matrix. From equation (3.40), the gradient $\nabla f = f'(\xi)^*$ and the Hessian $Hf = f''(\xi)$ of the residual f at ξ are

$$\nabla \mathrm{f} = \mathrm{D}'(\xi)^*\mathrm{D}(\xi) = F'(\xi)^*(F(\xi) - V) \qquad (3.45)$$

$$Hf = D'(\xi)^*\, D'(\xi) + D''(\xi)D(\xi) = F'(\xi)^*F'(\xi) + \textstyle\sum_i F''_i(\xi)(F_i(\xi) - V_i). \qquad (3.46)$$

When minimum is approached, the second-derivative terms in equation (3.46) becomes negligible, therefore we can assume

$$\textstyle\sum_i F_i''(\xi)(F_i(\xi) - V_i) \approx 0 \;\; . \qquad (3.47)$$

With this assumption and using (3.46), we can reformulate the residual (3.40) as

$$f(\xi + h) = f(\xi) + f'(\xi)h + \tfrac{1}{2}f''(\xi)h^2 \qquad (3.48a)$$

$$= f(\xi) + \big(D'(\xi)^*D(\xi)\big)h + \tfrac{1}{2}\big(D'(\xi)^*D'(\xi)\big)h^2 \qquad (3.48b)$$

$$= f(\xi) + \big(F'(\xi)^*(F(\xi) - V)\big)h + \tfrac{1}{2}(F'(\xi)^*F(\xi))h^2 \qquad (3.48c)$$

Setting the gradient of (3.48) to zero yields

$$\nabla \mathrm{f} = F'(\xi)^*(F(\xi) - V) + \; hF'(\xi)^*F'(\xi), \qquad (3.49)$$

from where the step h is derived as

$$h_{GN} = \left(\left(F'(\xi)^* F'(\xi)\right)^{-1} F'(\xi)^* \left(V - F(\xi)\right)\right) \qquad (3.50a)$$

$$\xi_{k+1} = \xi_k + h_{GN} \qquad (3.50b)$$

Equation (3.50) combined with the Newton-Raphson formula (3.44) gives the well known Gauss-Newton algorithm. It is worth noting that the convergence of the method (3.50) depends on the validity of assumption (3.47) and the size of step h. Alternatively, the second derivative terms in (3.46) may be approximated with λI, where $\lambda \in \mathbf{R}$ is a positive scalar and I the identity matrix. This effectively changes the assumption (3.47) to

$$\sum_i F_i''(\xi)(F_i(\xi) - V_i) \approx \lambda I. \qquad (3.51)$$

As obtained in (3.48), the error residual is now expressed as

$$f(\xi + h) = f(\xi) + f'(\xi)h + \frac{1}{2} f''(\xi)h^2 \qquad (3.52a)$$

$$f(\xi + h) = f(\xi) + \left(D'(\xi)^* D(\xi)\right)h + \frac{1}{2}(D'(\xi)^* D'(\xi) + \lambda I)h^2 \qquad (3.52b)$$

$$= f(\xi) + F'(\xi)^*(F(\xi) - V)h + \frac{1}{2}(F'(\xi)^* F(\xi) + \lambda I)h^2 \qquad (3.52c)$$

and setting the gradient to zero

$$\nabla \mathrm{f} = F'(\xi)^* F(\xi) - F'(\xi)^* V + (F'(\xi)^* F'(\xi) + \lambda I)h = 0 \qquad (3.53)$$

leads to Tikhonov regularized solution

$$h = (F'(\xi)^* F'(\xi) + \lambda I)^{-1} F'(\xi)^* \left(V - F(\xi)\right). \qquad (3.54)$$

Substituting this result into the Newton-Raphson formula (3.44) gives the Levenberg-Marquardt method

$$h_{LM} = (F'(\xi)^* F'(\xi) + \lambda_k I)^{-1} F'(\xi)^* \left(V - F(\xi)\right) \qquad (3.55a)$$

$$\xi_{k+1} = \xi_k + h_{LM} \qquad (3.55b)$$

In the Levenberg-Marquardt method for well posed problems, as the solution is approached, λ_k is reduced to zero, thus in effect (3.55a) is gradually transformed into a Gauss-Newton step. This method can also be derived by linearizing $f(\xi)$ around ξ_k within the nonlinear Tikhonov functional

$$f(\xi) = \|F(\xi) - V\|_2{}^2 + \lambda \|L(\xi - \xi_k)\|_2{}^2 \xi_K\|_2{}^2 \qquad (3.56)$$

where L is either the identity or any other regularization matrix (as discussed in section 3.1.2) imparting some prior assumption about ξ and λ the positive scalar regularization parameter. Linearizing F around ξ yields the minimization problem

$$\arg\min_h \{ \|F'(\xi)h - V\|_2{}^2 + \lambda \|L(h - \xi)\|_2{}^2 \} \qquad (3.57)$$

for which the linear generalized Tikhonov solution is

$$h_{GT} = (F'(\xi)^* F'(\xi) + \lambda L^* L)^{-1} (F'(\xi)^* V + \lambda L^* L \xi) \qquad (3.58)$$

The solution of equation (3.58) can be efficiently computed without forming the normal equations coefficient matrix, by forming the augmented system

$$h_{GT} = \begin{bmatrix} F'(\xi) \\ \sqrt{\lambda L} \end{bmatrix}^{\dagger} \begin{bmatrix} V - F(\xi) \\ \sqrt{\lambda L}\xi \end{bmatrix} \text{(Polydorides 2002).} \qquad (3.59)$$

For the $k+1$ iteration, one can minimize the functional

$$\|F(\xi_k) - V - F'(\xi_k)(h - \xi_k)\|_2{}^2 + \lambda\|L(h - \xi_k)\|_2{}^2 \qquad (3.60)$$

which has an algebraic solution

$$h = (F'(\xi_k)^* F'(\xi_k) + \lambda L^* L)^{-1}\left(F'(\xi_k)^*\big(V - F(\xi_k)\big) + \lambda L^* L(\xi_k)\right) \qquad (3.61a)$$

$$\xi_{k+1} = \xi_k + h \qquad (3.61b)$$

It worth mentioning that, unlike (3.55), this time the regularization parameter, λ, is kept constant in each iterative loop .

In EIDORS, the inverse computations are carried out by the inv_sol function which solves the nonlinear inverse problem implementing the algorithm described in (3.61) (Polydorides *et al.* 2002). The regularization matrices are provided by the functions iso_f_smooth and iso_s_smooth, which construct the discrete forms of the first and second differential operators with adjustable positive weight. These impose certain isotropic smoothing assumptions on the required solution. MATLAB implements the techniques mentioned above using the backslach operator (\) which performs QR decomposition on $F'(\xi)$, thus avoiding the explicit computationally expensive inversion of the $F'(\xi_k)^* F'(\xi_k)$ matrix (Polydorides *et al.* 2002).

From equation 3.61b, an improved image is obtained with the computation of the new conductivity values distributed within the domain of homogeneous or background solution. The simulated voltage (predicted voltage) computed when the finite element forward model operator , ***F***, acts on the new conductivity distribution is then compared with the measured voltage, in order to check if the iteration stops at this stage, or it continues. As long as the difference in the measured voltage and the computed voltage is not minimum, given the conductivity variable in the forward model, the iteration continues. The bottom left hand side of the flow chart in figure 3.1 shows a number of operations involved in seeking for stable conductivity distribution that minimizes the residue error arising from the comparison of measured and simulated voltages.

3.2 Numerical Computations of Operations for the Forward Problem Using Free Library of MATLAB functions - EIDORS

The computation of the voltages of the periphery electrodes of the tomography rig or vessel, given the conductivity distribution within the domain for a well defined sequence of current injection, is how the forward problem is posed. Thus, the continuous cylindrical domain necessarily has to be discretised into a finite number of tetrahedral elements such that the polynomial of the trial solution satisfies the continuity and completeness condition in order for the approximate solution by FEM to converge to the accurate solution. Using the public library of MATLAB functions, numerical computations required for solving the forward problem are documented in section J2.1 to J2.10 of appendix J2.

3.3 Numerical Computations of Operations for the Inverse Problem Using Free Library of MATLAB functions - EIDORS

A stable solution of conductivity distribution which minimises the residual error of the difference between the simulated and the measured voltage values is required to solve the inverse problem of computing the conductivity distribution over each element of the discretised domain given the measured boundary voltages arising from sequences of current injections. The required numerical procedure for addressing the inverse problem for which EIDORS could be used are outlined in section J4.1 to J4.3 of appendix J4.

3.4 Obtaining the Best Measurement Strategy for Effective Analysis of the Voltage Signal

The UCT tomography setup allows adjacent and opposite current injection sequences with adjacent voltage measurement sequences through peripheral electrodes only. Based on this limitation, opposite and adjacent measurement schemes over two, three and four ring of electrodes system were explored out of a number of possible measurement sequences using the $mk\_stim\_patterns$ function in EIDORS in order to determine the best measurement strategy. The exploration lead to the development of loading functions needed to load measured voltage data from the boundary of the UCT tomography rig for current injection sequences through the two rings, three rings and four rings electrode systems using MATLAB syntax. Three data-loading functions were written for each of the six reconstruction programme including both opposite and adjacent current injection sequences for two, three and four rings respectively. Each written function was linked to the appropriate reconstruction programme as indicated in table 3.3.

Table 3.1. MATLAB functions for loading data to the reconstruction codes of the two, three and four rings electrodes system

S/N	Number of Rings	Current Injection Sequences	Distribution of Conductivity in the Vessel	Name of Loading Function
1	2 rings	Adjacent	Inhomo (FC)	`meas_inhomo2rg_adjacent`
2			Homo (FC)	`getcalibrationdata2rg_adjacent_current`
3			Homo (NC)	`getcalibrationdata2rg_adjacent_nocurrent`
4	2 rings	Opposite	Inhomo (FC)	`meas_inhomo2rg_opp`
5			Homo (FC)	`getcalibrationdata2rg_opp_current`
6			Homo (NC)	`getcalibrationdata2rg_opp_no_current`
7	3 rings	Adjacent	Inhomo (FC)	`meas_inhomo_3rings_adjacent`
8			Homo (FC)	`getcalibrationdata3rings_adj_current`
9			Homo (NC)	`getcalibrationdata3rings_adj_no_current`
10	3 rings	Opposite	Inhomo (FC)	`meas_3rginhomo`
11			Homo (FC)	`getcalibrationdata3rings_opp_currrent`
12			Homo (NC)	`getcalibrationdata3rings_opp_nocurrent`
13	4 rings	Adjacent	Inhomo (FC)	`meas_4RINGShomo_ADJ`
14			Homo (FC)	`getcalibrationdata4rings_adj_current`
15			Homo (NC)	`getcalibrationdata4rings_adj_no_current`
16	4 rings	Opposite	Inhomo (FC)	`meas_4RINGShomo_OPP`
17			Homo (FC)	`getcalibrationdata4rings_opp_current`
18			Homo (NC)	`getcalibrationdata4rings_opp_no_current`

* S/N: Serial numbers

Keys: Inhomo - Inhomogeneous solution. Homo - Homogeneous solution. FC - Fixed current. NC - No current.

CHAPTER 4

EXPERIMENTAL DESIGN AND ANALYSIS TOOLS

4.1 Hardware Materials for the Experimental Set-up

The UCT ERT system comprises of rings of electrodes fitted around the circumference of a pipe or vessel to excite and detect signals (sensors), a data acquisition system, a PC that controls and communicates the injection and measurement sequences with the data acquisition system and a data processing software.

4.1.1 UCT Tomography Rig

The UCT tomography rig is a non-conducting cylindrical vessel fitted with rings of electrode, which is filled with salt water (approximately 100mg/l NaCl) to certain level. This provides a medium of homogeneous conductivity that leaves the electric field lines between two electrodes situated on the rings of electrode system unperturbed (Figure 4.2). In this set-up, the radius and height of the tomography rig are 22 centimetres and 13 centimetres, respectively, while the length and breadth of the rectangular shaped electrodes are 1 centimetres and 2.2 centimetres respectively. The tomography rig is fitted with four rings of 16 electrodes that are equally spaced, and fitted at 1.1 centimetres, 4.9 centimetres, 8.7 centimetres and 12.5 centimetres, respectively from the base of the vessel (Figure 4.1).

Since the boundary voltages take the value of the isopotential surface in 3-D, it is necessary to specify the voltage measurement sequences in three dimensions, i.e. all over the entire domain of the solution (Figure 4.2). From literature, it has been confirmed that the more independent measured data there is the more accurate the reconstructed image will be. The voltage measurement and current injection sequences through pairs of electrodes is specified using an electrode select sequence table format (Figure D1), and implemented by the data acquisition system. The data acquisition system (Figure 4.5) communicates with the PC to load the measurement and injection sequences and returns the measured data into the PC for display in graphical form, as in (Figure 4.4) for opposite current injection sequences, and as in (Figure 4.7) for adjacent current injection sequences.

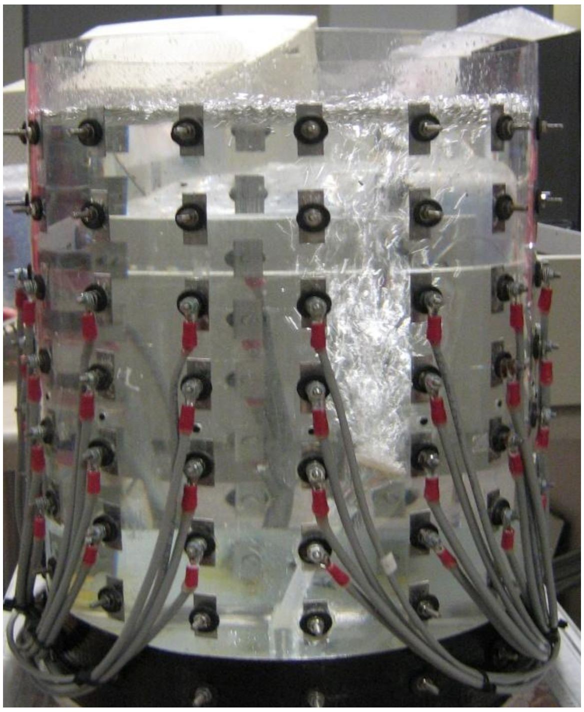

Figure 4.1: The UCT tomography rig

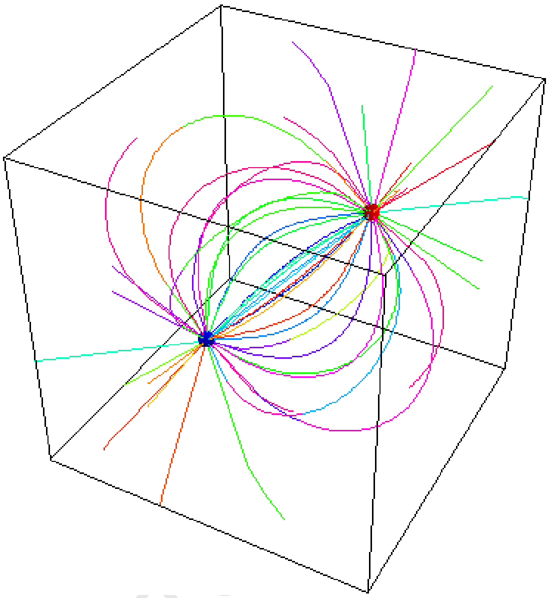

Figure 4.2: An isopotential surface due to opposite current injection sequences.

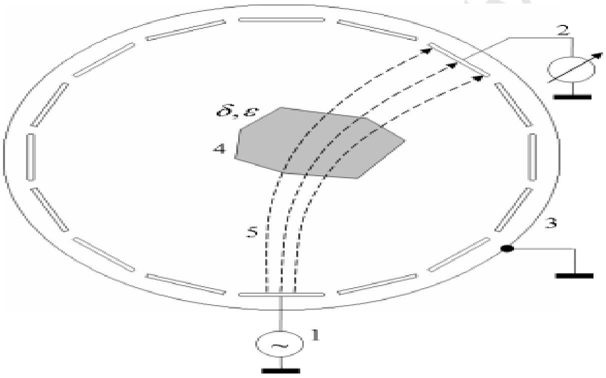

Figure 4.3: Unperturbed electric field lines

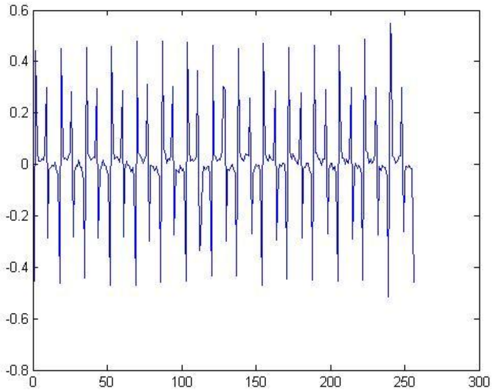

Figure 4.4: Graphical display of data sets measured by opposite electrode pairs sequences

Figure 4.5: The UCT data acquisition system

Figure 4.6: The Internal view of the UCT data acquisition instrument

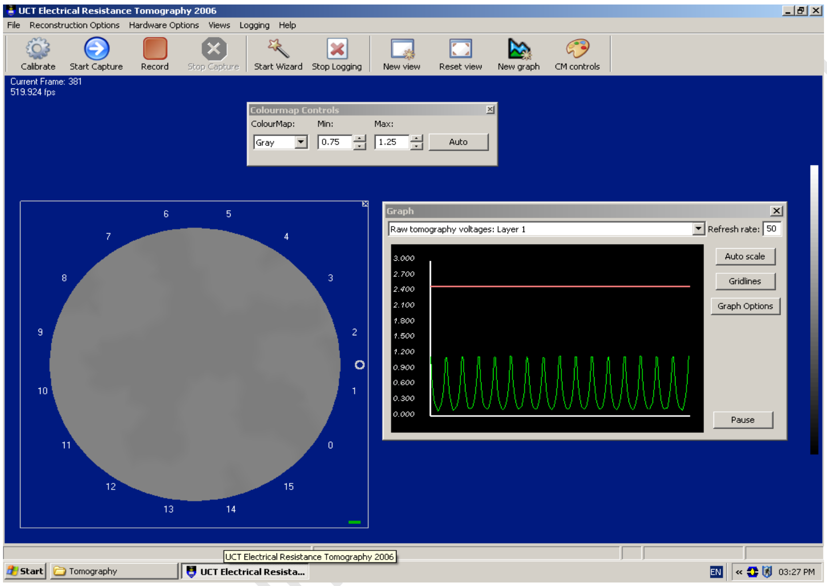

UCT Electrical Resistance Tomography 2006

Current Frame: 381
519.924 fps

Colourmap Controls
ColourMap: Gray
Min: 0.75
Max: 1.25

Graph
Raw tomography voltages: Layer 1
Refresh rate: 50

Figure 4.7: Graphical display of data sets measured by adjacent electrode pairs sequences

Although the UCT tomography rig has eight rings of electrodes with a black tape fastened around the boundary where the first ring is fixed as in Figure 4.1, for the purpose of this research only four rings of the electrode system were used. Each ring of the tomography rig is hard wired to the data acquisition system through a 16 way cabling system such that 256 data sets are recovered from each ring owing to 16 possible current injection sequences, (i.e. 16 X 16).

4.1.2 The UCT Data Acquisition System of the Tomography Set-up

The UCT data acquisition system with a built-in four multiplexer system allows three dimensional data acquisition. It has capability for current injection for both adjacent and opposite sequences within a plane (a ring of electrode) as well as adjacent planar pairs. In other words, it has the capability for any current injection sequences in ERT with adjacent voltage measurement from each ring. However, as the injection scheme is hard-wired, the device will require a replacement of its "key card" in order to carry out an opposite voltage measurement sequences. For the purpose of three dimensional image reconstruction, in which a three dimensional voltage measurement is required, adjacent voltage measurements in between pairs of electrodes in all rings are required for every current injection in between pairs of electrodes in any plane of the electrode system.

Typically, there are two possible forms of sixteen current injection sequences, which are opposite and adjacent pair electrode injections. For the opposite pair injections, a constant current was injected between opposite electrodes in a sequential manner as such that there was reciprocity of poles of charges, say electrode 1 and 9, electrode 2 and 10, electrode 3 and 11, electrode 9 and 1, electrode 10 and 2, e.tc. Similarly, a 16 current injection sequence in which current was pushed and pulled through electrodes 1 and 2, electrode 2 and 3, electrode 3 and 4 and so on implies an adjacent injection sequence respectively. Considering a ring of electrode numbering from 1 to 16, voltage measurement that involved an electrode acting as the source or sink of current was discarded from the measurement used for image reconstruction. A description of total number of measurement from respective rings of electrodes used for each experiment and the total number of data used for reconstruction is provided in table 4.1.

Table 4.1. Number of adjacent measurement from rings of electrode and number of measurements used for image reconstruction

S/N	Current injection strategy (Sixteen Sequences)	Number of rings	Total number of adjacent measurement	Total number measurement used for reconstruction
1	Opposite	Two rings	1024	896
2	Adjacent	Two rings	1024	928
3	Opposite	Three rings	2304	2112
4	Adjacent	Three rings	2304	2160
5	Opposite	Four rings	4096	3840
6	Adjacent	Four rings	4096	3904

Three voltage data sets are to be collected in order to use the implemented algorithm to reconstruct images. These are boundary voltage distribution for homogeneous distribution of conductivity when no sequence of current injection is made, for homogeneous distribution of conductivity when a sequence of current injection of fixed magnitude is made and for inhomogeneous distribution of conductivity when a sequence of current injection of same magnitude as the homogeneous is made. These three measured voltage data sets enable the inverse solver (inv_solve) in EIDORS to be used based on the difference between the voltage data sets for homogeneous and inhomogeneous with current stimulated into the bulk solution and voltage data sets for homogeneous solution with no current stimulated into the bulk solution. Figures 4.8, 4.9 and 4.10 illustrate the voltage data set to be measured for stimulation of current through adjacent electrode pairs. Figures (4.8 and 4.11) inform that the UCT device detect series of spikes of low amplitude of voltage signals resulting from low magnitude of electric flux when the control bar was dragged to zero point on the scale to stimulate no current into the bulk homogeneous solution. Figures (4.8 and 4.11) illustrate the current stimulation through adjacent and opposite electrode pairs respectively.

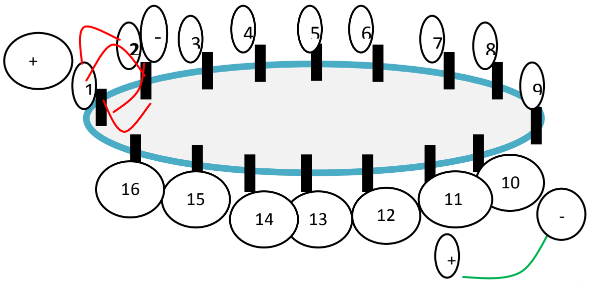

Figure 4.8. Schematic of an implementation of a sequence of current injections through adjacent electrode pairs (electrode 1 and 2) and voltage measurements through adjacent electrode pairs (electrode 11 and 10)on the boundary of a vessel containing a homogeneous solution with no current stimulation. The surface bounded by red lines indicates the isopotential surface while the green line indicates the measured voltage at the boundary.

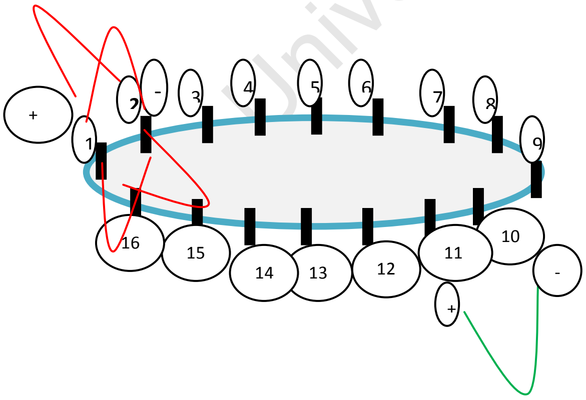

Figure 4.9. Schematic of an implementation of a sequence of current injections through adjacent electrode pairs (electrode 1 and 2) and voltage measurements through adjacent electrode pairs (electrode 11 and 10) on the boundary of a vessel containing a homogeneous solution with fixed magnitude of current stimulation. The surface bounded by red lines indicates the isopotential surface while the green line indicates the measured voltage at the boundary.

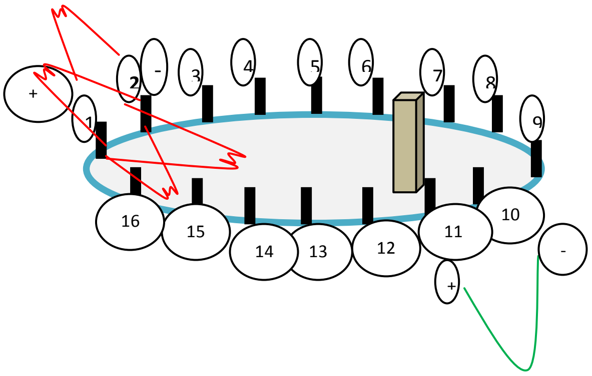

Figure 4.10. Schematic of an implementation of a sequence of current injections through adjacent electrode pairs (electrode 1 and 2) and voltage measurements through adjacent electrode pairs (electrode 11 and 10) on the boundary of a vessel containing an inhomogeneous solution with fixed magnitude of current stimulation. The surface bounded by red lines indicates the isopotential surface while the green line indicates the measured voltage at the boundary.

To demonstrating the voltage measurements to be made when current is stimulated through opposite electrode pairs, the schematic diagrams displayed in figures 4.11, 4.12 and 4.13 are used.

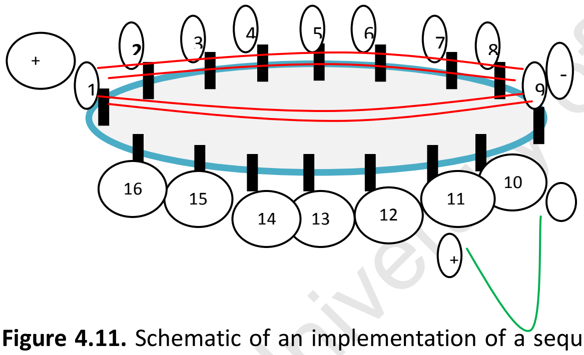

Figure 4.11. Schematic of an implementation of a sequence of current injections through opposite electrode pairs (electrode 1 and 2) and voltage measurements through adjacent electrode pairs (electrode 11 and 10) on the boundary of a vessel containing a homogeneous solution with no current stimulation. The surface bounded by red lines indicates the isopotential surface while the green line indicate the measured voltage at the boundary.

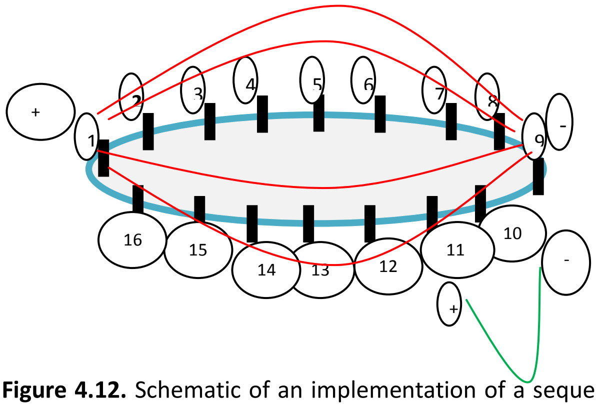

Figure 4.12. Schematic of an implementation of a sequence of current injections through opposite electrode pairs (electrode 1 and 2) and voltage measurements through adjacent electrode pairs (electrode 11 and 10) on the boundary of a vessel containing a homogeneous solution with fixed magnitude of current stimulation. The surface

bounded by red lines indicates the isopotential surface while the green line indicates the measured voltage at the boundary.

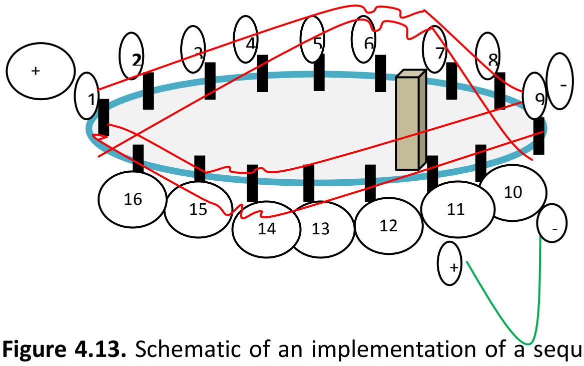

Figure 4.13. Schematic of an implementation of a sequence of current injections through opposite electrode pairs (electrode 1 and 2) and voltage measurements through adjacent electrode pairs (electrode 11 and 10) on the boundary of a vessel containing an inhomogeneous solution with fixed magnitude of current stimulation. The surface bounded by red lines indicates the isopotential surface while the green line indicates the measured voltage at the boundary.

4.1.3 Computer System Component of the UCT Tomography Set-up

Two computers constitute some of the components of the UCT tomography hardware set-up. The first system with Celero$n^{(R)}$ central processing unit of 2.67 GHz and (RAM) of 504 MB operating on Window Xp professional Version 2002 make is employed for downloading the machine code and various measurement sequences tables into the data acquisition device and for loading measured voltage data from the data acquisition unit communicating with the tomography rig via the 16 - way cabling system. The second system is dedicated for image reconstruction purposes, owing to the large storage space and fast processing power required. It has an AMD Phenom (Tm) II X4 946 processor 3.40 GHz with 8GB of RAM and, it operates on a 64-bit operating system of Windows 7 Enterprise.

4.2 Applicable Software for Electrical Resistance Tomography: EIDORS and NETGEN

Two public domain open source software libraries EIDORS and NETGEN were explored in the course of this research. EIDORS was the software of choice owing to its capability of addressing the non-linear and ill-posed inverse problem of electrical resistance tomography, as well as its compatibility with an automatic three-dimensional mesh generator such as DISTMESH and NETGEN. Furthermore, EIDORS had been explored to reconstructing images in two-dimensions in previous work on the UCT ERT system (Long 2006, Stevenson 2006 and Sudhakaran 2010). Basic steps required to download NETGEN and EIDORS are illustrated in section I1 and I2 of the appendix.

4.3 NETGEN : Automatic 3-D Mesh Generator for Modelling the UCT ERT Rig

In addressing the inverse problem nature of image reconstruction, which requires an initial forward solution of the boundary voltages, there is a need to discretize the domain of interest into a finite number of elements. Primarily for 3-D imaging of the conductivity distribution within a medium, tetrahedral finite elements with four nodes yields more accurate approximate numerical solution than hexahedral (Fish and Betytschko 2007). The tetrahedral elements allow the continuous geometry of the body to be modelled more approximately than any other quadrilateral. NETGEN is an automatic three dimensional tetrahedral mesh generator, compatible with the MATLAB syntax of EIDORS. Due to its capability to create sophisticated 2D and 3D models, mesh optimization and hierarchical mesh refinement, it is the software of choice the in modelling of the cylindrical UCT tomography rig with boundary electrodes (Figure 4.14). It accepts input from constructive solid geometry (CSG) or boundary representation (BRep) in the STL file format. It was developed by Joachim Schöberl (from Johannes Kepler University Linz, Austria) with significant contributions by Johannes Gerstmayr and Robert Gaisbauer who assisted with STL geometry and OpenCascade interface respectively. NETGEN can be run on Unit/Linux and Windows operating system.

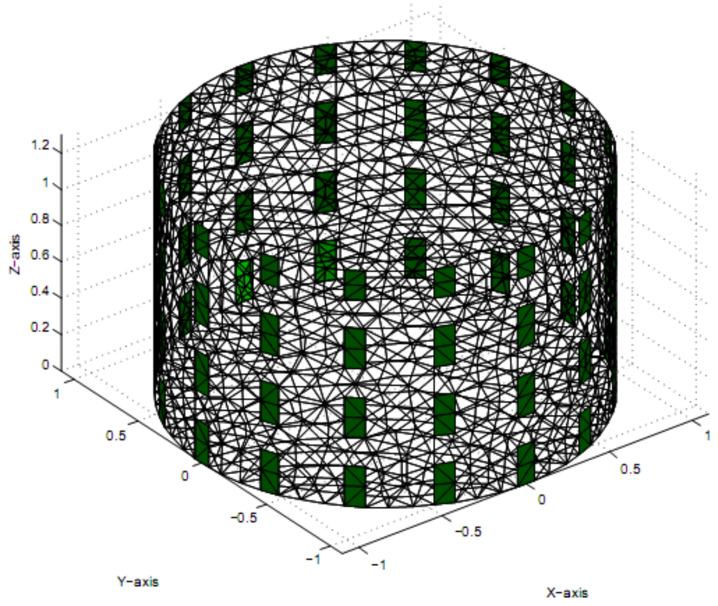

Figure 4.14: The UCT tomography rig modelled using NETGEN

4.4 FEM by EIDORS: Step-wise Approach to Solving the Forward Problem

The forward problem in ERT is simply stated as : Given the constant conductivity value over each element within the domain and the current injection through the boundary electrodes, what are boundary potential differences (Voltages). The finite element analysis procedure used for addressing the forward problem could be summarized to four steps: (a) preprocessing, in which the mesh is constructed, (b) formulation of the discrete finite element equation, (c) solving the discrete equation, (d) postprocessing, where the solution is displayed and various variables that do not emanate directly from the solution are calculated (Fish and Betytschko 2007). In addressing the pre-processing requirement of FEM, NETGEN was employed in generating a 3-D mesh as in figure 4.15b to model the UCT tomography rig(figure 4.15a). Ingredients for the solving the forward problem developed from the mathematical theories stated in chapter 3 are :

(a) A 3-D Mesh to discretize the domain of interest. There is a need to discretize the domain into finite elements such that the approximate solution by the finite element method converges to the accurate solution. The approximate solutions are the nodal voltage values which can be compared to the accurate solution by evaluating the accurate solution at the coordinates of the nodes. NETGEN was employed for discretizing the cylindrical UCT tomography rig vessel into a finite number of tetrahedral elements as in (figure 4.15c) using the function $ng\_mk\_cyl\_models$.

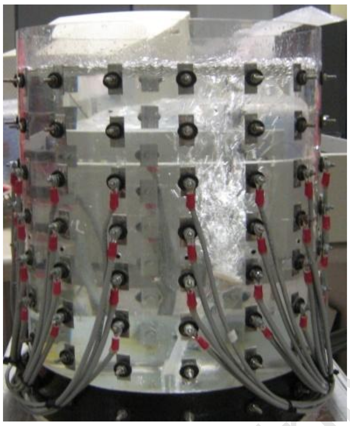

Figure 4.15(a): Continuous domain of UCT rig

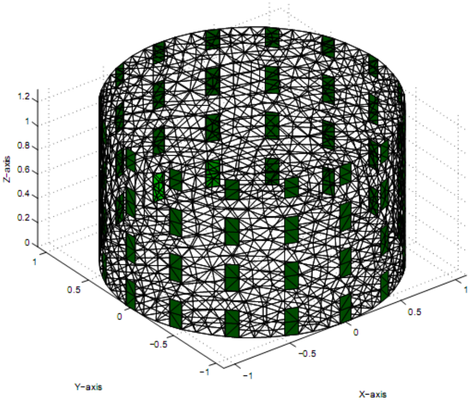

Figure 4.15(b): Discretised domain of UCT rig

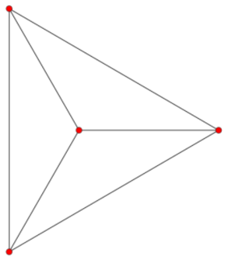

Figure 4.15(c): A tetrahedral element.

In EIDORS, a shape function that interpolates the nodal voltage values of each element is a linear polynomial function as in (4.1), as this satisfies the continuity and completeness conditions needed for the approximate solution to converge to the accurate solution.

$$\theta^e(x) = \propto_o{}^e + \propto_1{}^e\, x \tag{4.1}$$

$$\theta^e(x) = [1 \quad x]\begin{bmatrix} \propto_o{}^e \\ \propto_1{}^e \end{bmatrix} \tag{4.2a}$$

$$\theta^e(x) = P(x) \propto^e \tag{4.2b}$$

Based on FEM, an appropriate polynomial for each element will be that in which the coefficient of the polynomials can be expressed uniquely in terms of the solution at the nodal points. However, the choice of linear function for a four nodes element implemented in the latest EIDORS 3D version released to the public, does not allow the coefficients of the polynomials to be expressed in terms of the solution at the nodal points uniquely.

$$\theta_1{}^e(x) = \propto_o{}^e + \propto_1{}^e\ x_1{}^e \tag{4.3a}$$

$$\theta_2{}^e(x) = \propto_o{}^e + \propto_1{}^e\ x_2{}^e \tag{4.3b}$$

$$\theta_3{}^e(x) = \propto_o{}^e + \propto_1{}^e\ x_3{}^e \tag{4.3c}$$

$$\theta_4{}^e(x) = \propto_o{}^e + \propto_1{}^e\ x_4{}^e \tag{4.3d}$$

$$\begin{bmatrix} \theta_1{}^e \\ \theta_2{}^e \\ \theta_3{}^e \\ \theta_4{}^e \end{bmatrix} = \begin{bmatrix} 1 & x_1{}^e \\ 1 & x_1{}^e \\ 1 & x_1{}^e \\ 1 & x_1{}^e \end{bmatrix} \begin{bmatrix} \propto_o{}^e \\ \propto_1{}^e \end{bmatrix} \tag{4.4a}$$

$$d^e = \qquad M^e \quad \propto^e \quad ; \ \propto^e = \ (M^e)^{-1}\ d^e \tag{4.4b}$$

In this way, $\theta^e(x) = P(x)(M^e)^{-1}\ d^e$, and $\theta^e(x) = N^e(x)d^e$ (4.4c)
where $N^e(x) = [N_1{}^e \quad N_2{}^e \quad N_3{}^e \quad N_4{}^e] = P(x)(M^e)^{-1}$.

$N^e(x)$ is the element shape function matrix consisting of the element shape functions associated with element e . The Shape function is non-zero only at a single node and at that node it is unity. It is an interpolation of the nodal data owing to the fact that the function passes exactly through the data. The coefficients of the polynomial function are expressed in terms of nodal voltages since the FEM approximation is exactly equal to the nodal voltages at the nodes as in (4.4b). $\theta^e(x)$ is the trial solution expressed in terms of the shape function and nodal voltages as in (4.4c). Transformation of the strong form of the Poisson equation to the weak form reduces the order of the derivative from 2 to 1. Thus, one order derivative of the trial solution of each element is needed as in (4.5)

$$\frac{d\theta^e}{dx} = \frac{d(N^e d^e)}{dx} = \frac{dN^e}{dx} d^e = \frac{dN_1{}^e}{dx}\theta_1{}^e + \frac{dN_2{}^e}{dx}\theta_2{}^e + \frac{dN_3{}^e}{dx}\theta_3{}^e + \frac{dN_4{}^e}{dx}\theta_4{}^e. \tag{4.5}$$

In matrix form, the derivative is expressed as $\frac{d\theta^e}{dx} = \begin{bmatrix} \frac{dN_1{}^e}{dx} & \frac{dN_2{}^e}{dx} & \frac{dN_3{}^e}{dx} & \frac{dN_4{}^e}{dx} \end{bmatrix} \begin{bmatrix} \theta_1{}^e \\ \theta_2{}^e \\ \theta_3{}^e \\ \theta_4{}^e \end{bmatrix} = B^e d^e$ (4.6)

This local derivative of the trial solution of each element (4.6), local matrix system, is assembled into the global matrix system for the domain using the function $np\_calc\_system\_mat$. Subsequent steps to be considered in order to solve the forward problem are documented in section J1 of the appendix.

4.5 The Concept of Probability in Addressing the Inverse Problem

Probability theory enables one to address the inverse problem of reconstructing an image of an unknown distribution, given the boundary voltage measurements and current injection sequences, by predicting the most likely actual image as there is no practicable way of affirming what the correct image looks like. Through this method, the likely image is obtained by fitting it to the actual voltage measurements or some prior assumption about the solution.

For a set of n continuous random variables $x \epsilon R^n$, there exists a probability density function (pdf) $p_x \,\epsilon\, [0, 1]$. If l and u are respectively the lower and upper bound on x, then the probability of x_i being within the closed interval [l, u] is

$$p(x_i \,\epsilon [l,\ u]) = \int_l^u p_x \, dx. \tag{4.7}$$

Suppose this probability is a multivariate Gaussian distribution, its density function is

$$p_x = \frac{1}{2\pi v^{n/2}} e^{-\|x-\mu\|^2/2v} \tag{4.8}$$

where v is its variance and μ the mean $expected$ value of x derived from

$$\mu = \int_{-\infty}^{+\infty} \int_{-\infty}^{+\infty} . . . \int_{-\infty}^{+\infty} p_x \, dx_1 \, dx_2 . . . \, dx_n \tag{4.9}$$

In addition, a symmetric non-diagonal covariance matrix can be defined as

$$C(x) = v\delta_{ij} \tag{4.10}$$

where δ is the Kronecker delta function (Trefethen 1994). Conversely, when the covariance matrix is known and invertible then the pdf of the set x is the multivariate Gaussian distribution

$$p_x = \frac{1}{(2\pi)^{n/2} (\det A)^{1/2}} e^{\frac{1}{2}\|x-\mu\|_A^2} \tag{4.11}$$

where $$A = C(x)^{-1}$$

is the inverse of the positive definite covariance matrix, det A the determinant of A, and $\|.\|_A$ a weighted norm of a vector d satisfying

$$\|d\|_A = (d^* A d)^{1/2} \text{ (Polidorides 2002).} \tag{4.12}$$

In practice, the closest to actual conductivity distribution is obtained having known some prior knowledge about it, together with a degree of confidence regarding the distribution of noise in the measurements. More often, the measured peripheral voltage data are added to some Gaussian noise distribution with mean, μ, zero and variance v. That is , if $V \epsilon\, C^m$ is the noise-free measurement, then

$$\tilde{V} = V + \varepsilon\varepsilon \qquad (4.13)$$

are the noise-contaminated measurements, where $\varepsilon\varepsilon \, \epsilon \, R^m$ is the Gaussian noise distribution (Polidorides 2002). In the designing of a data acquisition circuit, the measurement scheme is defined as such that a constant covariance

$$C(\varepsilon\varepsilon) = KI \qquad (4.14)$$

is maintained for all measurement (i.e. all measurements are exposed to the same noise). A full-rank and a positive definite covariance matrix $C(\varepsilon\varepsilon)$ can be constructed from an independent set of boundary measurements as

$$C(\varepsilon\varepsilon) = C(V) = Q^{-1}, \qquad (4.15)$$

where Q is the inverse of the covariance matrix with a well defined square root, $Q^{1/2}$ (Polidorides 2002). In essence, the set of correlated random data with a noise signal of zero mean and variance one is stated as

$$\tilde{V} = Q^{1/2}V \qquad (4.16)$$

with an estimated covariance

$$C(\tilde{V}) = Q^{1/2}C(V)(Q^{1/2})^{*} \qquad (4.17)$$

where A^{*} is the complex conjugate transpose of A in contrast to the transpose A^T (Polidorides 2002)

With a view to modelling the conductivity distribution, one can use a probabilistic distribution to reflect confidence about the model parameter of conductivity distribution. For instance, one can provide a good initial guess x_p or effect the information that the distribution conforms to some kind of smoothing imposed by a discrete differential operator, $P.$ Significantly, the latter implies that the P-norm of the distribution is small enough, i.e.

$$\|x\|_p < k \qquad (4.18)$$

where k is a small positive scalar (Polidorides 2002). In other words, this ensures a better form of correlation among nearby elements of the model, effectively preventing them from varying independently. If

$$\breve{x} = W(x - x_p) \tag{4.19}$$

is the correlated conductivity distribution. Where W is a discrete differential operator, the associated covariance is

$$C(\breve{x}) = vI \tag{4.20}$$

and

$$C(x) = (W^*W)^{-1} = P^{-1} \tag{4.21}$$

provided that P is invertible and positive definite so that $W = P^{1/2}$ (Polidorides 2002). It is noteworthy that the regularization technique used in addressing the inverse problem is a means of introducing the image prior information and can be used to de-correlate the noise signals from the measurements or to correlate the value of the pixels in the image according to some prior knowledge about the conductivity solutions. Addressing the inverse problem of computing the conductivity distribution given the boundary voltages for a sequence of current stimulation pattern, follows the sequence of computational operations illustrated in section J2 of the appendix. Since the explored libraries provide no means for researchers to develop an image-prior code from measured data from their laboratories, image prior function developed using data from other laboratories was used in this work.

4.5.1 Writing of MATLAB Code to Solve the Inverse Problem

Three data sets are required to solve the inverse problem in ERT. The measured voltage for homogeneous distribution of conductivity with a fixed current injected, for inhomogeneous distribution of conductivity with the same current injected and the electric field in the interior from which the Jacobian matrix is computed have to be obtained in order to solve the inverse problem. Through the exploration of EIDORS, the inverse problem is solved with the function ``inv_solve'' on line 26 in section 3.3.3 of chapter 3. The function accepts the simulated voltage for homogeneous distribution of conductivity and simulated voltage for inhomogeneous distribution of conductivity as an input variable. The simulated voltage for homogeneous distribution of conductivity was computed by solving the forward problem when the conductivity of each tetrahedron was set to be one as in section 3.2.6 and 3.2.7. The simulated measured voltage data sets for inhomogeneous solution was computed from the product of ratio of simulated measured voltage for homogeneous solution to measured voltage for homogeneous solution (scaling factor) and the measured voltage for inhomogeneous solution as in the code on lines 6 - 8 of section 3.2.10. Thus, since the inverse solver function solves for resistivity distribution in the domain from the difference between the two measured voltage data sets, the solution of the inverse problem (output of inv_solve) is a distribution of the difference in resistivity value over each tetrahedron element.

4.6 Description of Experimental Work for Imaging the Movement of Solid Objects Suspended in a Mildly Saline Bulk Homogeneous Solution

In addressing one of the objectives of this research that focuses on exploring EIDORS with a view to obtaining the best 3-D measurement strategy for 3-D image reconstruction, a number of experiments were carried out by suspending cuboid shaped perspex and polyvinylchloride insulators of various volumes into a homogeneous, conductive solution.

4.6.1 Purpose of the Experiment

The aims of the experiments were as follow: (a) to test the written reconstruction codes from the impemented algorithm in order to determine the hyperparameter value, number of iteration involved in solving the inverse problem, the reconstruction type and image prior function that are most suitable for the UCT tomography rig.(b) to obtain the best 3-D measurement strategy, this was done through a comparative study of the volume and position of axis of symmetry (PAS) along the diameter of the vessel of the suspended phantom objects and the reconstructed image.

4.6.2 Material for the Experimental Set-up

In figure 4.16, the six suspended cuboid perspex and PVC insulating materials that were suspended into the homogeneous medium so as to initiate region of low conductivity distribution are displayed. Three rulers as well as six pieces of short length of twine were used to suspend various insulating materials in the course of the experiment in the 22cm diameter cylinder as shown in figure 4.15a. The conductivity of bulk solution in all experimental work was 100mg/l NaCl solution. Considering the specification of the computing system used in this work, the minimum volume of the region of resistivity distribution that can be modelled is 0.24ml. The choice of size and geometry of the suspended objects was made with a view to carrying out appropriate comparative study of the object and image in order to achieve the optimal measurement scheme.

Figure 4.16: Cuboid shaped perspex and polyvinylchloride (PVC) insulating materials suspended into the homogeneous conductive solution to introduce region of low conductivity distribution. From the left to right, the volume of the insulating materials are 11.6ml, 11.6ml, 42.6ml, 39.5ml, 37.5ml and 42.6ml.

4.6.3 Experimental plan to Search for the Best Measurement Sequence for the UCT tomography Set-up

Thirty set of measurements were performed as detailed in the experimental plan of table 4.2 in order to determine an optimal measurement strategy. The experimental plan entails the suspending a solid object at various position along the diameter of the vessel and relating the volume and the centre of gravity of the suspended phantom with the reconstructed image.

4.6.4 Analysis Tools Developed for the Experimental Data

For the purpose of this research, an optimal measurement strategy should yield voltage data sets with which the distribution of the resistivity values resulting from solution of the inverse problem should be the same as the actual distribution. The correspondence of the distribution of resisitivity was measured by comparing the volume of the suspended phantoms with the volume of the region of high resistivity values. The region of high resistivity is assumed to be the region between 0 and 20% on the colour bar scale that maps increasing conductivity of each element to the respective colour code from bottom to the top as in Figure 4.17. The degree of 'blueness' increases with the resistivity of the region, while the degree of 'redness' increases with conductivity of the region.

Table 4.2: An Experimental Plan to Search for an Best Measurement Sequence for the Designed UCT Tomography Hardware.

S/N	Number of Rings	Distance of Phantom (volume of 39.5 ml) from the boundary (cm)	Current Injection Pattern	Voltage measurement sequence (No measurement on injection electrode)
1	2	3.0	Opposite	Adjacent
2		7.0		
3		11.0		
4		15.0		
5		19.0		
6	2	3.0	Adjacent	Adjacent
7		7.0		
8		11.0		
9		15.0		
10		19.0		
11	3	3.0	Opposite	Adjacent
12		7.0		
13		11.0		
14		15.0		
15		19.0		
16	3	3.0	Adjacent	Adjacent
17		7.0		
18		11.0		
19		15.0		
20		19.0		
21	4	3.0	Opposite	Adjacent
22		7.0		
23		11.0		
24		15.0		
25		19.0		
26	4	3.0	Adjacent	Adjacent
27		7.0		
28		11.0		
29		15.0		
30		19.0		

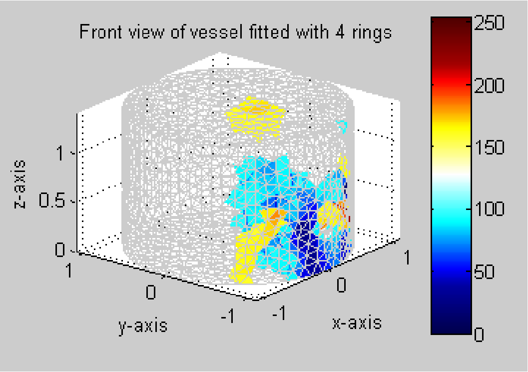

Figure 4.17: A map of the resistivity values of the tetrahedral element to colour bar scale. In this case, 'blueness' values of 0 to 50 (20% of the total) would be considered as imaging the solid object (Phantom).

For a tetrahedron with vertices **a** = (a_1, a_2, a_3), **b** = (b_1, b_2, b_3), **c** = (c_1, c_2, c_3), and **d** = (d_1, d_2, d_3), the volume is $\frac{1}{6} \cdot |\det(a-b, b-c, c-d)|$. In product form, the volume is expressed as

$$V = \frac{|(a-b)\cdot((b-d)\times(c-d))|}{6}. \tag{4.22}$$

The volume of the region was computed by summation of the volume of those tetrahedra with resistivity values lying within the region of high resistivity values using equation 4.22. A piece of MATLAB code for executing the summation of the volumes of tetrahedra with high resistivity values is found in section K1 of the appendix. Furthermore, the location in space of an axis passing through the center of gravity of the volume of reconstructed image and parallel to the z-axis moving along the y-axis (along the diameter of the vessel) for a fixed x-axis value is referred to as the position of the axis of symmetry (PAS). It was compared to that of the actual suspended phantom.

The center of gravity of a system of particle is defined as the average of their positions, r_i, weighted by their gravityes, m_i. The centre of gravity, $R = (X_{cm}, Y_{cm}, Z_{cm})$, is expressed as

$$R = \frac{\sum m_p r_p}{\sum m_p},$$

where $r_p = (x_p, y_p, z_p)$ and m_p is the gravity of each tetrahedral element. Alternatively, It could be written with respect to the reference coordinate as

$$X_{cm} = \frac{\sum \rho x_p v_p}{\sum \rho v_p},$$

$$Y_{cm} = \frac{\sum \rho y_p v_p}{\sum \rho v_p} \text{ and}$$

$$Z_{cm} = \frac{\sum \rho z_p v_p}{\sum \rho v_p},$$

where ρ is the density of each tetrahedron assumed to be constant for all tetrahedra considered, v_p is the volume of each tetrahedron element, p is the index of the tetrahedral element and x_p, y_p, z_p are the mean of each of the coordinates along the reference axis for the four nodes. The mean $x_p, y_p\ and\ z_p$ are defined as follows.

$$x_p = \frac{1}{4}\left(\sum_{i=1}^{4} x_i{}^p\right) \qquad (4.23a)$$

$$y_p = \frac{1}{4}\left(\sum_{i=1}^{4} y_i{}^p\right) \qquad (4.23b)$$

$$z_p = \frac{1}{4}\left(\sum_{i=1}^{4} z_i{}^p\right) \qquad (4.23c)$$

Thus, X_{cm}, Y_{cm} and Z_{cm} are expressed as

$$X_{cm} = \frac{\sum_{p=1}^{n}(x_p\, v_p)}{\sum_{p=1}^{n} v_p},$$

$$Y_{cm} = \frac{\sum_{p=1}^{n}(y_p\, v_p)}{\sum_{p=1}^{n} v_p} \text{ and}$$

$$Z_{cm} = \frac{\sum_{p=1}^{n}(z_p\, v_p)}{\sum_{p=1}^{n} v_p}.$$

A piece of MATLAB code for the computation of PAS of the region of high resistivity values is found in section K2 of the appendix. The coordinate of PAS of the actual suspended phantom was computed by determining the point of intersection of the three planes bisecting the length, breath and height of the cuboid shaped insulating material as in figure 4.18.

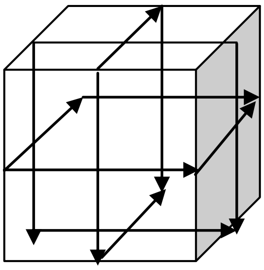

Figure 4.18: A cuboid shaped insulating material bisected by three intersecting planes at the coordinate of its PAS.

4.7 Experimental Design for the Study of Movement of Conductive Fluid Using the 3-D Reconstruction Code Implementing the Best Measurement Sequences

The reconstruction code for the four rings electrode system based on current stimulation through opposite electrode pairs and voltage measurement through adjacent electrode pairs was applied in the imaging of the flow of highly conductive solution within the bulk mildly conductive homogeneous solution.

4.7.1 Application of the 3-D Reconstruction Software to Visualise the Spherical Diffusion of Various Concentration of Experimental Solution in a Bulk Mildly Saline Solution

An investigation into the applicability of this reconstruction software in monitoring the flow of higher conductive solution is directed at ascertaining the physical phenomena that are influencing the movement of the fluid. Hypothetically, gravitational force, frictional force, force due to mixing of the fluid and diffusion of the fluid are assumed to influence the mixing of the fluids at various concentration in the vessel. The series of experiment conducted by Baxter and Brighton (2010) to determine the extent of applicability of the 3-D ERT reconstruction software to study the movement of conductive fluids can broadly be categorised into the following:

(a) Investigating the applicability of the 3-D ERT reconstruction software to examine the spherical geometry of diffusion of higher conductive experimental solution injected into a bulk mildly saline solution.

(b) Studying the applicability of the 3-D ERT reconstruction software to analyse the radial geometry of diffusion of higher conductive experimental solution injected into a mildly bulk saline solution.

(c) Ascertaining the use of the 3-D ERT reconstruction software to view the planar geometry of diffusion of higher conductive experimental solution injected into the base of a mildly bulk saline solution.

(d) The use of the 3-D ERT reconstruction software to visualise the flow of higher conductive fluid through a packed bed.

In addressing the extent of applicability of the 3-D ERT software to imaging spherical diffusion, table 4.3 highlights the sequence of experiments that were conducted. For all the experiments in table 4.3, the bulk homogeneous saline solution was prepared by the dissolution of 1.8g of NaCl into 6.7 litres of water to form a concentrated solution of approximately 0.005 molality. The temperature of the bulk saline solution was maintained at 22^0C, while the temperature of air within the laboratory was measured to be between 23^0C and 24^0C. Highly conductive solution was injected in various manners to spread by diffusion through the less saline bulk solution. The Scilab based modelling of the movement of NaCl ions due to diffusion carried out by Baxter and Brighton (2010) provided the time-scale, indicating how far solution would have migrated, and thus when data sets are to be measured from the periphery electrodes.

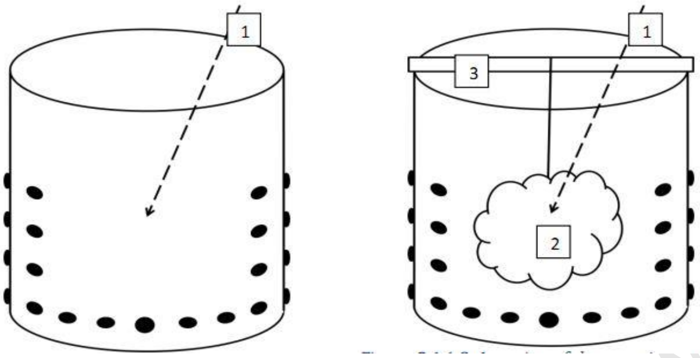

(a) (b)

Figure 4.19. (a) Location of experimental solution injection in the empty tank. 1 = Syringe injection
(b) Location of experimental solution into a tank containing the bath sponge. 1= Syringe injection. 2 = Bath sponge. 3 = Support for sponge.

Table 4.3: Experimental plan to study the movement of conductive fluid due to spherical diffusion within an unimpeded medium using four rings electrode system

S/N	Description of Injected conductive fluid	Time	Current injection strategy	Voltage Measurement strategy
1	Injection of 4ml of 1M of NaCl solution into the center of the tank, using a ceramic dispersion head syringe (figure 4.19a)	0 sec.	Opposite	Adjacent
		5 sec.		
		10 mins.		
2	Injection of 4ml of 1M of NaCl solution at the top of the tank using a ceramic dispersion head syringe	0 sec.	Opposite	Adjacent
		5 secs.		
		10 secs.		
		90 mins.		
3	Injection of 4ml of 1M of NaCl solution through a needle into the centre of a bath sponge suspended at the centre of the tank (figure 4.19b)	5 secs.	Opposite	Adjacent
		10 secs.		
		15 secs.		
		30 secs.		
4	Injection of 4ml of 1M of NaCl solution through a needle into the centre of a bath sponge suspended at the centre of the tank	5 sec.	Adjacent	Adjacent
		10 secs.		
		30 secs.		
		2 mins.		
		15 mins.		

Following the rapid rate of dropping of the injected conductive experimental solution in an unimpeded medium at various location as shown in table 4.3, the set of experiment described in table 4.4 were carried out in a more impeded medium (a saturated foam sponge).

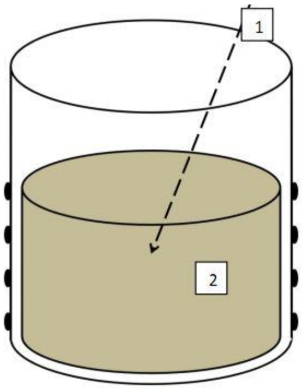

Figure 4.20: Location of experimental solution injection into the tank filled with foam. 1 = Syringe injection. 2 = Saturated foam

Table 4.4: Experimental plan to study the movement of conductive fluid due to spherical diffusion within a foam impeded medium using four rings electrode system.

S/N	Description of Injected conductive fluid	Time	Current injection strategy	Voltage Measurement strategy
1	Spherical injection of solution of 10% acetic acid into the centre of highly porous foam saturated with mildly saline solution (figure 4.20)	0 sec. 3 sec. 10 mins. 17.5 hours	Opposite	Adjacent
2	Spherical injection of solution of 1M NaCl into the centre of highly porous foam saturated with mildly saline solution (figure 4.20)	30 sec. 16 hours. 68 hours.	Opposite	Adjacent

4.7.2 Application of the 3-D Reconstruction Software to Study the Radial Diffusion of Various Concentration of Experimental Solution in A Bulk Mildly Saline Solution

The applicability of the reconstruction code for the four ring electrode system, based on stimulation through opposite electrode pairs and voltage measurement through adjacent electrode pairs for visualising the movement of conductive fluid due to radial diffusion, was tested. In order to visualise the movement of fluid in a mildly conductive solution following radial diffusion, a column of higher conductive fluid was suspended in the tank. This was done by suspending a porous rubber tube filled with 20ml of 1M salt solution at the centre of the tank, as described in the first experiment on table 4.5. In the second experiment, a perspex tube riddled with small holes and inserted into a canvas tube was then used in order to reduce the influence of forces such as gravitational or frictional force other than radial diffusion in the movement of the higher conductive solution. As done in previous experiments, a time scale for the voltage measurement was determined from the model of movement of conductive fluid owing to radial diffusion (Baxter and Brighton 2010). This enabled easy comparison of the movement of fluid in the rig with that of the model.

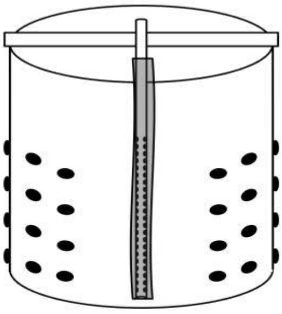

Figure 4.21. Canvas covered Perspex tube positioned within the tank

Table 4.5: Experimental plan to study the movement of conductive fluid due to radial diffusion within an unimpeded medium using four rings electrode system.

S/N	Description of Injected conductive fluid	Time	Current injection strategy	Voltage Measurement strategy
1	Porous rubber tube filled with 1M salt solution as a column of high resistive medium suspended in the centre of the tank	5 mins. 15 mins. 4.5 hours.	Opposite	Adjacent
2	Perspex tube riddled with small holes filled with 20ml of 1M salt solution inserted into a canvas tube (figure 4.21)	3 secs. 10 secs. 60 secs. 3 mins.	Opposite	Adjacent

4.7.3 Application of the 3-D Reconstruction Software to Examine the Planar Diffusion of Various Concentration of Experimental Solution in a Bulk Mildly Saline Solution.

The 3-D reconstruction software requiring data sets from four rings of electrode array was employed in studying the diffusion of higher conductive solution relative to the bulk homogeneous solution in planar geometry, from the base to the top of the tomography vessel. The experimental design involved the injection of a 50ml of 0.5M NaCl solution at the base of the tank through the draining tube using the peristaltic pump as in figure 4.22. The experimental solution was introduced into the bulk solution using the peristaltic pump with a view to ensuring that no eddies were created and minimal mixing were made during injection. Measurement of sensed voltage at the boundary electrodes were made at specified time as stated in table 4.6 so as to visualise the upward movement of the fluid from the base of the tank.

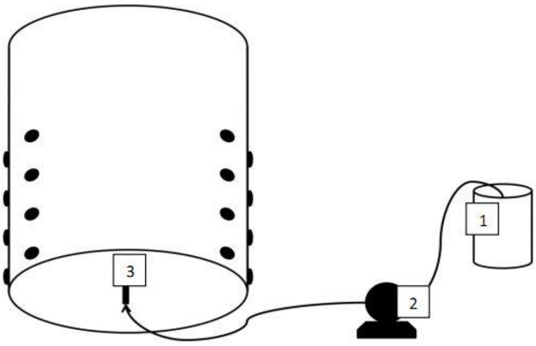

Figure 4.22. Experimental set-up from the bottom view, for getting experimental solution into the bottom of the tank. 1 = Beaker containing the experimental solution. 2 = Peristaltic pump. 3 = Nozzle at the bottom of the tank.

Table 4.6: Experimental plan to study the movement of conductive fluid due to planar diffusion within an unimpeded medium using four rings electrode system.

S/N	Description of Injected conductive fluid	Time	Current injection strategy	Voltage Measurement strategy
1	Injection of 50ml of 0.5M salt into the base of the tank (figure 4.22)	1 mins.	Opposite	Adjacent
		13 mins.		
		38.5 hours		
		50 hours		
		71 hours		

4.7.4 Application of the 3-D Reconstruction Software to Visualise the Flow of conductive Solution through Packed Beds.

The experiments described in table 4.7 were designed to examine the imaging of fluid flow through a packed bed in the tomography rig. The tomography rig contained 15mm diameter glass marbles and a highly porous, low density sponge embedded within. The sponge was immersed so as to introduce some resistance to flow, in addition to the marbles. An experimental solution of 0.1M NaCl solution was sucked from the beaker containing the ionic solution and released into the top of the tank at the rate of 2ml/minute using a dual cartridge peristaltic pump. At the same time an equal amount of the bulk solution was removed through the base of the tank and released into a sink using the same pump, as illustrated in figure 4.23. Because of the small flow rates and the precision at which the two flow rates had to be maintained, a dual cartridge peristaltic pump was used for the pumping of the fluid before a set of readings was taken at a specific time, as stated in table 4.7.

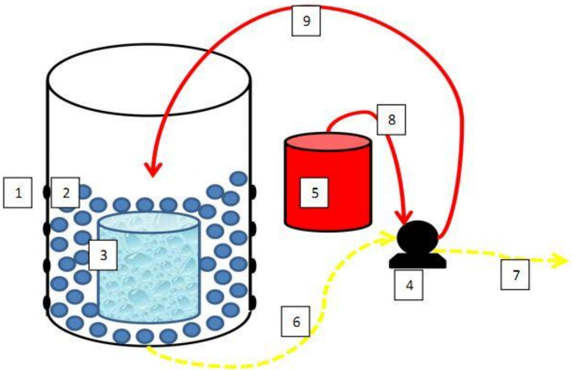

Figure 4.23. Experimental set-up for flow experiments. 1 = Electrodes attached to the tank. 2 = 15mm diameter marbles. 3 = Highly porous, low density sponge. 4 = Dual cartridge peristaltic pump. 5 = Ionic experimental solution. 6 = Drain tube from the bottom of the tank. 7 = Drain tube from the bottom of the tank via pump to sink. 8 = Experimental solution feed to pump. 9 = Experimental solution feed to tank.

Table 4.7: Experimental plan to study the movement of conductive fluid through a packed bed medium using four rings electrode system

S/N	Description of Injected conductive fluid	Time	Current injection strategy	Voltage Measurement strategy
1	Injection of 0.1M NaCl solution dropped in from the top at the same rate as liquid was removed through the base of the tank filled with marbles around a sponge core (figure 4.23).	3 mins. 10 mins. 15 mins. 5.5 hours	Opposite	Adjacent

CHAPTER 5

RESULTS AND DISCUSSIONS

5.1 Analysis of the Position of a Suspended Solid Phantom Using the 3-D Reconstruction Code

The reconstruction code for imaging conductivity distribution considering a two, three and four rings tank for current stimulation through opposite electrode pairs are displayed in sections B2, B4 and B6 of the appendix, respectively, while those for current stimulation through adjacent electrode pairs are reported in section B1, B3 and B5 of the appendix respectively.

A fixed magnitude of current was introduced to stimulate an inhomogeneous conductive medium, which lead to voltage signals on the boundary electrodes. Using the adjacent measurement sequence table, voltage measurements from the boundary electrodes in the two, three and four ring electrode systems were taken when a sequence of current injections through both opposite and adjacent electrode pairs were made.

5.1.1 Reconstruction of Solid Suspended Phantom from Data Sets Measured over Two Rings Due to Stimulation through Opposite Electrode Pairs

Figure 5.1 (a-f) displays the solution of the inverse problem, when the data sets were loaded to an appropriate reconstruction code. The code modelled the tomography vessel by discretising the continuous domain into 3959 finite elements of tetrahedrals with 950 nodal points. Each solution of the inverse problem displayed in figures 5.1 (a-f) were obtained from 2692 measured voltage data frames captured after 3 seconds and each reconstruction was obtained after 25 seconds processing time. A frame rate is the set of 256 voltage data point from 16 sequences of current injection in a ring of electrode with which an image can be reconstructed. The dark blue tetrahedra indicate the location of the suspended solid phantoms, i.e. region of lower conductivity. As the inverse problem was addressed through an iterative numerical technique, it is expected that resolution of the images should be improved with increase in number of iteration. However, from a series of experimental work, more distortion in resolution of images due to noise artefact effects was noticed with increase in number of iterative loop. This unexpected observation is assumed to be related to the use of an image prior developed with data set from other laboratories. The variable "parameter.max_iteration" was set to one to obtain a loop of iteration. Since this setting yields the most improved image quality, this variable was fixed at one in all reconstructed images.

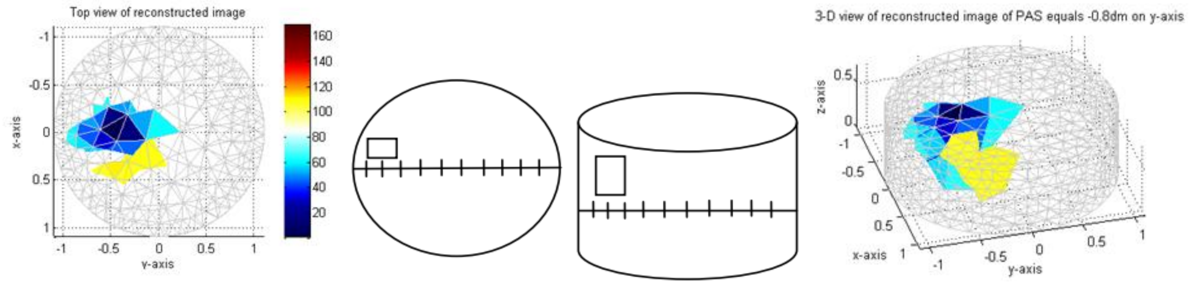

Figure 5.1(a). Plot of solution of the inverse problem for a suspended cuboid perspex phantom at 3cm from the boundary.

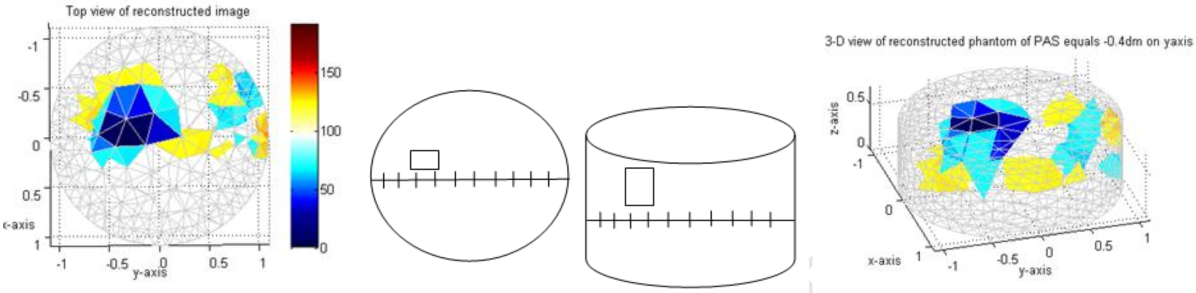

Figure 5.1(b). Plot of solution of the inverse problem for a suspended cuboid perspex phantom at 7cm from the boundary.

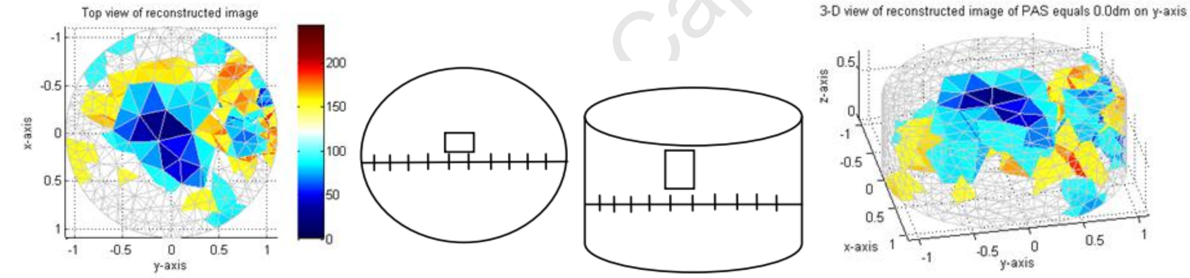

Figure 5.1(c). Plot of solution of the inverse problem for a suspended cuboid perspex phantom at 11cm from the boundary.

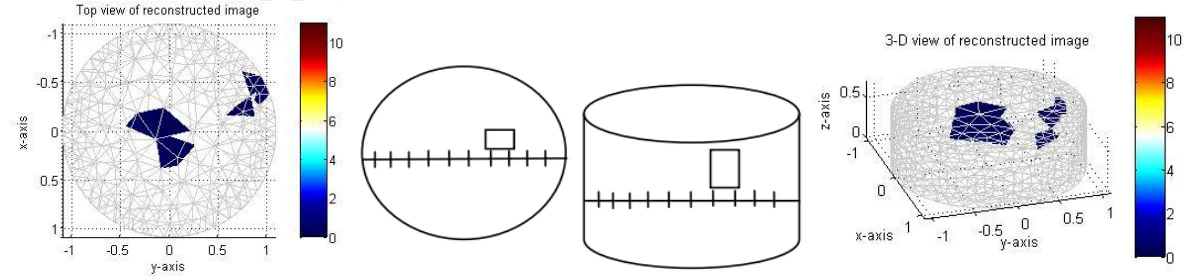

Figure 5.1(d). Plot of solution of the inverse problem with the artefact effects erased for a suspended cuboid perspex phantom at 11cm from the boundary.

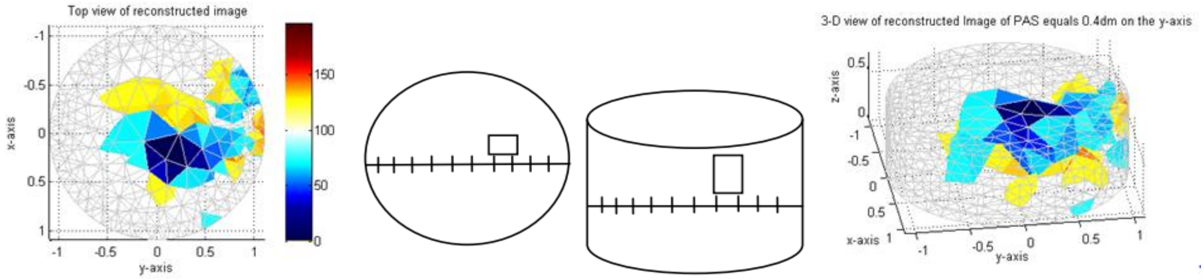

Figure 5.1(e). Plot of solution of the inverse problem for a suspended cuboid perspex phantom at 15cm from the boundary.

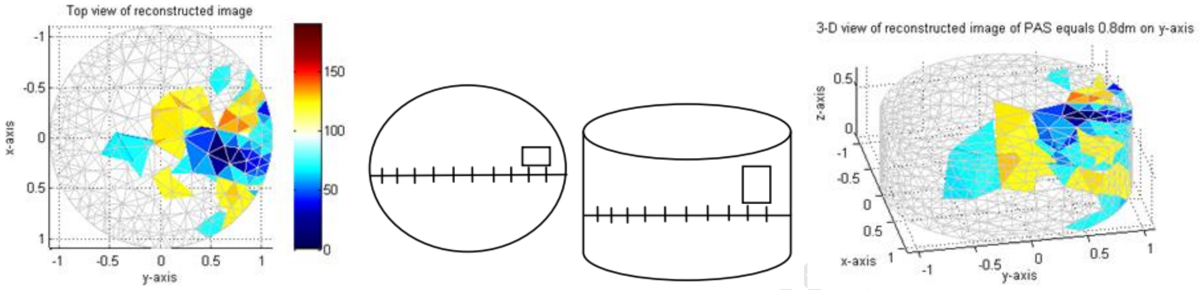

Figure 5.1(f). Plot of solution of the inverse problem for a suspended cuboid perspex phantom at 19cm from the boundary.

Table 5.1 gives an illustration of computed volume and position of axis of symmetry (PAS) parallel to the vertical axis (z-axis) with a view to correlating physical properties of suspended phantoms with that of the reconstructed image. Graphical analysis of the data is presented in figure 5.2(a) and 5.2(b).

Table 5.1. Computed volume and PAS of reconstructed image for various positions of suspended cuboid Perspex phantom for sequence of stimulation of current through opposite electrode pairs in a two rings system.

S/N - Physical Quantities	**1**	**2**	**3**	**4**	**5**
Distance of Phantom from boundary (cm)	3.0	7.0	11.0	15.0	19.0
PAS of phantom (x-axis, y-axis)(cm)	(-1.9, -8.0)	(-1.9,-4.0)	(-1.9,0.0)	(-1.9,4.0)	(-1.9,8.0)
PAS of image (x-axis, y-axis) (cm)	(-0.3, -4.7)	(-0.8, -3.1)	(-0.2,1.5)	(2.3, 1.6)	(1.4, 5.5)
Volume of Phantom (ml)	39.4	39.4	39.4	39.4	39.4
Volume of Image (ml)	18.1	41.3	107.0	39.4	23.3
Error in volume (%)	-54.1	-4.6	171.1	0.2	40.9

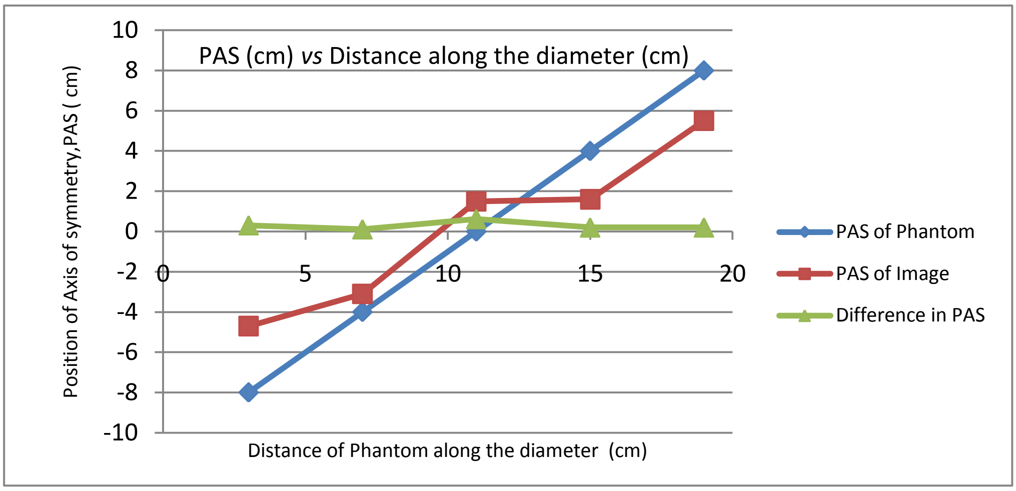

Figure 5.2(a). Variation of position of the axis of symmetry (PAS) of reconstructed image and suspended phantom with distance along the diameter of the tomography rig for the two rings electrode system based on opposite current injection sequences.

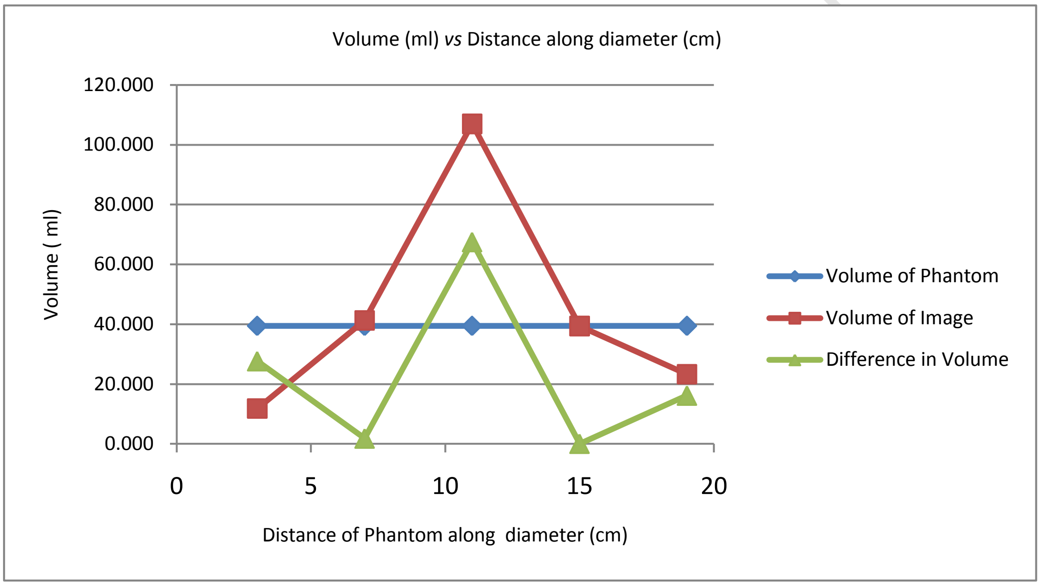

Figure 5.2(b). Variation of volume of reconstructed image and suspended phantom with distance along the diameter of the tomography rig for the two rings electrode system based on opposite current injection sequences.

Figures 5.2 (a and b) show the plot of absolute values of the difference in PAS and volume between the reconstructed image and suspended phantom, respectively.

5.1.2 Analysis of major sources of error associated with all reconstructed images

The plot of absolute values of the difference in PAS and volume between the reconstructed image and suspended phantom is linearly related to the three major errors of the solution of the inverse problem with regards to the loaded UCT data sets.

Firstly, error of the solution of the inverse problem considering the loaded UCT data sets is due to inappropriate polynomial functions with which the electric field lines are modelled as explained in section 4.4. In EIDORS 3D (the version released to the public domain), modified and customised for analysing measured voltage signals from the UCT tomography rig, the shape function that interpolates the nodal voltage values of each element is a first order polynomial function (linear polynomial). Since electric field lines are not straight lines but curves in 2-D, the shape function used in developing EIDORS 3D will model the electric field lines near the boundary of the vessel and not at a point far from the boundary (centre of the vessel) as the field lines are approximately straight lines near the boundary. The inappropriate modelling of the electric field lines will not be improved with either opposite or adjacent current stimulation strategy as the stimulation strategy improves the sensitivity of the Jacobian matrix to pertubation of the electric field and not the shape of the electric field lines.

Secondly, the variation of mesh densities from fine mesh near the boundary to coarse mesh towards the centre produces error in forward solution. The mesh near the boundary and especially near the electrodes is small enough to preserve the accuracy of the measurements, however, the larger meshes within the centre region produce some error in the forward computation, though they reduce the computation time . Thus, a small volume of perturbation close to the centre or at the centre by suspending a small phantom will cause voltage signals to be detected on the boundary electrodes as solution of the forward problem. When the inverse problem is solved with respect to these voltage values, the conductivity distribution will be solved over larger volumes of tetrahedra as the nodal points of these tetrahedra interpolate the solution of the forward problem. Thus, the accuracy of the mesh in appropriately reconstructing images of the same volume as that of the suspended phantom close to the centre of the vessel is reduced due to the increase in coarseness of the mesh towards the centre. In addition, the fineness of the mesh towards the boundary justifies the closeness of the value of volume of suspended phantom near the boundary of the vessel with that of the volume of reconstructed image about the same zone. As the accuracy of the measurement is not preserved towards the centre of the vessel owing to coarseness of the mesh, the accuracy of PAS of the suspended phantom relative to the reconstructed image is reduced as well.

Thirdly, in the development of EIDORS v3.3 explored in this work, the dual model approach requiring the use of a fine mesh for the forward model and a coarse mesh for the image reconstruction was implemented. Since the dual models design entails the use of large mesh FEM for forward modelling, the accuracy of the first order tetrahedra models commonly used in EIT research was explored in the work of Adler *et al*.(2008). It was reported that simple tetrahedra first-order finite element models (FEMs) are not as good as generally assumed in EIT research. Their test showed that models with less than 2500 elements for 2-D imaging and 150,000 elements for 3-D imaging are not able to reproduce the accuracy of the tank phantom measurements (Adler *et al* 2008). Given the specification of the computer system that was employed for reconstructing the images (8GB of RAM and 3.40GHz processor) coupled with the use of first-order finite element models based on dual models in the development of EIDORS v3.3, the required minimum finite element of 150,000 could not be achieved. This is due to limitation of the memory of the computer system used. As such, error due to inaccuracy in reproducing the tank phantom measurements is associated with all the reconstructed images.

5.1.3 Analysis of variation of absolute values of the difference in volume and PAS between reconstructed image and suspended phantom, with distance along the diameter of the vessel for a two rings electrode system based on opposite current injection sequences

In figures 5.2 (a and b), the plots are nearly symmetric about the centre of the vessel. The decrease in the absolute values of the difference in PAS and volume between the suspended phantom and reconstructed image informs that there was progressive decrease in error of the solution of the inverse problem as the phantom was moved away from the boundary to the mid-point between the boundary and the centre of the vessel. As the region of low conductivity (suspended phantom) was moved closer to the centre, the error increases to its peak value. Although the progressive decrease in error towards the mid-point between the boundary and the centre of the vessel cannot be related to inappropriately modelled electric field lines, noisy artefact which made the resolution of reconstructed images poor account for this. Since the noise inherently associated with the UCT hardware cannot be measured, the inconsistency in the noise associated with the device and that added to the simulated voltages in the forward problem, introduces noisy artefact in the images. In addition, the low number of voltage data sets collected over two rings from the UCT vessel is equally responsible for the noisy artefact in the reconstructed images.

The peak value of the error at the centre of the vessel is due to over-approximation of the quadratic shape of the electric field lines at the centre in 2-D (figure 4.2) by the use of linear polynomial shape function in the development of EIDORS 3D.

5.1.4 Reconstruction of solid suspended phantom from data sets measured over two rings due to stimulation through adjacent electrode pairs

Figures 5.3(a - e) show the solutions of the inverse problem for voltage measurements from the two rings electrode system based on adjacent current injection sequences. Each plot of of the solution at various position of the insulating material took 23 seconds when 2440 measured voltage data frames were loaded into the appropriate reconstruction code. The 2440 measured voltage data sets were captured on the data acquisition system after 3 seconds. The tomography rig was modelled with 3959 tetrahedra elements with 950 nodal points in each of the plot of figures 5.3 (a – e).

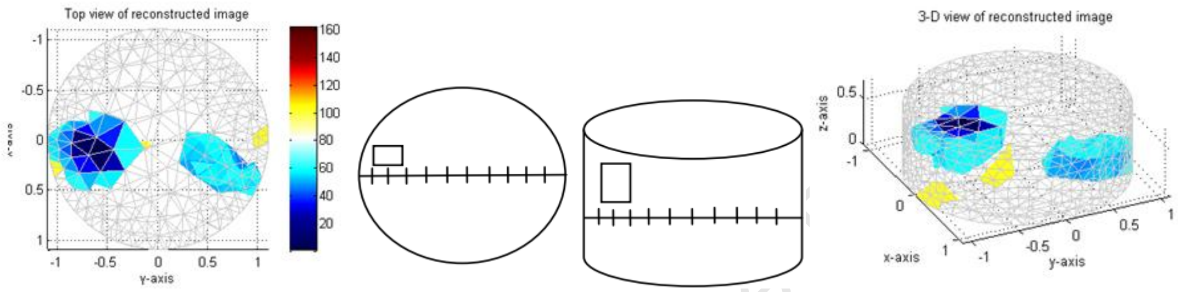

Figure 5.3(a). Plot of solution of the inverse problem for a suspended cuboid perspex phantom at 3cm from the boundary.

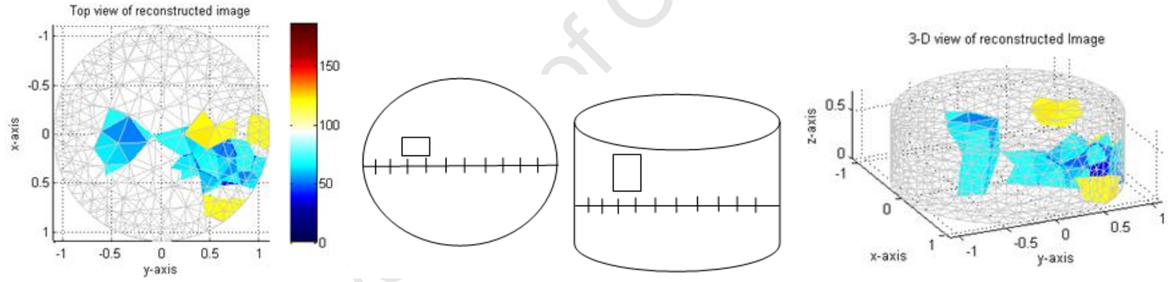

Figure 5.3(b). Plot of solution of the inverse problem for a suspended cuboid perspex phantom at 7cm from the boundary.

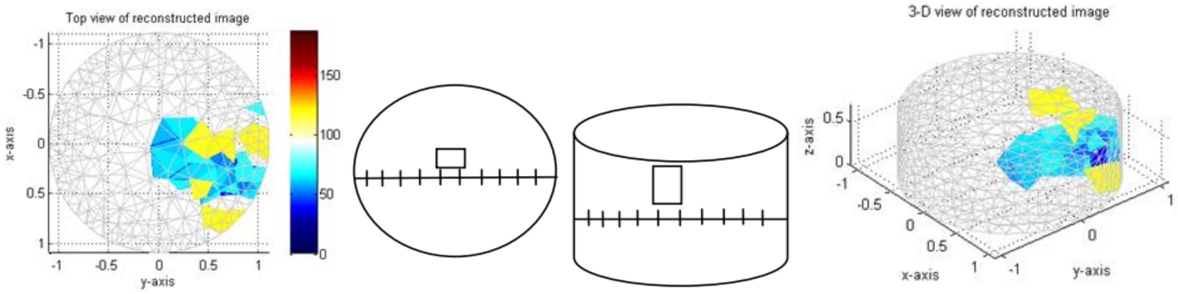

Figure 5.3(c). Plot of solution of the inverse problem for a suspended cuboid perspex phantom at 11cm from the boundary.

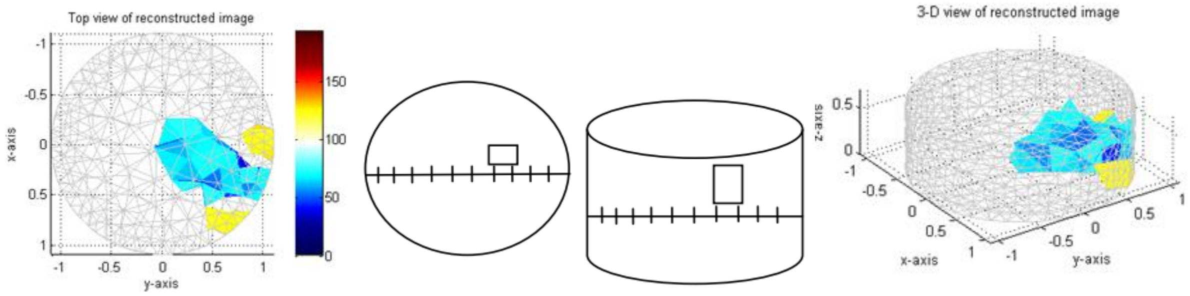

Figure 5.3(d). Plot of solution of the inverse problem for a suspended cuboid perspex phantom at 15cm from the boundary.

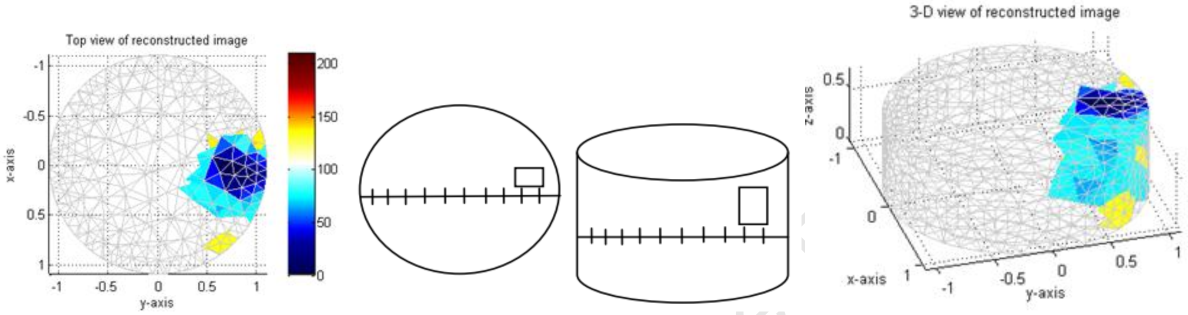

Figure 5.3(e). Plot of solution of the inverse problem for a suspended cuboid perspex phantom at 19cm from the boundary.

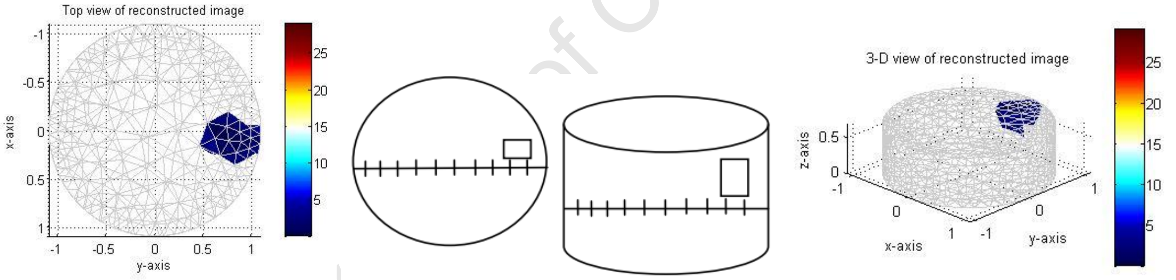

Figure 5.3(f). Plot of solution of the inverse problem with the artefact effects erased for a suspended cuboid perspex phantom at 19cm from the boundary.

The volume and PAS of the reconstructed image were computed from the plot of solutions. Table 5.2 displays the values of these physical quantities and figures 5.4(a - b) give a graphical illustration of the data in order to relate the volume and PAS of the reconstructed image with that of suspended phantoms.

Table 5.2. Computed volume and PAS of reconstructed image for various positions of suspended cuboid perspex phantom for sequence of stimulation of current through adjacent electrode pairs in two rings

S/N - Physical Quantities	**1**	**2**	**3**	**4**	**5**
Distance of Phantom from boundary (cm)	3.0	7.0	11.0	15.0	19.0
PAS of phantom (x-axis, y-axis)(cm)	(-1.9,-8.0)	(-1.9,-4.0)	(-1.9,0.0)	(-1.9,4.0)	(-1.9,8.0)
PAS of image (x-axis, y-axis) (cm)	(1.3, -6.3)	(3.2, 6.7)	(3.1, 6.6)	(2.7, 5.4)	(0.7, 7.9)
Volume of Phantom (ml)	39.5	39.5	39.5	39.5	39.5
Volume of Image(ml)	24.9	19.5	19.8	27.5	26.2
Error in volume (%)	-36.9	-50.5	-49.9	-30.4	-33.5

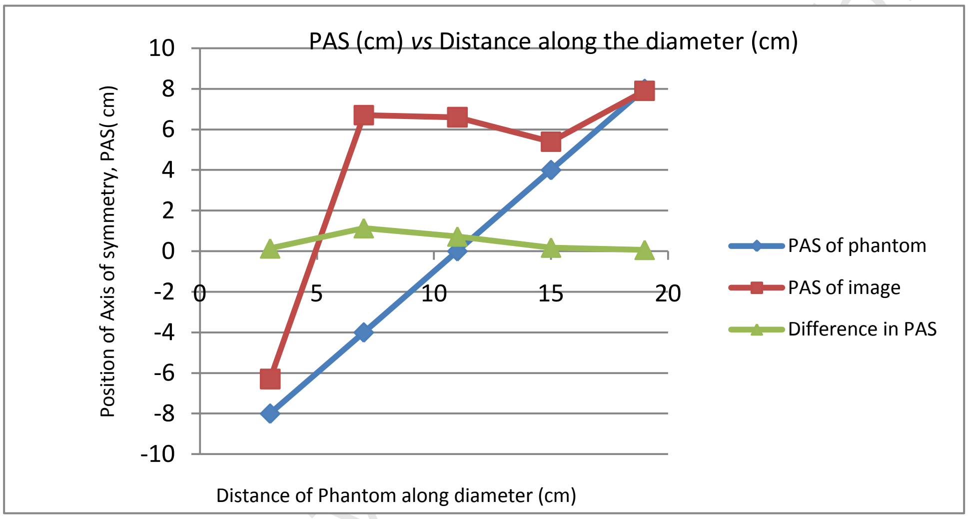

Figure 5.4(a). Variation of position of the axis of symmetry (PAS) of reconstructed image and suspended phantom with distance along the diamter of the tomography rig for two rings electrode system based on adjacent current injection sequences.

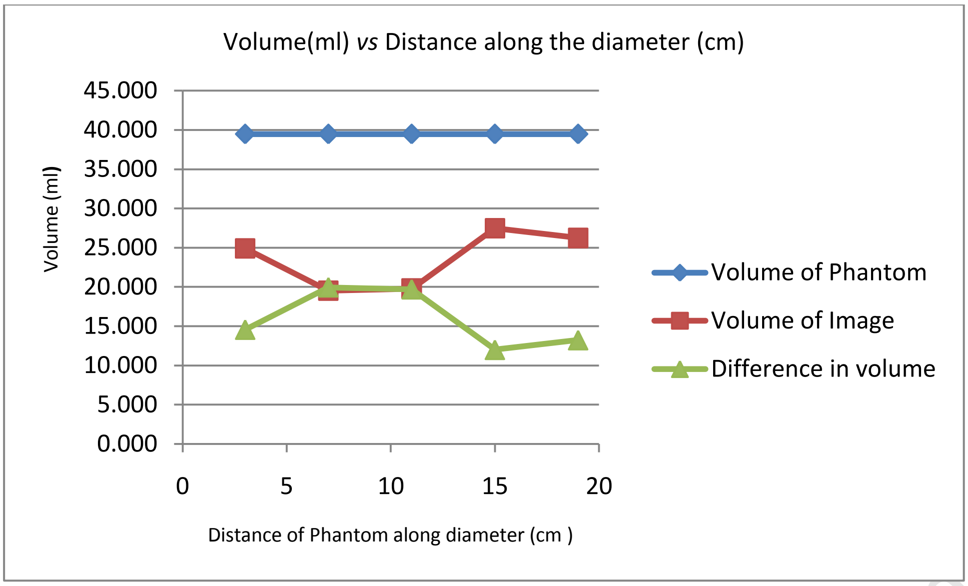

Figure 5.4(b). Variation of volume of the reconstructed image and suspended phantom with distance along the diameter of the tomography rig for the two rings electrode system based on adjacent current injection sequence.

5.1.5 Analysis of Variation of Absolute Values of the Difference in Volume and PAS between Reconstructed Image and Suspended Phantom with Distance along the Diameter of the Vessel for a Two rings Electrode System Based on Adjacent Current Injection Sequences

In figures 5.4 (a and b), the plot of absolute values of the difference in PAS and volume between reconstructed image and suspended phantom is not symmetric about the centre of the vessel. However, from the two ends of the diameter (boundary of the vessel), the error in volume increases as the region of low conductivity is moved away from the boundary towards the centre of the vessel. The peak value of the error was noticed near the centre. This is due to the variation of the zone of much coarseness of the mesh from the centre or near the centre. NETGEN, being an automatic 3-D mesh generation generates meshes with varying density distribution at various times, even with the dimension of the vessel and the electrodes fixed. Also, the location of the peak value of the error (similar to location of the peak value of the error for injection through opposite electrode pairs) confirms that the variation of stimulation strategy from opposite to adjacent does not eliminate the error due to inappropriate modelling of the electric field lines. The peak value of the error at the centre indicate an over-approximation of the electric field lines at the centre considering the use of linear polynomial shape function in EIDORS v3.3 and degree of coarseness of the mesh at centre of the tank. It should be noted that the volume are underestimated in adjacent injection sequences, whereas overestimated in opposite injection sequences.

More so, the noisy artefact shown in the plot in figure 5.3 (a and b), which look like the second phantom is due to inaccurate voltage measurement at the boundary, resulting from a less sensitive Jacobian matrix that was developed from an electric field flux spreading over smaller area owing to stimulation through adjacent electrode pairs.

5.1.6 Reconstruction of Solid Suspended Phantom from Data Sets Measured over Three Rings Due to Stimulation through Opposite Electrode Pairs

Paivi *et al*. (1999) stated that the more the data measured on the boundary of the tomography rig are, the more accurate the approximate solution of the inverse problem should be. This was examined by measuring the boundary voltage on a three rings electrode system. Figure 5.5 (a - e) illustrate the solution of the inverse problem for 2520 frames of adjacent voltage measurements captured over 3 seconds from the three rings electrode system based on opposite current injection sequence. The tomography rig for each of the plot was modelled using 7279 tetrahedra elements with 1608 nodal points. Each reconstructed image displayed in figures 5.5 (a – e) was obtained after 43 seconds.

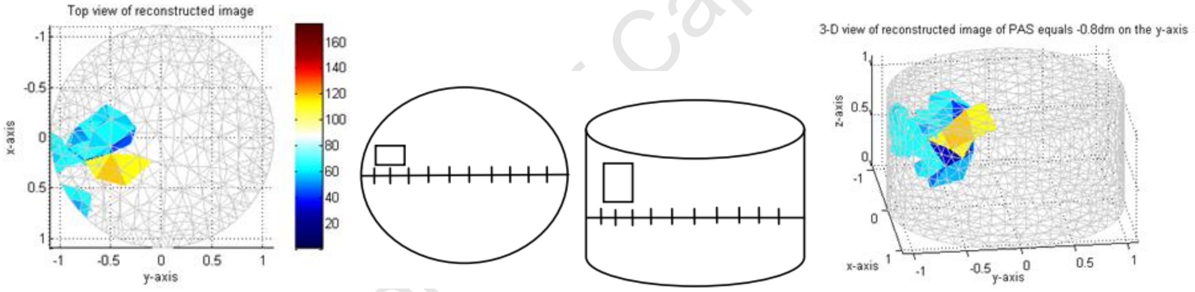

Figure 5.5(a). Plot of solution of the inverse problem for a suspended cuboid perspex phantom at 3cm from the boundary

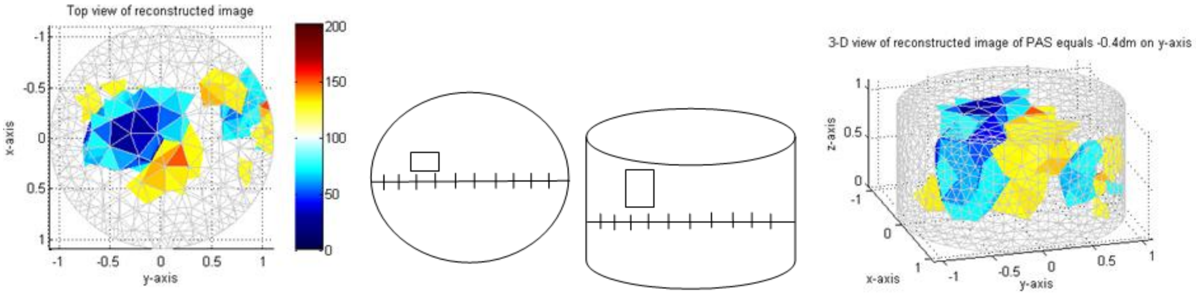

Figure 5.5(b). Plot of solution of the inverse problem for a suspended cuboid perspex phantom at 7cm from the boundary

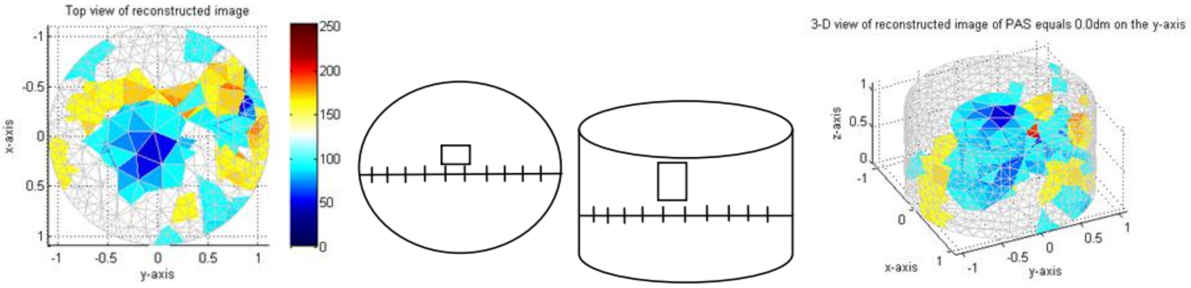

Figure 5.5(c). Plot of solution of the inverse problem for a suspended cuboid perspex phantom at 11cm from the boundary

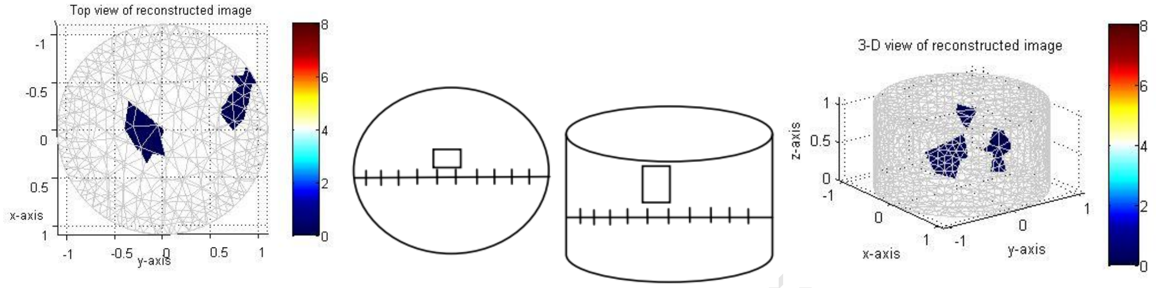

Figure 5.5(d). Plot of solution of the inverse problem with the artefact effects erased for a suspended cuboid perspex phantom at 11cm from the boundary

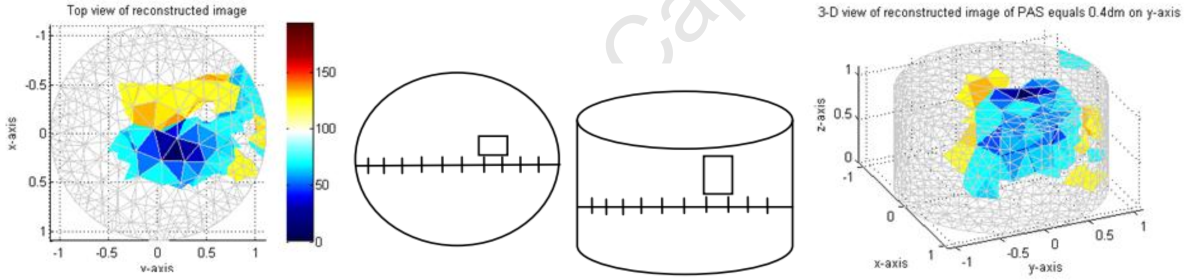

Figure 5.5(e). Plot of solution of the inverse problem for a suspended cuboid perspex phantom at 15cm from the boundary

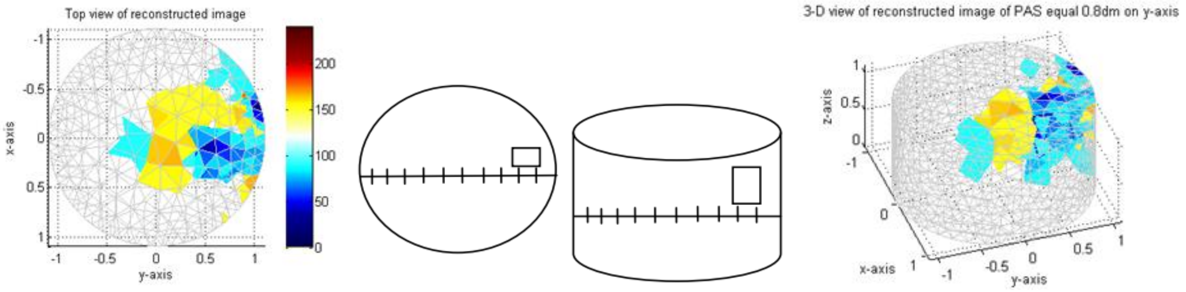

Figure 5.5(f). Plot of solution of the inverse problem for a suspended cuboid perspex phantom at 19cm from the boundary

The volume and the position of the axis of symmetry (PAS) of the reconstructed image were estimated from the plot of the solution as shown in table 5.3. In figures 5.6(a) and (b), the PAS and the volume of reconstructed image were correlated to that of the suspended phantoms respectively.

Table 5.3. Computed volume and PAS of reconstructed image for various positions of suspended cuboid Perspex phantom for sequence of stimulation of current through opposite electrode pairs in three rings

S/N - Physical Quantities	**1**	**2**	**3**	**4**	**5**
Distance of Phantom from boundary (cm)	3.0	7.0	11.0	15.0	19.0
PAS of phantom (x-axis, y-axis)(cm)	(-1.9,-8.0)	(-1.9,-4.0)	(-1.9,0.0)	(-1.9,4.0)	(-1.9,8.0)
PAS of image (x-axis, y-axis) (cm)	(0.3, -5.9)	(-0.4, -3.3)	(-0.2, 1.1)	(1.8, 1.7)	(1.6, 6.7)
Volume of Phantom (ml)	39.5	39.5	39.5	39.5	39.5
Volume of Image (ml)	10.9	102.1	279.9	69.5	54.2
Error in volume (%)	-72.3	158.5	654.6	76.1	37.2

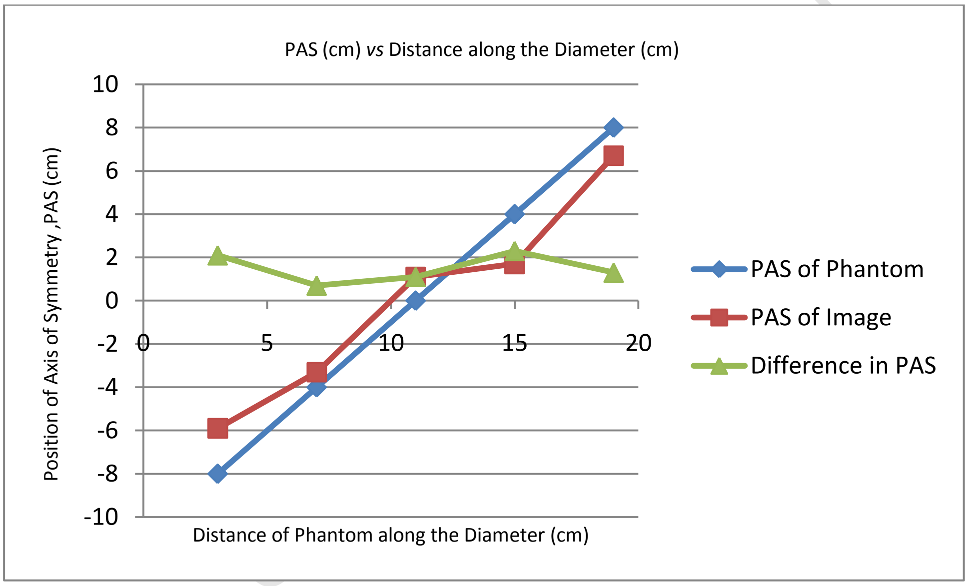

Figure 5.6(a). Variation of position of the axis of symmetry (PAS) of the reconstructed image and suspended phantom with distance along the diameter of the tomography rig for three rings electrode system based on opposite current injection sequences.

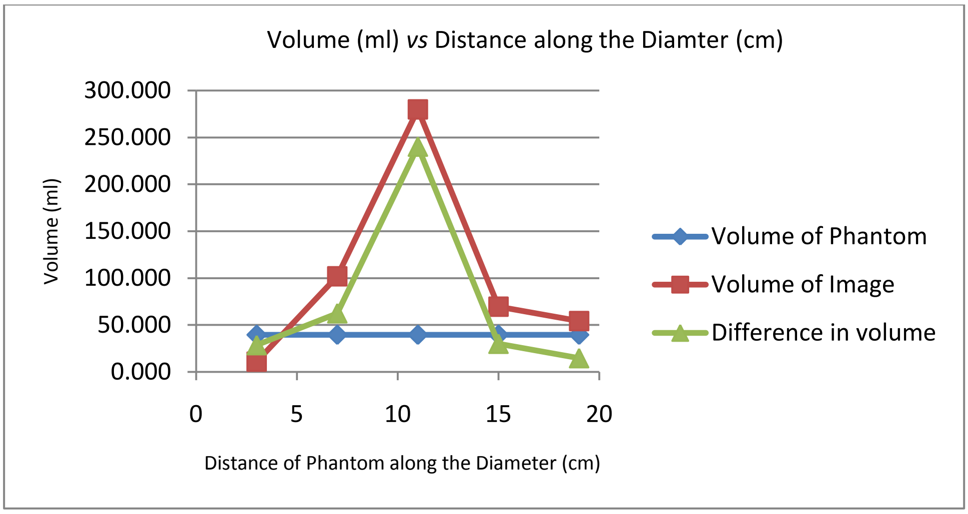

Figure 5.6(b). Variation of the volume of the reconstructed image and suspended phantom with distance along the diameter of the tomography rig for the three rings electrode system based on opposite current injection sequences.

5.1.7 Analysis of variation of absolute values of the difference in volume and PAS between reconstructed image and suspended phantom with distance along the diameter of the vessel for three rings electrode system based on opposite current injection sequences

In figures 5.6 (b), the plot of absolute values of the difference in volume between the reconstructed image and suspended phantom is nearly symmetric about the centre of the vessel. It was noticed that the error increases as the region of low conductivity was moved from the boundary of the vessel to its centre. As previously stated, this is due to the inappropriate modelling of the electric field lines using a linear polynomial shape function and the increase in the degree of coarseness of the mesh towards the centre as explained earlier.

Furthermore, the plot of absolute values of the difference in PAS between the reconstructed image and the suspended phantom in figure 5.6 (a) is not symmetric about the centre of the vessel. There is progressive decrease in the error of the solution as suspended phantom was moved from left end of the boundary to the mid-point of the first radius of the vessel. However, the error of the solution increases when the suspended phantom was moved further from this mid-point. When the suspended phantom was moved further from the centre to the other end of the diameter, the error increases progressively and attains a maximum value at the mid-point of the other radius. The inconsistency in the plot of the absolute value of the difference in volume with the PAS is due to the use of a much less dense mesh for 3-D imaging in this work. As explained in the third major source of error of section 5.1.2, a discretised domain for 3-D imaging should have finite number of element of the order of 10^5. A discretised domain of such would provide an efficient discrete medium that could detect effectively the actual change in the position of the suspended phantom within the five seconds time-interval between successive capture of data. Considering the 7279 tetrahedra elements for the dimension of the process vessel, this finite medium is not efficient at detecting the actual position of the suspended phantom given the time-interval between successive movement and data capture. Thus, the error in PAS as described above. There is overestimation in volume of the images towards the centre because of more coarse mesh near and at the centre. The larger discretised medium of 3 rings (figure 5.6b) containing more coarse mesh near and at the centre as compared with that of 2 rings (figure 5.2b) medium is responsible for more over-prediction in volume for 3 rings than 2 rings

5.1.8 Reconstruction of Solid Suspended Phantom from Data Sets Measured over Three Rings due to Stimulation through Adjacent Electrode Pairs

A sequence of current injection through adjacent electrodes pair in a three rings system was carried out in order to confirm the relative improvement in the accuracy of the solution, given a different stimulation strategy for the same number of electrode. Figure 5.7 (a - f) show the plot of the solution for various position of suspended phantom when 2299 measured voltage data frames captured over 3 seconds were loaded to appropriate reconstruction code. In figures 5.7 (a - e), each reconstructed image was obtained after 42.32 seconds with tomography rig discetised into 7279 tetrahedra elements and 1608 nodal points.

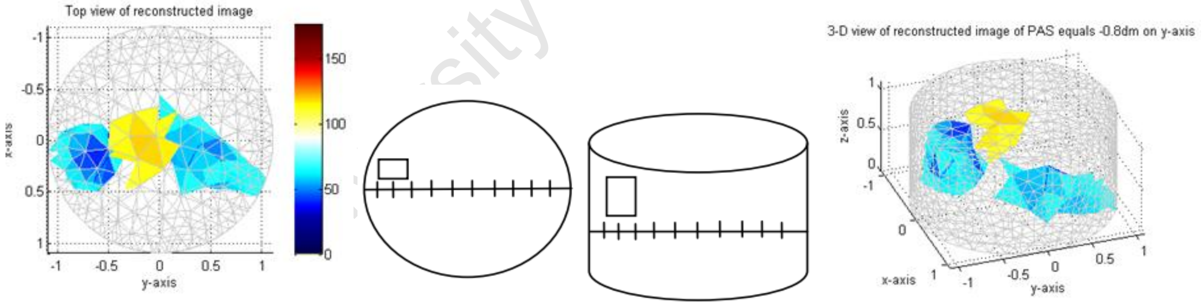

Figure 5.7(a). Plot of the solution of the inverse problem for a suspended cuboid perspex phantom at 3cm from the boundary.

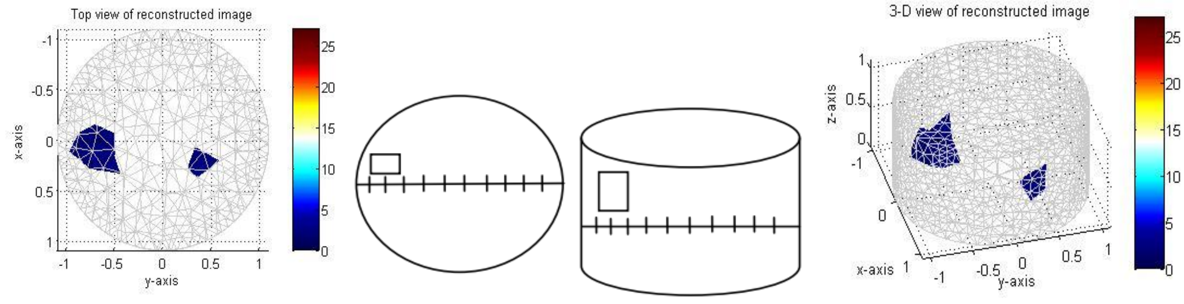

Figure 5.7(b). Plot of the solution of the inverse problem with the artefact effects erased for a suspended cuboid perspex phantom at 3cm from the boundary.

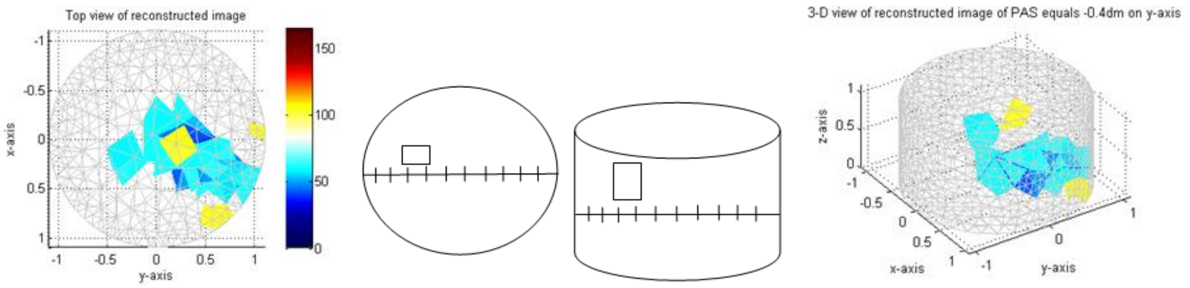

Figure 5.7(c). Plot of the solution of the inverse problem for a suspended cuboid perspex phantom at 7cm from the boundary.

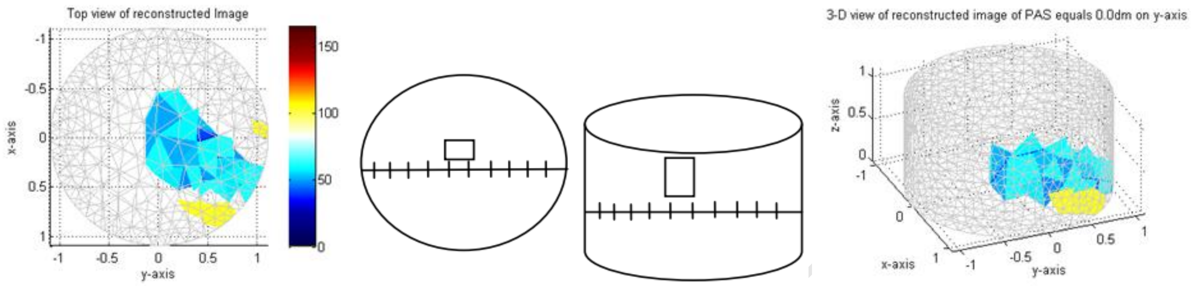

Figure 5.7(d). Plot of the solution of the inverse problem for a suspended cuboid perspex phantom at 11cm from the boundary.

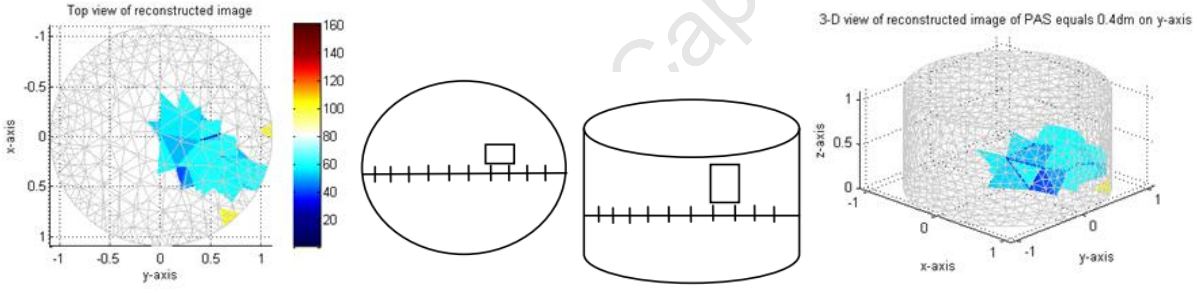

Figure 5.7(e). Plot of the solution of the inverse problem for a suspended cuboid perspex phantom at 15cm from the boundary.

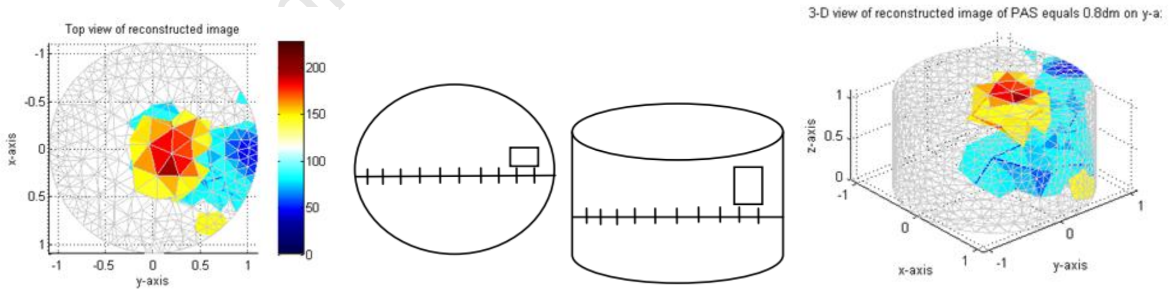

Figure 5.7(f). Plot of the solution of the inverse problem for a suspended cuboid perspex phantom at 19cm from the boundary.

The calculated volume, PAS and the mass of the reconstructed image from the plot of the solutions are shown in table 5.4. Graphical analysis of the calculated values are presented in figures 5.8 (a) and (b) with a view to comparing these quantities for the reconstructed image and region of low conductivity in the rig.

Table 5.4. Computed volume and PAS of reconstructed image for various positions of suspended cuboid perspex phantom for a sequence of stimulations of current through adjacent electrode pairs in three rings.

S/N - Physical Quantities	**1**	**2**	**3**	**4**	**5**
Distance Phantom from boundary (cm)	3.0	7.0	11.0	15.0	19.0
PAS of phantom (x-axis, y-axis)(cm)	(-1.9,-8.0)	(-1.9,-4.0)	(-1.9,0.0)	(-1.9,4.0)	(-1.9,8.0)
PAS of image (x-axis, y-axis) (cm)	(0.9, -7.3)	(2.2, 4.6)	(2.3, 4.2)	(1.9, 4.2)	(1.7, 4.4)
Volume of Phantom (ml)	39.5	39.5	39.5	39.5	39.5
Volume of Image (ml)	16.9	17.6	17.6	17.6	106.2
Error in volume (%)	-57.2	-55.5	-55.5	-55.5	169.0

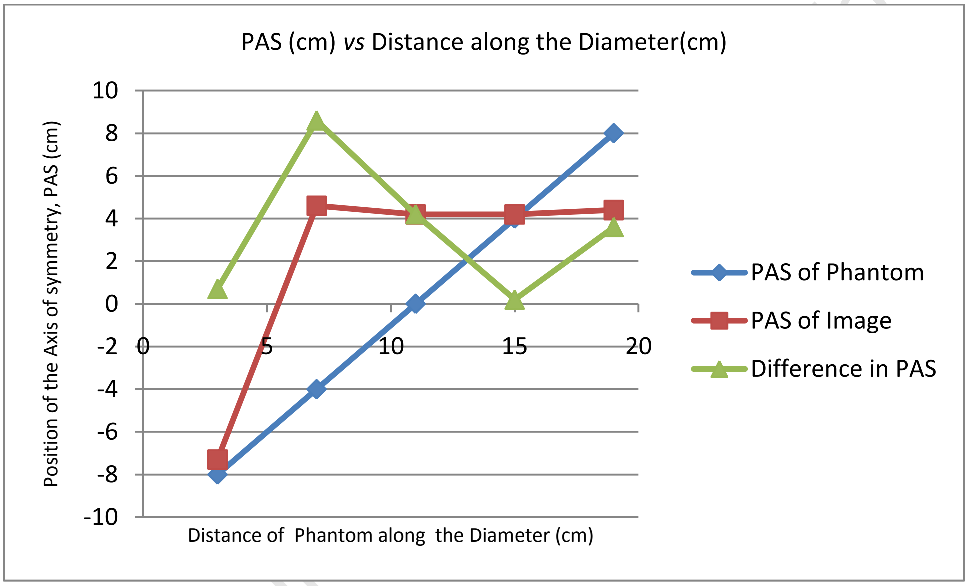

Figure 5.8(a). Variation of position of the axis of symmetry (PAS) of reconstructed image and suspended phantom with distance along the diameter of the tomography rig for the three rings electrode system based on adjacent current injection sequences.

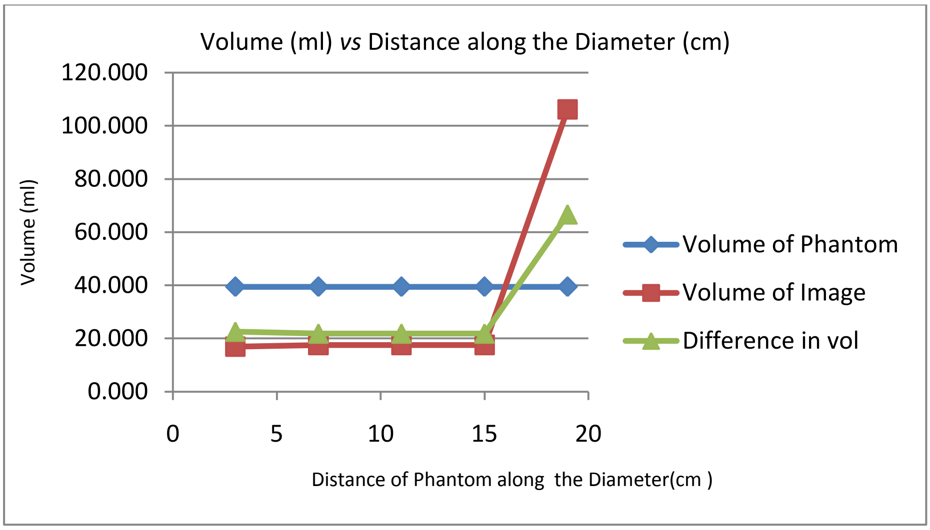

Figure 5.8(b). Variation of the volume of reconstructed image and suspended phantom with distance along the diameter of the tomography rig for the three rings electrode system based on adjacent current injection sequences.

5.1.9 Analysis of Variation of Absolute Values of the Difference in Volume and PAS between Reconstructed Image and Suspended Phantom with Distance along the Diameter of the Vessel for Three Rings Electrode System based on Adjacent Current Injection Sequences

The plot of variation of absolute values of the difference in PAS between the reconstructed image and the suspended phantom with distance along the diameter of the vessel for voltage measured through adjacent electrode pairs due to the sequence of current stimulation through adjacent electrode pairs in a three rings electrode system is shown in figure 5.8(a). The plot is not symmetric about its centre. From one end of the boundary, the error of the inverse solution increases as the region of low conductivity was moved from the boundary to its peak value at the mid-point between the boundary and the centre of the rig. The error decreases as the region was moved towards the centre. From the other end, however, the error in the inverse solution decreases as the region of low conductivity was moved from the boundary to the mid-point between the centre of the vessel and boundary. Further away from this point, the error increases toward the centre of the vessel. The plot of absolute values of the difference in volume between the reconstructed image and suspended phantom for the same measurement strategy is displayed in figure 5.8 (b). The error of the solution of the inverse problem remains fixed with the difference in volume being $21.90ml$ as the region of low conductivity was moved from one end of the diameter pass the centre to the mid-point of the other radius. However, the peak value of the error was noticed at the other end of the boundary with the difference in volume being $66.71ml$.

The plot of the absolute values of the difference in volume in figure 5.8(b) is not consistent with variation of error in relation to figure 5.6 (b) for current stimulation through opposite electrode pairs. Since both current stimulation strategies are evenly affected by the identified major sources of error, it is strongly suspected that current injection through adjacent electrode pairs yields less accurate voltage values at the periphery electrodes. Thus the plot of the PAS is inherently affected by distorted measured voltage signals using adjacent current injection sequences.

The presence of the noisy artefact that mimic a second image in figure 5.7(a) is similar to the plots in figure 5.3 (a and b), in which current stimulation through adjacent electrode pairs was made over two rings. The observed second image is due to inaccuracy in the measured voltage due to less sensitive jacobian matrix developed from an electric field spreading over small area. Figure 5.7(a) shows this error in the measurement is not improved upon with increase in the number of measured data over three rings.

5.1.10 Reconstruction of Solid Suspended Phantom from Data Sets Measured over Four Rings Due to Stimulation through Opposite Electrode Pairs

The solutions of the inverse problem for 3101 frames of voltage measurement from the four ring electrode system based on opposite current injection sequences are displayed in figures 5.9 (a - f). The data sets were collected over 3 seconds. Each reconstruction code in figures 5.9 (a – f) was obtained after 179 seconds using a modelled rig of 16293 tetrahedral elements with 3309 nodal points.

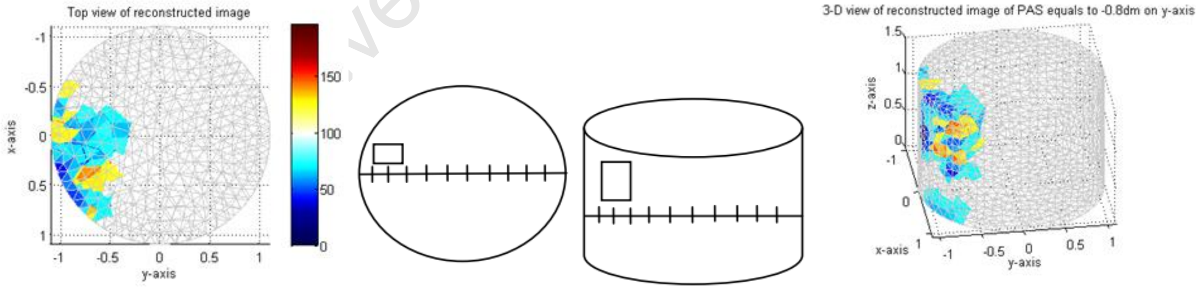

Figure 5.9(a). Plot of the solution of the inverse problem for a suspended cuboid perspex phantom at 3cm from the boundary.

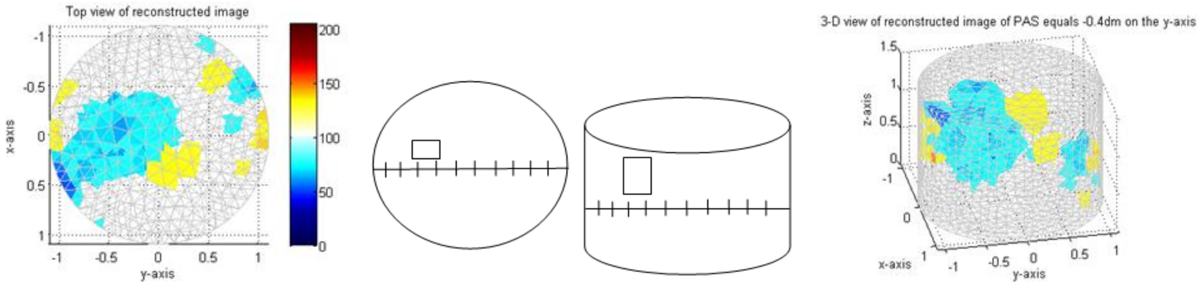

Figure 5.9(b). Plot of the solution of the inverse problem for a suspended cuboid perspex phantom at 7cm from the boundary.

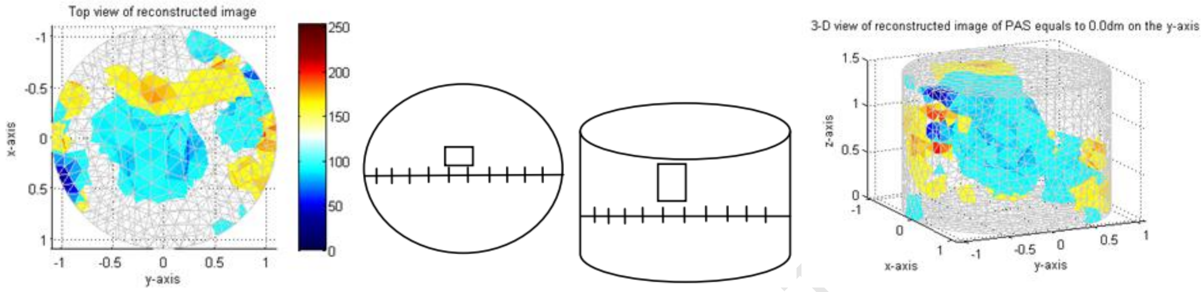

Figure 5.9(c). Plot of the solution of the inverse problem for a suspended cuboid perspex phantom at 11cm from the boundary.

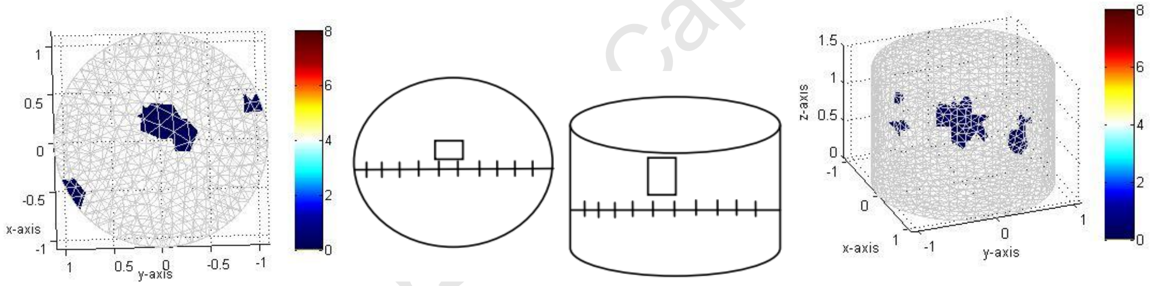

Figure 5.9(d). Plot of the solution of the inverse problem with the artefact effects erased for a suspended cuboid perspex phantom at 11cm from the boundary (centre).

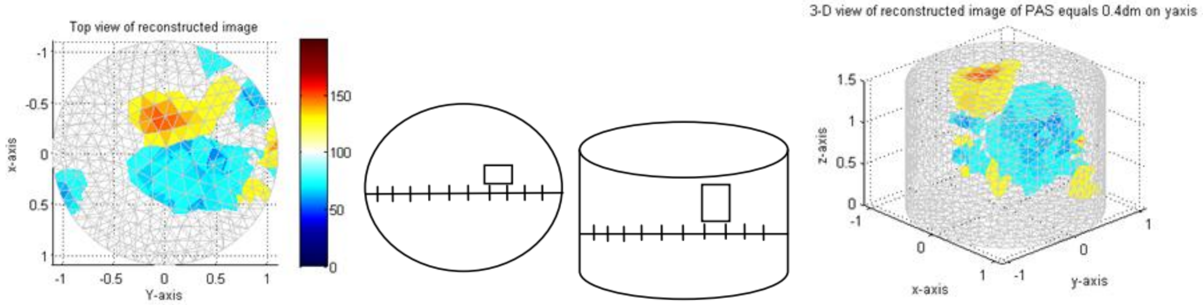

Figure 5.9(e). Plot of the solution of the inverse problem for a suspended cuboid perspex phantom at 15cm from the boundary.

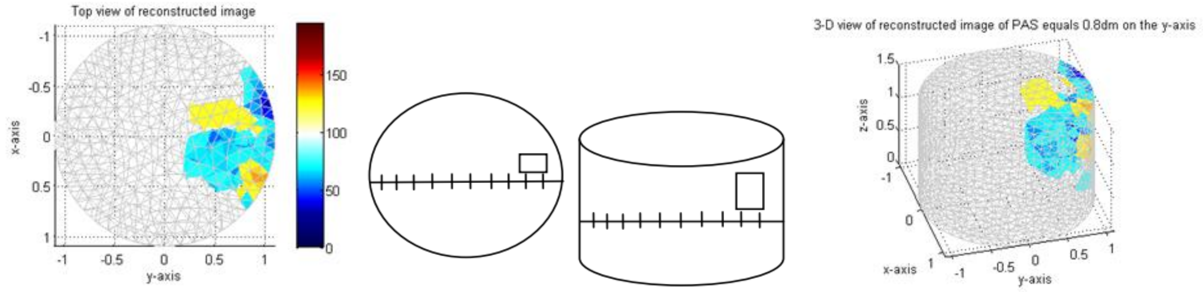

Figure 5.9(f). Plot of the solution of the inverse problem for a suspended cuboid perspex phantom at 19cm from the boundary.

The values of the physical quantities were estimated from the plot of the solution and are presented in table 5.5. Figure 5.10 (a) and (b) are graphical plots relating the estimated physical quantities, PAS and volume, for the region of low conductivity (volume of suspended phantom) and reconstructed image.

Table 5.5: Computed volume and PAS of the reconstructed image for various positions of suspended cuboid perspex phantom for a sequence of current stimulations of current through opposite electrode pairs in four rings

S/N - Physical Quantities	**1**	**2**	**3**	**4**	**5**
Distance Phantom from boundary (cm)	3.0	7.0	11.0	15.0	19.0
PAS of phantom (x-axis, y-axis)(cm)	(-1.9,-8.0)	(-1.9,-4.0)	(-1.9,0.0)	(-1.9,4.0)	(-1.9,8.0)
PAS of image (x-axis, y-axis) (cm)	(0.9, -8.0)	(-0.0, -3.9)	(1.0,-0.7)	(2.1, 3.0)	(1.9, 6.2)
Volume of Phantom (ml)	39.5	39.5	39.5	39.5	39.5
Volume of Image (ml)	33.5	64.8	376.6	67.5	37.3
Error in volume (%)	-15.0	64.2	853.8	71.0	-5.4

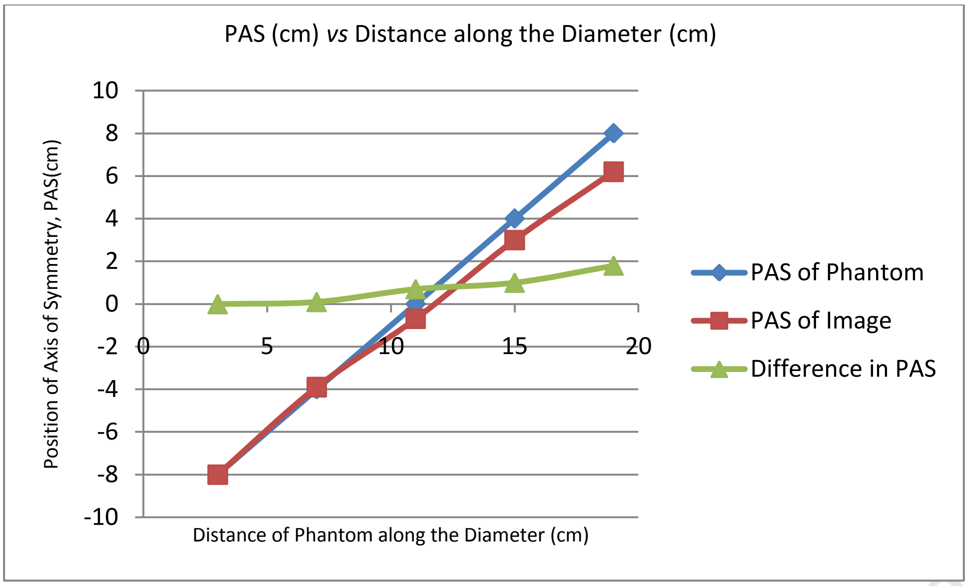

Figure 5.10(a). Variation of position of the axis of symmetry (PAS) of reconstructed image and suspended phantom with distance along the diameter of the tomography rig for the four rings electrode system based on opposite current injection sequences.

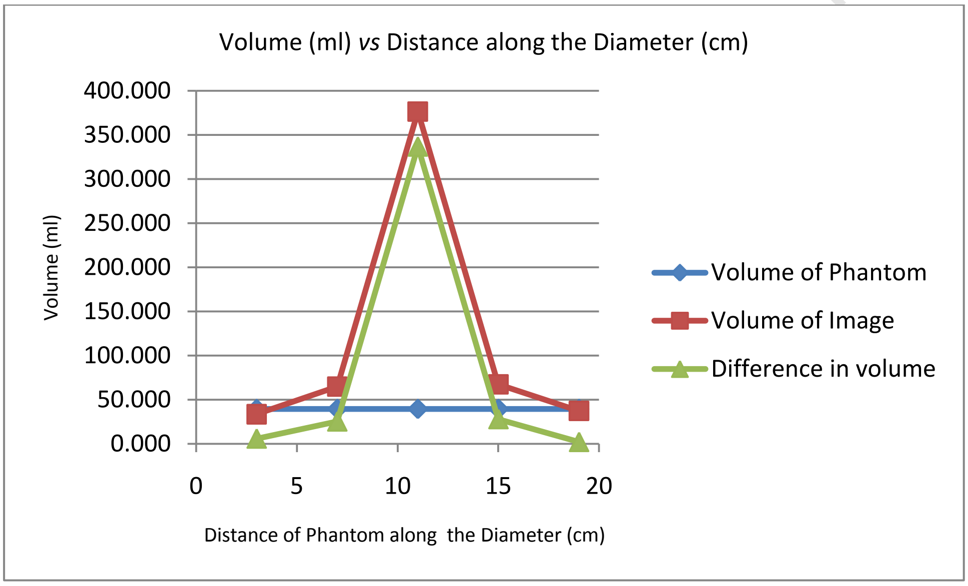

Figure 5.10(b). Variation of volume of reconstructed image and suspended phantom with distance along the diamter of the tomography rig for four rings electrode system based on opposite current injection sequences.

5.1.11 Analysis of Variation of Absolute Values of the Difference in Volume and PAS between Reconstructed Image and Suspended Phantom with Distance along the Diameter of the Vessel for Four Rings Electrode System Based on Opposite Current Injection Sequences

The variation of PAS of reconstructed image, suspended phantom and absolute values of the difference of the difference in PAS of the reconstructed image and suspended phantom with the distance along the diameter are displays in Figure 5.10 (a). The plot of variation of absolute values of the difference in volume between the reconstructed image and suspended phantom is displayed in figure 5.10 (b) and is symmetric about the centre of the vessel. It was observed that the error increases as the suspended phantom was moved from the boundary to the centre. The increase in error lead to increase in magnitude of the difference in volume between the reconstructed image and suspended phantom from the boundary to the centre with the peak value of $337.08ml$ (8 times suspended phantom) for volume at the centre of the vessel. The disparity in volume of the suspended phantom and reconstructed image towards the centre of the vessel is due to the highlighted three major sources of error associated to the with the solution of the inverse problem with respect to UCT data. The major sources of error are on account of the explored public library of MATLAB functions, the automatic mesh generator and the limitation of the RAM and processing power of the computer system used for reconstructing images as discussed in section 5.1.2.

As the suspended phantom was moved from one end of the boundary to the centre of the vessel, the PAS of the reconstructed image is approximately equal to the PAS of the suspended phantom. Further from the centre, the absolute values of the difference in PAS of the reconstructed image and suspended phantom increases very slightly. The slight disparity in the PAS is as a result of distortion of the volume of the image towards the centre and inconsistency in the inherent noise in the data and that added to the solution of the forward problem.

5.1.12 Reconstruction of Solid Suspended Phantom from Data Sets Measured Over Four Rings due to Stimulation through Adjacent Electrode Pairs

In order to verify the dependent of the accuracy of the solution of the inverse problem on the current stimulation strategy, voltage measurement over the four ring electrode system due to stimulation through adjacent electrode pairs was made. The voltage measurement through adjacent electrode pair was maintained in all experiments, as it yields more data required for 3-D imaging. Solutions of the inverse problem with this measurement strategy are presented in figure 5.11 (a - f). The tomography vessel was modelled with 14830 tetrahedra elements with 2982 nodal points for each of the reconstructed images obtained from 2237 measured voltage frames. The data sets were captured over 3 seconds and images were reconstructed after 143.52 seconds, as shown in figures 5.11 (a – f).

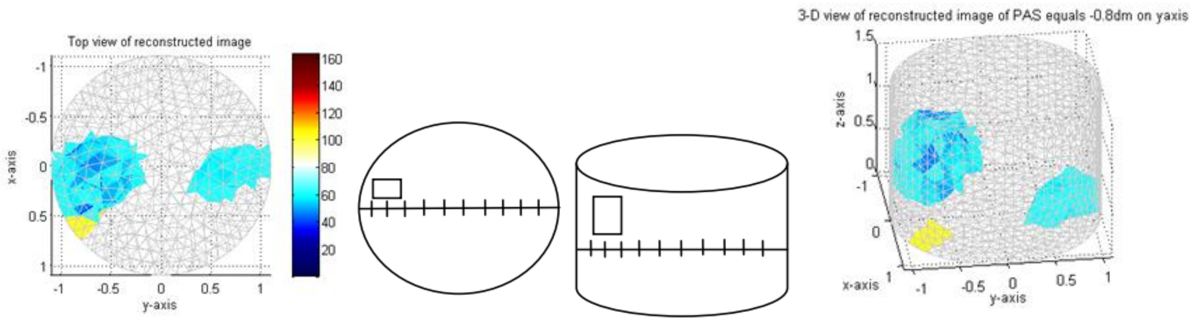

Figure 5.11(a). Plot of the solution of the inverse problem for a suspended cuboid perspex phantom at 3cm from the boundary.

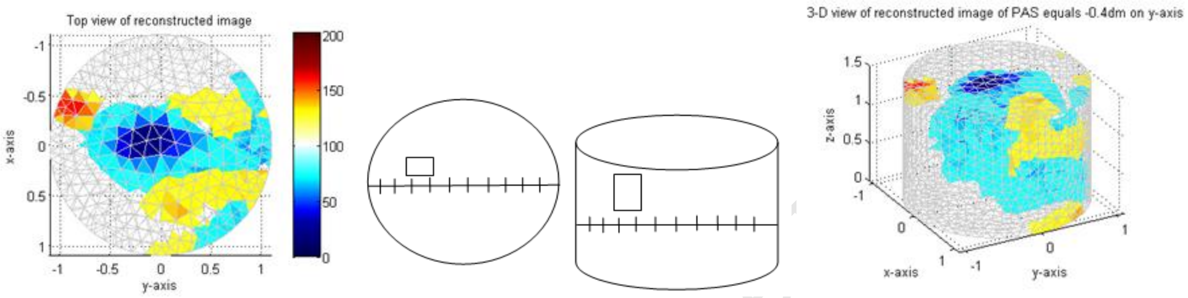

Figure 5.11(b). Plot of the solution of the inverse problem for a suspended cuboid perspex phantom at 7cm from the boundary.

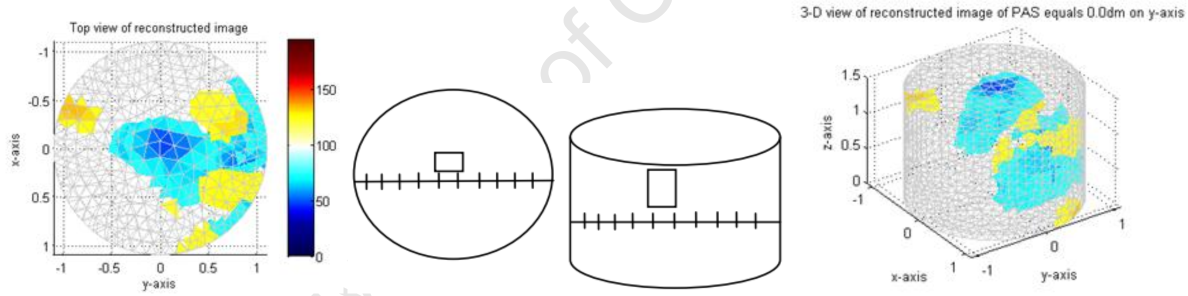

Figure 5.11(c). Plot of the solution of the inverse problem for a suspended cuboid perspex phantom at 11cm from the boundary.

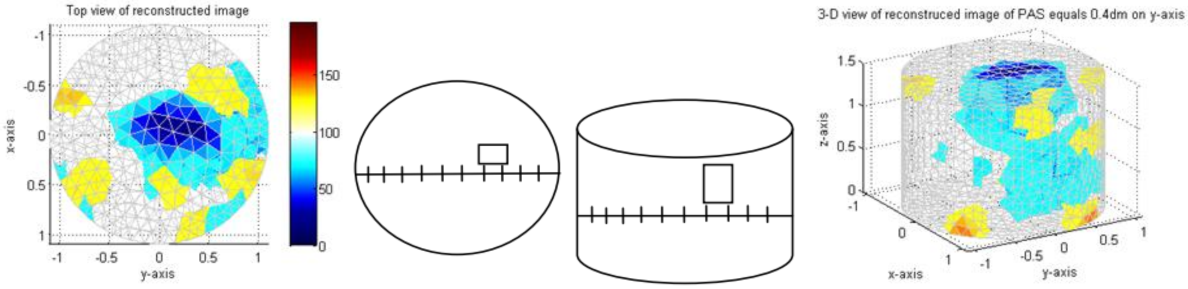

Figure 5.11(d). Plot of solution of the inverse problem for a suspended cuboid perspex phantom at 15cm from the boundary.

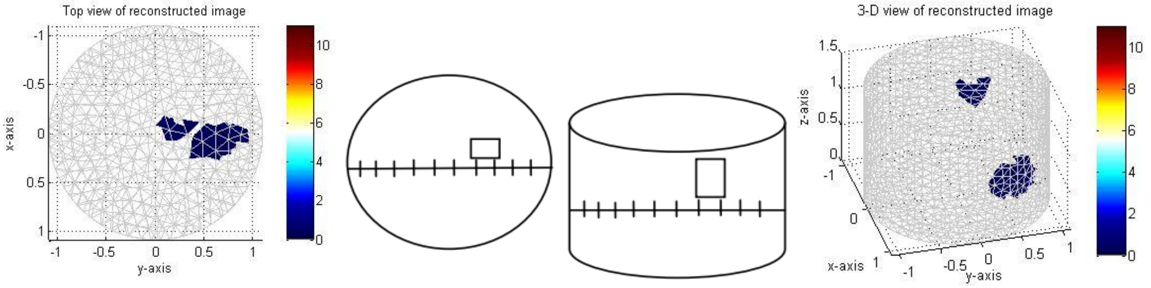

Figure 5.11(e). Plot of solution of the inverse problem with the artefact effects erased for a suspended cuboid perspex phantom at 15cm from the boundary.

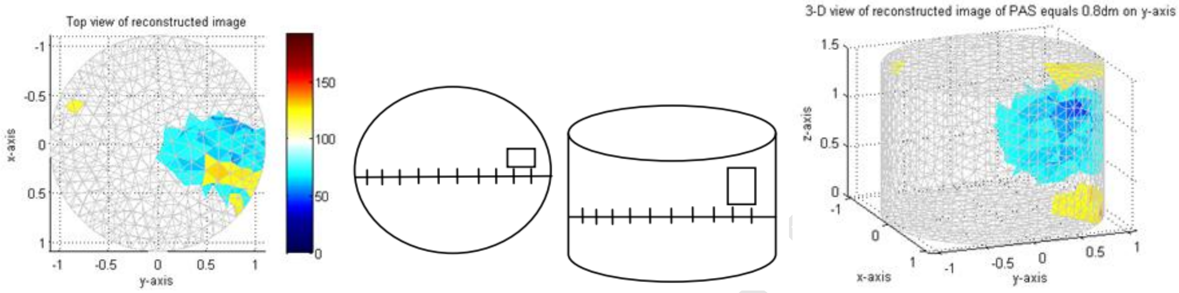

Figure 5.11(f). Plot of the solution of the inverse problem for a suspended cuboid perspex phantom at 19cm from the boundary.

Table 5.6 shows the estimated values for the volume, position of the axis of symmetry (PAS) and mass of the reconstructed image. The graphical analyses in figures 5.12(a) and (b) juxtaposes the physical quantities of the region of low conductivity of the reconstructed image with the actual region in the tomography rig.

Table 5.6. Computed volume and PAS of reconstructed image for various positions of the suspended cuboid perspex phantom for a sequence of current stimulation through adjacent electrode pairs in four rings

S/N - Physical Quantities	**1**	**2**	**3**	**4**	**5**
Distance Phantom from boundary (cm)	3.0	7.0	11.0	15.0	19.0
PAS of phantom (x-axis, y-axis)(cm)	(-1.9,-8.0)	(-1.9,-4.0)	(-1.9,0.0)	(-1.9,4.0)	(-1.9,8.0)
PAS of image (x-axis, y-axis) (cm)	(1.2, -7.1)	(0.0, 0.1)	(0.5, 7.2)	(0.2, 4.6)	(1.0, 7.4)
Volume of Phantom (ml)	39.5	39.5	39.5	39.5	39.5
Volume of Image (ml)	26.2	133.4	56.1	96.4	68.4
Error in volume(%)	-33.7	237.8	42.0	144.3	73.3

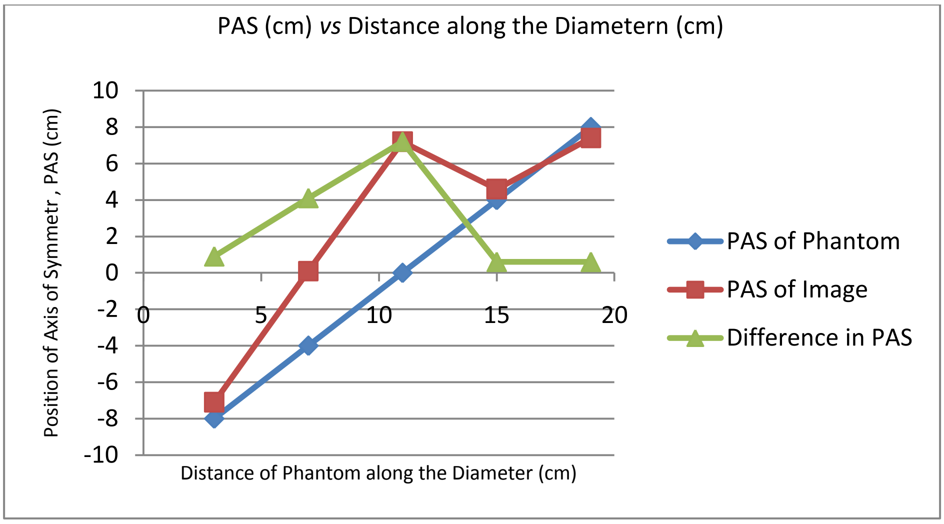

Figure 5.12(a). Variation of the position of the axis of symmetry (PAS) of reconstructed image and suspended phantom with distance along the diameter of the tomography rig for the four rings electrode system based on adjacent current injection sequences.

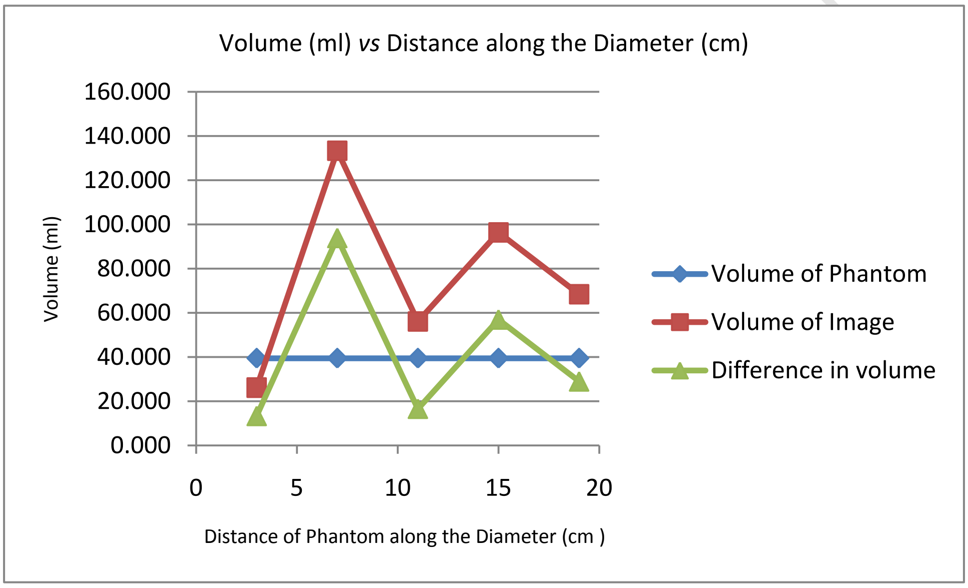

Figure 5.12(b). Variation of the volume of reconstructed image and suspended phantom with distance along the diameter of the tomography rig for the four rings electrode system based on adjacent current injection sequences.

5.1.13 Analysis of Variation of Absolute Values of the Difference in Volume and PAS between Reconstructed Image and Suspended Phantom with Distance along the Diameter of the Vessel for Four Rings of Electrode System Based on Adjacent Current Injection Sequences

The plots of the variation in volume are symmetric about the centre of the vessel such that the difference increases from the boundary to a peak value at the mid-point between the boundary and the centre of the rig. Further from, the mid-point to the centre of the vessel, the difference decreases to a lower value of $16.57ml$ for volume at the centre of the rig. The plots in figures

5.12(b) is similar to 5.8(b) and 5.4(b) in terms of the error in the measured data sets that is independent of the highlighted three major sources of error. Stimulation of current through adjacent electrode pairs produces an electric field flux that is less sensitive to perturbation. Figures 5.11 (a - f) confirms that there is no significant improvement in the insensitivity of the electric field flux due to current stimulation through adjacent electrode pairs with increase in size of measured voltage data sets at the periphery of the vessel. Thus, stimulation of current through adjacent electrode pairs yields inferior electric field lines compared to that produced by stimulation through opposite electrode pairs. Accordingly, with regards to the major sources of error of the solution of the inverse problem that are not linked of the current stimulation strategy, a sequence of current injection through opposite electrode pairs and voltage measurement through adjacent electrode pairs arranged in a four rings electrode systems is observed to be the best measurement strategy for 3-D data sets. It is recommended as the best measurement strategy since it yields more data sets which will be more accurate if the highlighted major sources of error are addressed.

The plots of variation in PAS are nearly symmetric about the centre as in figure 5.12 (a). It was observed that the difference in PAS between the reconstructed image and suspended phantom increases from the boundary to the centre. This is due to the three major sources of error in addition to the insensitive electric field flux generated by the current stimulation through adjacent electrode pairs.

The plot of solutions of the inverse problem for both opposite and adjacent current stimulation strategies ranging from two to four rings electrode systems confirms the work of Paivii *et al*. (1999), who stated that " the more independent data are obtained the better the spacial resolution can be achieved". A better spacial resolution was measured for the six written codes from their accuracy in reconstructing volume of region of low conductivity distribution, and the spacial coordinates of the axis of symmetry through the volume and parallel to the vertical axis (z-axis). Furthermore, a current stimulation pattern combined with a voltage measurement strategy leading to a better spacial resolution is said to produce the best measurement sequence.

5.1.14 Reconstruction of Two, Four and Six Solid Suspended Phantom from Data Sets Measured Using the Best Measurement Strategy

The best measurement sequence was employed for measuring voltage from boundary electrodes using the three-dimensional measurement strategy, when two, four and six cuboid perspex phantoms were suspended in a saline solution to introduce regions of low conductivity within the conductive domain. Figures 5.13 and 5.14 are plots of the solutions when two phantoms were suspended close to the boundary and the center of the vessel respectively. Solution of the inverse problem when four phantoms were suspended near the boundary and near centre of the vessel are shown in figures 5.15 and 5.16 respectively. Finally, six cuboid perspex phantoms were suspended near the boundary of the vessel and the plot of the solution of the inverse problem resulting from the measured voltage data sets is displayed in figure 5.17.

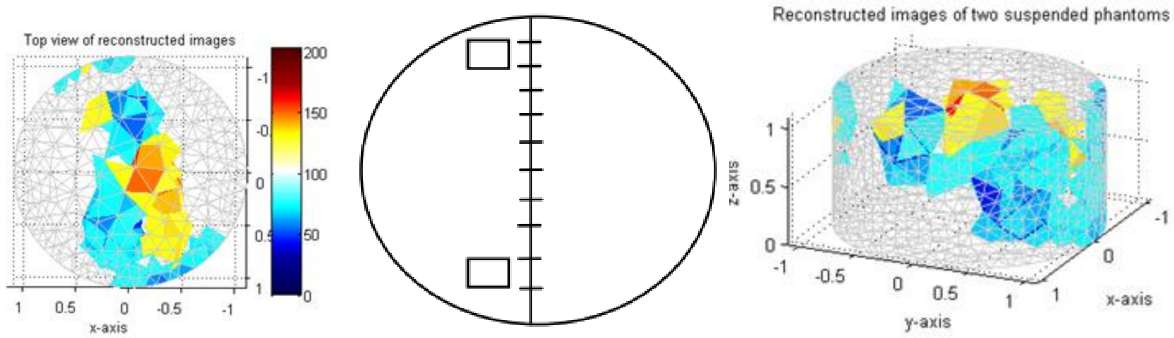

Figure 5.13. Two suspended cuboid perspex and PVC phantoms at 3cm and 19cm along the diameter of the vessel.

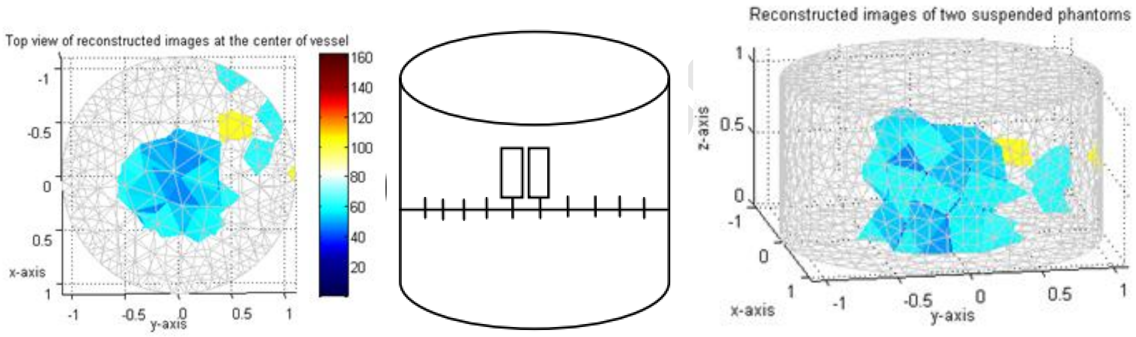

Figure 5.14. Two suspended cuboid perspex and PVC phantoms at 10cm and 12cm along the diameter of the vessel.

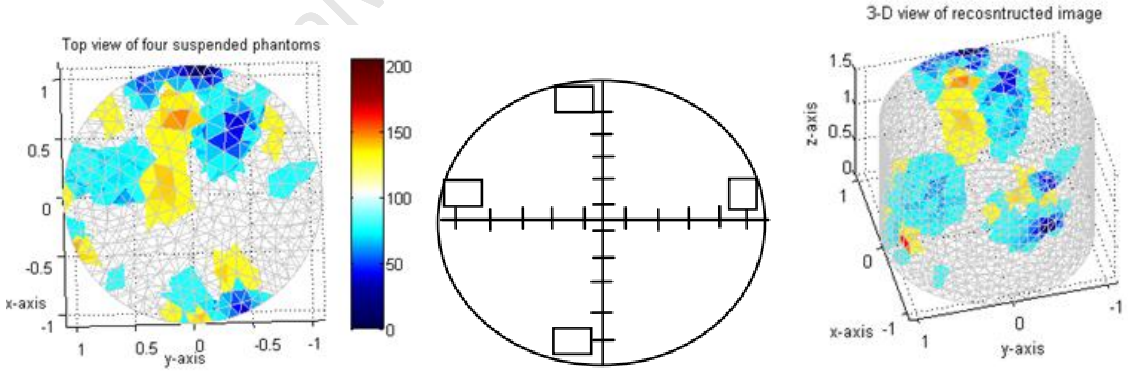

Figure 5.15. Four suspended cuboid perspex phantoms at 1.0cm (of volume 11.6ml), 1.5cm (of volume 42.6 ml), 1.0cm (of volume 39.5ml) and 2.0cm (of volume 47.9ml) respectively from the boundary of the vessel along two perpendicularly placed rulers along the diamters of the vessel.

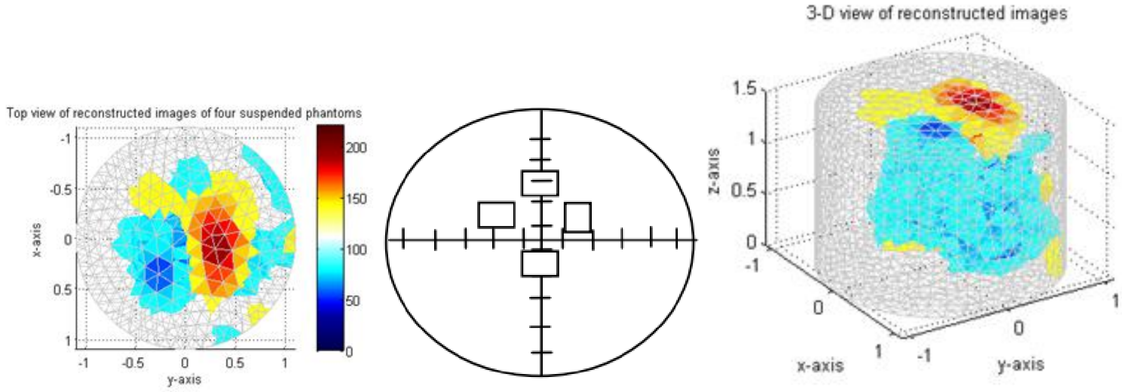

Figure 5.16. Four suspended cuboid perspex phantoms along two perpendicularly placed rulers close to the intersection point of the two rulers with volume as indicated in figure 5.12.

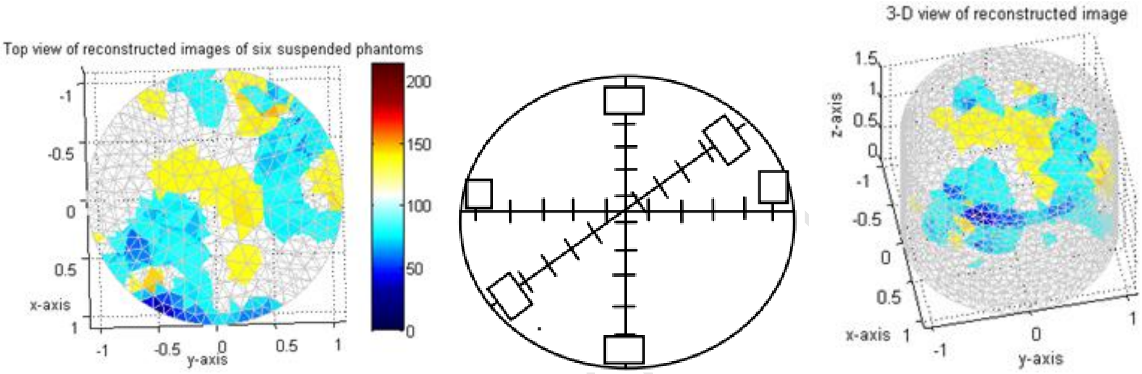

Figure 5.17. Six cuboid suspended phantoms consisting of four perspex phantoms and two PVC at 1.0cm (of volume 11.6ml), 1.5cm (of volume 4.26ml), 1.0cm (of volume 3.95ml), 2.0cm (of volume 4.79ml), 3.0cm (of volume 11.6ml) and 3.0cm (of volume 37.5ml) from the boundary of the vessel respectively.

In addition to the effect of the two major sources of error such as inappropriate modelling of the electric flux using the 1st order FEM for the dual models implemented in EIDORS v3.3 and lack of suitable computing devise to discretise the continuous domain to finite element of the order of 10^5 tetrahedra, the effect of variation of density of the mesh is significant in the reconstructed images of the multiple suspended phantoms. The variation of the density of the mesh from fine to coarse mesh at the centre in order to preserve accurate measurement of the voltage on the boundary electrode and reduction of the computation time yield less accurate values for voltage signals sensed at the boundary for perturbation near and at the centre of the veesel. This error in the solution of the inverse problem as a result of the distorted signals is equally noticed for multiple phantom system similar to single phantom system. For multiple suspended phantoms near the boundary, the detected voltage signals on electrodes are more accurate. Figures 5.13 to 5.17 show the sensitivity of the electric field flux generated using the best measurement strategy, especially at detecting the precise degree of perturbation near the boundary of the vessel.

Furthermore, the lack of feature in the explored EIDORS v3.3 with which researchers can develop their image prior with earlier measured resisitivity values to form an expectable resistivity distribution near which the true resisitivity distribution is assumed, was a challenge in this work. EIDORS v3.3 does not provide means for assessing the code used in developing the image- prior used in this work. Since the explored image prior was developed from data taken from other laboratories, the counteraction of the data sets with that of the UCT data contribute to the poor resolution of the reconstructed images. This can be addressed by a user-written image-prior code developed using ealier measured resisitivity distribution for the UCT data to form expectable resistivity distribution in the first iteration. Thereafter, subsequent iterative loop should use the previous solution of the inverse problem for the next iterative step. Alternatively, the provision of a feature that allows user of EIDORS library to modify or customise the available image-priors in the later versions of EIDORS V3.3 to be released will prove useful.

5.2 Analysis of the movement of conductive fluid using the 3-D reconstruction code

In addition to imaging suspended solid phantoms within the discretised domain of bulk mildly saline homogeneous solution at various position along the diameter of the vessel, the obtained best measurement strategy requiring voltage data measurement over four rings of electrodes was tested and applied in visualising the movement of conductive solution. The sets of experiments presented in table 4.3, 4.4, 4.5 and 4.6 of section 4.7 of chapter 4 were designed to monitor the movement of conductive fluid through diffusion process in a spherical, radial and planar geometry respectively, using the visualisation aid provided by the reconstructed image. In order to do so, a point injection was made into a free bulk solution, a column of more conductive solution was suspeded in the bulk solution and an injection through the nozzle of a peristaltic pump at the base of the tank were made. Based on the sequence table, utilising the best measurement sequences established above, voltage measurements were taken through the periphery electrodes at specific times after injection of the conductive fluid so as to reconstruct the conductivity distribution in the vessel.

5.2.1 Plot of reconstructed images in studying the movement of conductive fluid due to spherical diffusion within an unimpeded medium

As detailed in the table 4.3 in chapter 4, the first sets of experiment were designed such that the measurement were made at various time to visualise the movement of 4ml of 1M NaCl solution injected into the centre of the tank through a ceramic dispersion head syringe. The plot of the region of higher conductive solution at various time are displayed in figures 5.18 (a - c).

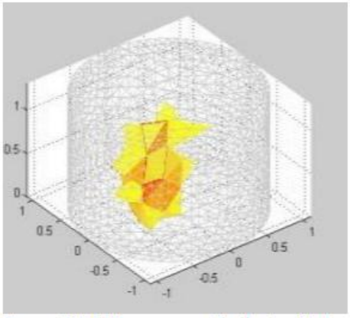

Figure 5.18 (a). Tomogram of spherical injection through ceramic head in the centre at 0 sec.

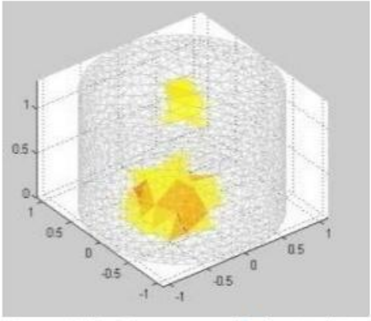

Figure 5.18 (b). Tomogram of spherical injection through ceramic head at 5 sec.

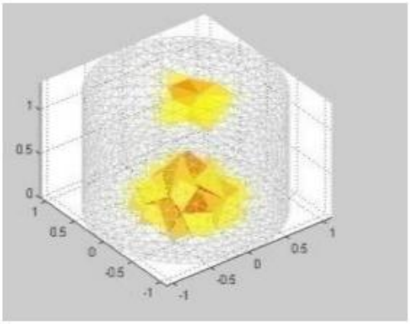

Figure 5.18 (c). Tomogram of spherical injection through ceramic head in the centre at 10 mins.

The second set of experiments were made by injecting the experimental solution of 4ml of 1M NaCl solution at the top of the tank to confirm if the movement of conductive fluid through the bulk solution is influenced by variation of the spot of injection. Figures 5.19 (a - d) highlight the movement of the conductive experimental solution at the specified time when the spherically shaped conductive solution was injected at the top of the tank through the head of a ceramic dispersion syringe.

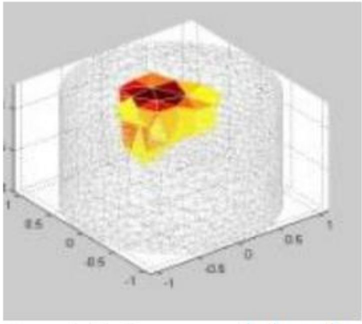

Figure 5.19(a). Tomogram of spherical injection through ceramic head at the top at 0 sec.

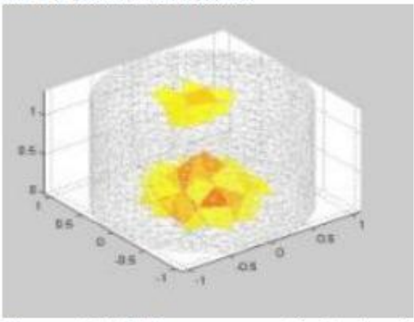

Figure 5.19(b). Tomogram of spherical injection through ceramic head at the top at 5 sec.

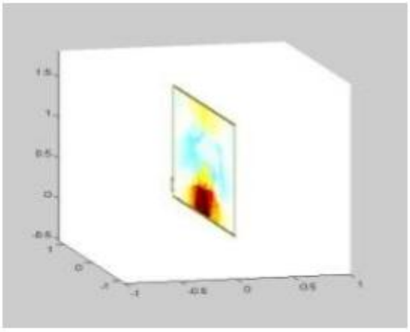

Figure 5.19(c). Vertical slice through 3-D tomogram injection of spherical injection through ceramic head at the top at 10 sec.

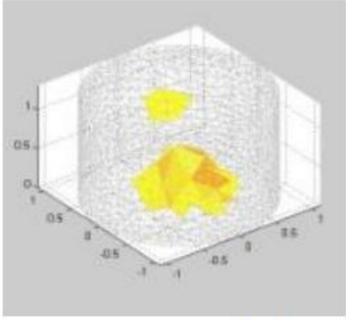

Figure 5.19(d). Tomogram of spherical injection through ceramic head at the top at 90 sec.

Having observed that the movement of higher conductive experimental solution for the two mentioned cases were similar, Baxter and Brighton (2010) studied the movement of the fluid by injecting the same solution at the centre of a sponge suspended at the centre of the tank at specified time as indicated in third experiment on table 4.3. The plots of the 3-D tomogram at specified time are displayed figures 5.20 (a - d).

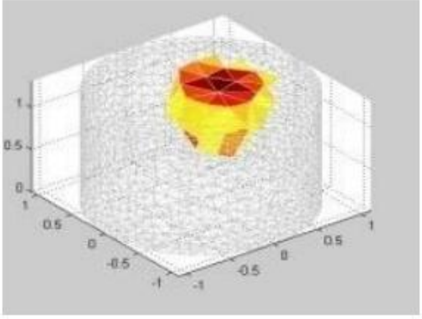

Figure 5.20(a). Tomogram of spherical injection into central sponge at 5 sec.

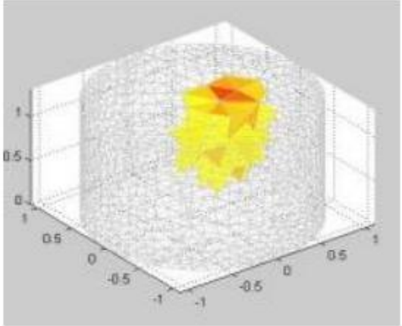

Figure 5.20(b). Tomogram of spherical injection into central sponge at 10 sec.

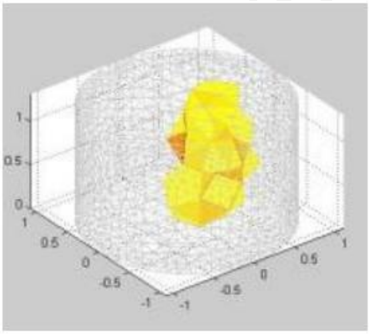

Figure 5.20(c). Tomogram of spherical injection into central sponge at 15 sec.

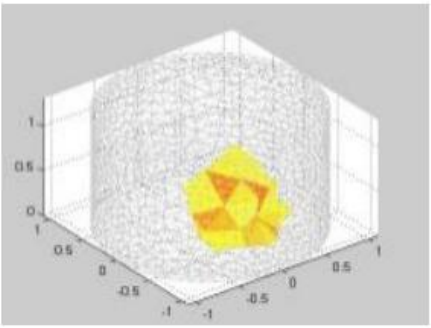

Figure 5.20(d). Tomogram of spherical injection into central sponge at 30 sec.

To confirm the effect of changing the current stimulation strategy on the reconstructed image using measured voltage data, a sequence of current stimulation through adjacent electrode pairs was implemented in studying the movement of injected conductive solution at specified time as indicated in the fourth experiment on table 4.3. Figures 5.21(a - e) illustrates the use of the 3-D reconstruction software in imaging the movement of the fluid at various time for a sequence of current injection through adjacent electrode pairs.

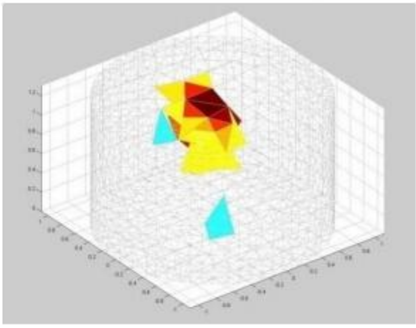

Figure 5.21(a). Tomogram of spherical injection into central sponge using adjacent current injection at 5 sec.

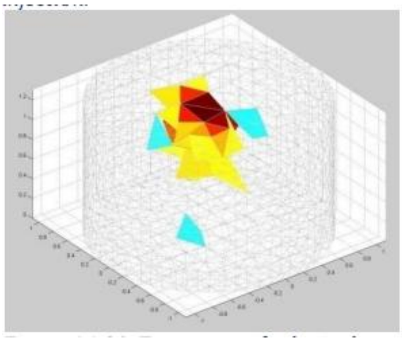

Figure 5.21(b). Tomogram of spherical injection into central sponge using adjacent current injection at 10 sec. .

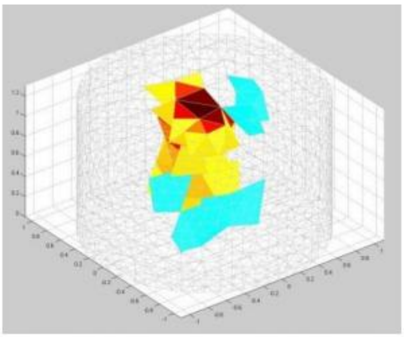

Figure 5.21(c). Tomogram of spherical injection into central sponge using adjacent current injection at 30 sec.

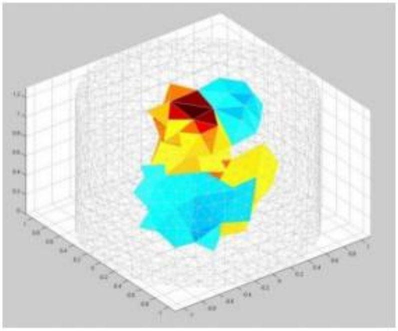

Figure 5.21(d). Tomogram of spherical injection into central sponge using adjacent current injection at 2 mins.

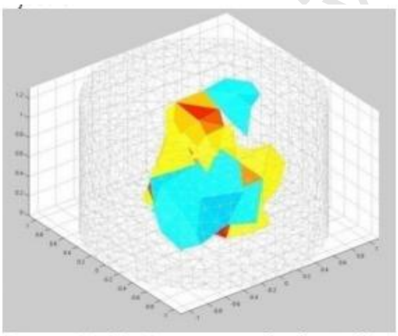

Figure 5.21(e). Tomogram of spherical injection into central sponge using adjacent current injection at 15 mins.

5.2.2 The Movement of a Conductive Fluid Due to Spherical Diffusion within a Foam and Marble Impeded Medium

In the first set of experiments (table 4.4), a 10% acetic acid experimental solution was injected into the centre of a bed of marbles and highly porous foam. Since the 10% acetic acid solution is only 0.5% denser than the bulk homogeneous solution, it was chosen so as to eliminate the rapid dropping of the conductive fluid due to the difference in density. Using the 3-D reconstruction software for the four ring of electrodes system, imaging of the movement of the fluid is shown in figures 5.22 (a - c).

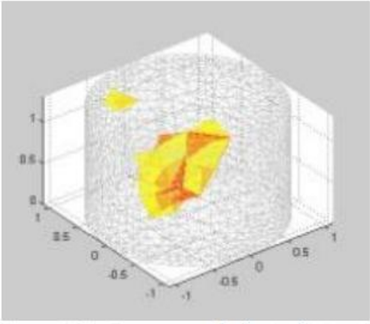

Figure 5.22(a). Tomogram of spherical injection of 10% acetic acid into centre foam and marble at 0 sec.

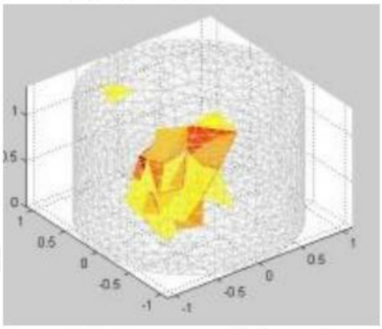

Figure 5.22(b). Tomogram of spherical injection of 10% acetic acid into the centre foam and marble at 3 mins.

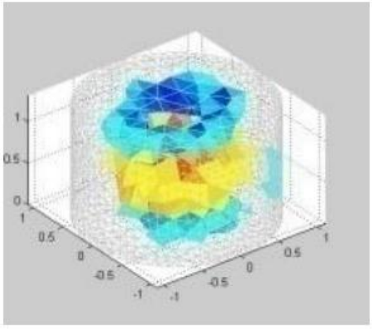

Figure 5.22(c). Tomogram of spherical injection of 10% acetic acid into the centre of foam and marble at 17.5 hours.

The movement of the fluid was then monitored in a foam impeded medium only so as to determine the extent of the resistance to flow that was provided with the marble bed. Figures 5.23 (a - c) show the region of higher conductivity at various times as indicated in each plot after 1M NaCl solution of spherical geometry was injected into the centre of the form.

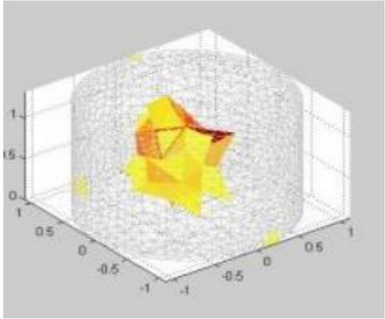

Figure 5.23(a). Tomogram of spherical injection into centre of a foam at 30 sec.

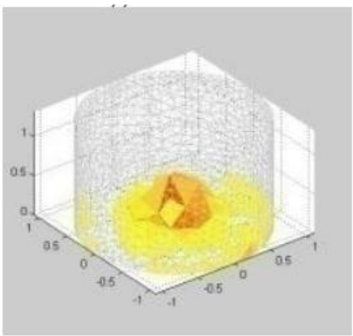

Figure 5.23(b). Tomogram of spherical injection into centre of foam at 16 hours

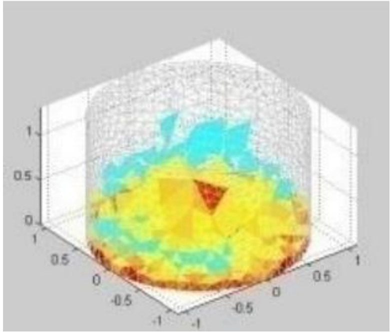

Figure 5.23(c). Tomogram of spherical injection into centre of foam at 68 hours.

5.2.3 Analysis of the Reconstructed Images to Examine the Spherical Diffusion of Higher Conductive Solution Injected into a Bulk Mildly Saline Solution

An estimation of the physical phenomena influencing the movement of the fluid in the UCT ERT rig was acquired from the comparison of the various plots of the tomogram to the model obtained from the Scilab-based modelling of movement of NaCl ions due to diffusion only in the three geometries considered - spherical, planar and radial. From the model of spherical geometry of diffusion, a significant widening of the spherical injection is expected over 10 000 seconds or three hours (Baxter and Brighton, 2010). However, all the plots of the tomograms in sections 5.2.1 and 5.2.2 displayed significant dropping of the conductive fluid in less than 10 minutes even with the use of impeded materials and a less dense solution. This informs that the downward movement of the fluid is determined largely by gravitational forces due to density differences between the bulk and more conductive solution, as diffusion has little influence on the movement of the solution.

5.2.4 Plot of reconstructed images in studying the movement of conductive fluid due to radial diffusion

This set of experiments (table 4.5) was conducted due to a search for an efficient method to provide a central column of highly conductive solution to diffuse radially into the tank. In the first set of experiments, the column of highly conductive solution was created by using a porous rubber tube, while in the second set of experiments the region of higher conductive solution was introduced using a perspex tube riddled with small holes which was inserted into a canvas tube (figure 4.15). Figures 5.24(a- c) shows the reconstructed images of the movement of the column of conductive solution in the porous rubber tube at respective times.

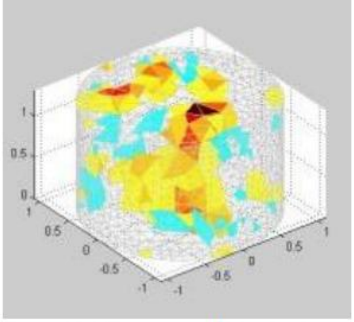

Figure 5.24(a). Tomogram of injection into a vertical porous rubber tube at 5 mins.

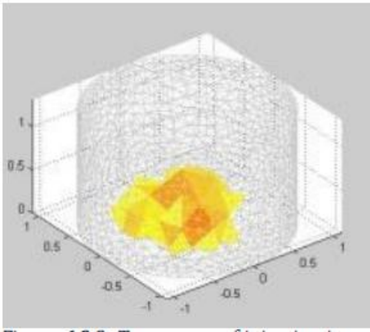

Figure 5.24(b). Tomogram of injection into a vertical porous rubber tube at 15 mins.

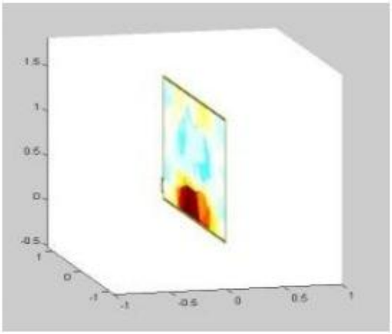

Figure 5.24(c). Vertical slice of tomogram of injection into a vertical porous rubber tube at 4.5 hours

A set of four measurement were then taken at specified times for a column of 20ml of 1M salt solution filled into a perspex tube riddled with small holes and inserted into a canvas tube. The results are shown in figures 5.25 (a - d).

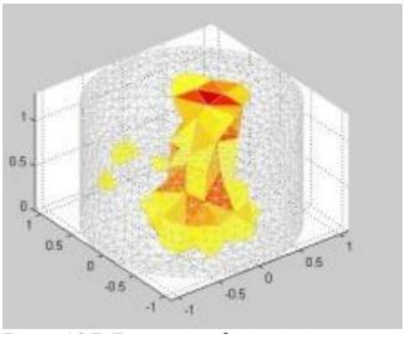

Figure 5.25(a). Tomogram of injection into vertical perspex tube in canvas at 3 sec.

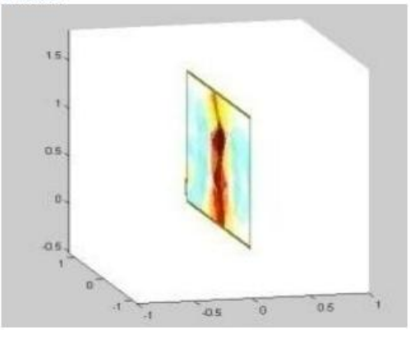

Figure 5.25(b). Vertical slice of tomogram of injection into vertical perspex tube in canvas at 10 sec.

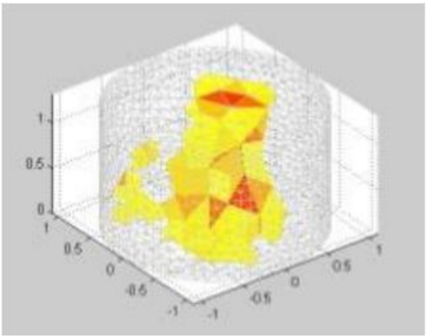

Figure 5.25(c). Tomogram of injection into vertical perspex tube in canvas at 60 sec.

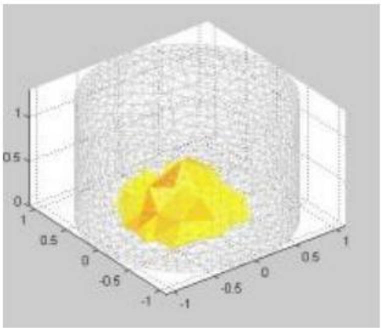

Figure 5.25(d). Tomogram of injection into vertical perspex tube in canvas at 3 mins.

5.2.5 Analysis of the reconstructed images to examine the radial diffusion of higher conductive solution injected into a bulk mildly saline solution

The plots in figures 5.25 (a - d) monitors the movement of the conductive fluid more accurately than figures 5.24 (a – c). The porous rubber tube proved to be more suitable column of higher concentration for observing the movement of fluid when compared with the other column. The rate of movement of the fluid out of the column as shown in figures 5.25 (a - d) differs from the rate of radial diffusion model, which predicts that the whole conductive fluid should move to the base of the tank after three hours (Baxter and Brighton, 2010). In addition, figures 5.24a indicate increase in the radial size minutes after the start of the experiment and dropped completely after fifteen minutes (figures 5.24b) a time-scale in which limited diffusion effects will be seen (Baxter and Brighton, 2010). The plots in figures 5.25 (a - d) indicate the movement of the conductive solution is due to convective effects arising from density differences between the bulk and the more conductive solution.

5.2.6 Plots of Reconstructed Images in The Study of Movement of Conductive Fluid Due to Planar Diffusion within A Bulk Mildly Saline Solution

The 3-D reconstruction software was tested through the study of the upward movement of conductive solution injected at the base of the tomography rig with time. An injection of more conductive fluid was made at the base to eliminate the effect of gravitational force in the downward movement, owing to density differences between the injected solution and the bulk solution. Thus, the upward movement of the fluid with time is suspected to be in response to the planar diffusion process, or other fluid mixing processes, sustained by initial momentum of the injected solution released by the pump. The plots of the solution of the inverse problem for the measured voltages at specified times are shown in figures 5.26 (a - e).

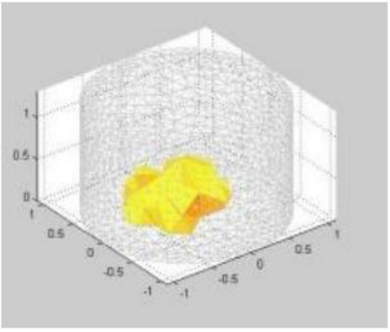

Figure 5.26(a). Tomogram of injection of 0.5M of NaCl solution into the base of the tank at 1 min.

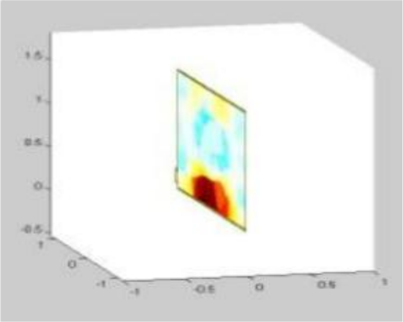

Figure 5.26(b). Vertical slice of tomogram of injection 0.5M NaCl solution into the base of the tank at 13 hours.

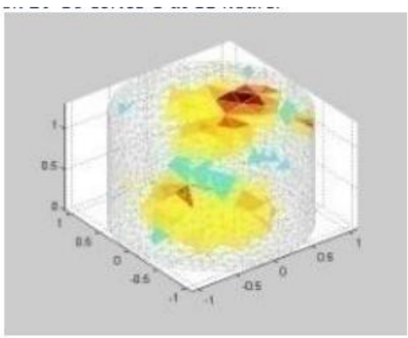

Figure 5.26(c). Tomogram of injection of 0.5M Nacl solution into the base of the tank at 38.5 hours.

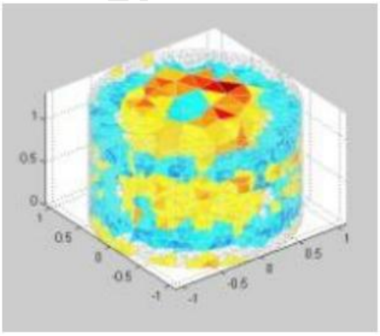

Figure 5.26(d). Tomogram of injection of 0.5M Nacl solution into the base of the tank at 50 hours.

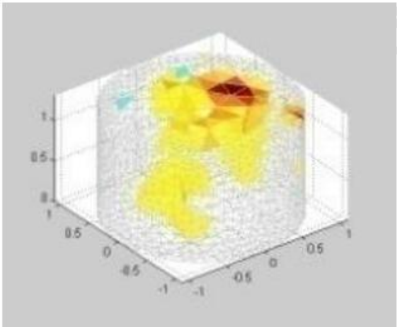

Figure 5.26(e). Tomogram of injection of 0.5M Nacl solution into the base of the tank at 71 hours.

5.2.7 Analysis of the Reconstructed Images to Examine The Planar Diffusion of Higher Conductive Solution Injected into A Bulk Mildly Saline Solution

The plot of the tomogram in figures 5.26 (a - e) indicating that there was significant movement and mixing in the whole tank in less than three days is not in agreement with the planar diffusion model. The model suggests that the time taken for the diffusion only system to reach a relatively even concentration at the middle of the tank is in excess of 300 000 seconds (3.5 days) (Baxter and Brighton, 2010). The plot of the reconstructed images do not match planar diffusion models in which the movement of the conductive fluid due to concentration difference is expected along the vertical direction only. This support the observation that the fluid movement being imaged at various times is not due to diffusion process but convective effects that are enhanced by initial momentum of the injected solution released by the pump. The larger size of the volume of reconstructed image relative to the actual injected solution is related to the highlighted three major sources of error as well as the limitation in the reconstruction code in term of use of image-prior that is inconsistent with the UCT data sets, as discussed in section 5.1.2.

5.2.8 Studying the Flow of Conductive Solution through A Packed Bed.

The 3-D reconstruction software was applied in visualising the movement of fluid within packed beds made from a collection of marbles enclosing a sponge core. The experimental procedure required the injection of 0.1M NaCl solution fed in from the top at the same rate as the liquid was removed through the base of the tank filled with marbles around a sponge core. The experiment is designed to test the effectiveness of the software in analysing flow of conductive solution in processes such as heap leaching and dump leaching, but also any type of hydrological process. The tomogram of the movement of the conductive fluid through the marbles and sponge, constituents of the packed bed at various times are highlighted in figures 5.27 (a - d).

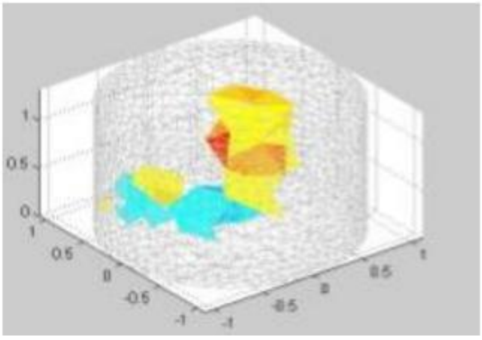

Figure 5.27(a). Tomogram of flow of 0.1M NaCl solution at 1.82ml/min at 3 mins.

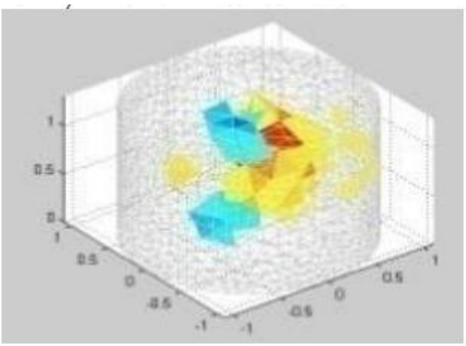

Figure 5.27(b). Tomogram of flow of 0.1M NaCl solution at 1.82ml/min at 10 mins.

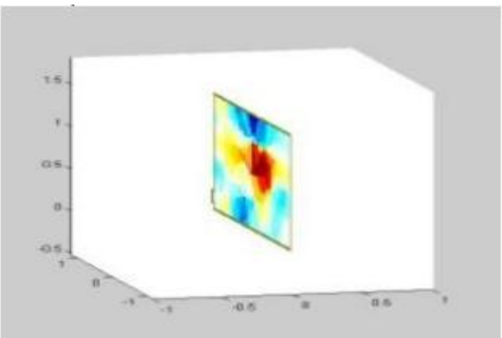

Figure 5.27(c). Tomogram of flow of 0.1M NaCl at 1.82ml/min at 15 mins.

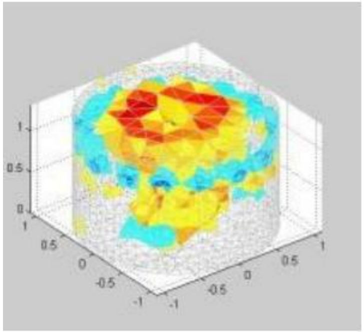

Figure 5.27(d). Tomogram of flow of 0.1M NaCl solution at 1.82ml/min at 5.5 hours

5.2.9 Analysis of the reconstructed images to examine the flow of conductive solution through a packed bed

The plot of the tomogram for the movement of the fluid through packed marbles enclosing a sponge core after 3 minutes shows there is downward movement of the high conductivity fluid through the central injection point onto the surface, as in figure 5.27 (a). It was noticed 10 minutes after the start of the experiment that the region of higher conductivity widens with phantoms, as shown in figure 5.27(b). Figure 5.27(c) is the 2-D slice of the tomograms plot after 15 minutes showing a high conductivity region at the centre of the tank and a low conductivity region above and below it. After five and a half hours, there is a high conductivity region which spread across the top and narrows down towards the nozzle in the centre of the bottom of the tank through which the fluid was pumping as shown in figure 5.27(d). The movement of the conductive solution could be visualised by the ERT technique, though the resolution of the images are distorted by the highlighted errors. An improved resolution of the images will be achieved if the sources of error are addressed as recommended in the conclusion.

5.2.10 Analysis of movement of conductive fluid using the 3-D reconstruction code

A study of change in a region of high conductivity within the homogeneous domain in both vertically downward and upward direction for all the conducted experiments is in agreement with the movement of the fluid due to either gravitational force or frictional force or fluid mixing processes. The tomogram from the loaded measured voltage shows that the 3-D reconstruction software provides a practical means of visualising the movement of conductive fluid with time. It was noticed in the plot of the tomogram for various experiment that the volume of the reconstructed image is much larger than the injected conductive solution using either needle or pump (Baxter and Brighton, 2010).This is due to the increase in the coarseness of the mesh towards the centre, the use of much less dense mesh relative to that recommended for 3-D imaging (150,000 tetrahedra elements), as well as the mentioned error of the solution of the inverse problem with regards to the UCT voltage data sets, resulting in less accurate sensed voltage at the boundary. The less dense mesh provides an inefficient discretised domain to solve both the forward and the inverse problem.

In summary, considering the rate of movement of the conductive experimental solution in all the experimental design to visualise the movement of fluid due to spherical, radial and planar diffusion, it may be said that the movement of the of the more conductive solution is due to convective effects as the movement cannot be accounted for by the diffusion model. Thus, the ERT technique is suitable to visualise the migration of the conductive solution due to convective effects in both impeded and unimpeded media.

CHAPTER 6

CONCLUSIONS AND RECOMMENDATIONS

6.1 Conclusions

An open source free library of MATLAB functions, EIDORS 3D, has been explored, modified and customised for imaging the resistivity distribution within a conductive saline solution in three dimensions contained in the UCT tomography rig, fitted with two, three and four rings of sixteen electrodes. This led to the development of six reconstruction software codes for reconstructing images from a sequence of voltage measurement through periphery adjacent electrode pairs due to a sequence of current stimulation through both opposite and adjacent electrode pairs.

The six reconstruction codes were used to image the position of a region of low conductivity (solid suspended phantoms) within a more conductive solution along the diameter of the vessel in order to determine the best measurement strategy. A sequence of voltage measurements through adjacent electrode pairs due to a sequence of current stimulation through opposite electrode pairs in a four rings electrode system was observed to the best measurement strategy for the UCT tomography rig. The best measurement strategy was employed to image two, four and six distinct solid suspended phantoms within the rig

A comparative study of the reconstructed images with the suspended phantom using the volume and coordinate of the centre of gravity (PAS) facilitate the measurement of the resolution of the reconstructed images. For the best measurement strategy, the plot in figure 5.10 (a) comparing the volume of suspended phantom and reconstructed image shows that the resolution of the images reduces towards the centre of the vessel. The percentage error in the calculated volume of the image relative to the suspended phantom is observed to increase from 15% at the boundary to 853% at the centre from one end of the vessel (table 5.5). However, the reduction in resolution of the reconstructed images was observed not to reduce the precision of the PAS significantly as shown in figure 5.10 (a).

In the best measurement strategy obtained, likely sources of error such as an insufficient data set for 3-D reconstruction and less sensitive Jacobian matrix owing to electric field lines resulting from current injection through adjacent electrode pairs were eliminated since data sets measured over four rings were induced from current stimulation through opposite electrode pairs.

However, three sources of errors distorted the accuracy of the measured voltage at the boundary in the solution of both the forward and the inverse problem. This lead to increase in volume of reconstructed images toward the centre. In the explored public domain library function written with MATLAB syntax (EIDORS), first-order FEM based on the dual model approach were implemented in solving the forward and the inverse problems. Due to this, the electric field lines, which are curves in 2-D, particularly towards the centre are not appropriately modelled. In modelling the UCT rig, an automatic 3-D mesh generator (NETGEN) was explored. NETGEN discretised the domain of the rig with varying mesh densities from fine mesh near the boundary to coarse mesh toward the centre. The increase in coarseness of the mesh towards the centre yields less accurate voltage values at the boundary for a phantom suspended near the centre of the vessel. Furthermore, the limitation in the memory and processing power of the computer system used for reconstructing the images restrict the generation of number of element to less than 16,000 as compared to 150,000 elements recommended for high resolution 3-D imaging. The inconsistency in the inherent noise associated with the data collected from the UCT vessel added to the that of solution of the forward problem, affects the quality of the reconstructed images. Moreover, the image prior developed by Nick Polidorides (2002) included in the open source code was explored in the defining the image-prior in the implemented algorithm. This image-prior was developed from data sets from other laboratory. The use of this image-prior rendered the resolution of the images imperfect as the image prior was not developed with data sets from UCT laboratory. These sources of error in both the forward and the inverse problems are noticed to reduce the resolution of the images towards the centre of the rig.

The developed signal analysis software from the best measurement sequence for static phantom was used to investigate the flow of conductive solution within a bulk saline homogeneous solution, in order to visualise fluid movement due to spherical, radial and planar diffusion or other physical phenomenon in an undergraduate project work (2010) in the department of Chemical Engineering, University of Cape Town. Analysis of the tomograms reveals that the developed reconstruction code is efficient at reconstructing images through which the movement of the conductive fluid due to convective effects, can be visualised. The convective movement of the solution was noticed to be sustained by the initial momentum with which the conductive fluid was injected at the base of the solution in some experiments. Further analysis of the tomograms informs that the movement of the conductive fluid was not due to diffusion processes alone. However, this does not establish the unsuitability of the ERT technique to visualise the movement of the conductive solution due to diffusion as the experimental design needs to be appraised to ascertain the design is adequate for diffusion of the injected solution to be observed.

6.2 Recommendations

The error in the solution of the inverse problem (reconstructed image) due to inaccuracy in reproducing the tank phantom measurements can be eliminated by developing a 3-D algorithm with a second-other FEM and availability of a computer system of much larger memory and high processing power with which 150, 000 finite elements can be obtained (as recommended by Adler *et al*, 2008).

In order to eliminate the error in the solution of the forward problem due to increase in degree of coarseness of the mesh towards the centre of the vessel, the use of fine mesh in the entire domain or an adaptive mesh that automatically generates finer mesh over the region of a target phantom will prove useful. This can be achieved by exploring other automatic 3-D mesh generators or a user-developed 3-D mesh.

Furthermore, the inconsistency in the inherent noise associated with the data collected from the UCT vessel to that added to the solution of the forward problem (25 decibel signal to noise ratio) can be addressed by adequate measurement of the noise level from every source within the laboratory, and adding this to the solution of the forward problem.

It is proposed that significant improvement in the resolution of the reconstructed images will be achieved if a user-written image-prior code is developed using earlier measured UCT resistivity data in the first iterative loop and the solution of the inverse problem of this loop should be used as the initial guess in the next iteration. In addition, since the performance of the regularization method is closely related to the smoothening coefficient, the development of an algorithm that automatically determines a good coefficient depending on the experimental data will improve the resolution of the reconstructed images.

REFERENCES

Adler A and Lionheart W.R.B (2006). Uses and abuses of EIDORS: An extensible software base for EIT. Institute of Physics Publishing. Physiol Meas. (2006) S25 - S42.

Adler A and Lionheart W.R.B (2005). EIDORS: Towards a community-based extensible software base for EIT. VI conf. Electrical Impedance Tomography, London, UK, 2005.

Adler A, Borsic A, Polydorides Nick and Lionheart W.R.B (2008). Simple FEMs aren't as good as we thought: experience developing EIDORS V3.3. Manchester Institute for Mathematical Sciences, School of Mathematics, The University of Manchester. M19 9PL,UK. ISSN 1749-9097.

Barber BC, Brown BH and Freeston IL (1983). Imaging spatial distributions of resistivity using applied potential tomography. Electronics Let, 19:933-935.

Baxter M and Brighton M (2010). The use of electrical resistance tomography to study the movement of conductive fluids. Undergraduate project report. The department of Chemical Engineering University of Cape Town, South Africa.

Blue R. S, Isaacson D and Newell J.C (2000). Real time three-dimensional electrical impedance imaging. Physiol. Meas. 21 (2002) 15-26.

Bolton G. T, Qui C. H and Wang M (2002). A novel electrical tomography sensor for monitoring the phase distribution in industrial reactors. *Proc. Fluid Mixing 7*, Bradford, UK, 2002.

Dickiny F and Wangz Mi (1996). Electrical resistance tomography for process applications.
Meas. Sci. Technol. **7** (1996) 247–260.

Drupal (2010) "Industrial Process Tomography Systems" "www.itoms.com" 30th Sept., 2010" "http://www.itoms.com/applications/flow".

Field D.A (1988). Laplacian Smoothing and delaunay triangulations. Comm. Appl. Num. Meth., 4:709, 1988.

Fish Jacob and Betytschko Ted (2007). A first course in finite elements. West Sussex, England: John Wiley & Sons Publishing, June 6, 2007.

Goble J, Cheney M and ISAACSON D (1992). Electrical impedance tomography in three dimensions. Journal of computational electromagnetic. pp 128-147, 1992.

Gockenbac M.S (2006). Understanding and implementing the finite element method. Philadephia. SIAM Publications, 2006.

Golub G.H and Van Loan C.F (1989). Matrix computations**.** Baltimore, MD: The Johns Hopkins Univ. Press, 1989.

Graham L , Hamilton R, Rudman M, Strode P and Pullum L (2002). Coarse solids concentration profiles in laminar pipe flow. *Proc. Hydrotransport 15*, Banff, Canada, 2002.

Holden P. J, Mann R, Wang M, Dickin F. J and Edwards R. B (1998). Imaging stirred-vessel macromixing using electrical resistance tomography. *AIChE Journal* 1998, *44*, 780–790.

Holden P.J, Wang M, Mann R, Dickin F. J and Edwards R.B (1999). On detecting mixing pathologies inside a stirred vessel using electrical resistance tomography. *Tran IChemE* 1999, *77*, 709–712.

Jolliffe I.T(1986). Principal component Analysis. Berlin Germany: Springer-Verlag,1986.

Jossinet J and Kardous G (1987). Physical study of the sensitivity distribution of multi -electrode systems. Clin. Ph,vs. Phv-siol. Me&, 1987, 8, Suppl. A, pp. 33-37

Kim M. C, Ko Y. J, Kim S and Kim K. Y (2005). Impedance Imaging of the Particle Concentration Distribution in Suspensions. *Proc. 4th World Cong. Ind. Proc. Tomogr.*, Aizu, Japan, 2005, 398–403.

Le Hyaric A and Pidcock M K (2002). An image reconstruction algorithm for three dimensional electrical impedance tomography. IEEE Trans. Biomed.Eng. 48 230-5.

Long T.M (2006). An on-line velocity flow profiling system using electrical resistance tomography. M.sc thesis (2006). University of Cape Town, South Africa.

Mann R, Stanley S. J, Vlaev D, Wabo E and Primrose K (2001). Augmented-reality visualisation of fluid mixing in stirred chemical reactors using electrical resistance tomography. *J. Electron. Imaging* 2001, *10 (3)*, 620–629.

Metherall P, Barber D.C, Smallwodd R.H and Brown. B.H (1996). Three-dimensional electrical impedance tomography. *Nature,* April 1996, 380**,** pp. 509-512

Mitchell S and Vavasis S.(2000). Quality Mesh Generation in Higher Dimensions. Final version appeared in *SIAM J. Comput.* 29 (2000) 1334-1370.

Pinheiro P.A.T, Loh W.W and Dickin F.J (1998). Three-dimensional Reconstruction Algorithm for Electrical Resistance Tomography. IEE proceedings, 1998. IEE Proc.-Sci. Meas. Technol., Vol. 145, No. 3, May 1998.

Polydorides N (2002). Image reconstruction algorithms for soft-field tomography, Ph.D. thesis, University of Manchester Institute of Science and Technology, Sept. 2002.

Polydorides N and Lionheart W.R.B (2002). A MATLAB Toolkit for three-dimensional electrical impedance tomography: a contribution to the electrical impedance and diffuse optical reconstruction software project. Institute of Phyiscs Publishing, Meas. Sci. Technol. 13 (2002) 1871-1883.

Paulson K.(1992). Parallel algorithms for three-dimensional electrical impedance tomography. PhD Thesis, Oxford Brookes University; November 1992.

Qiu C.H, Dickin F.J, James A.E and Wang M (1994). Electrical resistance tomography for imaging sub-seabed sediment porosity: initial findings from laboratory-scale experiments using spherical glass beads, *Proc. of 3rd European Concerted Action on Process Tomography*, 24-26 March, Oporto, Portugal.

Randall E.W, Long T and Sutherland A.P.N (2007). The UCT Electrical Resistance Tomography instrument and its applications. The South African Institute of Mining and Metallurgy. Tomography symposium.

Ricard F, Brechtelsbauer C, Xu X. Y and Lawrence C. J (2005). Monitoring of Multiphase Pharmaceutical Processes Using Electrical Resistance Tomography. *Chem. Eng. Res. Des.* **2005**, *83*, 794–805.

Ronson Philip (2010). "Virtual centre for industrial process tomography" "www.vcipt.org.uk" 30th Sept., 2010" "http://www.vcipt.org/wcipt1.html".

Stanley S. J, Hristov H, Mann R and Primrose K (2005). On reconciling tomographic measurements with a fluid mixing model for semi-batch operation of a stirred vessel. *CJChE* 2005, *83*, 1–7.

Stephenson D.R, York T.A and Mann R (2007). Performance and Requirement of Process ERT Instruments. 5th World Congress on Industrial Process Tomography, Bergen, Norway. PP 895 - 901.

Steven J.S and Gary T.B (2008). A Review of recent Electrical Resistance Tomography (ERT) applications for wet particulate processing. Part. Part. Syst. Charact. *25* (2008) 207–215.

Stevenson Ryan (2006). Analysis of particle suspension and mixing in biological systems: an application of tomography. Ph.D thesis (2006). University of Cape Town, South Africa.

Sudhakaran H (2010). Application of electrical resistance tomography in evaluating the influence of nozzle design on the gas hold-up distribution in boiling bubble column reactors. 6th World conference on Industrial process tomography, Beijing, 2010.

Trefethen N.L. and Bau D. III (1994). Numerical linear algebra, SIAM, Philadelphia, 1994. Vauhkonen M, Kaipio J.P, Somersalo E and Karjalainen P.A (1998). Electrical impedance tomography with basis constraints. Inverse problems 13(2) : 523-530, 1997.

Vauhkonen M, Vadasz D, Karjalainen P.A, Somersalo E and Kaipio J.P (1998). Tikhonov regularization and prior information in electrical impedance tomography. IEEE transaction on medical imaging, vol. 17, no. 2, April 1998.

Vauhkonen P.J, Vauhkonen M, Savolainen T and Kaipio J.P (1999). Three-dimensional electrical impedance tomography based on the complete electrode model. IEEE Transactions on Biomedical Engineering, Vol. 46, No. 9, September 1999. PP 1150-1160.

Vauhkonen M, Lionheart W.R.B, Heikkien L.M, Vauhkonen P J and Kaipio J P. (2000). A MATLAB package for the EIDORS project to reconstruct two-dimensional EIT images. Physiol. Meas. 22 107-11.

Wang M, Dorwood A, Vlaev D and Mann R (2000). Measurements of gas-liquid mixing in a stirred vessel using electrical resistance tomography. *Chem. Eng. Sci.* 2000, *77*, 93–98.

West R. M, Jia X and Williams R. A (1998). Quantification of solid-liquid mixing using electrical resistance and positron emission tomography. *Chem. Eng. Commun.* 1998, *175*, 71–97.

Wilkinson A.J, Randall E.W, Durrett D.R, Naidoo T and Cilliers J.J (2003). The design of a 1000 frames/second ERT Data Capture System and Calibration Techniques Employed, 3rd World Congress on Industrial Process Tomography, Banff, Canada, pp 504-509.

Williams R.A, Jia X and McKee S.L (1996). Development of slurry mixing models using resistance tomography. Powder Technology 1996, *87*, 21–27.

Williams R. A, Jia X, West R. M and Roberts K. J (1998). Online measurement of solid distribution in stirred tanks and crystallisers using electrical computed tomography. *International Conference on Mixing and Crystallization*, Tioman Island, Malaysia, 1998.

Zhou B and Greenhalgh S. A (2001). Finite element three-dimensional direct current resistivity modelling: accuracy and efficiency considerations. Geophys. J. Ins. (2001) 145, 679-688.

APPENDICES

APPENDIX A

Basic Step for Running of UCT ERT Set-up

The following basic steps are required for smooth running of the hardware set-up in order to generate three dimensional data sets for offline reconstruction are as follow:

Step 1: Initiating the starting screen

(a) The user needs ensure that the tomography instrument is switched on.

(b) that the tomo USB cable is plugged into a USB port on the PC

(c) that the USB serial adapter is plugged into the tomography instrument "comms port" and a PC USB port.

When these are done, user need locate and run the executable program file called UCT_Tomography.exe and screen display should be as that in Figure 3.11.

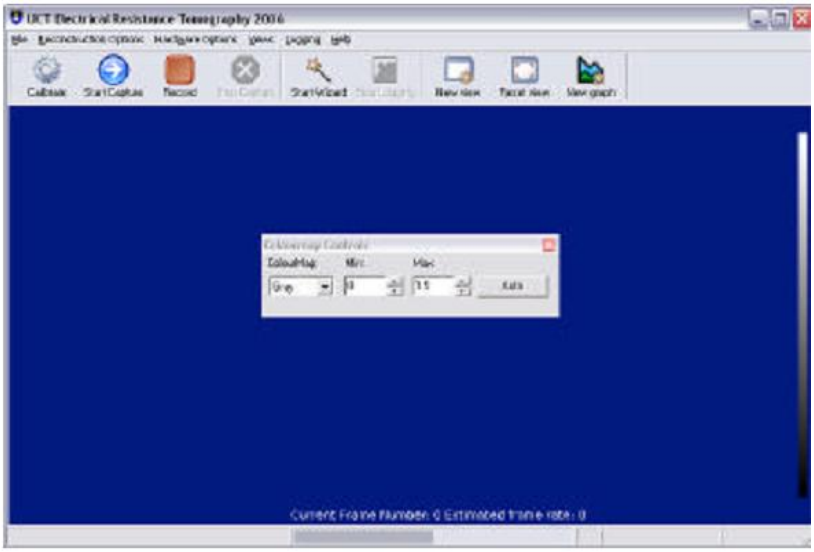

Figure A1: The initial start screen

Step 2: Setting up the measurement sequences and testing the serial comms that enables communication between the software and the tomography instrument.

(a) User needs select **Hardware Options >> Select Hardware** and choose the appropriate instrument connected to the computer. The system should prompt the user to select two files. One of the files is a download file, which is a binary file that runs on the tomography hardware. This should be chosen by selecting ' *Download Files\download_file.bin* '. The second files is the measurement sequence file. There are six measurement sequence files specifying the current injection sequences and voltage measurement sequences for two, three and four rings based on adjacent and opposite current injection respectively. Clicking on two_rings_netgen_injection_adjacent or two_rings_netgen_injection_opposite or three_rings_netgen_injection_adjacent or three_rings_netgen_injection_opposite or four_rings_netgen_injection_adjacent or four_rings_netgen_injection_opposite by the user informs the PC measurement sequence table to load into the data acquisition device. A progress bar as in Figure should appear signifying that the file is being downloaded to the instrument if the instruments are connected properly.

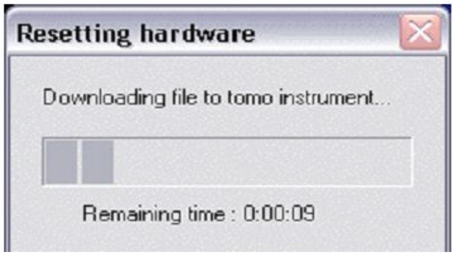

Downloading file to tomo instrument...

Remaining time : 0:00:09

Figure A2: Downloading measurement sequences table

If error message as in Figure is displayed it may be that the program is using the wrong comm port, thus the downloading was not successful.

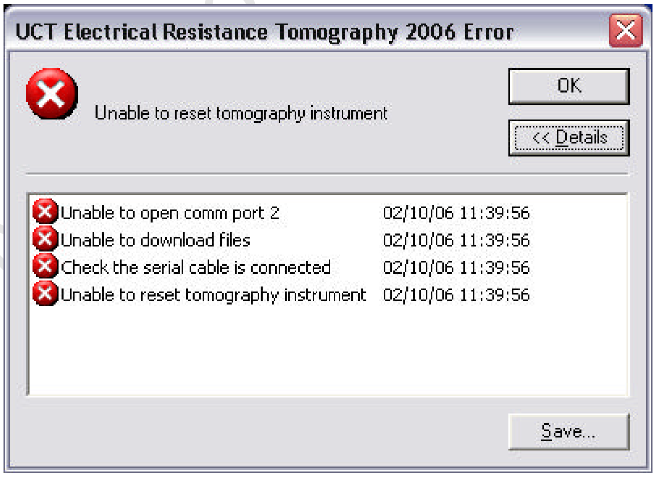

Unable to reset tomography instrument

```
Unable to open comm port 2              02/10/06 11:39:56
Unable to download files                02/10/06 11:39:56
Check the serial cable is connected     02/10/06 11:39:56
Unable to reset tomography instrument   02/10/06 11:39:56
```

Figure A3 : An expanded error message box

In order to specify the correct comm port, user should select **Hardware Options >> Change Comm Port**, and repeat step 2. The instrument may, then, be started in the data capture mode by clicking on the start Capture button on the menu bar (Figure). The 'running with current' LED (the bottom one) should be lit if the device is in a proper working condition. User should press 'Stop Capture' botton when this has been established.

Figure A4 : The Start Capture botton

Before the description of steps required in setting the injected current level into the conductive medium (saline solution) through peripheral electrode system, it is appropriate to define some measured data set recovered from the tomography rig. The raw tomography voltages for homogeneous solution graph is a plot of the voltage measurements taken

by the tomography instrument when a non-zero magnitude of current is injected into a homogenous solution without any processing. The calibration offsets are obtained when no current is injected into a homogeneous solution. The processed tomography voltages for homogenous solution is the plot of the data sets obtained from the difference between raw tomography voltages and calibration offsets about each data point. The Scaling factors voltages is the ratio of the simulated homogeneous voltage data sets to the measured processed tomography data set.The calibrated tomography voltages graph is a plot of the voltages once the calibration offsets and scaling factors have been applied. These are the values that are used in the reconstruction algorithm.

Step 3: Setting the current level

For the purpose of this experiment, the current level was adjusted manually by clicking on **Hardware Options >> Adjust current**. This selection should prompt open an interface where the slider can be moved to the right so as to increase the current level. To ensuring that the appropriate magnitude of current is input into the medium, one needs to select **View Options >> Add new graph** or click the **'add new graph**' button. This allows the raw voltage measurement to be visualised in a graph window and as such it possible to obtain suitable current level while the instrument is running. It is noteworthy that the number of frame to average should be kept at one (1) owing to manual calibration the algorithm employed. To set this, user should click **'Reconstruction Option'** >> ' **Number of Frame to average**' and enter 1 in the provided space. Furthermore, clicking on **Hardware Options >> Start Capture** or clicking the **'Start Capture'** button on the menu bar starts the instrument. If the current level was set to zero, the graph window displayed is Figure 3.16, while if the slide was moved to a level, the graph window obtained is similar to Figure 3.17 and Figure 3.18 for adjacent and opposite respectively. It should be noted that the extent of sliding is not the magnitude of the current introduced into the domain, though, there is a linear relationship between this and the value of current injected.

Raw tomography voltages: Layer 1

Refresh rate: 50

Figure A5 : Data Capture with no current applied

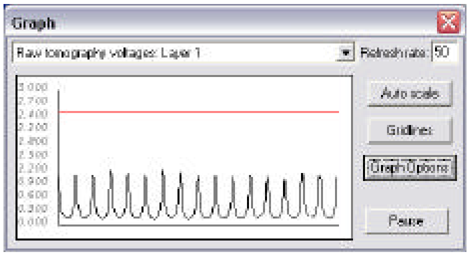

Raw tomography voltages: Layer 1

Refresh rate: 50

Figure A6: Data Capture with current applied through adjacent electrodes

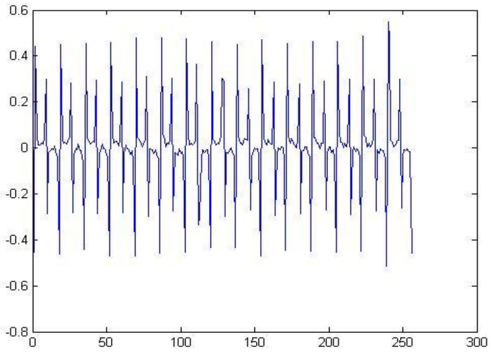

Figure A7 : Data Capture with current applied through opposite electrodes

Each "U" curve or "horseshoe" shaped data plot of Figure 3.17 is the selected thirteen of the sixteen measured voltage data set from a ring for each current injection.

Step 4: Calibration of measured voltages for inhomogeneous solution with current applied to the medium using measured voltages for homogeneous solution with current applied and offsets voltage voltages.

Although the automatic calibration data sets saved into the hard drive is not used in the image reconstruction algorithm, it is necessary that the user clicks "Calibrate" on the menu bar to prompt an interface where the value of the number of frame to average and the number of seconds to count before averaging are entered.

Figure A8: The 'Calibrate' button

With a view to calibrating the measurement from inhomogeneous saline solution with the introduction of an object of higher resistivity than the surrounding medium within the domain of the solution or by injecting some hyper-saline solution into a region of the domain, the raw tomography homogenous voltage with no current applied, the raw tomography voltages for homogeneous solution with current applied and the simulated measurement for homogeneous solution with same amplitude of current applied are needed. In this experiment, the offset voltages are the raw tomography voltages for homogeneous solution with no current applied. The offset data sets were deducted from the data sets of both the homogeneous solution with current applied and the inhomogeneous with current applied in order to derive processed data sets for both. Accordingly, scaling factor data sets were derived from the ratio of simulated homogeneous data with current applied to the processed homogeneous voltage data with same current applied about each data point. Thus, the calibrated data set used in the reconstruction was obtained from the product of the inhomogeneous data sets with the scaling factor data sets about each data point.

Step 5: Saving the voltage data via quick record

The moment the 'Record' button on the menu bar is clicked the system starts saving the measured voltage values to disc and when 'Stop Capture' is clicked, the system prompt up an interface where the name with which the file containing the data will be saved (Figure 3.20).

Figure A9: The record button

Appendix B

Six 3-D Reconstruction Codes for Both Opposite and Adjacent Current Injection Strategy in a Two, Three and Four Rings Electrode System

B1 : Reconstruction Code for A sequence of Current Stimulation through Adjacent Electrode Pairs and A Sequence of Voltage Measurement through Adjacent Electrode Pairs in a Two Rings of Electrode System

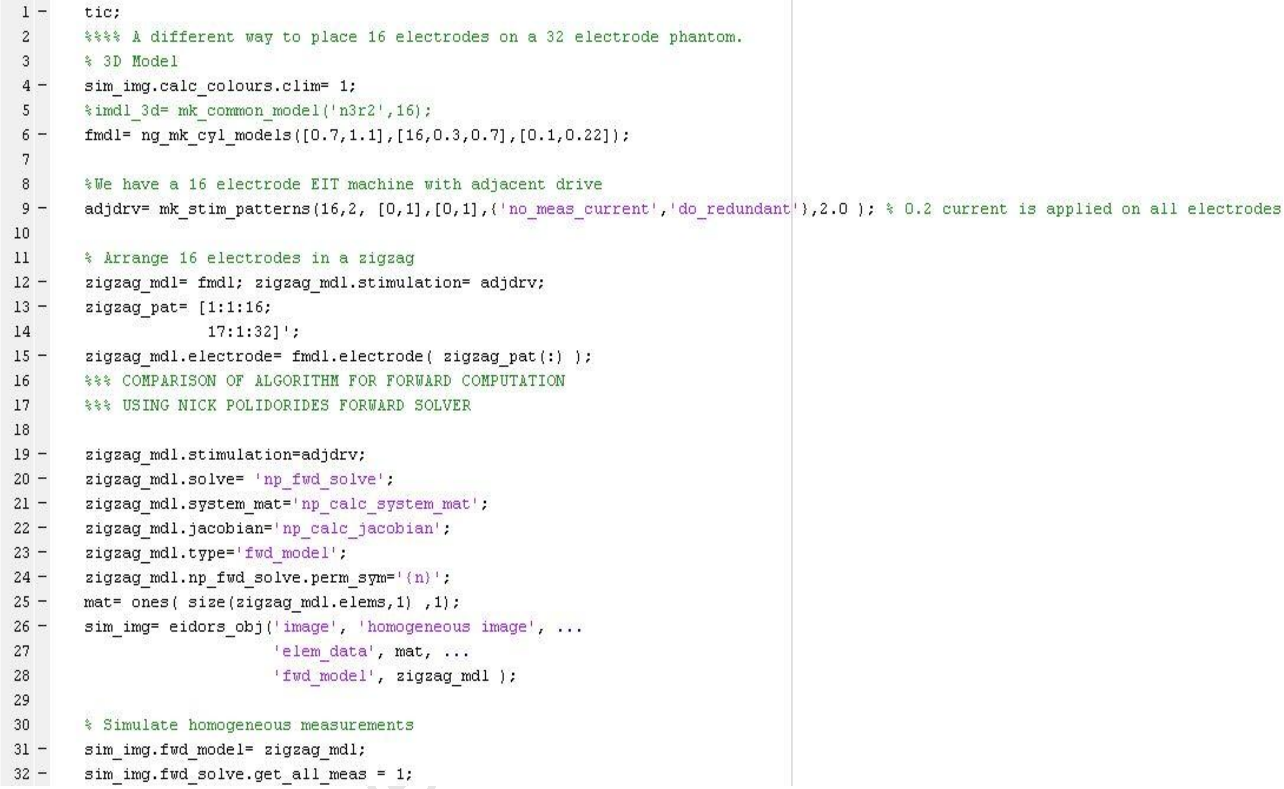

```
tic;
%%%% A different way to place 16 electrodes on a 32 electrode phantom.
% 3D Model
sim_img.calc_colours.clim= 1;
%imdl_3d= mk_common_model('n3r2',16);
fmdl= ng_mk_cyl_models([0.7,1.1],[16,0.3,0.7],[0.1,0.22]);

%We have a 16 electrode EIT machine with adjacent drive
adjdrv= mk_stim_patterns(16,2, [0,1],[0,1],{'no_meas_current','do_redundant'},2.0 ); % 0.2 current is applied on all electrodes

% Arrange 16 electrodes in a zigzag
zigzag_mdl= fmdl; zigzag_mdl.stimulation= adjdrv;
zigzag_pat= [1:1:16;
             17:1:32]';
zigzag_mdl.electrode= fmdl.electrode( zigzag_pat(:) );
%%% COMPARISON OF ALGORITHM FOR FORWARD COMPUTATION
%%% USING NICK POLIDORIDES FORWARD SOLVER

zigzag_mdl.stimulation=adjdrv;
zigzag_mdl.solve= 'np_fwd_solve';
zigzag_mdl.system_mat='np_calc_system_mat';
zigzag_mdl.jacobian='np_calc_jacobian';
zigzag_mdl.type='fwd_model';
zigzag_mdl.np_fwd_solve.perm_sym='{n}';
mat= ones( size(zigzag_mdl.elems,1) ,1);
sim_img= eidors_obj('image', 'homogeneous image', ...
                    'elem_data', mat, ...
                    'fwd_model', zigzag_mdl );

% Simulate homogeneous measurements
sim_img.fwd_model= zigzag_mdl;
sim_img.fwd_solve.get_all_meas = 1;
```

```
% Homogenous
zigzag_data_h= fwd_solve( zigzag_mdl,sim_img );

[INhomodata]=meas_inhomo2rg_adjacent('C:\Users\bode\Desktop\NOV_19TH_2ADJ\pvc_19cm.tomo');
%[homodata]=meas_homo2rg_adjacent('C:\Program Files\MATLAB\R2006b\work\july_9th Adjacent_single_object\homogeneous.tomo');
[currentdata]=getcalibrationdata2rg_adjacent_current('C:\Users\bode\Desktop\NOV_19TH_2ADJ\homo_with_current.tomo');
[nocurrentdata]=getcalibrationdata2rg_adjacent_nocurrent('C:\Users\bode\Desktop\NOV_19TH_2ADJ\homo_no_current.tomo');
% OFFSET (nocurrentdata) IS SUBSTRACTED FROM THE CURRENT DATA
% (currentdata):HOMOGENEOUS SOLUTION

%MEASURED DATA FOR HOMOGENEOUS Opp_homogeneous3_54.cal
Meas_HOMOdata=currentdata-nocurrentdata;
% OBTAINING THE SCALING CONSTANT FOR EACH HOMOGENEOUS SOLUTION
%%% Div is the scaling constant

JohnF= zigzag_data_h.meas;      %Homogeneous_adjacent('1') ;
% where JohnF is the modelled homogeneous data needed.
%Scaling factor is Homo_Fwd_mdel/Homo_measured_data
Sca_Fac=JohnF./Meas_HOMOdata;

%MEASURED DATA FOR INHOMOGENEOUS
% offset is deducted from the INhomodata
Meas_INHOMOdata=INhomodata-nocurrentdata;

%calibrated data for inhomogeous is

Calib_Inhomo=Meas_INHOMOdata.*Sca_Fac;
%zigzag_data_h.meas=JohnF;
% Create targets in image
%sim_img.elem_data([541:552])=10.0;
%PHANTOM IS NEAR THE BOUNDARY
```

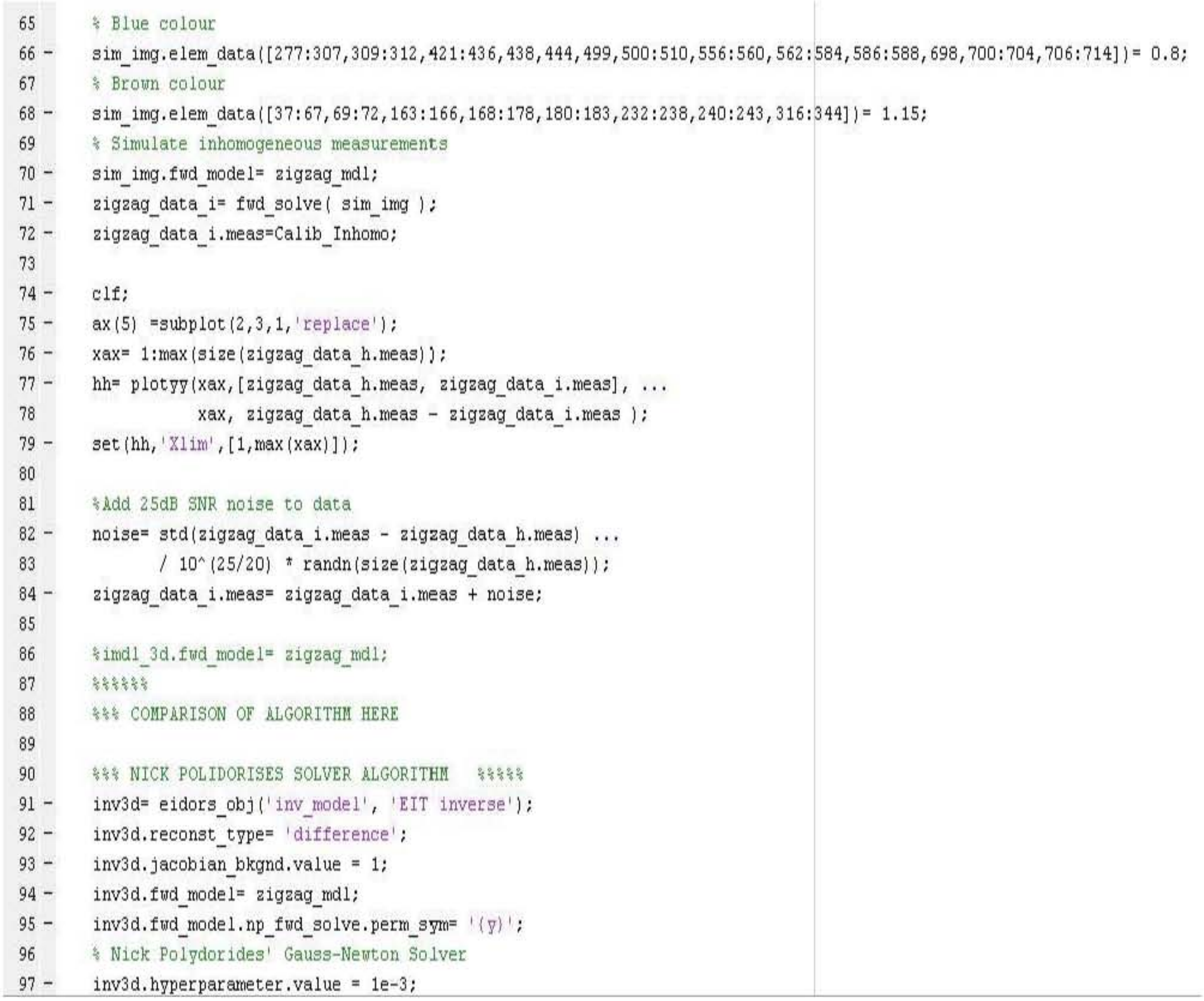

```
% Blue colour
sim_img.elem_data([277:307,309:312,421:436,438,444,499,500:510,556:560,562:584,586:588,698,700:704,706:714])= 0.8;
% Brown colour
sim_img.elem_data([37:67,69:72,163:166,168:178,180:183,232:238,240:243,316:344])= 1.15;
% Simulate inhomogeneous measurements
sim_img.fwd_model= zigzag_mdl;
zigzag_data_i= fwd_solve( sim_img );
zigzag_data_i.meas=Calib_Inhomo;

clf;
ax(5) =subplot(2,3,1,'replace');
xax= 1:max(size(zigzag_data_h.meas));
hh= plotyy(xax,[zigzag_data_h.meas, zigzag_data_i.meas], ...
           xax, zigzag_data_h.meas - zigzag_data_i.meas );
set(hh,'Xlim',[1,max(xax)]);

%Add 25dB SNR noise to data
noise= std(zigzag_data_i.meas - zigzag_data_h.meas) ...
       / 10^(25/20) * randn(size(zigzag_data_h.meas));
zigzag_data_i.meas= zigzag_data_i.meas + noise;

%imdl_3d.fwd_model= zigzag_mdl;
%%%%%%
%%% COMPARISON OF ALGORITHM HERE

%%% NICK POLIDORISES SOLVER ALGORITHM   %%%%%
inv3d= eidors_obj('inv_model', 'EIT inverse');
inv3d.reconst_type= 'difference';
inv3d.jacobian_bkgnd.value = 1;
inv3d.fwd_model= zigzag_mdl;
inv3d.fwd_model.np_fwd_solve.perm_sym= '{y}';
% Nick Polydorides' Gauss-Newton Solver
inv3d.hyperparameter.value = 1e-3;
```

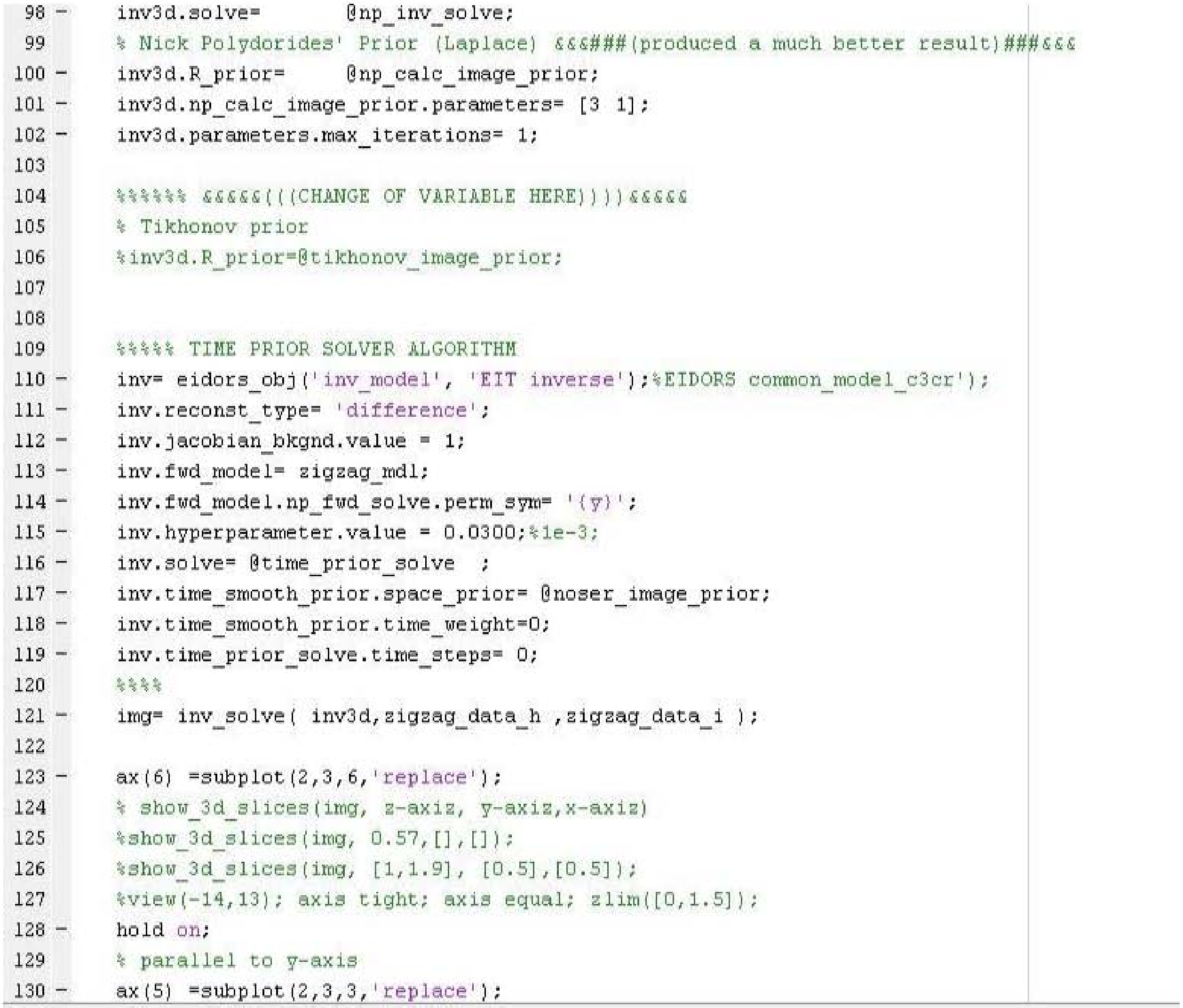

```matlab
inv3d.solve=       @np_inv_solve;
% Nick Polydorides' Prior (Laplace) &&&###(produced a much better result)###&&&
inv3d.R_prior=     @np_calc_image_prior;
inv3d.np_calc_image_prior.parameters= [3 1];
inv3d.parameters.max_iterations= 1;

%%%%%% &&&&&(((CHANGE OF VARIABLE HERE)))&&&&&
% Tikhonov prior
%inv3d.R_prior=@tikhonov_image_prior;


%%%%% TIME PRIOR SOLVER ALGORITHM
inv= eidors_obj('inv_model', 'EIT inverse');%EIDORS common_model_c3cr');
inv.reconst_type= 'difference';
inv.jacobian_bkgnd.value = 1;
inv.fwd_model= zigzag_mdl;
inv.fwd_model.np_fwd_solve.perm_sym= '{y}';
inv.hyperparameter.value = 0.0300;%1e-3;
inv.solve= @time_prior_solve  ;
inv.time_smooth_prior.space_prior= @noser_image_prior;
inv.time_smooth_prior.time_weight=0;
inv.time_prior_solve.time_steps= 0;
%%%%
img= inv_solve( inv3d,zigzag_data_h ,zigzag_data_i );

ax(6) =subplot(2,3,6,'replace');
% show_3d_slices(img, z-axiz, y-axiz,x-axiz)
%show_3d_slices(img, 0.57,[],[]);
%show_3d_slices(img, [1,1.9], [0.5],[0.5]);
%view(-14,13); axis tight; axis equal; zlim([0,1.5]);
hold on;
% parallel to y-axis
ax(5) =subplot(2,3,3,'replace');
```

```
show_fem(img)
hold on;
ax(3) =subplot(2,3,4,'replace');
show_fem(img)
hold on;
%show_3d_slices(img, [],[0.0],[]);
%show_3d_slices(img, [1,1.9], [0.5],[0.5]);
%view(-14,13); axis tight; axis equal; zlim([0,1.5]);
ax(1) =subplot(2,3,1,'replace');
show_fem(img)
hold on;
ax(4) =subplot(2,3,2,'replace');
rgb = imread('C:/users/bode/desktop/bode/IMG_1329.jpg');
image(rgb);
title('Top View of Phantom Suspended at 0.8dm on y-axis')
%parallel to x-axis
%show_3d_slices(img, [],[],[0.0]);
%view(-14,13); axis tight; axis equal; zlim([0,1.5]);
hold on;
ax(2) = subplot(2,3,5,'replace');
rgb = imread('C:/users/bode/desktop/bode/IMG_1335.jpg');
image(rgb);
title('Right side view of Phantom Suspended at 0.4dm on y-axis')
axis(ax,'image')

% Lowest limit
dadada=img.elem_data;
l_lim=min(dadada);%-0.6300;
% highest element values
high_value_elem_data=max(dadada);%0.2778;
%lowest element values
low_value_elem_data=min(dadada);%-0.6300;
% step change
```

```
delt=(high_value_elem_data-low_value_elem_data)/20;
[sav]=Sorting_elemindex(dadada);
[imggge]=Sorting_resistivity(dadada);
colour_map=[];
sav_new=[];
for uu=1:max(size(imggge(:,1)));
    gad=(imggge(uu)-l_lim)/delt;
    colour_map=[colour_map;gad*10,imggge(uu)];
    sav_new=[sav_new;sav(uu)];
    if colour_map(uu,1)>40
        break
    end
end
% SUMMATION OF VOLUME OF TETRAHEDRAL OF HIGHER RESISITIVITY VALUES

VVVOLUME=[];add_volume=0;sel_ele=[];sel_resist=[];mass_phant=[];
% SAV denotes indexes of the elements
for m=1:max(size(sav_new(:,1)));
 %aa1,bb1,cc1,dd1 are nodal points of an element.
elem_index=sav_new(m);
aa1=fmdl.elems(elem_index,1);
%b=1097(0.8744,0.1186,2.0), 1960
bb1=fmdl.elems(elem_index,2);
%c=436(1.0995,0.0328,2.0), 348
cc1=fmdl.elems(elem_index,3);
%d=1080(0.9291,-0.0481,2.0) 1959
dd1=fmdl.elems(elem_index,4);
% CALCULATING THE VOLUME OF A TETRAHEDRAL
% volume in meters
% V=|(a-d).((b-d)X(c-d))|/6
a1=fmdl.nodes(bb1,1)-fmdl.nodes(aa1,1); a2=fmdl.nodes(bb1,2)-fmdl.nodes(aa1,2);a3=fmdl.nodes(bb1,3)-fmdl.nodes(aa1,3);
b1=fmdl.nodes(cc1,1)-fmdl.nodes(aa1,1);b2=fmdl.nodes(cc1,2)-fmdl.nodes(aa1,2);b3=fmdl.nodes(cc1,3)-fmdl.nodes(aa1,3);
c1=fmdl.nodes(dd1,1)-fmdl.nodes(aa1,1);c2=fmdl.nodes(dd1,2)-fmdl.nodes(aa1,2);c3=fmdl.nodes(dd1,3)-fmdl.nodes(aa1,3);
```

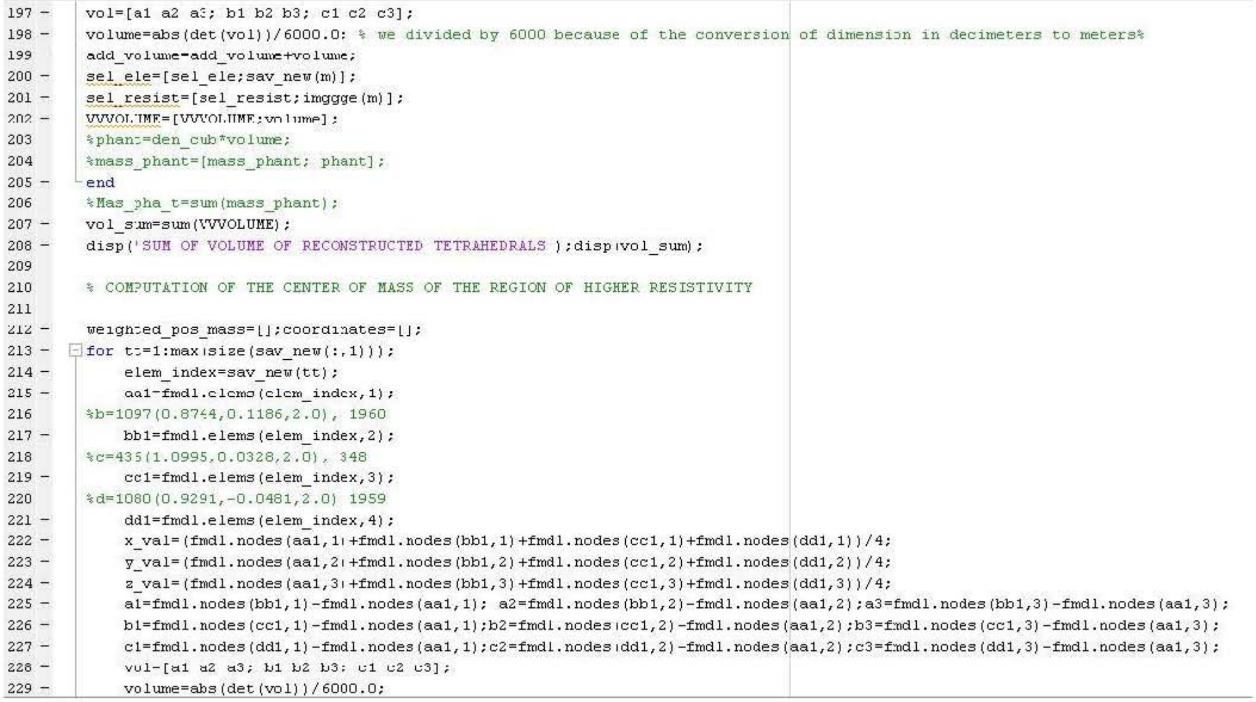

```
vol=[a1 a2 a3; b1 b2 b3; c1 c2 c3];
volume=abs(det(vol))/6000.0; % we divided by 6000 because of the conversion of dimension in decimeters to meters%
add_volume=add_volume+volume;
sel_ele=[sel_ele;sav_new(m)];
sel_resist=[sel_resist;imggge(m)];
VVVOLUME=[VVVOLUME;volume];
%phant=den_cub*volume;
%mass_phant=[mass_phant; phant];
end
%Mas_pha_t=sum(mass_phant);
vol_sum=sum(VVVOLUME);
disp('SUM OF VOLUME OF RECONSTRUCTED TETRAHEDRALS ');disp(vol_sum);

% COMPUTATION OF THE CENTER OF MASS OF THE REGION OF HIGHER RESISTIVITY

weighted_pos_mass=[];coordinates=[];
for tt=1:max(size(sav_new(:,1)));
    elem_index=sav_new(tt);
    aa1=fmdl.elems(elem_index,1);
%b=1097(0.8744,0.1186,2.0), 1960
    bb1=fmdl.elems(elem_index,2);
%c=435(1.0995,0.0328,2.0), 348
    cc1=fmdl.elems(elem_index,3);
%d=1080(0.9291,-0.0481,2.0) 1959
    dd1=fmdl.elems(elem_index,4);
    x_val=(fmdl.nodes(aa1,1)+fmdl.nodes(bb1,1)+fmdl.nodes(cc1,1)+fmdl.nodes(dd1,1))/4;
    y_val=(fmdl.nodes(aa1,2)+fmdl.nodes(bb1,2)+fmdl.nodes(cc1,2)+fmdl.nodes(dd1,2))/4;
    z_val=(fmdl.nodes(aa1,3)+fmdl.nodes(bb1,3)+fmdl.nodes(cc1,3)+fmdl.nodes(dd1,3))/4;
    a1=fmdl.nodes(bb1,1)-fmdl.nodes(aa1,1); a2=fmdl.nodes(bb1,2)-fmdl.nodes(aa1,2);a3=fmdl.nodes(bb1,3)-fmdl.nodes(aa1,3);
    b1=fmdl.nodes(cc1,1)-fmdl.nodes(aa1,1);b2=fmdl.nodes(cc1,2)-fmdl.nodes(aa1,2);b3=fmdl.nodes(cc1,3)-fmdl.nodes(aa1,3);
    c1=fmdl.nodes(dd1,1)-fmdl.nodes(aa1,1);c2=fmdl.nodes(dd1,2)-fmdl.nodes(aa1,2);c3=fmdl.nodes(dd1,3)-fmdl.nodes(aa1,3);
    vol=[a1 a2 a3; b1 b2 b3; c1 c2 c3];
    volume=abs(det(vol))/6000.0;
```

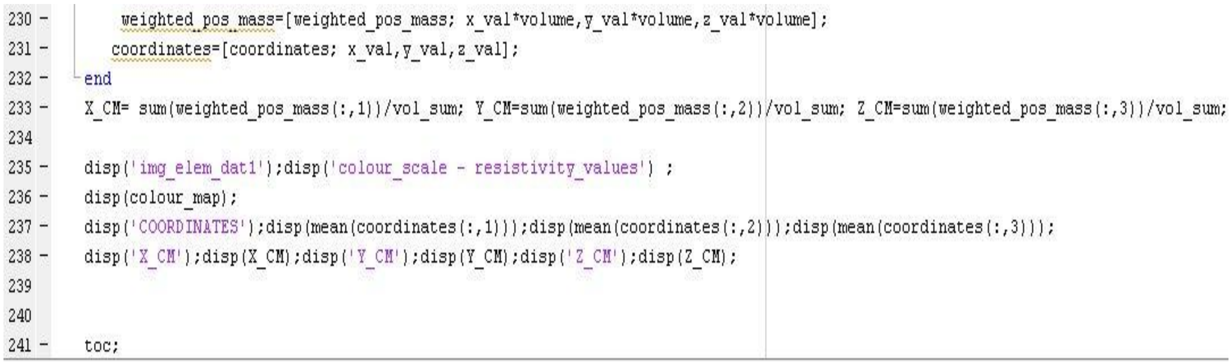

```
      weighted_pos_mass=[weighted_pos_mass; x_val*volume,y_val*volume,z_val*volume];
    coordinates=[coordinates; x_val,y_val,z_val];
end
X_CM= sum(weighted_pos_mass(:,1))/vol_sum; Y_CM=sum(weighted_pos_mass(:,2))/vol_sum; Z_CM=sum(weighted_pos_mass(:,3))/vol_sum;

disp('img_elem_dat1');disp('colour_scale - resistivity_values') ;
disp(colour_map);
disp('COORDINATES');disp(mean(coordinates(:,1)));disp(mean(coordinates(:,2)));disp(mean(coordinates(:,3)));
disp('X_CM');disp(X_CM);disp('Y_CM');disp(Y_CM);disp('Z_CM');disp(Z_CM);



toc;
```

B2 : Reconstruction Code for A sequence of Current Stimulation through Opposite Electrode Pairs and A Sequence of Voltage Measurement through Adjacent Electrode Pairs in a Two Rings of Electrode System

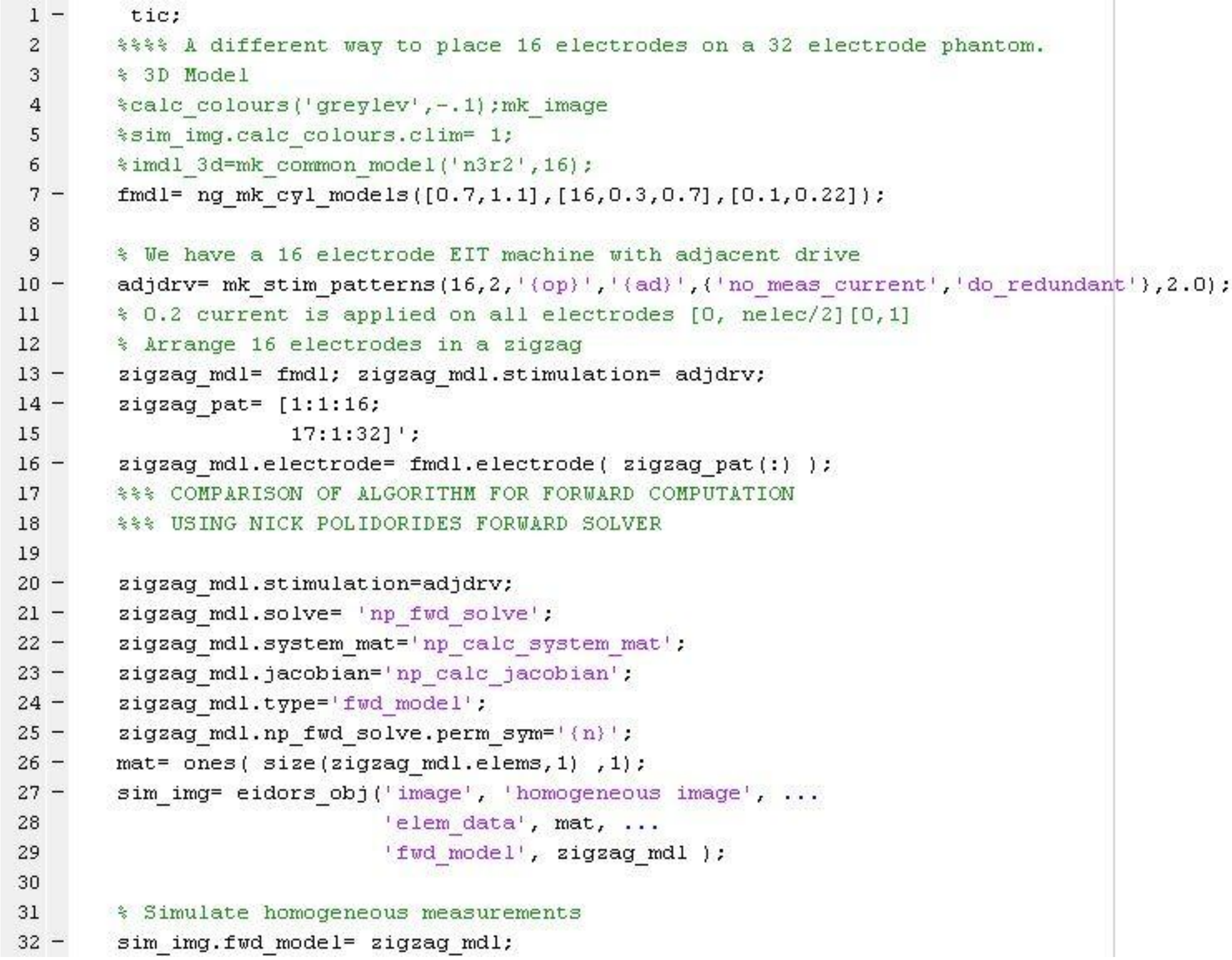

```
 tic;
%%%% A different way to place 16 electrodes on a 32 electrode phantom.
% 3D Model
%calc_colours('greylev',-.1);mk_image
%sim_img.calc_colours.clim= 1;
%imdl_3d=mk_common_model('n3r2',16);
fmdl= ng_mk_cyl_models([0.7,1.1],[16,0.3,0.7],[0.1,0.22]);

% We have a 16 electrode EIT machine with adjacent drive
adjdrv= mk_stim_patterns(16,2,'{op}','{ad}',{'no_meas_current','do_redundant'},2.0);
% 0.2 current is applied on all electrodes [0, nelec/2][0,1]
% Arrange 16 electrodes in a zigzag
zigzag_mdl= fmdl; zigzag_mdl.stimulation= adjdrv;
zigzag_pat= [1:1:16;
             17:1:32]';
zigzag_mdl.electrode= fmdl.electrode( zigzag_pat(:) );
%%% COMPARISON OF ALGORITHM FOR FORWARD COMPUTATION
%%% USING NICK POLIDORIDES FORWARD SOLVER

zigzag_mdl.stimulation=adjdrv;
zigzag_mdl.solve= 'np_fwd_solve';
zigzag_mdl.system_mat='np_calc_system_mat';
zigzag_mdl.jacobian='np_calc_jacobian';
zigzag_mdl.type='fwd_model';
zigzag_mdl.np_fwd_solve.perm_sym='{n}';
mat= ones( size(zigzag_mdl.elems,1) ,1);
sim_img= eidors_obj('image', 'homogeneous image', ...
                    'elem_data', mat, ...
                    'fwd_model', zigzag_mdl );

% Simulate homogeneous measurements
sim_img.fwd_model= zigzag_mdl;
```

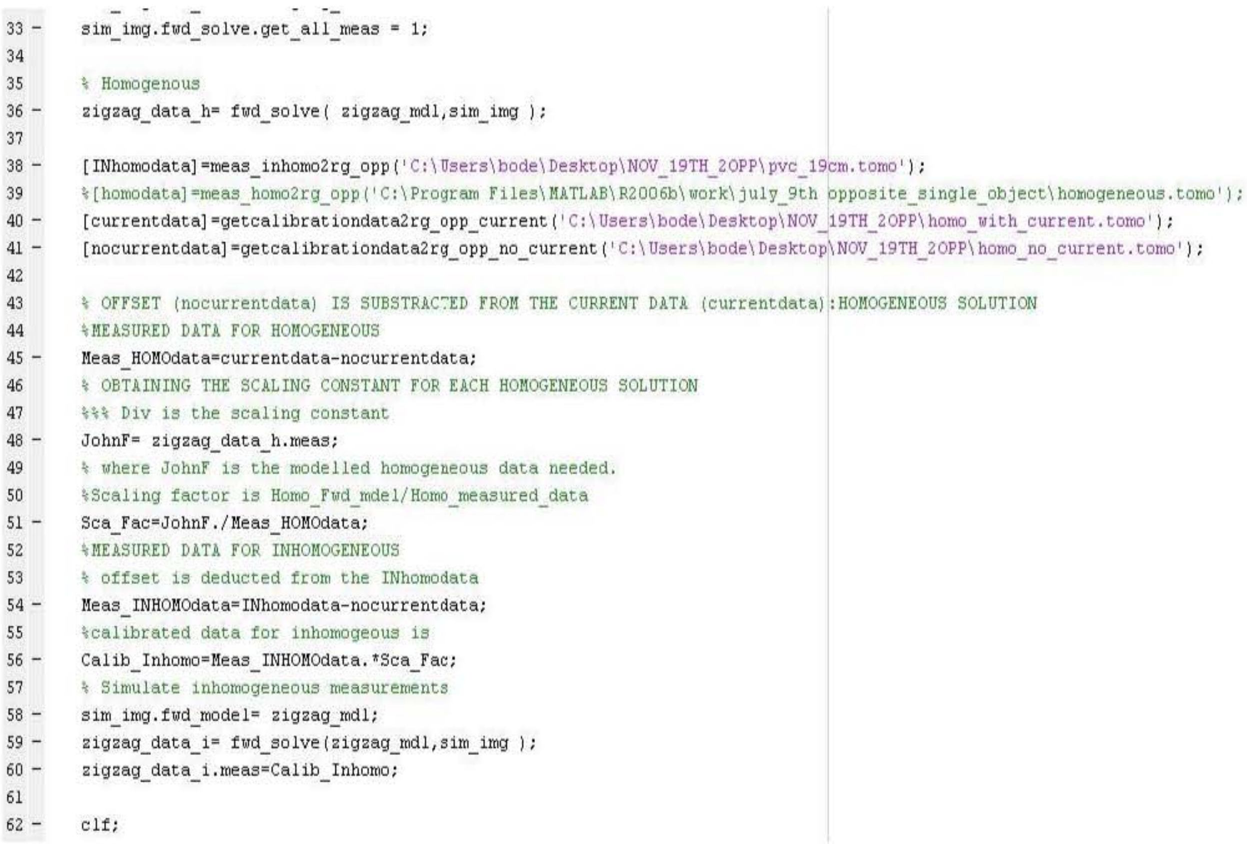

```matlab
sim_img.fwd_solve.get_all_meas = 1;

% Homogenous
zigzag_data_h= fwd_solve( zigzag_mdl,sim_img );

[INhomodata]=meas_inhomo2rg_opp('C:\Users\bode\Desktop\NOV_19TH_2OPP\pvc_19cm.tomo');
%[homodata]=meas_homo2rg_opp('C:\Program Files\MATLAB\R2006b\work\july_9th opposite_single_object\homogeneous.tomo');
[currentdata]=getcalibrationdata2rg_opp_current('C:\Users\bode\Desktop\NOV_19TH_2OPP\homo_with_current.tomo');
[nocurrentdata]=getcalibrationdata2rg_opp_no_current('C:\Users\bode\Desktop\NOV_19TH_2OPP\homo_no_current.tomo');

% OFFSET (nocurrentdata) IS SUBSTRACTED FROM THE CURRENT DATA (currentdata):HOMOGENEOUS SOLUTION
%MEASURED DATA FOR HOMOGENEOUS
Meas_HOMOdata=currentdata-nocurrentdata;
% OBTAINING THE SCALING CONSTANT FOR EACH HOMOGENEOUS SOLUTION
%%% Div is the scaling constant
JohnF= zigzag_data_h.meas;
% where JohnF is the modelled homogeneous data needed.
%Scaling factor is Homo_Fwd_mdel/Homo_measured_data
Sca_Fac=JohnF./Meas_HOMOdata;
%MEASURED DATA FOR INHOMOGENEOUS
% offset is deducted from the INhomodata
Meas_INHOMOdata=INhomodata-nocurrentdata;
%calibrated data for inhomogeous is
Calib_Inhomo=Meas_INHOMOdata.*Sca_Fac;
% Simulate inhomogeneous measurements
sim_img.fwd_model= zigzag_mdl;
zigzag_data_i= fwd_solve(zigzag_mdl,sim_img );
zigzag_data_i.meas=Calib_Inhomo;

clf;
```

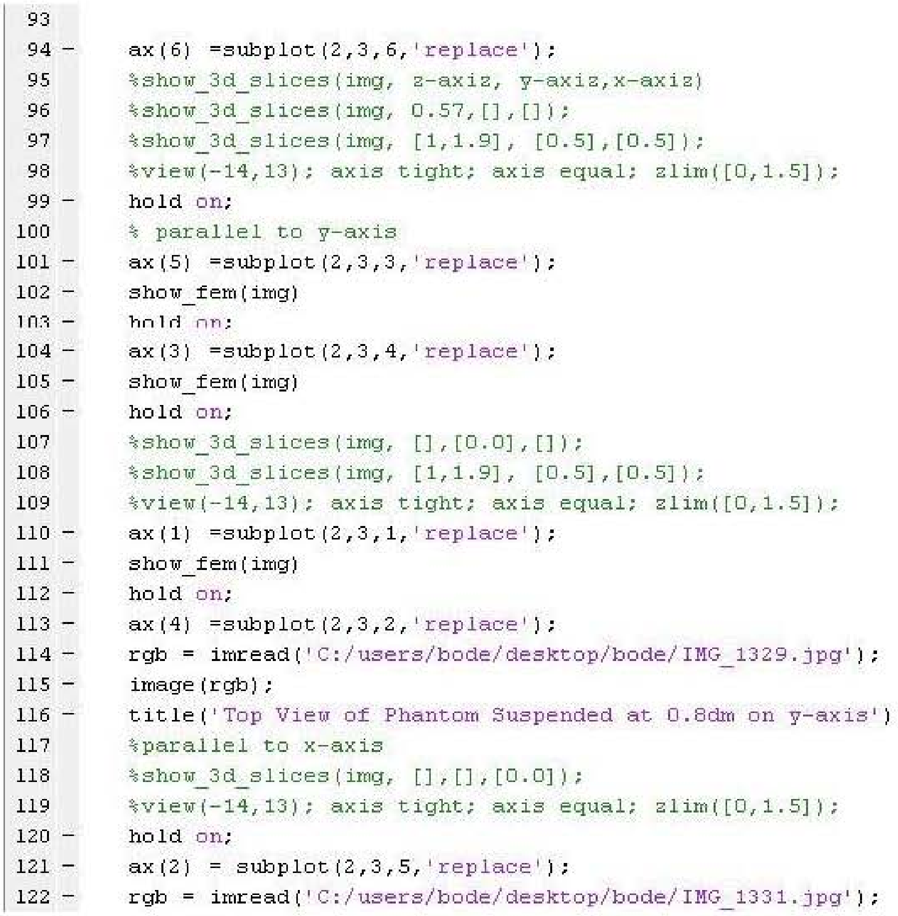

```

ax(6) =subplot(2,3,6,'replace');
%show_3d_slices(img, z-axiz, y-axiz,x-axiz)
%show_3d_slices(img, 0.57,[],[]);
%show_3d_slices(img, [1,1.9], [0.5],[0.5]);
%view(-14,13); axis tight; axis equal; zlim([0,1.5]);
hold on;
% parallel to y-axis
ax(5) =subplot(2,3,3,'replace');
show_fem(img)
hold on;
ax(3) =subplot(2,3,4,'replace');
show_fem(img)
hold on;
%show_3d_slices(img, [],[0.0],[]);
%show_3d_slices(img, [1,1.9], [0.5],[0.5]);
%view(-14,13); axis tight; axis equal; zlim([0,1.5]);
ax(1) =subplot(2,3,1,'replace');
show_fem(img)
hold on;
ax(4) =subplot(2,3,2,'replace');
rgb = imread('C:/users/bode/desktop/bode/IMG_1329.jpg');
image(rgb);
title('Top View of Phantom Suspended at 0.8dm on y-axis')
%parallel to x-axis
%show_3d_slices(img, [],[],[0.0]);
%view(-14,13); axis tight; axis equal; zlim([0,1.5]);
hold on;
ax(2) = subplot(2,3,5,'replace');
rgb = imread('C:/users/bode/desktop/bode/IMG_1331.jpg');
```

```
image(rgb);
title('Front view of Phantom Suspended at 0.0dm on y-axis')
axis(ax,'image')

% Lowest limit
dadada=img.elem_data;
l_lim=min(dadada);%-0.6300;
% highest element values
high_value_elem_data=max(dadada);%0.2778;
%lowest element values
low_value_elem_data=min(dadada);%-0.6300;
% step change
delt=(high_value_elem_data-low_value_elem_data)/20;
[sav]=Sorting_elemindex(dadada);
[imggge]=Sorting_resistivity(dadada);
colour_map=[];
sav_new=[];
for uu=1:max(size(imggge(:,1)));
    gad=(imggge(uu)-l_lim)/delt;
    colour_map=[colour_map;gad*10,imggge(uu)];
    sav_new=[sav_new;sav(uu)];
    if colour_map(uu,1)>40
        break
    end
end
% SUMMATION OF VOLUME OF TETRAHEDRAL OF HIGHER RESISITIVITY VALUES

VVVOLUME=[];add_volume=0;sel_ele=[];sel_resist=[];mass_phant=[];
% SAV denotes indexes of the elements
for m=1:max(size(sav_new(:,1)));
```

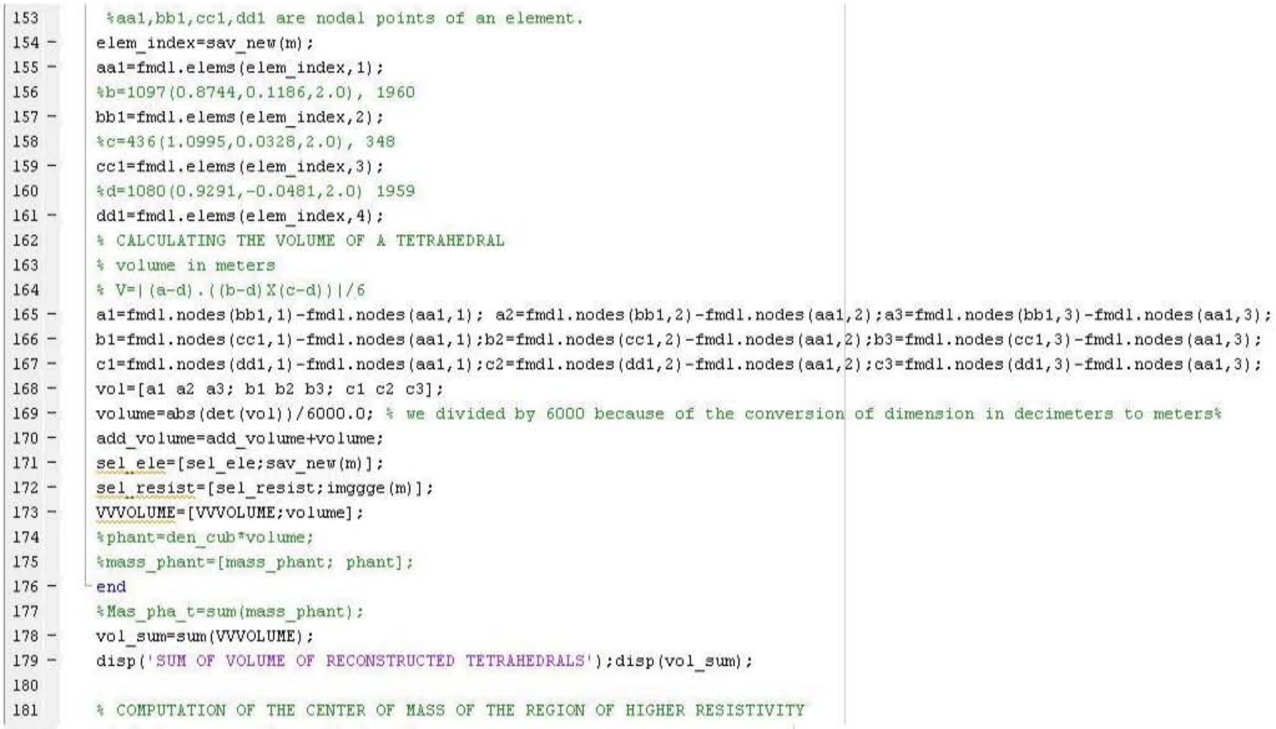

```
    %aa1,bb1,cc1,dd1 are nodal points of an element.
   elem_index=sav_new(m);
   aa1=fmdl.elems(elem_index,1);
   %b=1097(0.8744,0.1186,2.0), 1960
   bb1=fmdl.elems(elem_index,2);
   %c=436(1.0995,0.0328,2.0), 348
   cc1=fmdl.elems(elem_index,3);
   %d=1080(0.9291,-0.0481,2.0) 1959
   dd1=fmdl.elems(elem_index,4);
   % CALCULATING THE VOLUME OF A TETRAHEDRAL
   % volume in meters
   % V=|(a-d).((b-d)X(c-d))|/6
   a1=fmdl.nodes(bb1,1)-fmdl.nodes(aa1,1); a2=fmdl.nodes(bb1,2)-fmdl.nodes(aa1,2);a3=fmdl.nodes(bb1,3)-fmdl.nodes(aa1,3);
   b1=fmdl.nodes(cc1,1)-fmdl.nodes(aa1,1);b2=fmdl.nodes(cc1,2)-fmdl.nodes(aa1,2);b3=fmdl.nodes(cc1,3)-fmdl.nodes(aa1,3);
   c1=fmdl.nodes(dd1,1)-fmdl.nodes(aa1,1);c2=fmdl.nodes(dd1,2)-fmdl.nodes(aa1,2);c3=fmdl.nodes(dd1,3)-fmdl.nodes(aa1,3);
   vol=[a1 a2 a3; b1 b2 b3; c1 c2 c3];
   volume=abs(det(vol))/6000.0; % we divided by 6000 because of the conversion of dimension in decimeters to meters%
   add_volume=add_volume+volume;
   sel_ele=[sel_ele;sav_new(m)];
   sel_resist=[sel_resist;imggge(m)];
   VVVOLUME=[VVVOLUME;volume];
   %phant=den_cub*volume;
   %mass_phant=[mass_phant; phant];
   end
   %Mas_pha_t=sum(mass_phant);
   vol_sum=sum(VVVOLUME);
   disp('SUM OF VOLUME OF RECONSTRUCTED TETRAHEDRALS');disp(vol_sum);

   % COMPUTATION OF THE CENTER OF MASS OF THE REGION OF HIGHER RESISTIVITY
```

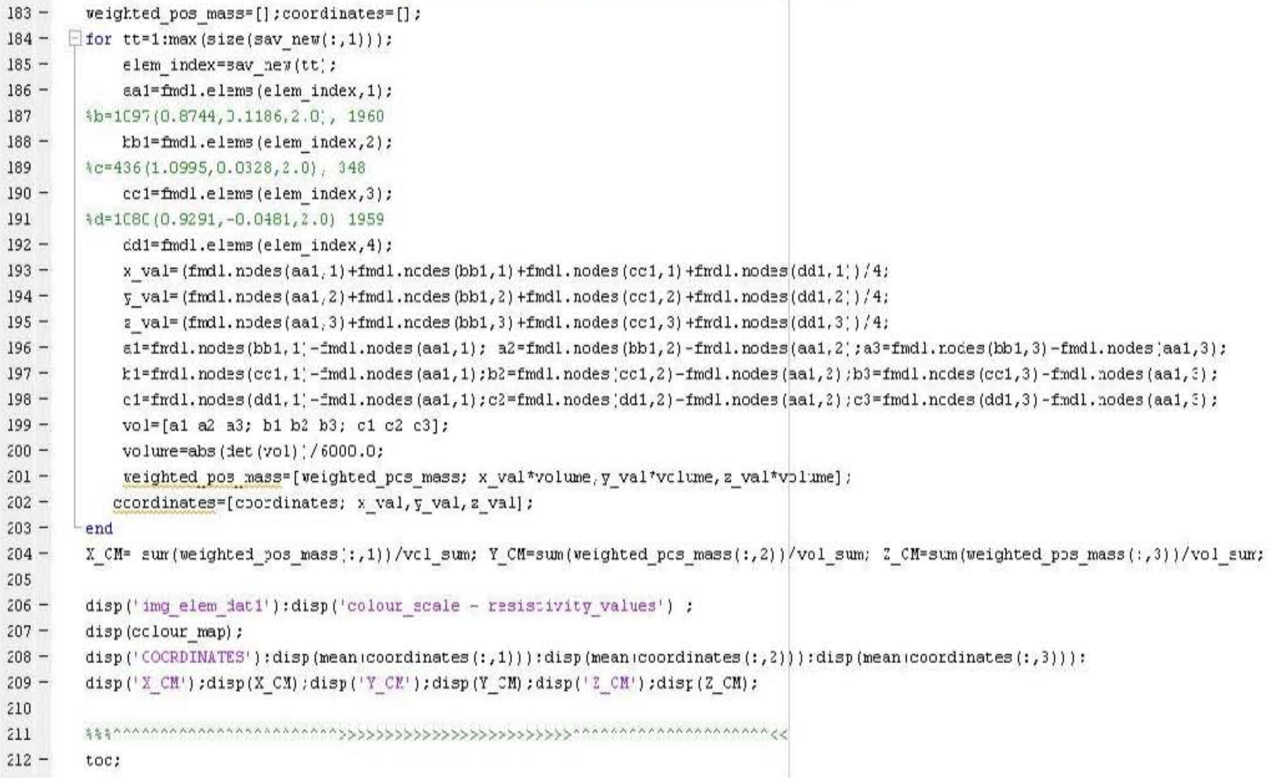

```
weighted_pos_mass=[];coordinates=[];
for tt=1:max(size(sav_new(:,1)));
    elem_index=sav_new(tt);
    aa1=fmdl.elems(elem_index,1);
%b=1097(0.8744,0.1186,2.0), 1960
    bb1=fmdl.elems(elem_index,2);
%c=436(1.0995,0.0328,2.0), 348
    cc1=fmdl.elems(elem_index,3);
%d=1080(0.9291,-0.0481,2.0) 1959
    dd1=fmdl.elems(elem_index,4);
    x_val=(fmdl.nodes(aa1,1)+fmdl.nodes(bb1,1)+fmdl.nodes(cc1,1)+fmdl.nodes(dd1,1))/4;
    y_val=(fmdl.nodes(aa1,2)+fmdl.nodes(bb1,2)+fmdl.nodes(cc1,2)+fmdl.nodes(dd1,2))/4;
    z_val=(fmdl.nodes(aa1,3)+fmdl.nodes(bb1,3)+fmdl.nodes(cc1,3)+fmdl.nodes(dd1,3))/4;
    a1=fmdl.nodes(bb1,1)-fmdl.nodes(aa1,1); a2=fmdl.nodes(bb1,2)-fmdl.nodes(aa1,2);a3=fmdl.nodes(bb1,3)-fmdl.nodes(aa1,3);
    b1=fmdl.nodes(cc1,1)-fmdl.nodes(aa1,1);b2=fmdl.nodes(cc1,2)-fmdl.nodes(aa1,2);b3=fmdl.nodes(cc1,3)-fmdl.nodes(aa1,3);
    c1=fmdl.nodes(dd1,1)-fmdl.nodes(aa1,1);c2=fmdl.nodes(dd1,2)-fmdl.nodes(aa1,2);c3=fmdl.nodes(dd1,3)-fmdl.nodes(aa1,3);
    vol=[a1 a2 a3; b1 b2 b3; c1 c2 c3];
    volume=abs(det(vol))/6000.0;
    weighted_pos_mass=[weighted_pos_mass; x_val*volume,y_val*volume,z_val*volume];
   coordinates=[coordinates; x_val,y_val,z_val];
end
X_CM= sum(weighted_pos_mass(:,1))/vol_sum; Y_CM=sum(weighted_pos_mass(:,2))/vol_sum; Z_CM=sum(weighted_pos_mass(:,3))/vol_sum;

disp('img_elem_dat1');disp('colour_scale - resistivity_values') ;
disp(colour_map);
disp('COORDINATES');disp(mean(coordinates(:,1)));disp(mean(coordinates(:,2)));disp(mean(coordinates(:,3)));
disp('X_CM');disp(X_CM);disp('Y_CM');disp(Y_CM);disp('Z_CM');disp(Z_CM);

%%%^^^^^^^^^^^^^^^^^^^^^^^^>>>>>>>>>>>>>>>>>>>>>>>>^^^^^^^^^^^^^^^^^^^^^<<
toc;
```

B3 : Reconstruction Code for A sequence of Current Stimulation through Adjacent Electrode Pairs and A Sequence of Voltage Measurement through Adjacent Electrode Pairs in a Three Rings of Electrode System

```
tic;
IMDL_3D=mk_common_model('c3cr',[16,3]);
 nelec= 16; nrings= 3;
ring_vert_pos = [0.3,0.7,1.05]; %[0.15,0.5,0.87]
extra={'ball','solid ball = sphere(-0.15,-0.1,0.5;0.1);'};
[fmdl]=ng_mk_cyl_models([1.1,1.1],[nelec,ring_vert_pos],[0.1,0.2]);

stim = mk_stim_patterns(16,3,[0,1],[0,1],{'no_meas_current','do_redundant'},2.0); %[0, nelec/2][0,1
fmdl.stimulation = stim;
%%% COMPARISON OF ALGORITHM FOR FORWARD COMPUTATION
%%% USING NICK POLIDORIDES FORWARD SOLVER
fmdl.stimulation=stim;
fmdl.solve= 'np_fwd_solve';
fmdl.system_mat='np_calc_system_mat';
fmdl.jacobian='np_calc_jacobian';
fmdl.type='fwd_model';
fmdl.np_fwd_solve.perm_sym='{n}';
mat= ones( size(fmdl.elems,1) ,1);
sim_img= eidors_obj('image', 'homogeneous image', ...
                    'elem_data', mat, ...
                    'fwd_model', fmdl );

% Simulate homogeneous measurements
sim_img.fwd_model= fmdl;
sim_img.fwd_solve.get_all_meas = 1;

sim_img.fwd_model= fmdl;
show_fem(sim_img);
sim_img.elem_data(mat) = 1; % Homogenous
vh = fwd_solve(fmdl,sim_img);

[INhomodata]=meas_inhomo_3rings_adjacent('C:\Users\bode\Desktop\NOV_19TH_3ADJ\pvc_19cm.tomo');
%[homodata]=meas_homo_3rings_adjacent('C:\Program Files\MATLAB\R2006b\work\June_23_data\jun_23_adj_homo_2.0current.tomo');
```

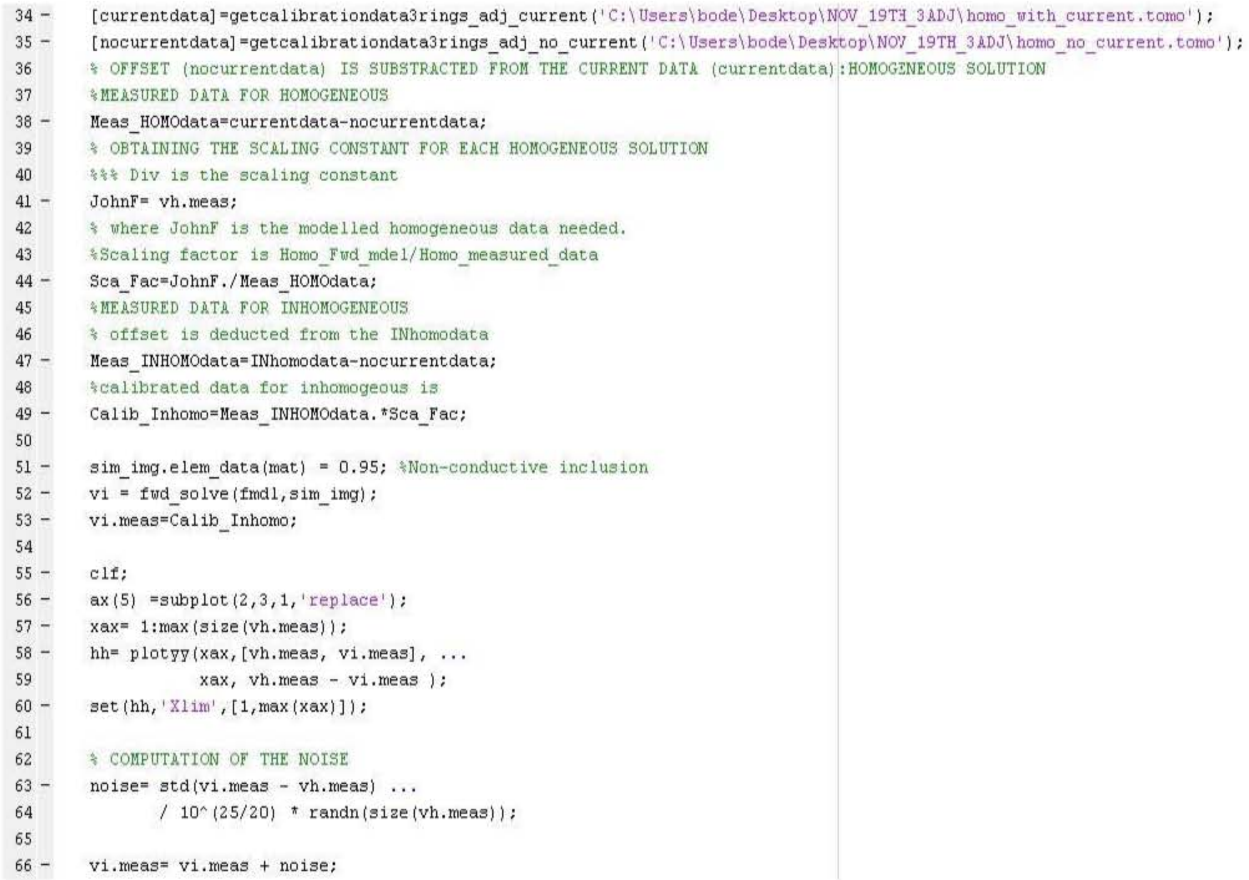

```
[currentdata]=getcalibrationdata3rings_adj_current('C:\Users\bode\Desktop\NOV_19TH_3ADJ\homo_with_current.tomo');
[nocurrentdata]=getcalibrationdata3rings_adj_no_current('C:\Users\bode\Desktop\NOV_19TH_3ADJ\homo_no_current.tomo');
% OFFSET (nocurrentdata) IS SUBSTRACTED FROM THE CURRENT DATA (currentdata):HOMOGENEOUS SOLUTION
%MEASURED DATA FOR HOMOGENEOUS
Meas_HOMOdata=currentdata-nocurrentdata;
% OBTAINING THE SCALING CONSTANT FOR EACH HOMOGENEOUS SOLUTION
%%% Div is the scaling constant
JohnF= vh.meas;
% where JohnF is the modelled homogeneous data needed.
%Scaling factor is Homo_Fwd_mdel/Homo_measured_data
Sca_Fac=JohnF./Meas_HOMOdata;
%MEASURED DATA FOR INHOMOGENEOUS
% offset is deducted from the INhomodata
Meas_INHOMOdata=INhomodata-nocurrentdata;
%calibrated data for inhomogeous is
Calib_Inhomo=Meas_INHOMOdata.*Sca_Fac;

sim_img.elem_data(mat) = 0.95; %Non-conductive inclusion
vi = fwd_solve(fmdl,sim_img);
vi.meas=Calib_Inhomo;

clf;
ax(5) =subplot(2,3,1,'replace');
xax= 1:max(size(vh.meas));
hh= plotyy(xax,[vh.meas, vi.meas], ...
           xax, vh.meas - vi.meas );
set(hh,'Xlim',[1,max(xax)]);

% COMPUTATION OF THE NOISE
noise= std(vi.meas - vh.meas) ...
       / 10^(25/20) * randn(size(vh.meas));

vi.meas= vi.meas + noise;
```

```
IMDL_3D.fwd_model= fmdl;
%%% COMPARISON OF ALGORITHM HERE

%%% NICK POLIDORISES SOLVER ALGORITHM   %%%%%
inv3d= eidors_obj('inv_model', 'EIT inverse');
inv3d.reconst_type= 'difference';
inv3d.jacobian_bkgnd.value = 1;
inv3d.fwd_model= fmdl;
inv3d.fwd_model.np_fwd_solve.perm_sym= '{y}';
% Nick Polydorides' Gauss-Newton Solver
inv3d.hyperparameter.value = 1e-3;
inv3d.solve=       @np_inv_solve;
% Nick Polydorides' Prior (Laplace) &&&###(produced a much better result)###&&&
inv3d.R_prior=     @np_calc_image_prior;
inv3d.np_calc_image_prior.parameters= [3 1];
inv3d.parameters.max_iterations= 1;

%%%%%% &&&&&(((CHANGE OF VARIABLE HERE))))&&&&&
% Tikhonov prior
%inv3d.R_prior=@tikhonov_image_prior;

%%%%% TIME PRIOR SOLVER ALGORITHM
inv= eidors_obj('inv_model', 'EIT inverse');%EIDORS common_model_c3cr');
inv.reconst_type= 'difference';
inv.jacobian_bkgnd.value = 1;
inv.fwd_model= fmdl;
%inv.fwd_model.np_fwd_solve.perm_sym= '{y}';
inv.hyperparameter.value = 0.0300;%1e-3;
inv.solve= @time_prior_solve  ;
inv.time_smooth_prior.space_prior= @noser_image_prior;
inv.time_smooth_prior.time_weight=0;
inv.time_prior_solve.time_steps= 0;
```

```
%%%%
img= inv_solve(inv3d, vh, vi); % or use (inv) same as IMDL_3D
ax(6) =subplot(2,3,6,'replace');
%show_3d_slices(img, z-axiz, y-axiz,x-axiz)
%show_3d_slices(img, 0.45,[],[]);
%show_3d_slices(img, [1,1.9], [0.5],[0.5]);
%view(-14,13); axis tight; axis equal; zlim([0,1.5]);
hold on;
% parallel to y-axis
ax(5) =subplot(2,3,3,'replace');
show_fem(img)
hold on;
ax(3) =subplot(2,3,4,'replace');
show_fem(img)
hold on;
%show_3d_slices(img, [],[0.0],[]);
%show_3d_slices(img, [1,1.9], [0.5],[0.5]);
%view(-14,13); axis tight; axis equal; zlim([0,1.5]);
ax(1) =subplot(2,3,1,'replace');
show_fem(img)
hold on;
ax(4) =subplot(2,3,2,'replace');
rgb = imread('C:/users/bode/desktop/bode/IMG_1329.jpg');
image(rgb);
title('Top View of Suspended Phantom at 0.8dm on y-axis')
%parallel to x-axis
%show_3d_slices(img, [],[],[0.0]);
%view(-14,13); axis tight; axis equal; zlim([0,1.5]);
hold on;
ax(2) = subplot(2,3,5,'replace');
rgb = imread('C:/users/bode/desktop/bode/IMG_1335.jpg');
image(rgb);
title('Front view of Phantom Suspended at 0.4dm on y-axis')
axis(ax,'image')
% Lowest limit
dadada=img.elem_data;
l_lim=min(dadada);%-0.6300;
% highest element values
high_value_elem_data=max(dadada);%0.2770;
%lowest element values
low_value_elem_data=min(dadada);%-0.6300;
% step change
delt=(high_value_elem_data-low_value_elem_data)/20;
[sav]=Sorting_elemindex(dadada);
[imgggc]=Sorting_resistivity(dadada);
colour_map=[];
sav_new=[];
for uu=1:max(size(imgggc(:,1)));
    gad=(imgggc(uu)-l_lim)/delt;
    colour_map=[colour_map;gad*10,imgggc(uu)];
    sav_new=[sav_new;sav(uu)];
    if colour_map(uu,1)>40
        break
    end
end
% SUMMATION OF VOLUME OF TETRAHEDRAL OF HIGHER RESISTIVITY VALUES

VVVOLUME=[];add_volume=0;sel_elem=[];sel_region=[];mass_phant=[];
% SAV denotes indexes of the elements
for m=1:max(size(sav_new(:,1)));
 %aa1,bb1,cc1,dd1 are nodal points of an element.
elem_index=sav_new(m);
aa1=fmdl.elems(elem_index,1);
%b-1097(0.8744,0.1186,2.0), 1960
bb1=fmdl.elems(elem_index,2);
%c-436(1.0995,0.0328,2.0), 348
cc1=fmdl.elems(elem_index,3);
```

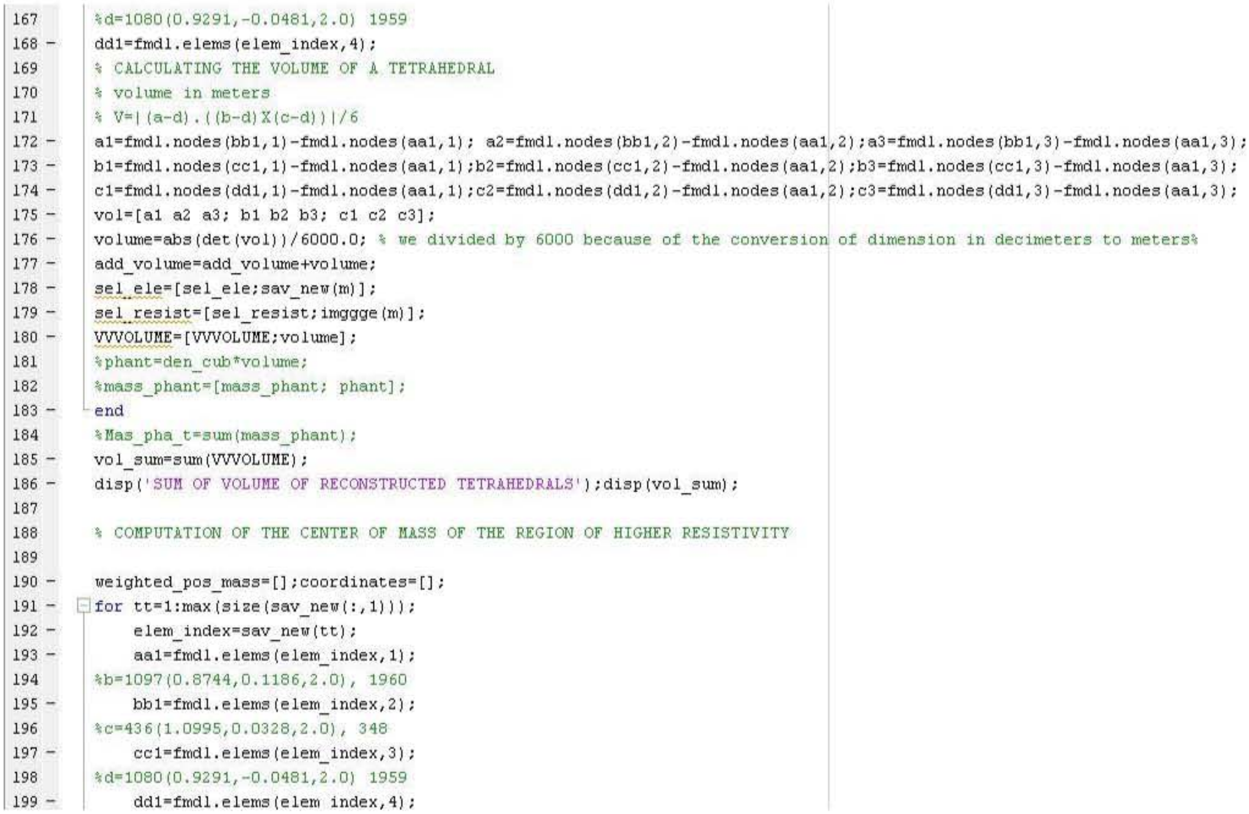

```
%d=1080(0.9291,-0.0481,2.0) 1959
dd1=fmdl.elems(elem_index,4);
% CALCULATING THE VOLUME OF A TETRAHEDRAL
% volume in meters
% V=|(a-d).((b-d)X(c-d))|/6
a1=fmdl.nodes(bb1,1)-fmdl.nodes(aa1,1); a2=fmdl.nodes(bb1,2)-fmdl.nodes(aa1,2);a3=fmdl.nodes(bb1,3)-fmdl.nodes(aa1,3);
b1=fmdl.nodes(cc1,1)-fmdl.nodes(aa1,1);b2=fmdl.nodes(cc1,2)-fmdl.nodes(aa1,2);b3=fmdl.nodes(cc1,3)-fmdl.nodes(aa1,3);
c1=fmdl.nodes(dd1,1)-fmdl.nodes(aa1,1);c2=fmdl.nodes(dd1,2)-fmdl.nodes(aa1,2);c3=fmdl.nodes(dd1,3)-fmdl.nodes(aa1,3);
vol=[a1 a2 a3; b1 b2 b3; c1 c2 c3];
volume=abs(det(vol))/6000.0; % we divided by 6000 because of the conversion of dimension in decimeters to meters%
add_volume=add_volume+volume;
sel_ele=[sel_ele;sav_new(m)];
sel_resist=[sel_resist;imggge(m)];
VVVOLUME=[VVVOLUME;volume];
%phant=den_cub*volume;
%mass_phant=[mass_phant; phant];
end
%Mas_pha_t=sum(mass_phant);
vol_sum=sum(VVVOLUME);
disp('SUM OF VOLUME OF RECONSTRUCTED TETRAHEDRALS');disp(vol_sum);

% COMPUTATION OF THE CENTER OF MASS OF THE REGION OF HIGHER RESISTIVITY

weighted_pos_mass=[];coordinates=[];
for tt=1:max(size(sav_new(:,1)));
    elem_index=sav_new(tt);
    aa1=fmdl.elems(elem_index,1);
%b=1097(0.8744,0.1186,2.0), 1960
    bb1=fmdl.elems(elem_index,2);
%c=436(1.0995,0.0328,2.0), 348
    cc1=fmdl.elems(elem_index,3);
%d=1080(0.9291,-0.0481,2.0) 1959
    dd1=fmdl.elems(elem_index,4);
```

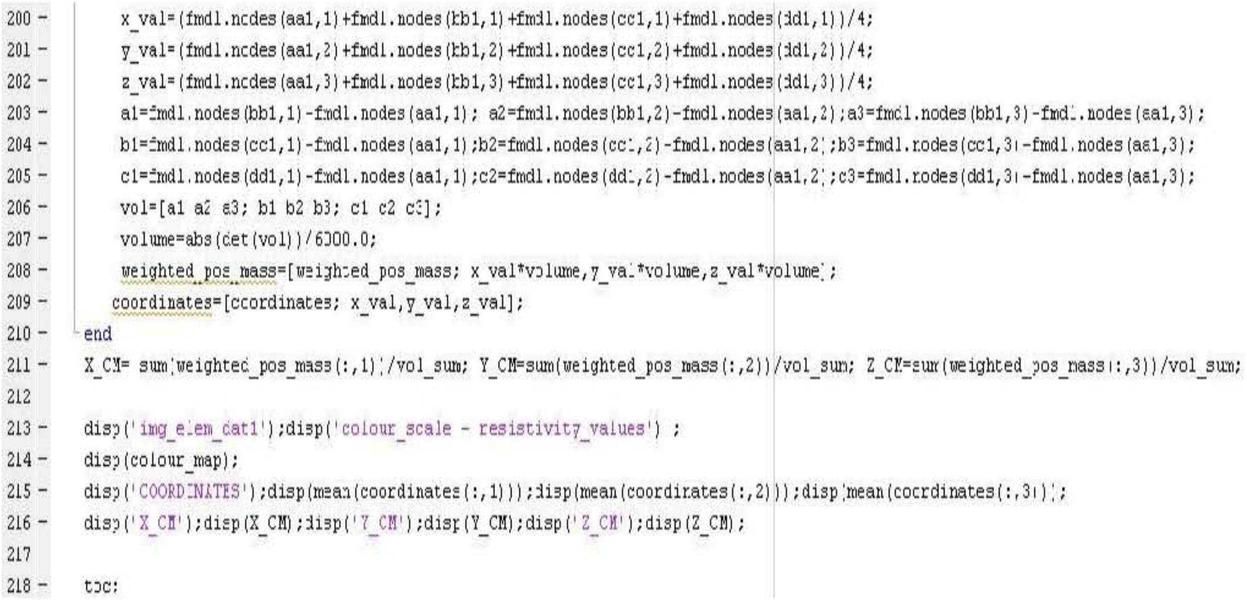

```
    x_val=(fmdl.nodes(aa1,1)+fmdl.nodes(bb1,1)+fmdl.nodes(cc1,1)+fmdl.nodes(dd1,1))/4;
    y_val=(fmdl.nodes(aa1,2)+fmdl.nodes(bb1,2)+fmdl.nodes(cc1,2)+fmdl.nodes(dd1,2))/4;
    z_val=(fmdl.nodes(aa1,3)+fmdl.nodes(bb1,3)+fmdl.nodes(cc1,3)+fmdl.nodes(dd1,3))/4;
    a1=fmdl.nodes(bb1,1)-fmdl.nodes(aa1,1); a2=fmdl.nodes(bb1,2)-fmdl.nodes(aa1,2);a3=fmdl.nodes(bb1,3)-fmdl.nodes(aa1,3);
    b1=fmdl.nodes(cc1,1)-fmdl.nodes(aa1,1);b2=fmdl.nodes(cc1,2)-fmdl.nodes(aa1,2);b3=fmdl.nodes(cc1,3)-fmdl.nodes(aa1,3);
    c1=fmdl.nodes(dd1,1)-fmdl.nodes(aa1,1);c2=fmdl.nodes(dd1,2)-fmdl.nodes(aa1,2);c3=fmdl.nodes(dd1,3)-fmdl.nodes(aa1,3);
    vol=[a1 a2 a3; b1 b2 b3; c1 c2 c3];
    volume=abs(det(vol))/6000.0;
    weighted_pos_mass=[weighted_pos_mass; x_val*volume,y_val*volume,z_val*volume];
   coordinates=[coordinates; x_val,y_val,z_val];
end
X_CM= sum(weighted_pos_mass(:,1))/vol_sum; Y_CM=sum(weighted_pos_mass(:,2))/vol_sum; Z_CM=sum(weighted_pos_mass(:,3))/vol_sum;

disp('img_elem_cat1');disp('colour_scale - resistivity_values') ;
disp(colour_map);
disp('COORDINATES');disp(mean(coordinates(:,1)));disp(mean(coordinates(:,2)));disp(mean(coordinates(:,3)));
disp('X_CM');disp(X_CM);disp('Y_CM');disp(Y_CM);disp('Z_CM');disp(Z_CM);

toc;
```

B4 : Reconstruction Code for A sequence of Current Stimulation through Opposite Electrode Pairs and A Sequence of Voltage Measurement through Adjacent Electrode Pairs in a Three Rings of Electrode System

```
 tic;
 IMDL_3D=mk_common_model('c3cr',[16,3]);
  nelec= 16; nrings= 3;
 ring_vert_pos =[0.3,0.7,1.05]; %[1.0,1.4,1.75,2.1]% [0.3,0.7,1.05]
 extra={'ball','solid ball = sphere(-0.15,-0.1,0.5;0.1);'};
 [fmdl]=ng_mk_cyl_models([1.1,1.1],[nelec,ring_vert_pos],[0.1,0.2]);

 stim = mk_stim_patterns(16,3,[0,nelec/2],[0,1],{'no_meas_current','do_redundant'},2.0); %[0, nelec/2][0,1]
 fmdl.stimulation = stim;
 %%% COMPARISON OF ALGORITHM FOR FORWARD COMPUTATION
 %%% USING NICK POLIDORIDES FORWARD SOLVER
 fmdl.stimulation=stim;
 fmdl.solve= 'np_fwd_solve';
 fmdl.system_mat='np_calc_system_mat';
 fmdl.jacobian='np_calc_jacobian';
 fmdl.type='fwd_model';
 fmdl.np_fwd_solve.perm_sym='{n}';
 mat= ones( size(fmdl.elems,1) ,1);
 sim_img= eidors_obj('image', 'homogeneous image', ...
                     'elem_data', mat, ...
                     'fwd_model', fmdl );

 % Simulate homogeneous measurements
 sim_img.fwd_model= fmdl;
 sim_img.fwd_solve.get_all_meas = 1;

 % Simulate homogeneous measurements
 sim_img.fwd_model= fmdl;
 show_fem(sim_img);
 sim_img.elem_data(mat) = 1; % Homogenous

 vh = fwd_solve(fmdl,sim_img);

[INhomodata]=meas_3rginhomo('C:\Users\bode\Desktop\NOV_19TH_3OPP\pvc_19cm.tomo');
[currentdata]=getcalibrationdata3rings_opp_currrent('C:\Users\bode\Desktop\NOV_19TH_3OPP\homo_with_current.tomo');
[nocurrentdata]=getcalibrationdata3rings_opp_nocurrent('C:\Users\bode\Desktop\NOV_19TH_3OPP\homo_no_current.tomo');
% OFFSET (nocurrentdata) IS SUBSTRACTED FROM THE CURRENT DATA (currentdata):HOMOGENEOUS SOLUTION
%MEASURED DATA FOR HOMOGENEOUS
Meas_HOMOdata=currentdata-nocurrentdata;
% OBTAINING THE SCALING CONSTANT FOR EACH HOMOGENEOUS SOLUTION
%%% Div is the scaling constant
JohnF= vh.meas;
% where JohnF is the modelled homogeneous data needed.
%Scaling factor is Homo_Fwd_mdel/Homo_measured_data
Sca_Fac=JohnF./Meas_HOMOdata;
%MEASURED DATA FOR INHOMOGENEOUS
% offset is deducted from the INhomodata
Meas_INHOMOdata=INhomodata-nocurrentdata;
%calibrated data for inhomogeous is
Calib_Inhomo=Meas_INHOMOdata.*Sca_Fac;

sim_img.elem_data(mat) = 0.95; %Non-conductive inclusion
vi = fwd_solve(fmdl,sim_img);
vi.meas=Calib_Inhomo;

clf; %>>>>>>>>>>>>>>>>>>>><<<<<<<<<<<<<<<<<<<<<<<
%ax(5)=subplot(2,3,1,'replace');
%xax= 1:max(size(vh.meas));
%hh= plotyy(xax,[vh.meas, vi.meas], ...
%            xax, vh.meas - vi.meas );
%set(hh,'Xlim',[1,max(xax)]);

% COMPUTATION OF THE NOISE
noise= std(vi.meas - vh.meas) ...
       / 10^(25/20) * randn(size(vh.meas));

```

```
vi.meas= vi.meas + noise;

IMDL_3D.fwd_model= fmdl;
%%% COMPARISON OF ALGORITHM HERE
%%% NICK POLIDORISES SOLVER ALGORITHM   %%%%%
inv3d= eidors_obj('inv_model', 'EIT inverse');
inv3d.reconst_type= 'difference';
inv3d.jacobian_bkgnd.value = 1;
inv3d.fwd_model= fmdl;
inv3d.fwd_model.np_fwd_solve.perm_sym= '{y}';
% Nick Polydorides' Gauss-Newton Solver
inv3d.hyperparameter.value = 1e-3;
inv3d.solve=       @np_inv_solve;

% Nick Polydorides' Prior (Laplace) &&&###(produced a much better result)###&&&
inv3d.R_prior=     @np_calc_image_prior;
inv3d.np_calc_image_prior.parameters= [3 1];
inv3d.parameters.max_iterations= 1;

%%%%%% &&&&&(((CHANGE OF VARIABLE HERE)))&&&&&
% Tikhonov prior
%inv3d.R_prior=@tikhonov_image_prior;

%%%%%
%%%%% TIME PRIOR SOLVER ALGORITHM
inv= eidors_obj('inv_model', 'EIT inverse');%EIDORS common_model_c3cr');
inv.reconst_type= 'difference';
inv.jacobian_bkgnd.value = 1;
inv.fwd_model= fmdl;
%inv.fwd_model.np_fwd_solve.perm_sym= '{y}';
inv.hyperparameter.value = 0.0300;%1e-3;
inv.solve= @time_prior_solve  ;
inv.time_smooth_prior.space_prior= @noser_image_prior;
inv.time_smooth_prior.time_weight=0;
```

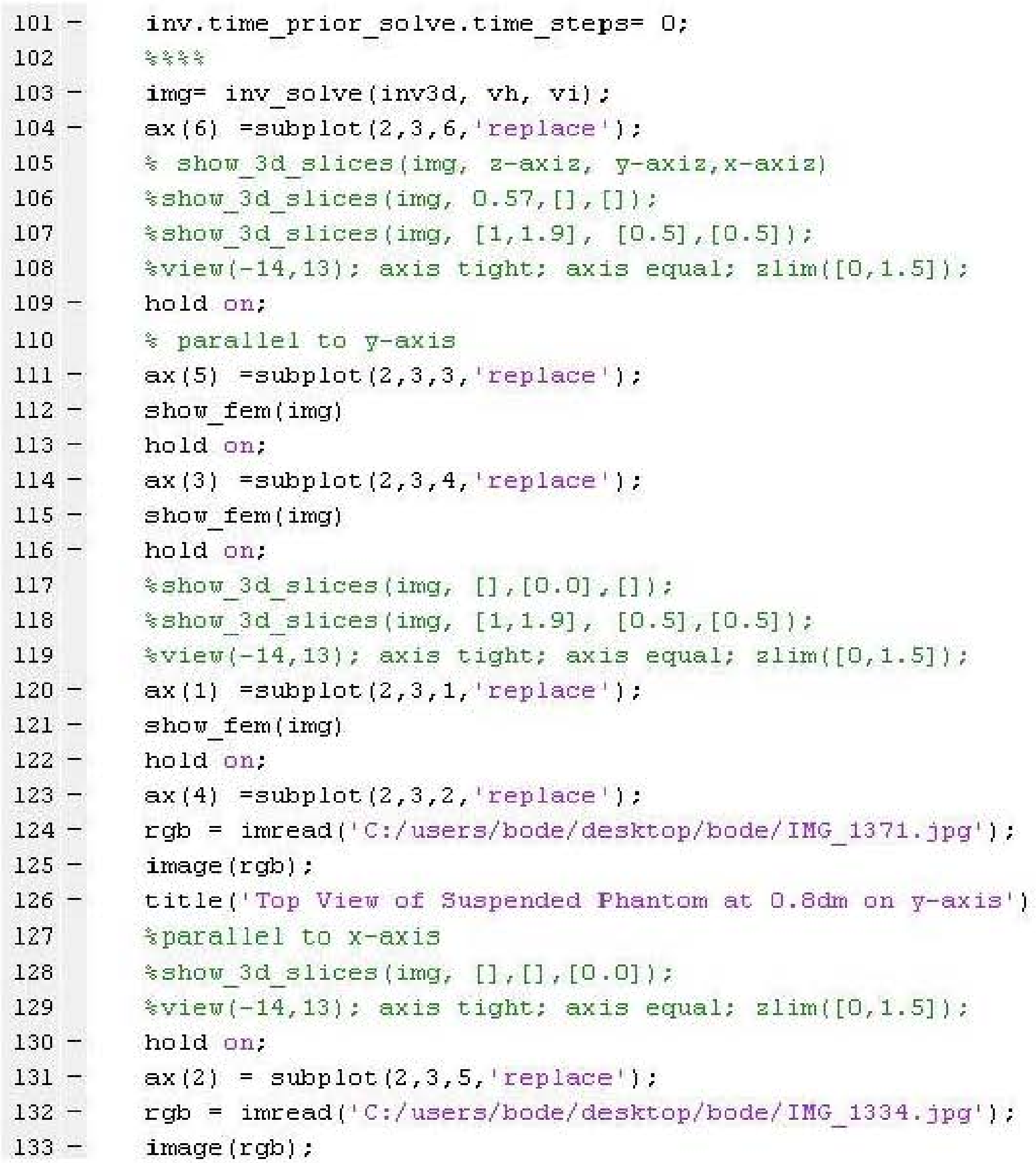

```
inv.time_prior_solve.time_steps= 0;
%%%%
img= inv_solve(inv3d, vh, vi);
ax(6) =subplot(2,3,6,'replace');
% show_3d_slices(img, z-axiz, y-axiz,x-axiz)
%show_3d_slices(img, 0.57,[],[]);
%show_3d_slices(img, [1,1.9], [0.5],[0.5]);
%view(-14,13); axis tight; axis equal; zlim([0,1.5]);
hold on;
% parallel to y-axis
ax(5) =subplot(2,3,3,'replace');
show_fem(img)
hold on;
ax(3) =subplot(2,3,4,'replace');
show_fem(img)
hold on;
%show_3d_slices(img, [],[0.0],[]);
%show_3d_slices(img, [1,1.9], [0.5],[0.5]);
%view(-14,13); axis tight; axis equal; zlim([0,1.5]);
ax(1) =subplot(2,3,1,'replace');
show_fem(img)
hold on;
ax(4) =subplot(2,3,2,'replace');
rgb = imread('C:/users/bode/desktop/bode/IMG_1371.jpg');
image(rgb);
title('Top View of Suspended Phantom at 0.8dm on y-axis')
%parallel to x-axis
%show_3d_slices(img, [],[],[0.0]);
%view(-14,13); axis tight; axis equal; zlim([0,1.5]);
hold on;
ax(2) = subplot(2,3,5,'replace');
rgb = imread('C:/users/bode/desktop/bode/IMG_1334.jpg');
image(rgb);
```

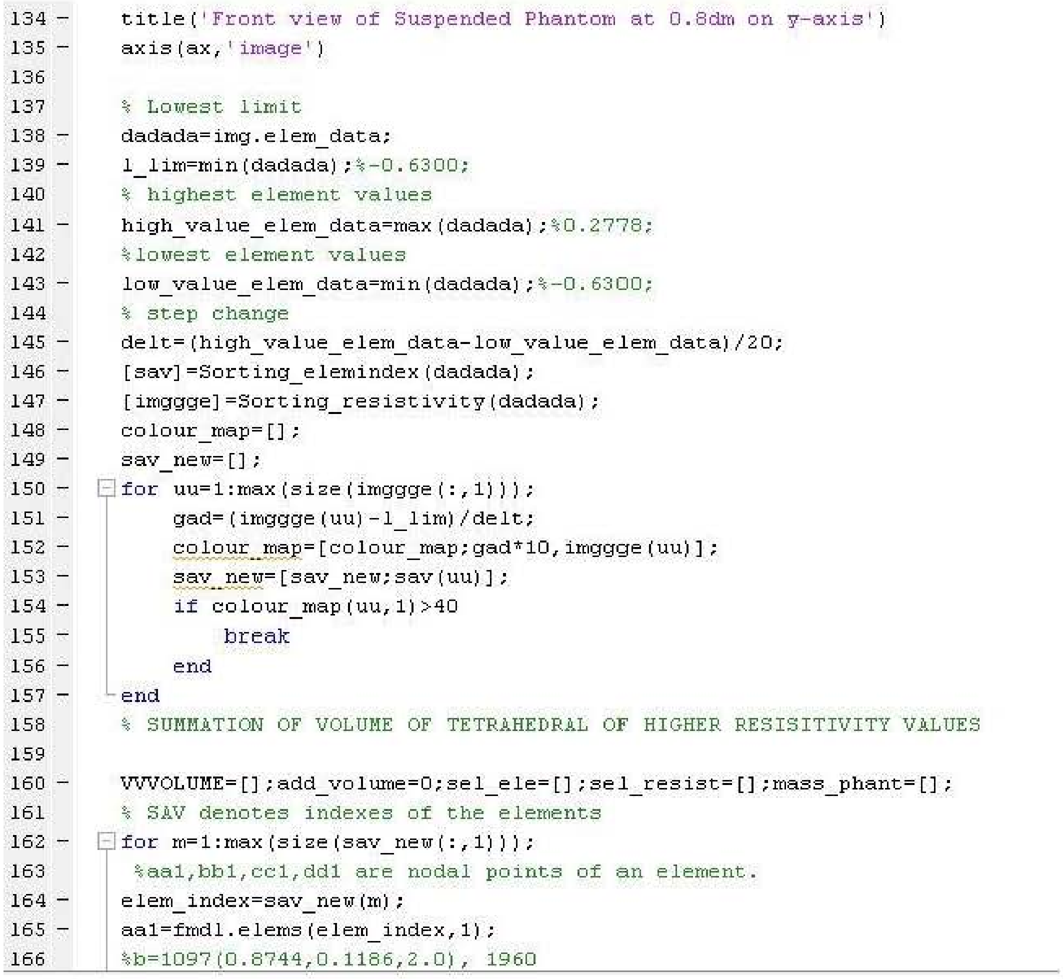

```
title('Front view of Suspended Phantom at 0.8dm on y-axis')
axis(ax,'image')

% Lowest limit
dadada=img.elem_data;
l_lim=min(dadada);%-0.6300;
% highest element values
high_value_elem_data=max(dadada);%0.2778;
%lowest element values
low_value_elem_data=min(dadada);%-0.6300;
% step change
delt=(high_value_elem_data-low_value_elem_data)/20;
[sav]=Sorting_elemindex(dadada);
[imggge]=Sorting_resistivity(dadada);
colour_map=[];
sav_new=[];
for uu=1:max(size(imggge(:,1)));
    gad=(imggge(uu)-l_lim)/delt;
    colour_map=[colour_map;gad*10,imggge(uu)];
    sav_new=[sav_new;sav(uu)];
    if colour_map(uu,1)>40
        break
    end
end
% SUMMATION OF VOLUME OF TETRAHEDRAL OF HIGHER RESISITIVITY VALUES

VVVOLUME=[];add_volume=0;sel_ele=[];sel_resist=[];mass_phant=[];
% SAV denotes indexes of the elements
for m=1:max(size(sav_new(:,1)));
 %aa1,bb1,cc1,dd1 are nodal points of an element.
elem_index=sav_new(m);
aa1=fmdl.elems(elem_index,1);
%b=1097(0.8744,0.1186,2.0), 1960
```

```
    bb1=fmdl.elems(elem_index,2);
    %c=436(1.0995,0.0328,2.0), 348
    cc1=fmdl.elems(elem_index,3);
    %d=1080(0.9291,-0.0481,2.0) 1959
    dd1=fmdl.elems(elem_index,4);
    % CALCULATING THE VOLUME OF A TETRAHEDRAL
    % volume in meters
    % V=|(a-d).((b-d)X(c-d))|/6
    a1=fmdl.nodes(bb1,1)-fmdl.nodes(aa1,1); a2=fmdl.nodes(bb1,2)-fmdl.nodes(aa1,2);a3=fmdl.nodes(bb1,3)-fmdl.nodes(aa1,3);
    b1=fmdl.nodes(cc1,1)-fmdl.nodes(aa1,1);b2=fmdl.nodes(cc1,2)-fmdl.nodes(aa1,2);b3=fmdl.nodes(cc1,3)-fmdl.nodes(aa1,3);
    c1=fmdl.nodes(dd1,1)-fmdl.nodes(aa1,1);c2=fmdl.nodes(dd1,2)-fmdl.nodes(aa1,2);c3=fmdl.nodes(dd1,3)-fmdl.nodes(aa1,3);
    vol=[a1 a2 a3; b1 b2 b3; c1 c2 c3];
    volume=abs(det(vol))/6000.0; % we divided by 6000 because of the conversion of dimension in decimeters to meters%
    add_volume=add_volume+volume;
    sel_ele=[sel_ele;sav_new(m)];
    sel_resist=[sel_resist;imggge(m)];
    VVVOLUME=[VVVOLUME;volume];
    %phant=den_cub*volume;
    %mass_phant=[mass_phant; phant];
end
%Mas_pha_t=sum(mass_phant);
vol_sum=sum(VVVOLUME);
disp('SUM OF VOLUME OF RECONSTRUCTED TETRAHEDRALS');disp(vol_sum);

% COMPUTATION OF THE CENTER OF MASS OF THE REGION OF HIGHER RESISTIVITY

weighted_pos_mass=[];coordinates=[];
for tt=1:max(size(sav_new(:,1)));
    elem_index=sav_new(tt);
    aa1=fmdl.elems(elem_index,1);
%b=1097(0.8744,0.1186,2.0), 1960
    bb1=fmdl.elems(elem_index,2);
%c=436(1.0995,0.0328,2.0), 348
    cc1=fmdl.elems(elem_index,3);
%d=1080(0.9291,-0.0481,2.0) 1959
    dd1=fmdl.elems(elem_index,4);
    x_val=(fmdl.nodes(aa1,1)+fmdl.nodes(bb1,1)+fmdl.nodes(cc1,1)+fmdl.nodes(dd1,1))/4;
    y_val=(fmdl.nodes(aa1,2)+fmdl.nodes(bb1,2)+fmdl.nodes(cc1,2)+fmdl.nodes(dd1,2))/4;
    z_val=(fmdl.nodes(aa1,3)+fmdl.nodes(bb1,3)+fmdl.nodes(cc1,3)+fmdl.nodes(dd1,3))/4;
    a1=fmdl.nodes(bb1,1)-fmdl.nodes(aa1,1); a2=fmdl.nodes(bb1,2)-fmdl.nodes(aa1,2);a3=fmdl.nodes(bb1,3)-fmdl.nodes(aa1,3);
    b1=fmdl.nodes(cc1,1)-fmdl.nodes(aa1,1);b2=fmdl.nodes(cc1,2)-fmdl.nodes(aa1,2);b3=fmdl.nodes(cc1,3)-fmdl.nodes(aa1,3);
    c1=fmdl.nodes(dd1,1)-fmdl.nodes(aa1,1);c2=fmdl.nodes(dd1,2)-fmdl.nodes(aa1,2);c3=fmdl.nodes(dd1,3)-fmdl.nodes(aa1,3);
    vol=[a1 a2 a3; b1 b2 b3; c1 c2 c3];
    volume=abs(det(vol))/6000.0;
    weighted_pos_mass=[weighted_pos_mass; x_val*volume,y_val*volume,z_val*volume];
   coordinates=[coordinates; x_val,y_val,z_val];
end
X_CM= sum(weighted_pos_mass(:,1))/vol_sum; Y_CM=sum(weighted_pos_mass(:,2))/vol_sum; Z_CM=sum(weighted_pos_mass(:,3))/vol_sum;

disp('img_elem_dat1');disp('colour_scale - resistivity_values') ;
disp(colour_map);
disp('COORDINATES');disp(mean(coordinates(:,1)));disp(mean(coordinates(:,2)));disp(mean(coordinates(:,3)));
disp('X_CM');disp(X_CM);disp('Y_CM');disp(Y_CM);disp('Z_CM');disp(Z_CM);


toc;
```

B5 : Reconstruction Code for A sequence of Current Stimulation through Adjacent Electrode Pairs and A Sequence of Voltage Measurement through Adjacent Electrode Pairs in a Four Rings of Electrode System

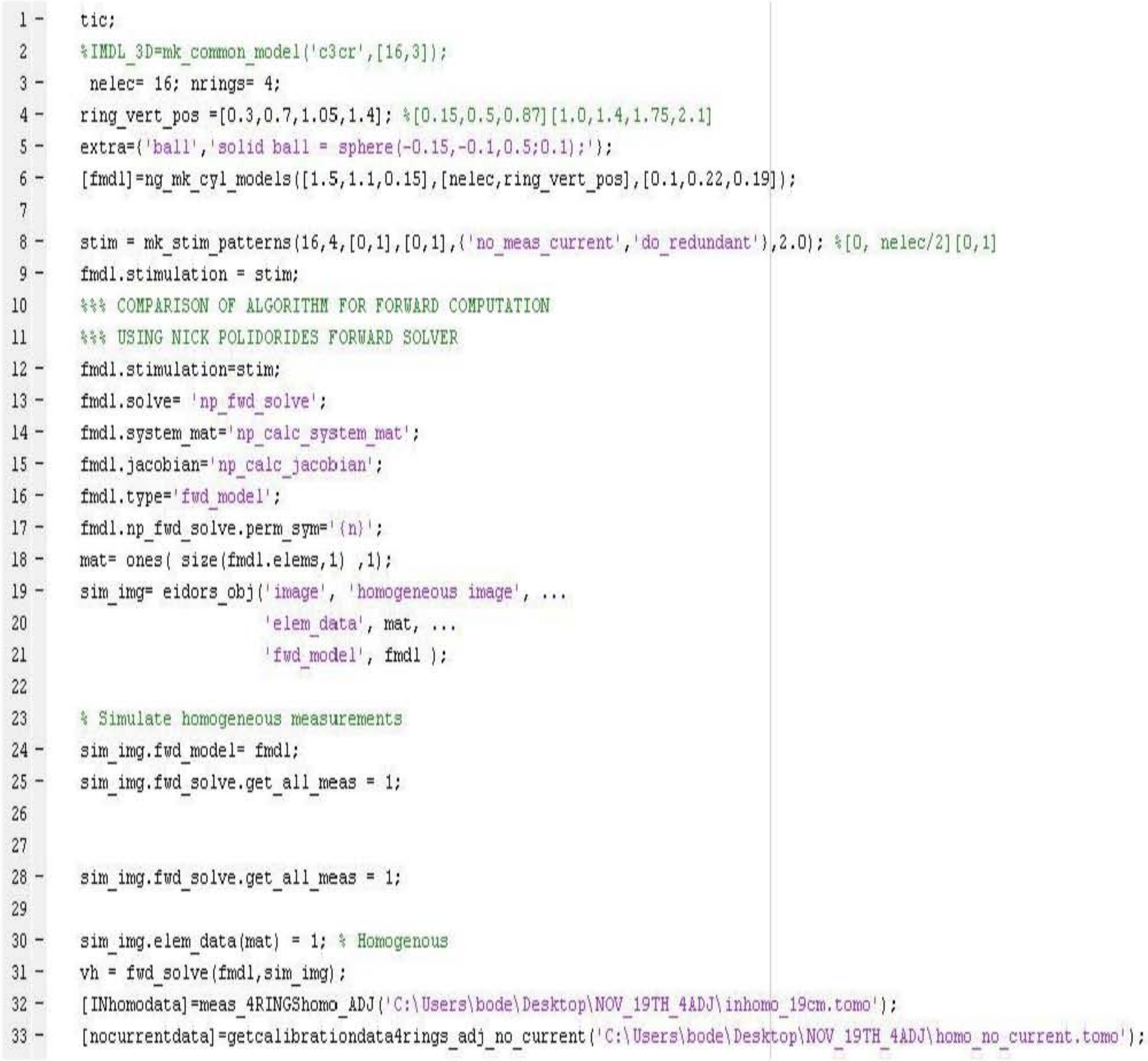

```
tic;
%IMDL_3D=mk_common_model('c3cr',[16,3]);
 nelec= 16; nrings= 4;
ring_vert_pos =[0.3,0.7,1.05,1.4]; %[0.15,0.5,0.87][1.0,1.4,1.75,2.1]
extra={'ball','solid ball = sphere(-0.15,-0.1,0.5;0.1);'};
[fmdl]=ng_mk_cyl_models([1.5,1.1,0.15],[nelec,ring_vert_pos],[0.1,0.22,0.19]);

stim = mk_stim_patterns(16,4,[0,1],[0,1],{'no_meas_current','do_redundant'},2.0); %[0, nelec/2][0,1]
fmdl.stimulation = stim;
%%% COMPARISON OF ALGORITHM FOR FORWARD COMPUTATION
%%% USING NICK POLIDORIDES FORWARD SOLVER
fmdl.stimulation=stim;
fmdl.solve= 'np_fwd_solve';
fmdl.system_mat='np_calc_system_mat';
fmdl.jacobian='np_calc_jacobian';
fmdl.type='fwd_model';
fmdl.np_fwd_solve.perm_sym='{n}';
mat= ones( size(fmdl.elems,1) ,1);
sim_img= eidors_obj('image', 'homogeneous image', ...
                    'elem_data', mat, ...
                    'fwd_model', fmdl );

% Simulate homogeneous measurements
sim_img.fwd_model= fmdl;
sim_img.fwd_solve.get_all_meas = 1;


sim_img.fwd_solve.get_all_meas = 1;

sim_img.elem_data(mat) = 1; % Homogenous
vh = fwd_solve(fmdl,sim_img);
[INhomodata]=meas_4RINGShomo_ADJ('C:\Users\bode\Desktop\NOV_19TH_4ADJ\inhomo_19cm.tomo');
[nocurrentdata]=getcalibrationdata4rings_adj_no_current('C:\Users\bode\Desktop\NOV_19TH_4ADJ\homo_no_current.tomo');
```

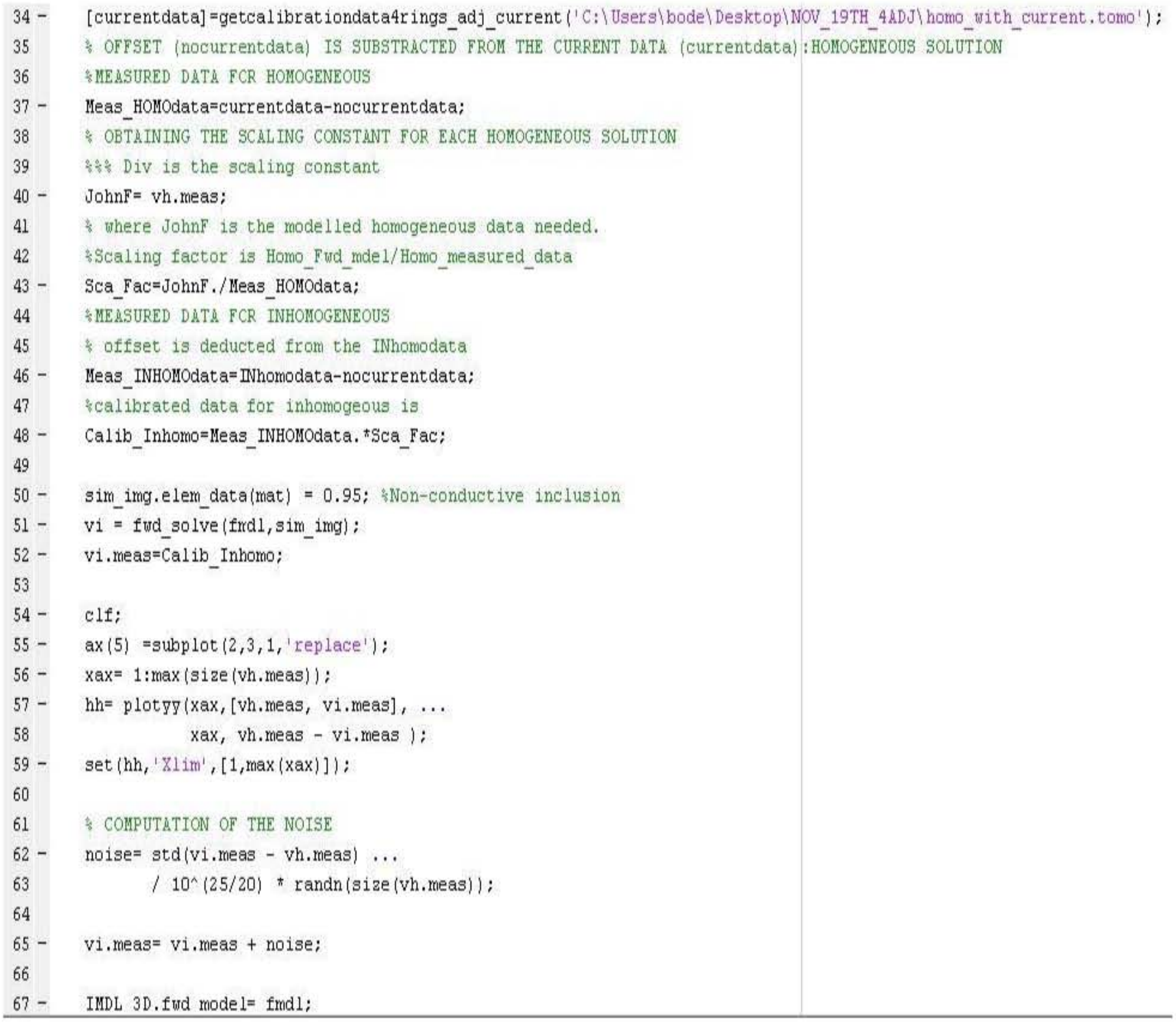

```
[currentdata]=getcalibrationdata4rings_adj_current('C:\Users\bode\Desktop\NOV_19TH_4ADJ\homo_with_current.tomo');
% OFFSET (nocurrentdata) IS SUBSTRACTED FROM THE CURRENT DATA (currentdata):HOMOGENEOUS SOLUTION
%MEASURED DATA FCR HOMOGENEOUS
Meas_HOMOdata=currentdata-nocurrentdata;
% OBTAINING THE SCALING CONSTANT FOR EACH HOMOGENEOUS SOLUTION
%%% Div is the scaling constant
JohnF= vh.meas;
% where JohnF is the modelled homogeneous data needed.
%Scaling factor is Homo_Fwd_mdel/Homo_measured_data
Sca_Fac=JohnF./Meas_HOMOdata;
%MEASURED DATA FCR INHOMOGENEOUS
% offset is deducted from the INhomodata
Meas_INHOMOdata=INhomodata-nocurrentdata;
%calibrated data for inhomogeous is
Calib_Inhomo=Meas_INHOMOdata.*Sca_Fac;

sim_img.elem_data(mat) = 0.95; %Non-conductive inclusion
vi = fwd_solve(fmdl,sim_img);
vi.meas=Calib_Inhomo;

clf;
ax(5) =subplot(2,3,1,'replace');
xax= 1:max(size(vh.meas));
hh= plotyy(xax,[vh.meas, vi.meas], ...
           xax, vh.meas - vi.meas );
set(hh,'Xlim',[1,max(xax)]);

% COMPUTATION OF THE NOISE
noise= std(vi.meas - vh.meas) ...
      / 10^(25/20) * randn(size(vh.meas));

vi.meas= vi.meas + noise;

IMDL 3D.fwd model= fmdl;
```

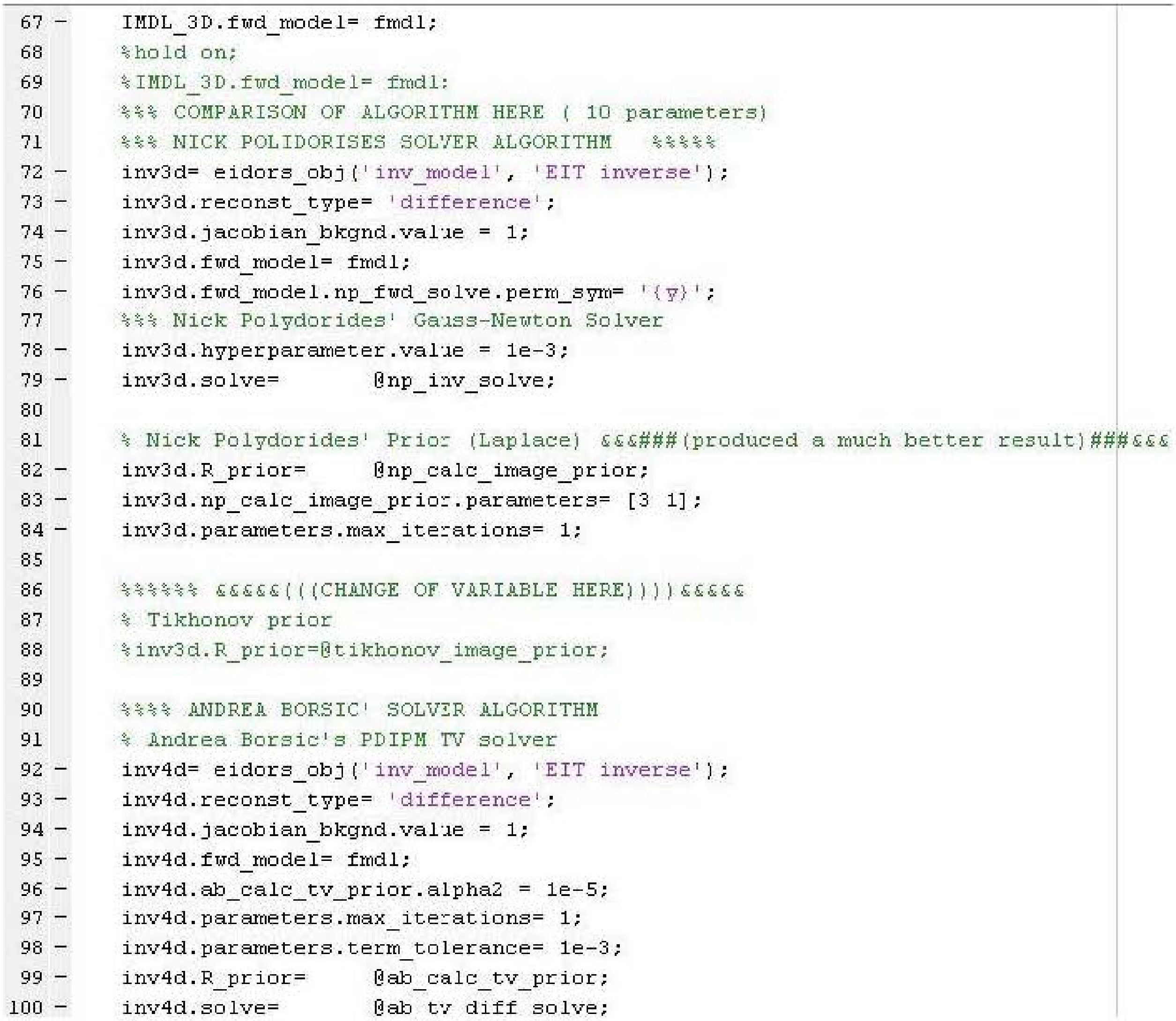

```
IMDL_3D.fwd_model= fmdl;
%hold on;
%IMDL_3D.fwd_model= fmdl:
%%% COMPARISON OF ALGORITHM HERE ( 10 parameters)
%%% NICK POLIDORISES SOLVER ALGORITHM   %%%%%
inv3d= eidors_obj('inv_model', 'EIT inverse');
inv3d.reconst_type= 'difference';
inv3d.jacobian_bkgnd.value = 1;
inv3d.fwd_model= fmdl;
inv3d.fwd_model.np_fwd_solve.perm_sym= '{y}';
%%% Nick Polydorides' Gauss-Newton Solver
inv3d.hyperparameter.value = 1e-3;
inv3d.solve=       @np_inv_solve;

% Nick Polydorides' Prior (Laplace) &&&###(produced a much better result)###&&&
inv3d.R_prior=     @np_calc_image_prior;
inv3d.np_calc_image_prior.parameters= [3 1];
inv3d.parameters.max_iterations= 1;

%%%%%% &&&&&(((CHANGE OF VARIABLE HERE)))&&&&&
% Tikhonov prior
%inv3d.R_prior=@tikhonov_image_prior;

%%%% ANDREA BORSIC' SOLVER ALGORITHM
% Andrea Borsic's PDIPM TV solver
inv4d= eidors_obj('inv_model', 'EIT inverse');
inv4d.reconst_type= 'difference';
inv4d.jacobian_bkgnd.value = 1;
inv4d.fwd_model= fmdl;
inv4d.ab_calc_tv_prior.alpha2 = 1e-5;
inv4d.parameters.max_iterations= 1;
inv4d.parameters.term_tolerance= 1e-3;
inv4d.R_prior=     @ab_calc_tv_prior;
inv4d.solve=       @ab_tv_diff_solve;
```

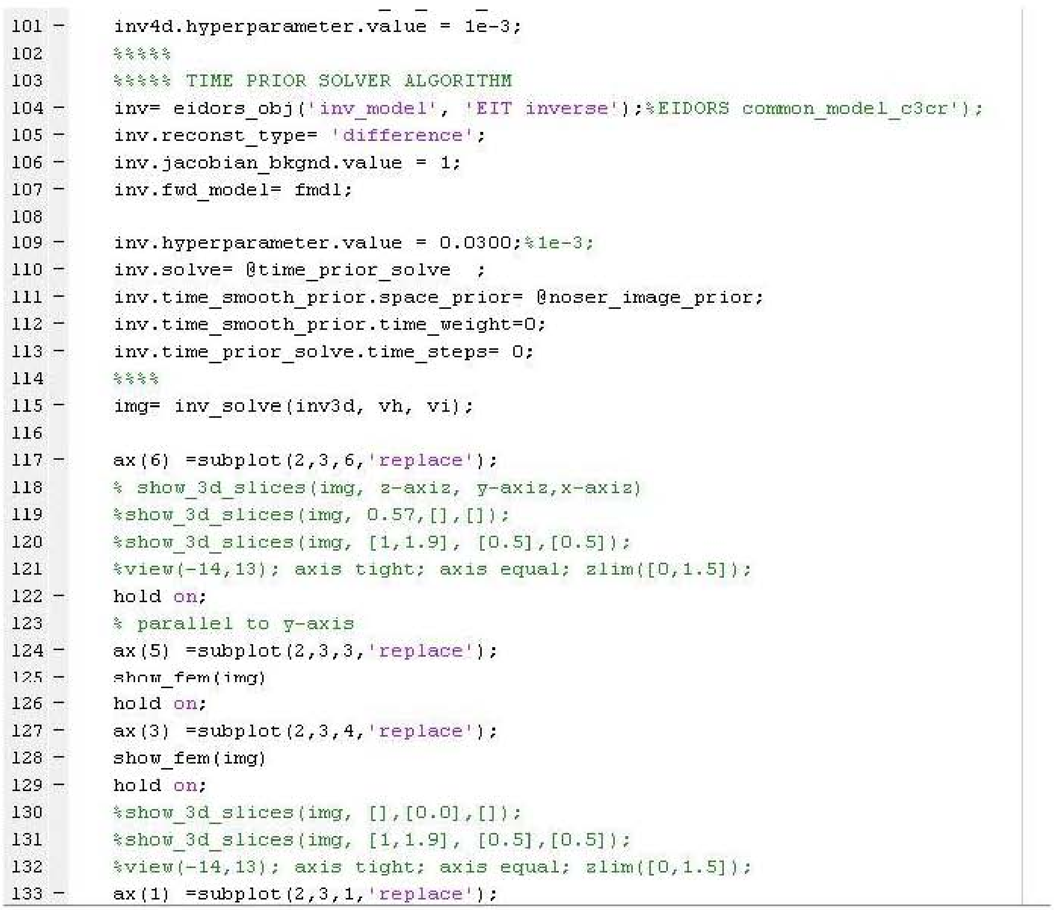

```
inv4d.hyperparameter.value = 1e-3;
%%%%%
%%%%% TIME PRIOR SOLVER ALGORITHM
inv= eidors_obj('inv_model', 'EIT inverse');%EIDORS common_model_c3cr');
inv.reconst_type= 'difference';
inv.jacobian_bkgnd.value = 1;
inv.fwd_model= fmdl;

inv.hyperparameter.value = 0.0300;%1e-3;
inv.solve= @time_prior_solve  ;
inv.time_smooth_prior.space_prior= @noser_image_prior;
inv.time_smooth_prior.time_weight=0;
inv.time_prior_solve.time_steps= 0;
%%%%
img= inv_solve(inv3d, vh, vi);

ax(6) =subplot(2,3,6,'replace');
% show_3d_slices(img, z-axiz, y-axiz,x-axiz)
%show_3d_slices(img, 0.57,[],[]);
%show_3d_slices(img, [1,1.9], [0.5],[0.5]);
%view(-14,13); axis tight; axis equal; zlim([0,1.5]);
hold on;
% parallel to y-axis
ax(5) =subplot(2,3,3,'replace');
show_fem(img)
hold on;
ax(3) =subplot(2,3,4,'replace');
show_fem(img)
hold on;
%show_3d_slices(img, [],[0.0],[]);
%show_3d_slices(img, [1,1.9], [0.5],[0.5]);
%view(-14,13); axis tight; axis equal; zlim([0,1.5]);
ax(1) =subplot(2,3,1,'replace');
```

```
show_fem(img)
hold on;
ax(4) =subplot(2,3,2,'replace');
rgb = imread('C:/users/bode/desktop/bode/IMG_1329.jpg');
image(rgb);
title('Top View of Phantom Suspended at 0.8dm on y-axis')
%parallel to x-axis
%show_3d_slices(img, [],[],[0.0]);
%view(-14,13); axis tight; axis equal; zlim([0,1.5]);
hold on;
ax(2) = subplot(2,3,5,'replace');
rgb = imread('C:/users/bode/desktop/bode/IMG_1334.jpg');
image(rgb);
title('Front view of Phantom Suspended at 0.8dm on y-axis')
axis(ax,'image')

% Lowest limit
dadada=img.elem_data;
l_lim=min(dadada);%-0.6300;
% highest element values
high_value_elem_data=max(dadada);%0.2778;
%lowest element values
low_value_elem_data=min(dadada);%-0.6300;
% step change
delt=(high_value_elem_data-low_value_elem_data)/20;
[sav]=Sorting_elemindex(dadada);
[imggge]=Sorting_resistivity(dadada);
colour_map=[];
sav_new=[];
for uu=1:max(size(imggge(:,1)));
    gad=(imggge(uu)-l_lim)/delt;
    colour_map=[colour_map;gad*10,imggge(uu)];
    sav_new=[sav_new;sav(uu)];
```

```
        if colour_map(uu,1)>40
            break
        end
end
% SUMMATION OF VOLUME OF TETRAHEDRAL OF HIGHER RESISITIVITY VALUES

VVVOLUME=[];add_volume=0;sel_ele=[];sel_resist=[];mass_phant=[];
% SAV denotes indexes of the elements
for m=1:max(size(sav_new(:,1)));
 %aa1,bb1,cc1,dd1 are nodal points of an element.
elem_index=sav_new(m);
aa1=fmdl.elems(elem_index,1);
%b=1097(0.8744,0.1186,2.0), 1960
bb1=fmdl.elems(elem_index,2);
%c=436(1.0995,0.0328,2.0), 348
cc1=fmdl.elems(elem_index,3);
%d=1080(0.9291,-0.0481,2.0) 1959
dd1=fmdl.elems(elem_index,4);
% CALCULATING THE VOLUME OF A TETRAHEDRAL
% volume in meters
% V=|(a-d).((b-d)X(c-d))|/6
a1=fmdl.nodes(bb1,1)-fmdl.nodes(aa1,1); a2=fmdl.nodes(bb1,2)-fmdl.nodes(aa1,2);a3=fmdl.nodes(bb1,3)-fmdl.nodes(aa1,3);
b1=fmdl.nodes(cc1,1)-fmdl.nodes(aa1,1);b2=fmdl.nodes(cc1,2)-fmdl.nodes(aa1,2);b3=fmdl.nodes(cc1,3)-fmdl.nodes(aa1,3);
c1=fmdl.nodes(dd1,1)-fmdl.nodes(aa1,1);c2=fmdl.nodes(dd1,2)-fmdl.nodes(aa1,2);c3=fmdl.nodes(dd1,3)-fmdl.nodes(aa1,3);
vol=[a1 a2 a3; b1 b2 b3; c1 c2 c3];
volume=abs(det(vol))/6000.0; % we divided by 6000 because of the conversion of dimension in decimeters to meters%
add_volume=add_volume+volume;
sel_ele=[sel_ele;sav_new(m)];
sel_resist=[sel_resist;imggge(m)];
VVVOLUME=[VVVOLUME;volume];
%phant=den_cub*volume;
%mass_phant=[mass_phant; phant];
```

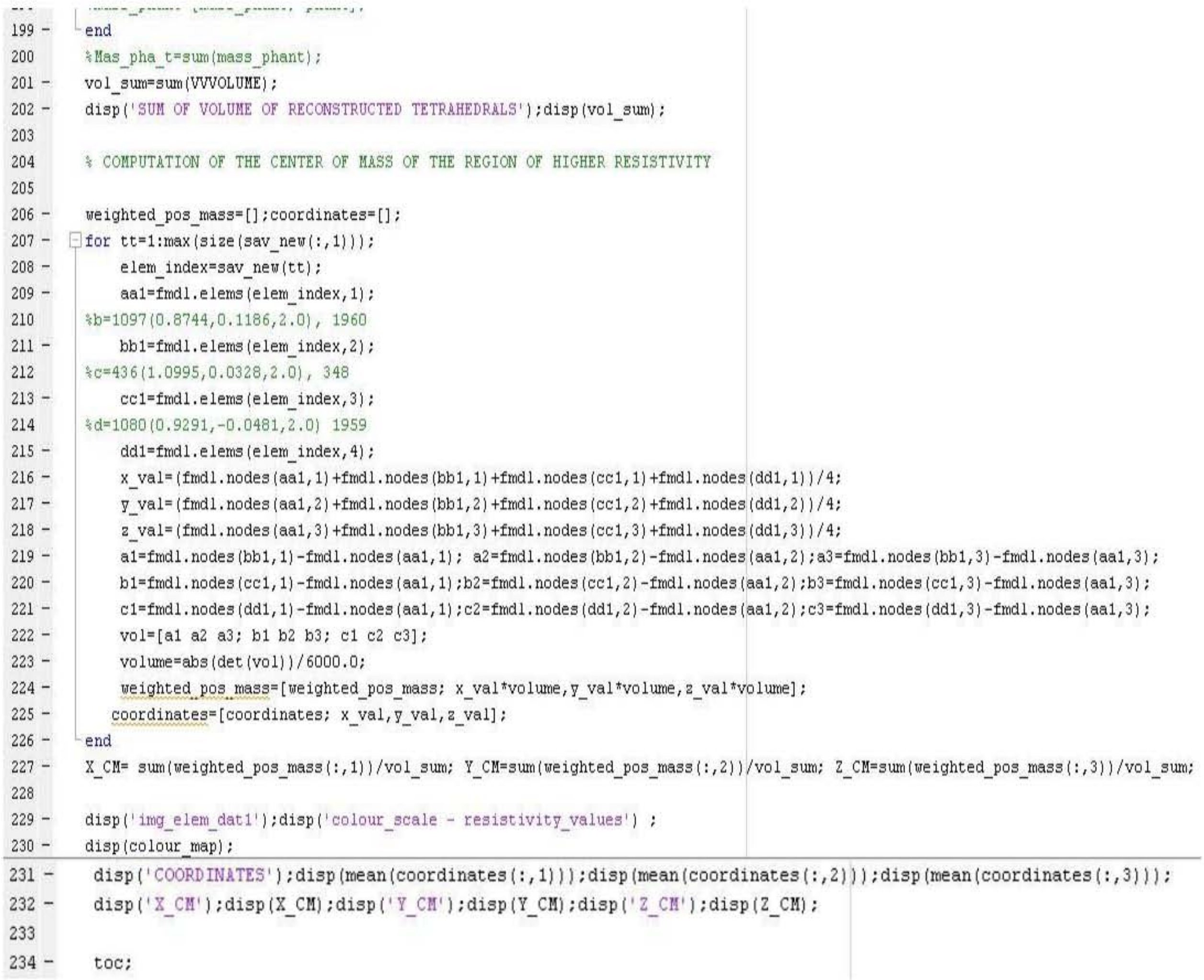

```
end
%Mas_pha_t=sum(mass_phant);
vol_sum=sum(VVVOLUME);
disp('SUM OF VOLUME OF RECONSTRUCTED TETRAHEDRALS');disp(vol_sum);

% COMPUTATION OF THE CENTER OF MASS OF THE REGION OF HIGHER RESISTIVITY

weighted_pos_mass=[];coordinates=[];
for tt=1:max(size(sav_new(:,1)));
    elem_index=sav_new(tt);
    aa1=fmdl.elems(elem_index,1);
%b=1097(0.8744,0.1186,2.0), 1960
    bb1=fmdl.elems(elem_index,2);
%c=436(1.0995,0.0328,2.0), 348
    cc1=fmdl.elems(elem_index,3);
%d=1080(0.9291,-0.0481,2.0) 1959
    dd1=fmdl.elems(elem_index,4);
    x_val=(fmdl.nodes(aa1,1)+fmdl.nodes(bb1,1)+fmdl.nodes(cc1,1)+fmdl.nodes(dd1,1))/4;
    y_val=(fmdl.nodes(aa1,2)+fmdl.nodes(bb1,2)+fmdl.nodes(cc1,2)+fmdl.nodes(dd1,2))/4;
    z_val=(fmdl.nodes(aa1,3)+fmdl.nodes(bb1,3)+fmdl.nodes(cc1,3)+fmdl.nodes(dd1,3))/4;
    a1=fmdl.nodes(bb1,1)-fmdl.nodes(aa1,1); a2=fmdl.nodes(bb1,2)-fmdl.nodes(aa1,2);a3=fmdl.nodes(bb1,3)-fmdl.nodes(aa1,3);
    b1=fmdl.nodes(cc1,1)-fmdl.nodes(aa1,1);b2=fmdl.nodes(cc1,2)-fmdl.nodes(aa1,2);b3=fmdl.nodes(cc1,3)-fmdl.nodes(aa1,3);
    c1=fmdl.nodes(dd1,1)-fmdl.nodes(aa1,1);c2=fmdl.nodes(dd1,2)-fmdl.nodes(aa1,2);c3=fmdl.nodes(dd1,3)-fmdl.nodes(aa1,3);
    vol=[a1 a2 a3; b1 b2 b3; c1 c2 c3];
    volume=abs(det(vol))/6000.0;
    weighted_pos_mass=[weighted_pos_mass; x_val*volume,y_val*volume,z_val*volume];
   coordinates=[coordinates; x_val,y_val,z_val];
end
X_CM= sum(weighted_pos_mass(:,1))/vol_sum; Y_CM=sum(weighted_pos_mass(:,2))/vol_sum; Z_CM=sum(weighted_pos_mass(:,3))/vol_sum;

disp('img_elem_dat1');disp('colour_scale - resistivity_values') ;
disp(colour_map);
 disp('COORDINATES');disp(mean(coordinates(:,1)));disp(mean(coordinates(:,2)));disp(mean(coordinates(:,3)));
 disp('X_CM');disp(X_CM);disp('Y_CM');disp(Y_CM);disp('Z_CM');disp(Z_CM);

 toc;
```

B6 : Reconstruction Code for A sequence of Current Stimulation through Opposite Electrode Pairs and A Sequence of Voltage Measurement through Adjacent Electrode Pairs in a Four Rings of Electrode System

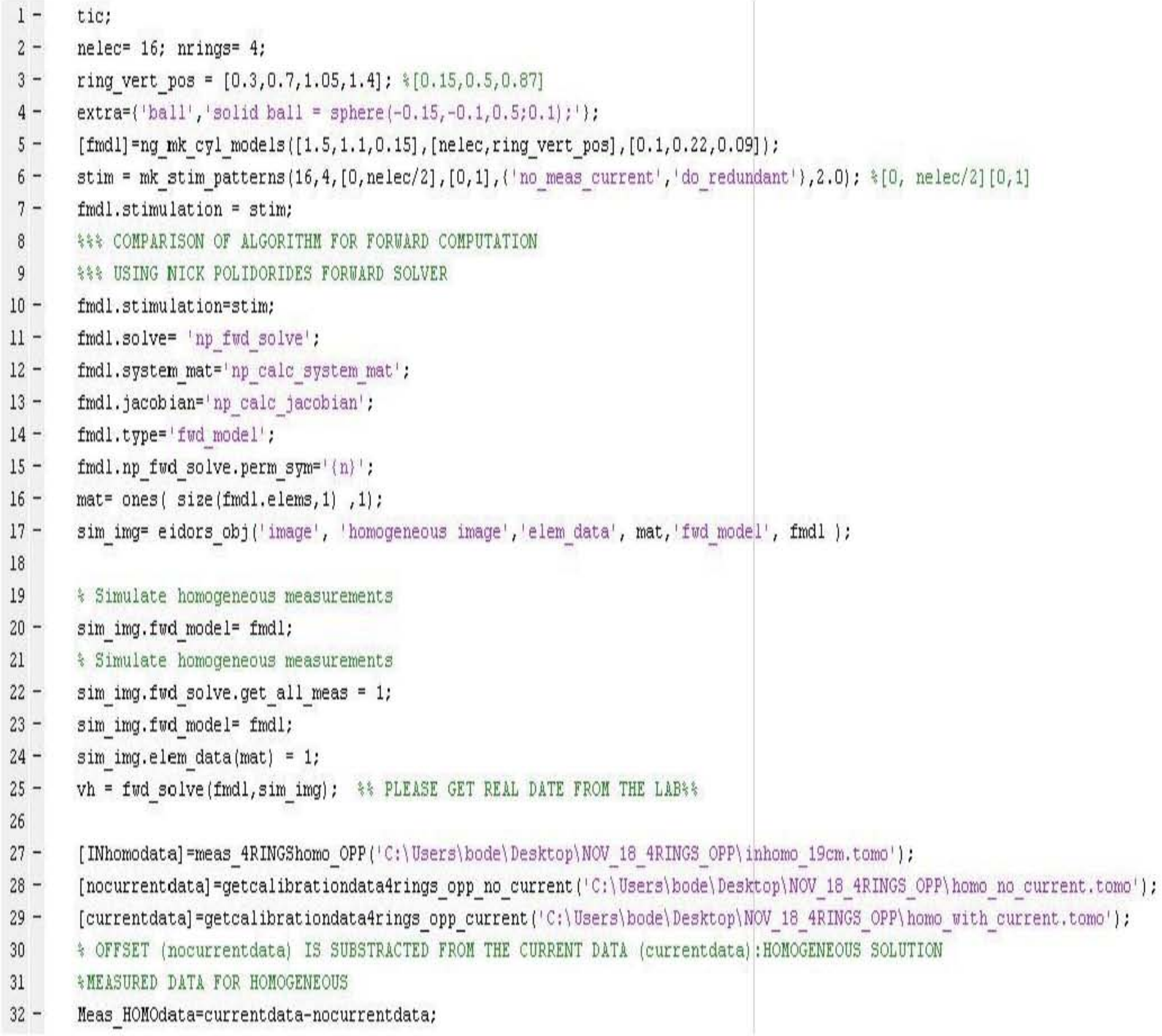

```matlab
tic;
nelec= 16; nrings= 4;
ring_vert_pos = [0.3,0.7,1.05,1.4]; %[0.15,0.5,0.87]
extra={'ball','solid ball = sphere(-0.15,-0.1,0.5;0.1);'};
[fmdl]=ng_mk_cyl_models([1.5,1.1,0.15],[nelec,ring_vert_pos],[0.1,0.22,0.09]);
stim = mk_stim_patterns(16,4,[0,nelec/2],[0,1],{'no_meas_current','do_redundant'},2.0); %[0, nelec/2][0,1]
fmdl.stimulation = stim;
%%% COMPARISON OF ALGORITHM FOR FORWARD COMPUTATION
%%% USING NICK POLIDORIDES FORWARD SOLVER
fmdl.stimulation=stim;
fmdl.solve= 'np_fwd_solve';
fmdl.system_mat='np_calc_system_mat';
fmdl.jacobian='np_calc_jacobian';
fmdl.type='fwd_model';
fmdl.np_fwd_solve.perm_sym='{n}';
mat= ones( size(fmdl.elems,1) ,1);
sim_img= eidors_obj('image', 'homogeneous image','elem_data', mat,'fwd_model', fmdl );

% Simulate homogeneous measurements
sim_img.fwd_model= fmdl;
% Simulate homogeneous measurements
sim_img.fwd_solve.get_all_meas = 1;
sim_img.fwd_model= fmdl;
sim_img.elem_data(mat) = 1;
vh = fwd_solve(fmdl,sim_img);  %% PLEASE GET REAL DATE FROM THE LAB%%

[INhomodata]=meas_4RINGShomo_OPP('C:\Users\bode\Desktop\NOV_18_4RINGS_OPP\inhomo_19cm.tomo');
[nocurrentdata]=getcalibrationdata4rings_opp_no_current('C:\Users\bode\Desktop\NOV_18_4RINGS_OPP\homo_no_current.tomo');
[currentdata]=getcalibrationdata4rings_opp_current('C:\Users\bode\Desktop\NOV_18_4RINGS_OPP\homo_with_current.tomo');
% OFFSET (nocurrentdata) IS SUBSTRACTED FROM THE CURRENT DATA (currentdata):HOMOGENEOUS SOLUTION
%MEASURED DATA FOR HOMOGENEOUS
Meas_HOMOdata=currentdata-nocurrentdata;
```

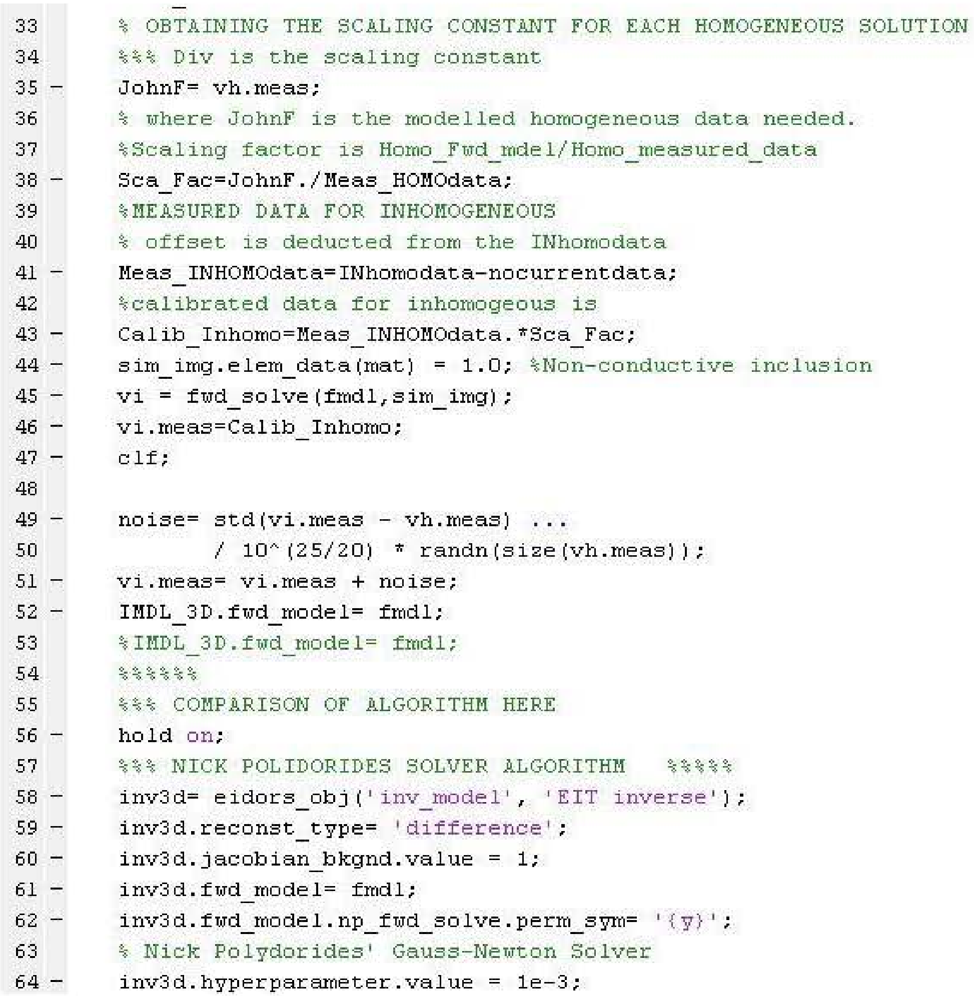

```
% OBTAINING THE SCALING CONSTANT FOR EACH HOMOGENEOUS SOLUTION
%%% Div is the scaling constant
JohnF= vh.meas;
% where JohnF is the modelled homogeneous data needed.
%Scaling factor is Homo_Fwd_mdel/Homo_measured_data
Sca_Fac=JohnF./Meas_HOMOdata;
%MEASURED DATA FOR INHOMOGENEOUS
% offset is deducted from the INhomodata
Meas_INHOMOdata=INhomodata-nocurrentdata;
%calibrated data for inhomogeous is
Calib_Inhomo=Meas_INHOMOdata.*Sca_Fac;
sim_img.elem_data(mat) = 1.0; %Non-conductive inclusion
vi = fwd_solve(fmdl,sim_img);
vi.meas=Calib_Inhomo;
clf;

noise= std(vi.meas - vh.meas) ...
       / 10^(25/20) * randn(size(vh.meas));
vi.meas= vi.meas + noise;
IMDL_3D.fwd_model= fmdl;
%IMDL_3D.fwd_model= fmdl;
%%%%%%
%%% COMPARISON OF ALGORITHM HERE
hold on;
%%% NICK POLIDORIDES SOLVER ALGORITHM   %%%%%
inv3d= eidors_obj('inv_model', 'EIT inverse');
inv3d.reconst_type= 'difference';
inv3d.jacobian_bkgnd.value = 1;
inv3d.fwd_model= fmdl;
inv3d.fwd_model.np_fwd_solve.perm_sym= '{y}';
% Nick Polydorides' Gauss-Newton Solver
inv3d.hyperparameter.value = 1e-3;
```

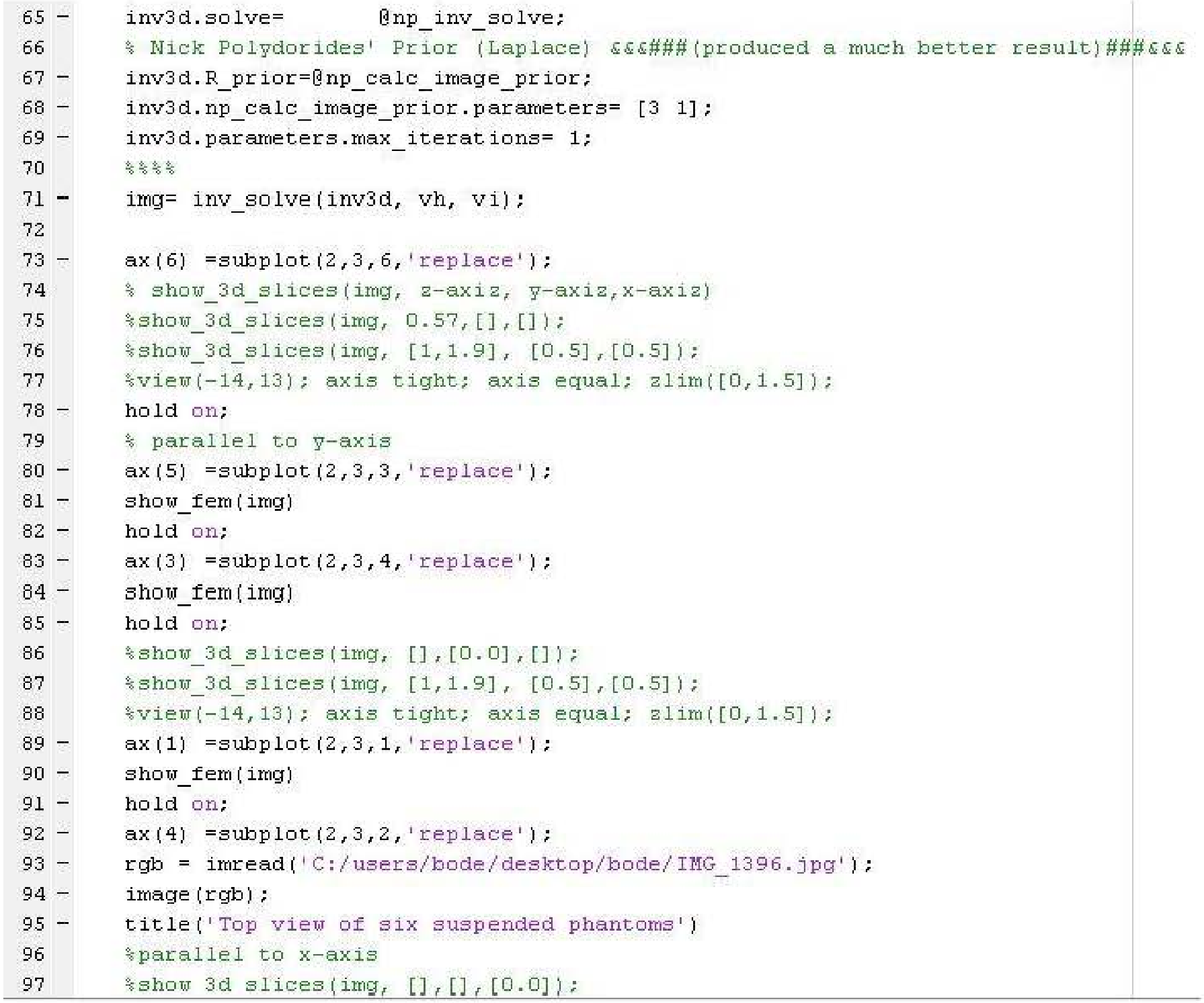

```
inv3d.solve=       @np_inv_solve;
% Nick Polydorides' Prior (Laplace) &&&###(produced a much better result)###&&&
inv3d.R_prior=@np_calc_image_prior;
inv3d.np_calc_image_prior.parameters= [3 1];
inv3d.parameters.max_iterations= 1;
%%%%
img= inv_solve(inv3d, vh, vi);

ax(6) =subplot(2,3,6,'replace');
% show_3d_slices(img, z-axiz, y-axiz,x-axiz)
%show_3d_slices(img, 0.57,[],[]);
%show_3d_slices(img, [1,1.9], [0.5],[0.5]);
%view(-14,13); axis tight; axis equal; zlim([0,1.5]);
hold on;
% parallel to y-axis
ax(5) =subplot(2,3,3,'replace');
show_fem(img)
hold on;
ax(3) =subplot(2,3,4,'replace');
show_fem(img)
hold on;
%show_3d_slices(img, [],[0.0],[]);
%show_3d_slices(img, [1,1.9], [0.5],[0.5]);
%view(-14,13); axis tight; axis equal; zlim([0,1.5]);
ax(1) =subplot(2,3,1,'replace');
show_fem(img)
hold on;
ax(4) =subplot(2,3,2,'replace');
rgb = imread('C:/users/bode/desktop/bode/IMG_1396.jpg');
image(rgb);
title('Top view of six suspended phantoms')
%parallel to x-axis
%show 3d slices(img, [],[],[0.0]);
```

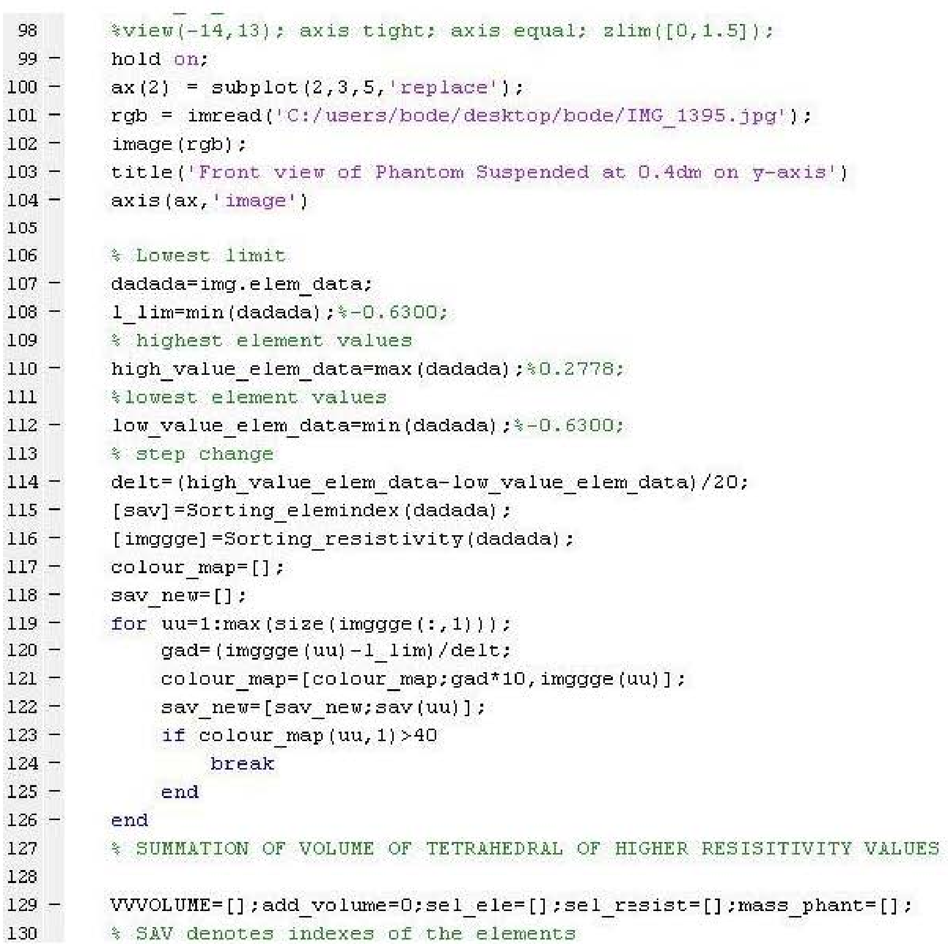

```
%view(-14,13); axis tight; axis equal; zlim([0,1.5]);
hold on;
ax(2) = subplot(2,3,5,'replace');
rgb = imread('C:/users/bode/desktop/bode/IMG_1395.jpg');
image(rgb);
title('Front view of Phantom Suspended at 0.4dm on y-axis')
axis(ax,'image')

% Lowest limit
dadada=img.elem_data;
l_lim=min(dadada);%-0.6300;
% highest element values
high_value_elem_data=max(dadada);%0.2778;
%lowest element values
low_value_elem_data=min(dadada);%-0.6300;
% step change
delt=(high_value_elem_data-low_value_elem_data)/20;
[sav]=Sorting_elemindex(dadada);
[imggge]=Sorting_resistivity(dadada);
colour_map=[];
sav_new=[];
for uu=1:max(size(imggge(:,1)));
    gad=(imggge(uu)-l_lim)/delt;
    colour_map=[colour_map;gad*10,imggge(uu)];
    sav_new=[sav_new;sav(uu)];
    if colour_map(uu,1)>40
        break
    end
end
% SUMMATION OF VOLUME OF TETRAHEDRAL OF HIGHER RESISITIVITY VALUES

VVVOLUME=[];add_volume=0;sel_ele=[];sel_resist=[];mass_phant=[];
% SAV denotes indexes of the elements
```

```
for m=1:max(size(sav_new(:,1)));
 %aa1,bb1,cc1,dd1 are nodal points of an element.
elem_index=sav_new(m);
aa1=fmdl.elems(elem_index,1);
%b=1097(0.8744,0.1186,2.0), 1960
bb1=fmdl.elems(elem_index,2);
%c=436(1.0995,0.0328,2.0), 348
cc1=fmdl.elems(elem_index,3);
%d=1080(0.9291,-0.0481,2.0) 1959
dd1=fmdl.elems(elem_index,4);
% CALCULATING THE VOLUME OF A TETRAHEDRAL
% volume in meters
% V=|(a-d).((b-d)X(c-d))|/6
a1=fmdl.nodes(bb1,1)-fmdl.nodes(aa1,1); a2=fmdl.nodes(bb1,2)-fmdl.nodes(aa1,2);a3=fmdl.nodes(bb1,3)-fmdl.nodes(aa1,3);
b1=fmdl.nodes(cc1,1)-fmdl.nodes(aa1,1);b2=fmdl.nodes(cc1,2)-fmdl.nodes(aa1,2);b3=fmdl.nodes(cc1,3)-fmdl.nodes(aa1,3);
c1=fmdl.nodes(dd1,1)-fmdl.nodes(aa1,1);c2=fmdl.nodes(dd1,2)-fmdl.nodes(aa1,2);c3=fmdl.nodes(dd1,3)-fmdl.nodes(aa1,3);
vol=[a1 a2 a3; b1 b2 b3; c1 c2 c3];
volume=abs(det(vol))/6000.0; % we divided by 6000 because of the conversion of dimension in decimeters to meters%
add_volume=add_volume+volume;
sel_ele=[sel_ele;sav_new(m)];
sel_resist=[sel_resist;imggge(m)];
VVVOLUME=[VVVOLUME;volume];
%phant=den_cub*volume;
%mass_phant=[mass_phant; phant];
end
%Mas_pha_t=sum(mass_phant);
vol_sum=sum(VVVOLUME);
disp('SUM OF VOLUME OF RECONSTRUCTED TETRAHEDRALS');disp(vol_sum);

% COMPUTATION OF THE CENTER OF MASS OF THE REGION OF HIGHER RESISTIVITY

weighted_pos_mass=[];coordinates=[];
for tt=1:max(size(sav_new(:,1)));
    elem_index=sav_new(tt);
    aa1=fmdl.elems(elem_index,1);
%b=1097(0.8744,0.1186,2.0), 1960
    bb1=fmdl.elems(elem_index,2);
%c=436(1.0995,0.0328,2.0), 348
    cc1=fmdl.elems(elem_index,3);
%d=1080(0.9291,-0.0481,2.0) 1959
    dd1=fmdl.elems(elem_index,4);
    x_val=(fmdl.nodes(aa1,1)+fmdl.nodes(bb1,1)+fmdl.nodes(cc1,1)+fmdl.nodes(dd1,1))/4;
    y_val=(fmdl.nodes(aa1,2)+fmdl.nodes(bb1,2)+fmdl.nodes(cc1,2)+fmdl.nodes(dd1,2))/4;
    z_val=(fmdl.nodes(aa1,3)+fmdl.nodes(bb1,3)+fmdl.nodes(cc1,3)+fmdl.nodes(dd1,3))/4;
    a1=fmdl.nodes(bb1,1)-fmdl.nodes(aa1,1); a2=fmdl.nodes(bb1,2)-fmdl.nodes(aa1,2);a3=fmdl.nodes(bb1,3)-fmdl.nodes(aa1,3);
    b1=fmdl.nodes(cc1,1)-fmdl.nodes(aa1,1);b2=fmdl.nodes(cc1,2)-fmdl.nodes(aa1,2);b3=fmdl.nodes(cc1,3)-fmdl.nodes(aa1,3);
    c1=fmdl.nodes(dd1,1)-fmdl.nodes(aa1,1);c2=fmdl.nodes(dd1,2)-fmdl.nodes(aa1,2);c3=fmdl.nodes(dd1,3)-fmdl.nodes(aa1,3);
    vol=[a1 a2 a3; b1 b2 b3; c1 c2 c3];
    volume=abs(det(vol))/6000.0;
    weighted_pos_mass=[weighted_pos_mass; x_val*volume,y_val*volume,z_val*volume];
   coordinates=[coordinates; x_val,y_val,z_val];
end
X_CM= sum(weighted_pos_mass(:,1))/vol_sum; Y_CM=sum(weighted_pos_mass(:,2))/vol_sum; Z_CM=sum(weighted_pos_mass(:,3))/vol_sum;

disp('img_elem_dat1');disp('colour_scale - resistivity_values') ;
disp(colour_map);
disp('COORDINATES');disp(mean(coordinates(:,1)));disp(mean(coordinates(:,2)));disp(mean(coordinates(:,3)));
disp('X_CM');disp(X_CM);disp('Y_CM');disp(Y_CM);disp('Z_CM');disp(Z_CM);


toc;
```

APPENDIX C

Measurement Sequence Table for Opposite and Adjacent Current Stimulation Strategy for Two, Three and Four Electrodes System

C1 : Sequence Table for Two Rings Adjacent Current Injection and Adjacent Voltage Measurement Sequence

I1V1: db (current injection on first ring and voltage measurement on first ring)
#$00,#$0F,#$00,#$00,#$10,#$00,#$00,#$21,#$00,#$00,#$32,#$00,#$00,#$43,#$00,#$00,#$54,#$00,#$00,#$65,#$00,#$00,#$76,#$00,#$00,#$87,#$00,#$00,#$98,#$00,#$00,#$A9,#$00,#$00,#$BA,#$00,#$00,#$CB,#$00,#$00,#$DC,#$00,#$00,#$ED,#$00,#$00,#$FE,#$00

I1V2: db (current injection on first ring and voltage measurement on second ring)
#$00,#$0F,#$11,#$00,#$10,#$11,#$00,#$21,#$11,#$00,#$32,#$11,#$00,#$43,#$11,#$00,#$54,#$11,#$00,#$65,#$11,#$00,#$76,#$11,#$00,#$87,#$11,#$00,#$98,#$11,#$00,#$A9,#$11,#$00,#$BA,#$11,#$00,#$CB,#$11,#$00,#$DC,#$11,#$00,#$ED,#$11,#$00,#$FE,#$11

I2V1: db (current injection on second ring and voltage measurement on first ring)
#$11,#$0F,#$00,#$11,#$10,#$00,#$11,#$21,#$00,#$11,#$32,#$00,#$11,#$43,#$00,#$11,#$54,#$00,#$11,#$65,#$00,#$11,#$76,#$00,#$11,#$87,#$00,#$11,#$98,#$00,#$11,#$A9,#$00,#$11,#$BA,#$00,#$11,#$CB,#$00,#$11,#$DC,#$00,#$11,#$ED,#$00,#$11,#$FE,#$00

I2V2: db (current injection on second ring and voltage measurement on second ring)
#$11,#$0F,#$11,#$11,#$10,#$11,#$11,#$21,#$11,#$11,#$32,#$11,#$11,#$43,#$11,#$11,#$54,#$11,#$11,#$65,#$11,#$11,#$76,#$11,#$11,#$87,#$11,#$11,#$98,#$11,#$11,#$A9,#$11,#$11,#$BA,#$11,#$11,#$CB,#$11,#$11,#$DC,#$11,#$11,#$ED,#$11,#$11,#$FE,#$11.

C2 : Sequence Table for Two Rings Opposite Current Injection and Adjacent Voltage Measurement Sequence

I1V1: db (current injection on the first ring and voltage measurement on first ring)
#$00,#$08,#$00,#$00,#$19,#$00,#$00,#$2A,#$00,#$00,#$3B,#$00,#$00,#$4C,#$00,#$00,#$5D,#$00,#$00,#$6E,#$00,#$00,#$7F,#$00,#$00,#$80,#$00,#$00,#$91,#$00,#$00,#$A2,#$00,#$00,#$B3,#$00,#$00,#$C4,#$00,#$00,#$D5,#$00,#$00,#$E6,#$00,#$00,#$F7,#$00
I1V2: db (current injection on the first ring and voltage measurement on second ring)
#$00,#$08,#$11,#$00,#$19,#$11,#$00,#$2A,#$11,#$00,#$3B,#$11,#$00,#$4C,#$11,#$00,#$5D,#$11,#$00,#$6E,#$11,#$00,#$7F,#$11,#$00,#$80,#$11,#$00,#$91,#$11,#$00,#$A2,#$11,#$00,#$B3,#$11,#$00,#$C4,#$11,#$00,#$D5,#$11,#$00,#$E6,#$11,#$00,#$F7,#$11
I2V1: db (current injection on second ring and voltage measurement on first ring)
#$11,#$08,#$00,#$11,#$19,#$00,#$11,#$2A,#$00,#$11,#$3B,#$00,#$11,#$4C,#$00,#$11,#$5D,#$00,#$11,#$6E,#$00,#$11,#$7F,#$00,#$11,#$80,#$00,#$11,#$91,#$00,#$11,#$A2,#$00,#$11,#$B3,#$00,#$11,#$C4,#$00,#$11,#$D5,#$00,#$11,#$E6,#$00,#$11,#$F7,#$00
I2V2: db (current injection on second ring and voltage measurement on second ring)
#$11,#$08,#$11,#$11,#$19,#$11,#$11,#$2A,#$11,#$11,#$3B,#$11,#$11,#$4C,#$11,#$11,#$5D,#$11,#$

11,#$6E,#$11,#$11,#$7F,#$11,#$11,#$80,#$11,#$11,#$91,#$11,#$11,#$A2,#$11,#$11,#$B3,#$11,#$11,#$C4,#$11,#$11,#$D5,#$11,#$11,#$E6,#$11,#$11,#$F7,#$11.

C3 : Sequence Table for Three Rings Adjacent Current Injection and Adjacent Voltage Measurement sequence

I1V1: db (current injection on first ring and voltage measurement on first ring)
#$00,#$0F,#$00,#$00,#$10,#$00,#$00,#$21,#$00,#$00,#$32,#$00,#$00,#$43,#$00,#$00,#$54,#$00,#$00,#$65,#$00,#$00,#$76,#$00,#$00,#$87,#$00,#$00,#$98,#$00,#$00,#$A9,#$00,#$00,#$BA,#$00,#$00,#$CB,#$00,#$00,#$DC,#$00,#$00,#$ED,#$00,#$00,#$FE,#$00

I1V2: db (current injection on first ring and voltage measurement on second ring)
#$00,#$0F,#$11,#$00,#$10,#$11,#$00,#$21,#$11,#$00,#$32,#$11,#$00,#$43,#$11,#$00,#$54,#$11,#$00,#$65,#$11,#$00,#$76,#$11,#$00,#$87,#$11,#$00,#$98,#$11,#$00,#$A9,#$11,#$00,#$BA,#$11,#$00,#$CB,#$11,#$00,#$DC,#$11,#$00,#$ED,#$11,#$00,#$FE,#$11

I1V3: db (current injection on first ring and voltage measurement on third ring)
#$00,#$0F,#$22,#$00,#$10,#$22,#$00,#$21,#$22,#$00,#$32,#$22,#$00,#$43,#$22,#$00,#$54,#$22,#$00,#$65,#$22,#$00,#$76,#$22,#$00,#$87,#$22,#$00,#$98,#$22,#$00,#$A9,#$22,#$00,#$BA,#$22,#$00,#$CB,#$22,#$00,#$DC,#$22,#$00,#$ED,#$22,#$00,#$FE,#$22

I2V1: db (current injection on second ring and voltage measurement on first ring)
#$11,#$0F,#$00,#$11,#$10,#$00,#$11,#$21,#$00,#$11,#$32,#$00,#$11,#$43,#$00,#$11,#$54,#$00,#$11,#$65,#$00,#$11,#$76,#$00,#$11,#$87,#$00,#$11,#$98,#$00,#$11,#$A9,#$00,#$11,#$BA,#$00,#$11,#$CB,#$00,#$11,#$DC,#$00,#$11,#$ED,#$00,#$11,#$FE,#$00

I2V2: db (current injection on second ring and voltage measurement on second ring)
#$11,#$0F,#$11,#$11,#$10,#$11,#$11,#$21,#$11,#$11,#$32,#$11,#$11,#$43,#$11,#$11,#$54,#$11,#$11,#$65,#$11,#$11,#$76,#$11,#$11,#$87,#$11,#$11,#$98,#$11,#$11,#$A9,#$11,#$11,#$BA,#$11,#$11,#$CB,#$11,#$11,#$DC,#$11,#$11,#$ED,#$11,#$11,#$FE,#$11

I2V3: db (current injection on second ring and voltage measurement on third ring)
#$11,#$0F,#$22,#$11,#$10,#$22,#$11,#$21,#$22,#$11,#$32,#$22,#$11,#$43,#$22,#$11,#$54,#$22,#$11,#$65,#$22,#$11,#$76,#$22,#$11,#$87,#$22,#$11,#$98,#$22,#$11,#$A9,#$22,#$11,#$BA,#$22,#$11,#$CB,#$22,#$11,#$DC,#$22,#$11,#$ED,#$22,#$11,#$FE,#$22

I3V1: db (current injection on third ring and voltage measurement on first ring)
#$22,#$0F,#$00,#$22,#$10,#$00,#$22,#$21,#$00,#$22,#$32,#$00,#$22,#$43,#$00,#$22,#$54,#$00,#$22,#$65,#$00,#$22,#$76,#$00,#$22,#$87,#$00,#$22,#$98,#$00,#$22,#$A9,#$00,#$22,#$BA,#$00,#$22,#$CB,#$00,#$22,#$DC,#$00,#$22,#$ED,#$00,#$22,#$FE,#$00

I3V2: db (current injection on third ring and voltage measurement on second ring)
#$22,#$0F,#$11,#$22,#$10,#$11,#$22,#$21,#$11,#$22,#$32,#$11,#$22,#$43,#$11,#$22,#$54,#$11,#$22,#$65,#$11,#$22,#$76,#$11,#$22,#$87,#$11,#$22,#$98,#$11,#$22,#$A9,#$11,#$22,#$BA,#$11,#$22,#$CB,#$11,#$22,#$DC,#$11,#$22,#$ED,#$11,#$22,#$FE,#$11

I3V3: db (current injection on third ring and voltage measurement on third ring)
#$22,#$0F,#$22,#$22,#$10,#$22,#$22,#$21,#$22,#$22,#$32,#$22,#$22,#$43,#$22,#$22,#$54,#$22,#$2

```
2,#$65,#$22,#$22,#$76,#$22,#$22,#$87,#$22,#$22,#$98,#$22,#$22,#$A9,#$22,#$22,#$BA,#$22,#$22,#
$CB,#$22,#$22,#$DC,#$22,#$22,#$ED,#$22,#$22,#$FE,#$22
```

C4 : Sequence Table for Three Rings Opposite Current Injection and Adjacent Voltage Measurement Sequence

I1V1: db (current injection on first ring and voltage measurement on first ring)

```
#$00,#$08,#$00,#$00,#$19,#$00,#$00,#$2A,#$00,#$00,#$3B,#$00,#$00,#$4C,#$00,#$00,#$5D,#$00,#$
00,#$6E,#$00,#$00,#$7F,#$00,#$00,#$80,#$00,#$00,#$91,#$00,#$00,#$A2,#$00,#$00,#$B3,#$00,#$00,
#$C4,#$00,#$00,#$D5,#$00,#$00,#$E6,#$00,#$00,#$F7,#$00
```

I1V2: db (current injection on first ring and voltage measurement on second ring)

```
#$00,#$08,#$11,#$00,#$19,#$11,#$00,#$2A,#$11,#$00,#$3B,#$11,#$00,#$4C,#$11,#$00,#$5D,#$11,#$
00,#$6E,#$11,#$00,#$7F,#$11,#$00,#$80,#$11,#$00,#$91,#$11,#$00,#$A2,#$11,#$00,#$B3,#$11,#$00,
#$C4,#$11,#$00,#$D5,#$11,#$00,#$E6,#$11,#$00,#$F7,#$11
```

I1V3: db (current injection on first ring and voltage measurement on third ring)

```
#$00,#$08,#$22,#$00,#$19,#$22,#$00,#$2A,#$22,#$00,#$3B,#$22,#$00,#$4C,#$22,#$00,#$5D,#$22,#$
00,#$6E,#$22,#$00,#$7F,#$22,#$00,#$80,#$22,#$00,#$91,#$22,#$00,#$A2,#$22,#$00,#$B3,#$22,#$00,
#$C4,#$22,#$00,#$D5,#$22,#$00,#$E6,#$22,#$00,#$F7,#$22
```

I2V1: db (current injection on second ring and voltage measurement on first ring)

```
#$11,#$08,#$00,#$11,#$19,#$00,#$11,#$2A,#$00,#$11,#$3B,#$00,#$11,#$4C,#$00,#$11,#$5D,#$00,#$
11,#$6E,#$00,#$11,#$7F,#$00,#$11,#$80,#$00,#$11,#$91,#$00,#$11,#$A2,#$00,#$11,#$B3,#$00,#$11,
#$C4,#$00,#$11,#$D5,#$00,#$11,#$E6,#$00,#$11,#$F7,#$00
```

I2V2: db (current injection on second ring and voltage measurement on second ring)

```
#$11,#$08,#$11,#$11,#$19,#$11,#$11,#$2A,#$11,#$11,#$3B,#$11,#$11,#$4C,#$11,#$11,#$5D,#$11,#$
11,#$6E,#$11,#$11,#$7F,#$11,#$11,#$80,#$11,#$11,#$91,#$11,#$11,#$A2,#$11,#$11,#$B3,#$11,#$11,
#$C4,#$11,#$11,#$D5,#$11,#$11,#$E6,#$11,#$11,#$F7,#$11
```

I2v3: db (current injection on second ring and voltage measurement on third ring)

```
#$11,#$08,#$22,#$11,#$19,#$22,#$11,#$2A,#$22,#$11,#$3B,#$22,#$11,#$4C,#$22,#$11,#$5D,#$22,#$
11,#$6E,#$22,#$11,#$7F,#$22,#$11,#$80,#$22,#$11,#$91,#$22,#$11,#$A2,#$22,#$11,#$B3,#$22,#$11,
#$C4,#$22,#$11,#$D5,#$22,#$11,#$E6,#$22,#$11,#$F7,#$22
```

I3V1: db (current injection on third ring and voltage measurement on first ring)

```
#$22,#$08,#$00,#$22,#$19,#$00,#$22,#$2A,#$00,#$22,#$3B,#$00,#$22,#$4C,#$00,#$22,#$5D,#$00,#$
22,#$6E,#$00,#$22,#$7F,#$00,#$22,#$80,#$00,#$22,#$91,#$00,#$22,#$A2,#$00,#$22,#$B3,#$00,#$22,
#$C4,#$00,#$22,#$D5,#$00,#$22,#$E6,#$00,#$22,#$F7,#$00
```

I3V2: db (current injection on third ring and voltage measurement on second ring)

```
#$22,#$08,#$11,#$22,#$19,#$11,#$22,#$2A,#$11,#$22,#$3B,#$11,#$22,#$4C,#$11,#$22,#$5D,#$11,#$
22,#$6E,#$11,#$22,#$7F,#$11,#$22,#$80,#$11,#$22,#$91,#$11,#$22,#$A2,#$11,#$22,#$B3,#$11,#$22,
#$C4,#$11,#$22,#$D5,#$11,#$22,#$E6,#$11,#$22,#$F7,#$11
```

I3v3: db (current injection on third ring and voltage measurement on third ring)
#$22,#$08,#$22,#$22,#$19,#$22,#$22,#$2A,#$22,#$22,#$3B,#$22,#$22,#$4C,#$22,#$22,#$5D,#$22,#$22,#$6E,#$22,#$22,#$7F,#$22,#$22,#$80,#$22,#$22,#$91,#$22,#$22,#$A2,#$22,#$22,#$B3,#$22,#$22,#$C4,#$22,#$22,#$D5,#$22,#$22,#$E6,#$22,#$22,#$F7,#$22

C5 : Sequence Table for Four Rings Adjacent Current Injection and Adjacent Voltage Measurement sequence

I1V1: db (current injection on first ring and voltage measurement on first ring)
#$00,#$0F,#$00,#$00,#$10,#$00,#$00,#$21,#$00,#$00,#$32,#$00,#$00,#$43,#$00,#$00,#$54,#$00,#$00,#$65,#$00,#$00,#$76,#$00,#$00,#$87,#$00,#$00,#$98,#$00,#$00,#$A9,#$00,#$00,#$BA,#$00,#$00,#$CB,#$00,#$00,#$DC,#$00,#$00,#$ED,#$00,#$00,#$FE,#$00

I1V2: db (current injection on first ring and voltage measurement on second ring)
#$00,#$0F,#$11,#$00,#$10,#$11,#$00,#$21,#$11,#$00,#$32,#$11,#$00,#$43,#$11,#$00,#$54,#$11,#$00,#$65,#$11,#$00,#$76,#$11,#$00,#$87,#$11,#$00,#$98,#$11,#$00,#$A9,#$11,#$00,#$BA,#$11,#$00,#$CB,#$11,#$00,#$DC,#$11,#$00,#$ED,#$11,#$00,#$FE,#$11

I1V3: db (current injection on first ring and voltage measurement on third ring)
#$00,#$0F,#$22,#$00,#$10,#$22,#$00,#$21,#$22,#$00,#$32,#$22,#$00,#$43,#$22,#$00,#$54,#$22,#$00,#$65,#$22,#$00,#$76,#$22,#$00,#$87,#$22,#$00,#$98,#$22,#$00,#$A9,#$22,#$00,#$BA,#$22,#$00,#$CB,#$22,#$00,#$DC,#$22,#$00,#$ED,#$22,#$00,#$FE,#$22

I1V4: db (current injection on first ring and voltage measurement on fourth ring)
#$00,#$0F,#$33,#$00,#$10,#$33,#$00,#$21,#$33,#$00,#$32,#$33,#$00,#$43,#$33,#$00,#$54,#$33,#$00,#$65,#$33,#$00,#$76,#$33,#$00,#$87,#$33,#$00,#$98,#$33,#$00,#$A9,#$33,#$00,#$BA,#$33,#$00,#$CB,#$33,#$00,#$DC,#$33,#$00,#$ED,#$33,#$00,#$FE,#$33

I2V1: db (current injection on second ring and voltage measurement on first ring)
#$11,#$0F,#$00,#$11,#$10,#$00,#$11,#$21,#$00,#$11,#$32,#$00,#$11,#$43,#$00,#$11,#$54,#$00,#$11,#$65,#$00,#$11,#$76,#$00,#$11,#$87,#$00,#$11,#$98,#$00,#$11,#$A9,#$00,#$11,#$BA,#$00,#$11,#$CB,#$00,#$11,#$DC,#$00,#$11,#$ED,#$00,#$11,#$FE,#$00

I2V2: db (current injection on second ring and voltage measurement on second ring)
#$11,#$0F,#$11,#$11,#$10,#$11,#$11,#$21,#$11,#$11,#$32,#$11,#$11,#$43,#$11,#$11,#$54,#$11,#$11,#$65,#$11,#$11,#$76,#$11,#$11,#$87,#$11,#$11,#$98,#$11,#$11,#$A9,#$11,#$11,#$BA,#$11,#$11,#$CB,#$11,#$11,#$DC,#$11,#$11,#$ED,#$11,#$11,#$FE,#$11

I2V3: db (current injection on second ring and voltage measurement on third ring)
#$11,#$0F,#$22,#$11,#$10,#$22,#$11,#$21,#$22,#$11,#$32,#$22,#$11,#$43,#$22,#$11,#$54,#$22,#$11,#$65,#$22,#$11,#$76,#$22,#$11,#$87,#$22,#$11,#$98,#$22,#$11,#$A9,#$22,#$11,#$BA,#$22,#$11,#$CB,#$22,#$11,#$DC,#$22,#$11,#$ED,#$22,#$11,#$FE,#$22

I2V4: db (current injection on second ring and voltage measurement on fourth ring)

```
#$11,#$0F,#$33,#$11,#$10,#$33,#$11,#$21,#$33,#$11,#$32,#$33,#$11,#$43,#$33,#$11,#$54,#$33,#$11,#$65,#$33,#$11,#$76,#$33,#$11,#$87,#$33,#$11,#$98,#$33,#$11,#$A9,#$33,#$11,#$BA,#$33,#$11,#$CB,#$33,#$11,#$DC,#$33,#$11,#$ED,#$33,#$11,#$FE,#$33
```

I3V1: db (current injection on third ring and voltage measurement on first ring)

```
#$22,#$0F,#$00,#$22,#$10,#$00,#$22,#$21,#$00,#$22,#$32,#$00,#$22,#$43,#$00,#$22,#$54,#$00,#$22,#$65,#$00,#$22,#$76,#$00,#$22,#$87,#$00,#$22,#$98,#$00,#$22,#$A9,#$00,#$22,#$BA,#$00,#$22,#$CB,#$00,#$22,#$DC,#$00,#$22,#$ED,#$00,#$22,#$FE,#$00
```

I3V2: db (current injection on third ring and voltage measurement on second ring)

```
#$22,#$0F,#$11,#$22,#$10,#$11,#$22,#$21,#$11,#$22,#$32,#$11,#$22,#$43,#$11,#$22,#$54,#$11,#$22,#$65,#$11,#$22,#$76,#$11,#$22,#$87,#$11,#$22,#$98,#$11,#$22,#$A9,#$11,#$22,#$BA,#$11,#$22,#$CB,#$11,#$22,#$DC,#$11,#$22,#$ED,#$11,#$22,#$FE,#$11
```

I3V3: db (current injection on third ring and voltage measurement on third ring)

```
#$22,#$0F,#$22,#$22,#$10,#$22,#$22,#$21,#$22,#$22,#$32,#$22,#$22,#$43,#$22,#$22,#$54,#$22,#$22,#$65,#$22,#$22,#$76,#$22,#$22,#$87,#$22,#$22,#$98,#$22,#$22,#$A9,#$22,#$22,#$BA,#$22,#$22,#$CB,#$22,#$22,#$DC,#$22,#$22,#$ED,#$22,#$22,#$FE,#$22
```

I3V4: db (current injection on third ring and voltage measurement on fourth ring)

```
#$22,#$0F,#$33,#$22,#$10,#$33,#$22,#$21,#$33,#$22,#$32,#$33,#$22,#$43,#$33,#$22,#$54,#$33,#$22,#$65,#$33,#$22,#$76,#$33,#$22,#$87,#$33,#$22,#$98,#$33,#$22,#$A9,#$33,#$22,#$BA,#$33,#$22,#$CB,#$33,#$22,#$DC,#$33,#$22,#$ED,#$33,#$22,#$FE,#$33
```

I4V1: db (current injection on fourth ring and voltage measurement on first ring)

```
#$33,#$0F,#$00,#$33,#$10,#$00,#$33,#$21,#$00,#$33,#$32,#$00,#$33,#$43,#$00,#$33,#$54,#$00,#$33,#$65,#$00,#$33,#$76,#$00,#$33,#$87,#$00,#$33,#$98,#$00,#$33,#$A9,#$00,#$33,#$BA,#$00,#$33,#$CB,#$00,#$33,#$DC,#$00,#$33,#$ED,#$00,#$33,#$FE,#$00
```

I4V2: db (current injection on fourth ring and voltage measurement on second ring)

```
#$33,#$0F,#$11,#$33,#$10,#$11,#$33,#$21,#$11,#$33,#$32,#$11,#$33,#$43,#$11,#$33,#$54,#$11,#$33,#$65,#$11,#$33,#$76,#$11,#$33,#$87,#$11,#$33,#$98,#$11,#$33,#$A9,#$11,#$33,#$BA,#$11,#$33,#$CB,#$11,#$33,#$DC,#$11,#$33,#$ED,#$11,#$33,#$FE,#$11
```

I4V3: db (current injection on fourth ring and voltage measurement on third ring)

```
#$33,#$0F,#$22,#$33,#$10,#$22,#$33,#$21,#$22,#$33,#$32,#$22,#$33,#$43,#$22,#$33,#$54,#$22,#$33,#$65,#$22,#$33,#$76,#$22,#$33,#$87,#$22,#$33,#$98,#$22,#$33,#$A9,#$22,#$33,#$BA,#$22,#$33,#$CB,#$22,#$33,#$DC,#$22,#$33,#$ED,#$22,#$33,#$FE,#$22
```

I4V4: db (current injection on fourth ring and voltage measurement on fourth ring)

```
#$33,#$0F,#$33,#$33,#$10,#$33,#$33,#$21,#$33,#$33,#$32,#$33,#$33,#$43,#$33,#$33,#$54,#$33,#$33,#$65,#$33,#$33,#$76,#$33,#$33,#$87,#$33,#$33,#$98,#$33,#$33,#$A9,#$33,#$33,#$BA,#$33,#$33,#$CB,#$33,#$33,#$DC,#$33,#$33,#$ED,#$33,#$33,#$FE,#$33
```

C6 : Sequence Table for Four Rings Opposite Current Injection and Adjacent Voltage Measurement Sequence

I1V1: db (current injection on first ring and voltage measurement on first ring)

```
#$00,#$08,#$00,#$00,#$19,#$00,#$00,#$2A,#$00,#$00,#$3B,#$00,#$00,#$4C,#$00,#$00,#$5D,#$00,#$
00,#$6E,#$00,#$00,#$7F,#$00,#$00,#$80,#$00,#$00,#$91,#$00,#$00,#$A2,#$00,#$00,#$B3,#$00,#$00,
#$C4,#$00,#$00,#$D5,#$00,#$00,#$E6,#$00,#$00,#$F7,#$00
```

I1V2: db (current injection on first ring and voltage measurement on second ring)

```
#$00,#$08,#$11,#$00,#$19,#$11,#$00,#$2A,#$11,#$00,#$3B,#$11,#$00,#$4C,#$11,#$00,#$5D,#$11,#$
00,#$6E,#$11,#$00,#$7F,#$11,#$00,#$80,#$11,#$00,#$91,#$11,#$00,#$A2,#$11,#$00,#$B3,#$11,#$00,
#$C4,#$11,#$00,#$D5,#$11,#$00,#$E6,#$11,#$00,#$F7,#$11
```

I1V3: db (current injection on first ring and voltage measurement on third ring)

```
#$00,#$08,#$22,#$00,#$19,#$22,#$00,#$2A,#$22,#$00,#$3B,#$22,#$00,#$4C,#$22,#$00,#$5D,#$22,#$
00,#$6E,#$22,#$00,#$7F,#$22,#$00,#$80,#$22,#$00,#$91,#$22,#$00,#$A2,#$22,#$00,#$B3,#$22,#$00,
#$C4,#$22,#$00,#$D5,#$22,#$00,#$E6,#$22,#$00,#$F7,#$22
```

I1V4: db (current injection on first ring and voltage measurement on fourth ring)

```
#$00,#$08,#$33,#$00,#$19,#$33,#$00,#$2A,#$33,#$00,#$3B,#$33,#$00,#$4C,#$33,#$00,#$5D,#$33,#$
00,#$6E,#$33,#$00,#$7F,#$33,#$00,#$80,#$33,#$00,#$91,#$33,#$00,#$A2,#$33,#$00,#$B3,#$33,#$00,
#$C4,#$33,#$00,#$D5,#$33,#$00,#$E6,#$33,#$00,#$F7,#$33
```

I2V1: db (current injection on second ring and voltage measurement on first ring)

```
#$11,#$08,#$00,#$11,#$19,#$00,#$11,#$2A,#$00,#$11,#$3B,#$00,#$11,#$4C,#$00,#$11,#$5D,#$00,#$
11,#$6E,#$00,#$11,#$7F,#$00,#$11,#$80,#$00,#$11,#$91,#$00,#$11,#$A2,#$00,#$11,#$B3,#$00,#$11,
#$C4,#$00,#$11,#$D5,#$00,#$11,#$E6,#$00,#$11,#$F7,#$00
```

I2V2: db (current injection on second ring and voltage measurement on second ring)

```
#$11,#$08,#$11,#$11,#$19,#$11,#$11,#$2A,#$11,#$11,#$3B,#$11,#$11,#$4C,#$11,#$11,#$5D,#$11,#$
11,#$6E,#$11,#$11,#$7F,#$11,#$11,#$80,#$11,#$11,#$91,#$11,#$11,#$A2,#$11,#$11,#$B3,#$11,#$11,
#$C4,#$11,#$11,#$D5,#$11,#$11,#$E6,#$11,#$11,#$F7,#$11
```

I2v3: db (current injection on second ring and voltage measurement on third ring)

```
#$11,#$08,#$22,#$11,#$19,#$22,#$11,#$2A,#$22,#$11,#$3B,#$22,#$11,#$4C,#$22,#$11,#$5D,#$22,#$
11,#$6E,#$22,#$11,#$7F,#$22,#$11,#$80,#$22,#$11,#$91,#$22,#$11,#$A2,#$22,#$11,#$B3,#$22,#$11,
#$C4,#$22,#$11,#$D5,#$22,#$11,#$E6,#$22,#$11,#$F7,#$22
```

I2V4: db (current injection on second ring and voltage measurement on fourth ring)

```
#$11,#$08,#$33,#$11,#$19,#$33,#$11,#$2A,#$33,#$11,#$3B,#$33,#$11,#$4C,#$33,#$11,#$5D,#$33,#$
11,#$6E,#$33,#$11,#$7F,#$33,#$11,#$80,#$33,#$11,#$91,#$33,#$11,#$A2,#$33,#$11,#$B3,#$33,#$11,
#$C4,#$33,#$11,#$D5,#$33,#$11,#$E6,#$33,#$11,#$F7,#$33
```

I3V1: db (current injection on third ring and voltage measurement on first ring)

```
#$22,#$08,#$00,#$22,#$19,#$00,#$22,#$2A,#$00,#$22,#$3B,#$00,#$22,#$4C,#$00,#$22,#$5D,#$00,#$
22,#$6E,#$00,#$22,#$7F,#$00,#$22,#$80,#$00,#$22,#$91,#$00,#$22,#$A2,#$00,#$22,#$B3,#$00,#$22,
#$C4,#$00,#$22,#$D5,#$00,#$22,#$E6,#$00,#$22,#$F7,#$00
```

I3V2: db (current injection on third ring and voltage measurement on second ring)

```
#$22,#$08,#$11,#$22,#$19,#$11,#$22,#$2A,#$11,#$22,#$3B,#$11,#$22,#$4C,#$11,#$22,#$5D,#$11,#$
22,#$6E,#$11,#$22,#$7F,#$11,#$22,#$80,#$11,#$22,#$91,#$11,#$22,#$A2,#$11,#$22,#$B3,#$11,#$22,
#$C4,#$11,#$22,#$D5,#$11,#$22,#$E6,#$11,#$22,#$F7,#$11
```

I3v3: db (current injection on third ring and voltage measurement on third ring)

```
#$22,#$08,#$22,#$22,#$19,#$22,#$22,#$2A,#$22,#$22,#$3B,#$22,#$22,#$4C,#$22,#$22,#$5D,#$22,#$
22,#$6E,#$22,#$22,#$7F,#$22,#$22,#$80,#$22,#$22,#$91,#$22,#$22,#$A2,#$22,#$22,#$B3,#$22,#$22,
#$C4,#$22,#$22,#$D5,#$22,#$22,#$E6,#$22,#$22,#$F7,#$22
```

I3V4: db (current injection on third ring and voltage measurement on fourth ring)

```
#$22,#$08,#$33,#$22,#$19,#$33,#$22,#$2A,#$33,#$22,#$3B,#$33,#$22,#$4C,#$33,#$22,#$5D,#$33,#$
22,#$6E,#$33,#$22,#$7F,#$33,#$22,#$80,#$33,#$22,#$91,#$33,#$22,#$A2,#$33,#$22,#$B3,#$33,#$22,
#$C4,#$33,#$22,#$D5,#$33,#$22,#$E6,#$33,#$22,#$F7,#$33
```

I4V1: db (current injection on fourth ring and voltage measurement on first ring)

```
#$33,#$08,#$00,#$33,#$19,#$00,#$33,#$2A,#$00,#$33,#$3B,#$00,#$33,#$4C,#$00,#$33,#$5D,#$00,#$
33,#$6E,#$00,#$33,#$7F,#$00,#$33,#$80,#$00,#$33,#$91,#$00,#$33,#$A2,#$00,#$33,#$B3,#$00,#$33,
#$C4,#$00,#$33,#$D5,#$00,#$33,#$E6,#$00,#$33,#$F7,#$00
```

I4V2: db (current injection on fourth ring and voltage measurement on second ring)

```
#$33,#$08,#$11,#$33,#$19,#$11,#$33,#$2A,#$11,#$33,#$3B,#$11,#$33,#$4C,#$11,#$33,#$5D,#$11,#$
33,#$6E,#$11,#$33,#$7F,#$11,#$33,#$80,#$11,#$33,#$91,#$11,#$33,#$A2,#$11,#$33,#$B3,#$11,#$33,
#$C4,#$11,#$33,#$D5,#$11,#$33,#$E6,#$11,#$33,#$F7,#$11
```

I4v3: db (current injection on fourth ring and voltage measurement on third ring)

```
#$33,#$08,#$22,#$33,#$19,#$22,#$33,#$2A,#$22,#$33,#$3B,#$22,#$33,#$4C,#$22,#$33,#$5D,#$22,#$
33,#$6E,#$22,#$33,#$7F,#$22,#$33,#$80,#$22,#$33,#$91,#$22,#$33,#$A2,#$22,#$33,#$B3,#$22,#$33,
#$C4,#$22,#$33,#$D5,#$22,#$33,#$E6,#$22,#$33,#$F7,#$22
```

I4V4: db (current injection on fourth ring and voltage measurement on fourth ring)

```
#$33,#$08,#$33,#$33,#$19,#$33,#$33,#$2A,#$33,#$33,#$3B,#$33,#$33,#$4C,#$33,#$33,#$5D,#$33,#$
33,#$6E,#$33,#$33,#$7F,#$33,#$33,#$80,#$33,#$33,#$91,#$33,#$33,#$A2,#$33,#$33,#$B3,#$33,#$33,
#$C4,#$33,#$33,#$D5,#$33,#$33,#$E6,#$33,#$33,#$F7,#$33
```

APPENDIX D

Electrode Select Sequence Table Format for Current Stimulations and Voltage Measurement in a Two, Three and Four rings Electrode systems

D1 :

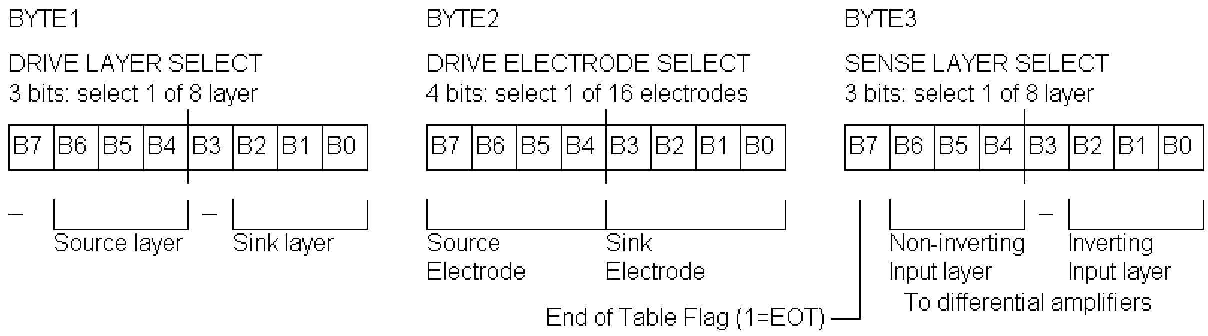

Figure D1: Electrode select sequence table format

D2 :

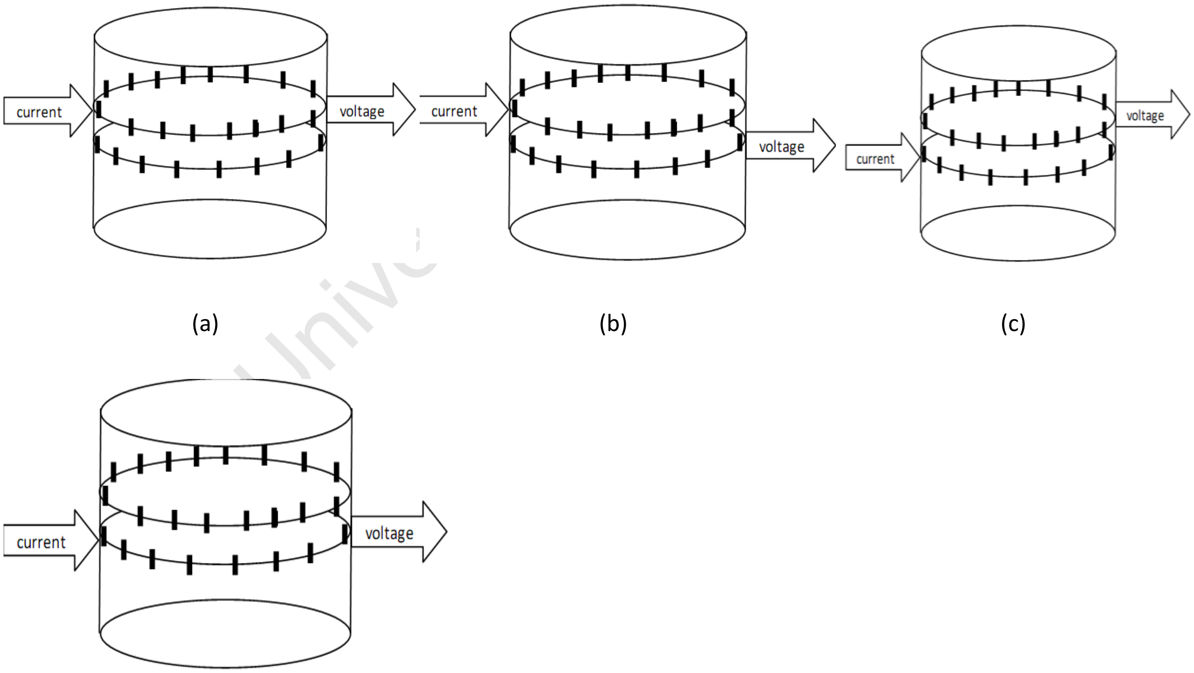

(a)

(b)

(c)

(d)

Figure D2. Diagrams **(a)** - **(d)** show the implementation figure D1 for sequence of current injections and voltage measurements to collecting data for 3-D image reconstruction using the two rings electrodes system. **(a)** Stimulation of current in first ring and measurement in the first ring, **(b)** Stimulation of current in first ring and measurement in the second ring, **(c)** Stimulation of current in second ring and measurement in the first ring and **(d)** Stimulation of current in second ring and measurement in the second ring.

D3 :

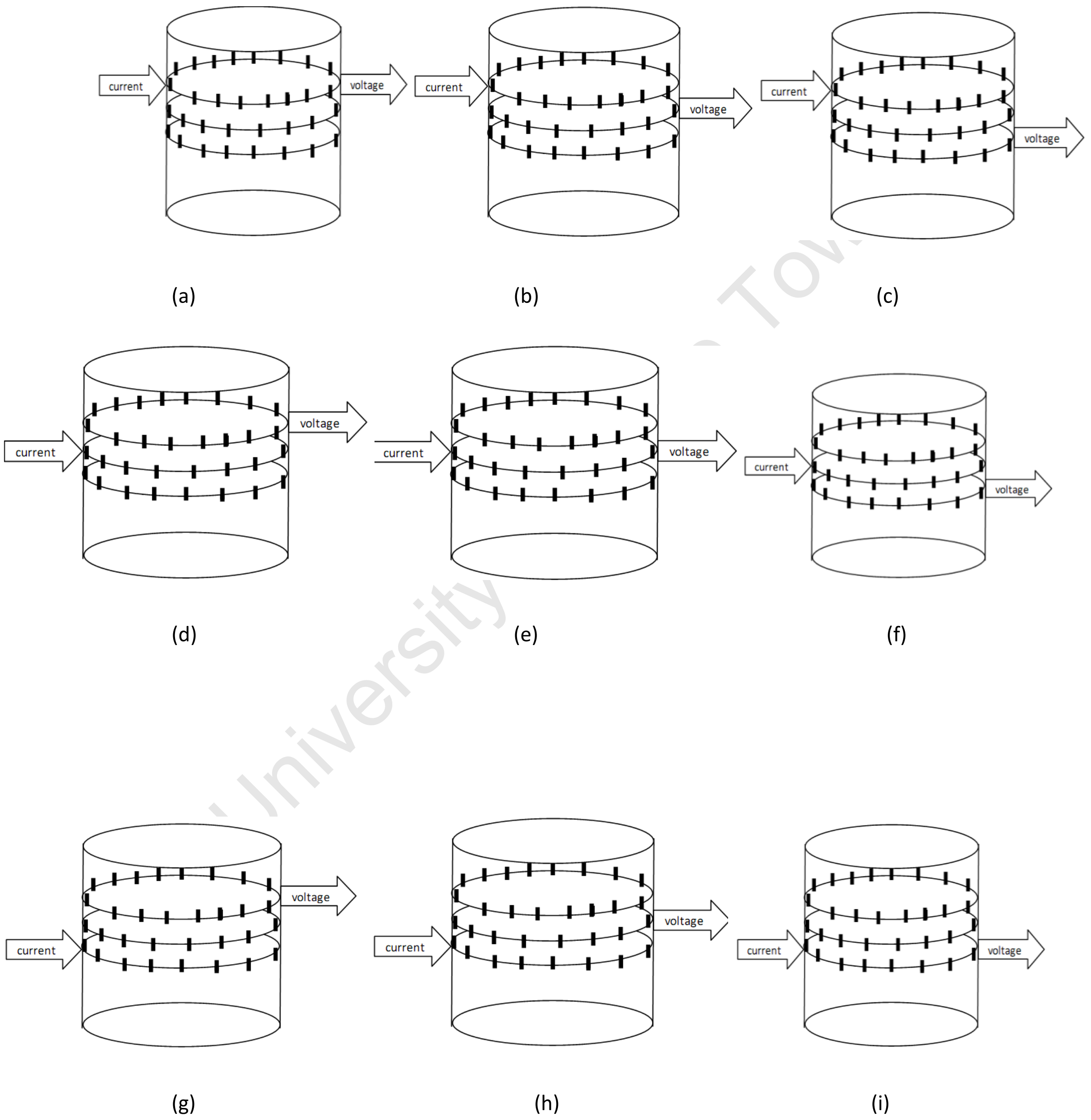

Figure D3. Diagrams **(a)** - **(i)** show the implementation of figure D1 for sequence of current injection and voltage measurement for collecting data for 3-D image reconstruction for three rings. **(a)** Stimulation of current in first ring and measurement in the same ring, **(b)** Stimulation of current in first ring and measurement in the second ring, **(c)** Stimulation of current in first ring and measurement in the third ring, **(d)** Stimulation of current in second ring and measurement in the first ring, **(e)** Stimulation of current in second ring and measurement in the second ring, **(f)** Stimulation of current in second ring and measurement in the third ring, **(g)** Stimulation of current in third ring and measurement in the first ring, **(h)** Stimulation of current in third ring and measurement in the second ring, **(i)** Stimulation of current in third ring and measurement in the third ring.

D4 :

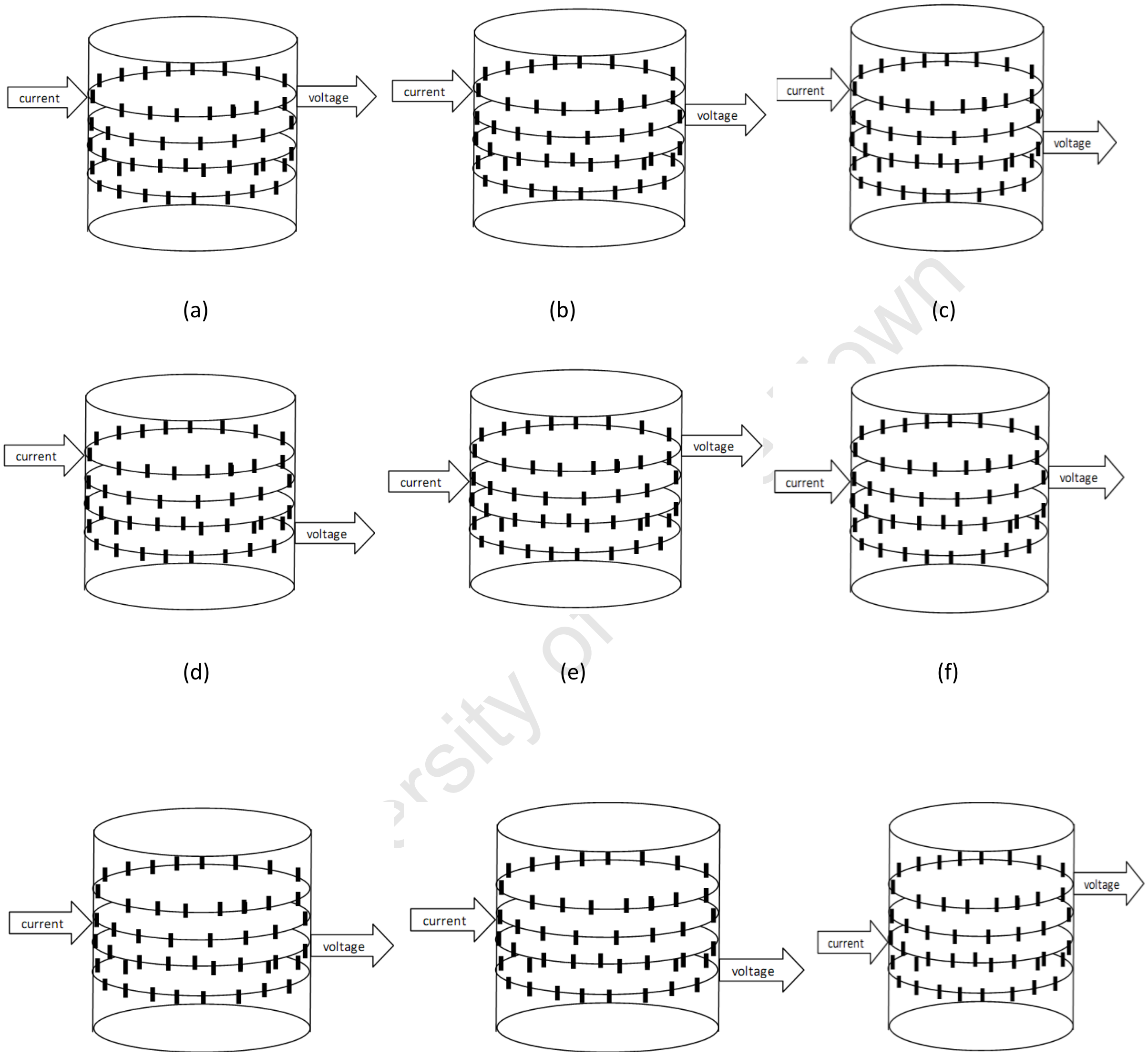

(a) (b) (c)

(d) (e) (f)

(g) (h) (i)

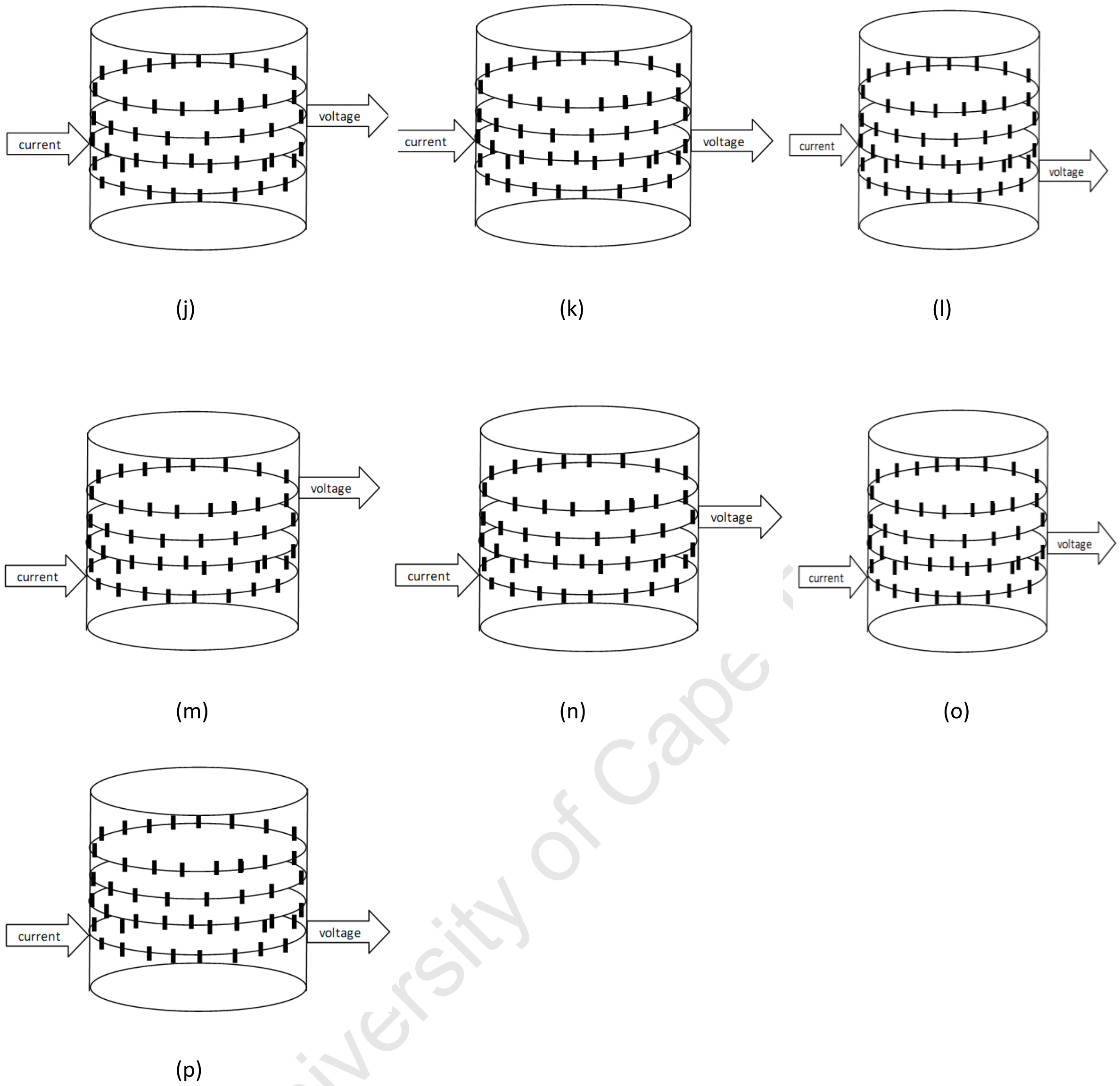

Figure D4: Diagrams **(a) - (p)** show the implementation of figure D1 for sequence of current injection and voltage measurement for collecting data for 3-D image reconstruction for four rings . **(a)** Stimulation of current in first ring and measurement in the same ring, **(b)** Stimulation of current in first ring and measurement in the second ring, **(c)** Stimulation of current in first ring and measurement in the third ring,**(d)** Stimulation of current in first ring and measurement in the fourth ring , **(e)** Stimulation of current in second ring and measurement in the first ring, **(f)** Stimulation of current in second ring and measurement in the second ring, **(g)** Stimulation of current in second ring and measurement in the third ring, **(h)** Stimulation of current in second ring and measurement in the fourth ring, **(i)** Stimulation of current in third ring and measurement in the first ring, **(j)** Stimulation of current in third ring and measurement in the second ring, **(k)** Stimulation of current in third ring and measurement in the third ring, **(l)** Stimulation of current in third ring and measurement in the fourth ring, **(m)** Stimulation of current in fourth ring and measurement in the first ring, **(n)** Stimulation of current in fourth ring and measurement in the second ring**, (o)** Stimulation of current in fourth ring and measurement in the third ring, **(p)** Stimulation of current in fourth ring and measurement in the fourth ring.

APPENDIX E: Data Sorting Format for The Required Measured Voltage for Image Reconstruction

E1 : Table E1: Selection of 13 data per stimulation yielding 208 data out of 256 data from 16 current stimulation through adjacent electrodes in a ring. Shaded readings are unused leaving out 13 data plotted for each of the 16 "u" curves in figure 2.13

S/N	E1/E	E2/E	E3/E	E4/E	E5/E	E6/E	E7/E8	E8/E	E9/E	E10/E	E11/	E12/	E13/E1	E14/E1	E15/	E16/
1	■	■														■
2	■	■	■													
3		■	■	■												
4			■	■	■											
5				■	■	■										
6					■	■	■									
7						■	■	■								
8							■	■	■							
9								■	■	■						
10									■	■	■					
11										■	■	■				
12											■	■	■			
13												■	■	■		
14													■	■	■	
15														■	■	■
16	■														■	■

E2 : Table E2: Selection of 12 data per stimulation yielding 192 data out of 256 data from 16 current stimulation through adjacent electrodes in a ring. Shaded readings are unused leaving out 12 data plotted for each of the 16 curves in figure 2.13

S/N	E1/E	E2/E	E3/E	E4/E	E5/E	E6/E	E7/E8	E8/E	E9/E	E10/E	E11/	E12/	E13/E1	E14/E1	E15/	E16/
1	■							■	■							■
2	■	■							■	■						
3		■	■							■	■					
4			■	■							■	■				
5				■	■							■	■			
6					■	■							■	■		
7						■	■							■	■	
8							■	■							■	■
9	■							■	■							■
10	■	■							■	■						
11		■	■							■	■					
12			■	■							■	■				
13				■	■							■	■			
14					■	■							■	■		
15						■	■							■	■	
16							■	■							■	■

APPENDIX F

Writing of Measurement Sequence Tables for Two, Three and Four Rings Electrode Systems Considering a Sequence of Current Stimulations through Opposite and Adjacent Electrode pairs (Addressing the Forward Problem of the UCT Tomography Rig)

An understanding acquired from the exploration of the stimulation function, $mk\_stim\_patterns$ of EIDORS by studying the format of data in the $stim.stim\_pattern$ function lead to the development of six measurement sequence tables for the two, three and four rings electrode system with regard to current stimulation through opposite and adjacent electrode pairs. The six measurement sequence tables were used to investigate the statement by Paivii (1999), who stated that the more independent measured data are obtained, the better the expected spatial resolution. The sequence tables which specify the position of the current injection electrode pair, voltage measurement electrode pair, ring of current injection electrode pair and the ring of voltage measurement electrode pair were developed from the format shown in figure 3.9. The six measurement sequence tables, three of which are for current injection through adjacent electrode pairs in two, three and four rings and the other three for current injection through opposite electrode pairs in two, three and four rings, are displayed in section 2.1.1 to 2.1.6 of the appendix.

Plots of measured voltage data from an array of rings on loading the measurement sequence table into a C++ code that runs the UCT tomography rig are displayed in figures 5.7 to 5.10. It was observed that rings of electrodes off the plane of current injection ring detected the electric field signals introduced into the conductive medium due to current stimulation. This shows that electric field flux is a surfaces and not curve, thus, disproving the assumption by Barber and Brown (1983) who in early days of electrical imaging research assumed isopotentials are curves rather than surfaces (Adler *et al*. 2006).

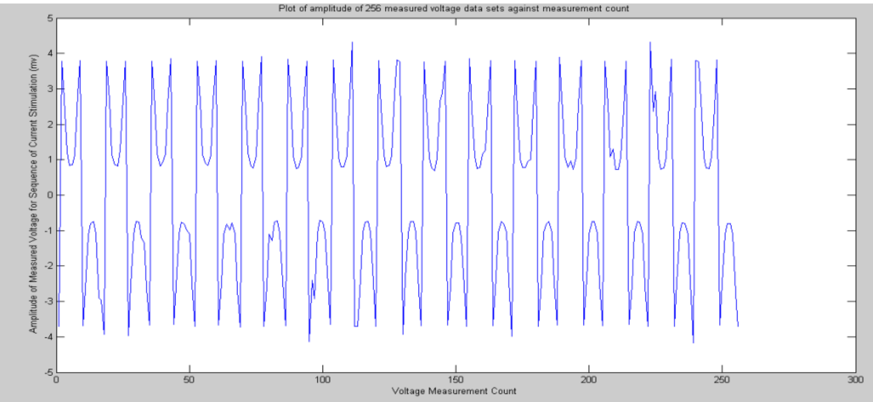

Figure F.1. A frame of 256 measured voltage signals made on the first ring due to a sequence of current injections through opposite electrode pairs in the first ring in a four rings electrode system.

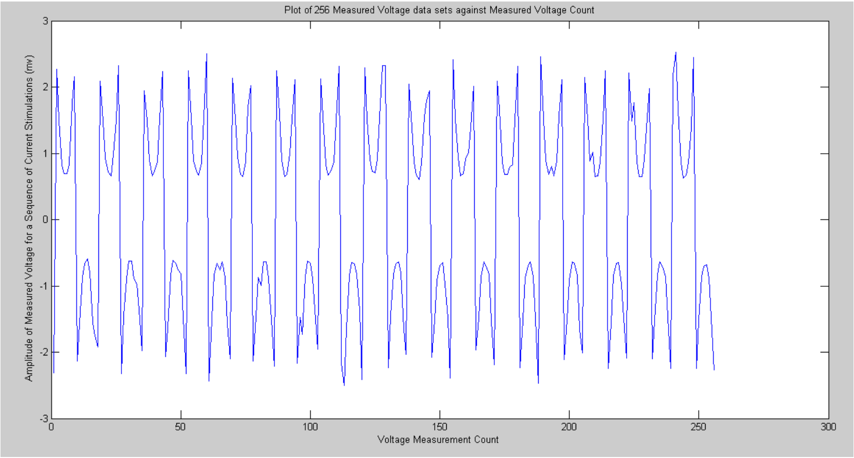

Figure F.2. A frame of 256 measured voltage signals made on the second ring due to a sequence of current injections through opposite electrode pairs in the first ring in a four rings electrode system.

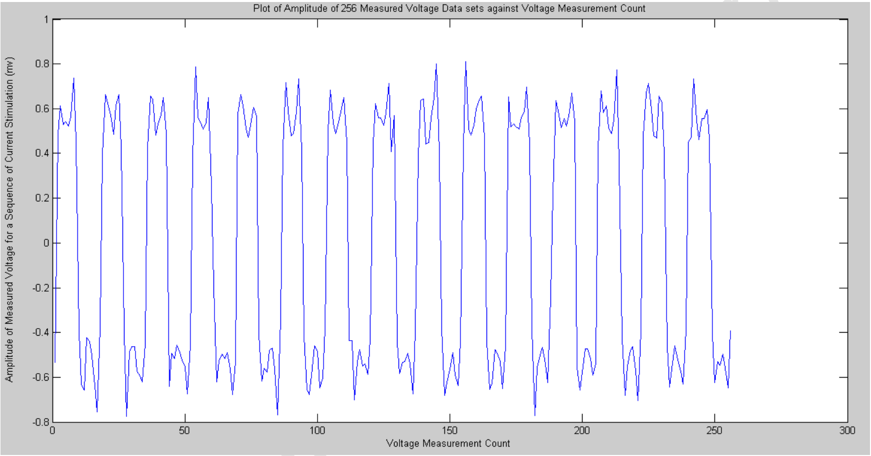

Figure F.3. A frame of 256 measured voltage signals made on the third ring due to a sequence of current injections through opposite electrode pairs in the first ring in a four rings electrode system.

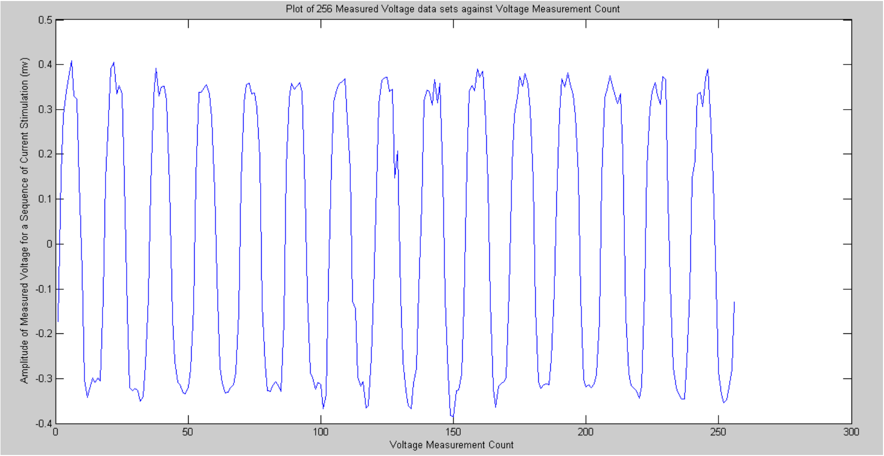

Figure F.4. A frame of 256 measured voltage signals made on the fourth ring due to a sequence of current injections through opposite electrode pairs in the first ring in a four rings electrode system.

The plots also confirm the assertion by Jossinet and Kardous (1987) who observed from their work on multi-electrode phantom study that sensitivity out of plane containing the injection electrode is far from being negligible. More importantly, the plots inform that the reconstruction of a complete 3-D image requires measurement of voltage on all planes, even if currents are only driven through one plane at a time for a system with several planes of electrodes as the flux spread out in all direction. This agrees with the suggestion of Polidorides *et al* (2002) for voltage measurement to reconstructing 3-D images.

Relative to the maximum amplitude of measured voltage signal in the current injection ring (the first ring), the maximum amplitude of measured voltage signals in the second, third and fourth ring decreases progressively from the first ring to the fourth ring. The maximum amplitude in the first, second, third and fourth ring are 4.3274mv, 2.5232mv, 0.8112mv and 0.4083mv respectively. The trend of progressive decrease in the maximum amplitude of the measured voltage signal from a set of rings at various distances from the current injection ring is in good agreement with the physical relationship between electric field potential at a point and the mean distance of the ring of electric charges from that point. That is, the magnitude of electric potential at a point is inversely proportional to the distance of the source of the electric field (rings of charges) from that point.

APPENDIX G

Writing of MATLAB Function Code to Load the Measured Voltage Signals from the Boundary of A Two, Three and Four Rings Electrode System Considering a Sequence of Current Stimulation through Opposite and Adjacent Electrode pairs

(Addressing the Inverse Problem of the UCT Tomography Rig)

Following the analysis of the sequence of simulated measured voltage data sets as contained in the $stim.meas\_pattern$ function included within the $mk\_stim\_pattern$ function of EIDORS, eighteen MATLAB loading functions were developed. For each of the six reconstruction codes written, three loading functions were written for loading measured voltage data from the boundary of the UCT rig containing a homogeneous solution with no current stimulation, a homogeneous solution with fixed magnitude of current stimulation and an inhomogeneous solution with a fixed magnitude of current stimulation respectively. The eighteen loading functions are highlighted in table 3.3. The three loading functions for each of the six reconstruction codes were written the same way, though each code for the loading of different measured voltage data sets. The six distinct loading functions for each of the six reconstruction code are written in appendix H1 through to H6.

APPENDIX H

MATLAB Functions for Loading Data to the Reconstruction Codes of the Two, Three and Four Rings Electrodes System

H1 : Loading Function for Adjacent Voltage Measurement Resulting from Stimulation through Opposite Electrode Pairs in A Two Rings Electrode System (i.e. "`meas_inhomo2rg_opp`", " `getcalibrationdata4rings_opp_no_current` " and " `getcalibrationdata4rings_opp_current` " were written the same form)

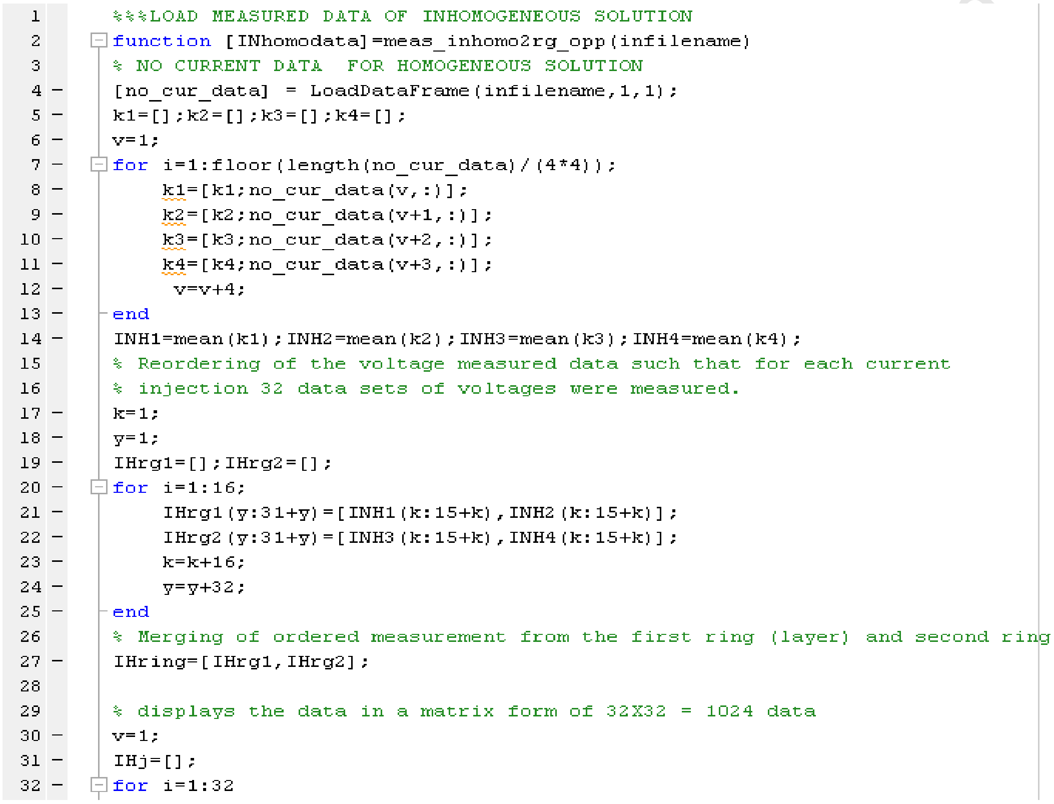

```
 %%%LOAD MEASURED DATA OF INHOMOGENEOUS SOLUTION
function [INhomodata]=meas_inhomo2rg_opp(infilename)
% NO CURRENT DATA  FOR HOMOGENEOUS SOLUTION
[no_cur_data] = LoadDataFrame(infilename,1,1);
k1=[];k2=[];k3=[];k4=[];
v=1;
for i=1:floor(length(no_cur_data)/(4*4));
    k1=[k1;no_cur_data(v,:)];
    k2=[k2;no_cur_data(v+1,:)];
    k3=[k3;no_cur_data(v+2,:)];
    k4=[k4;no_cur_data(v+3,:)];
     v=v+4;
end
INH1=mean(k1);INH2=mean(k2);INH3=mean(k3);INH4=mean(k4);
% Reordering of the voltage measured data such that for each current
% injection 32 data sets of voltages were measured.
k=1;
y=1;
IHrg1=[];IHrg2=[];
for i=1:16;
    IHrg1(y:31+y)=[INH1(k:15+k),INH2(k:15+k)];
    IHrg2(y:31+y)=[INH3(k:15+k),INH4(k:15+k)];
    k=k+16;
    y=y+32;
end
% Merging of ordered measurement from the first ring (layer) and second ring( layer)
IHring=[IHrg1,IHrg2];

% displays the data in a matrix form of 32X32 = 1024 data
v=1;
IHj=[];
for i=1:32
```

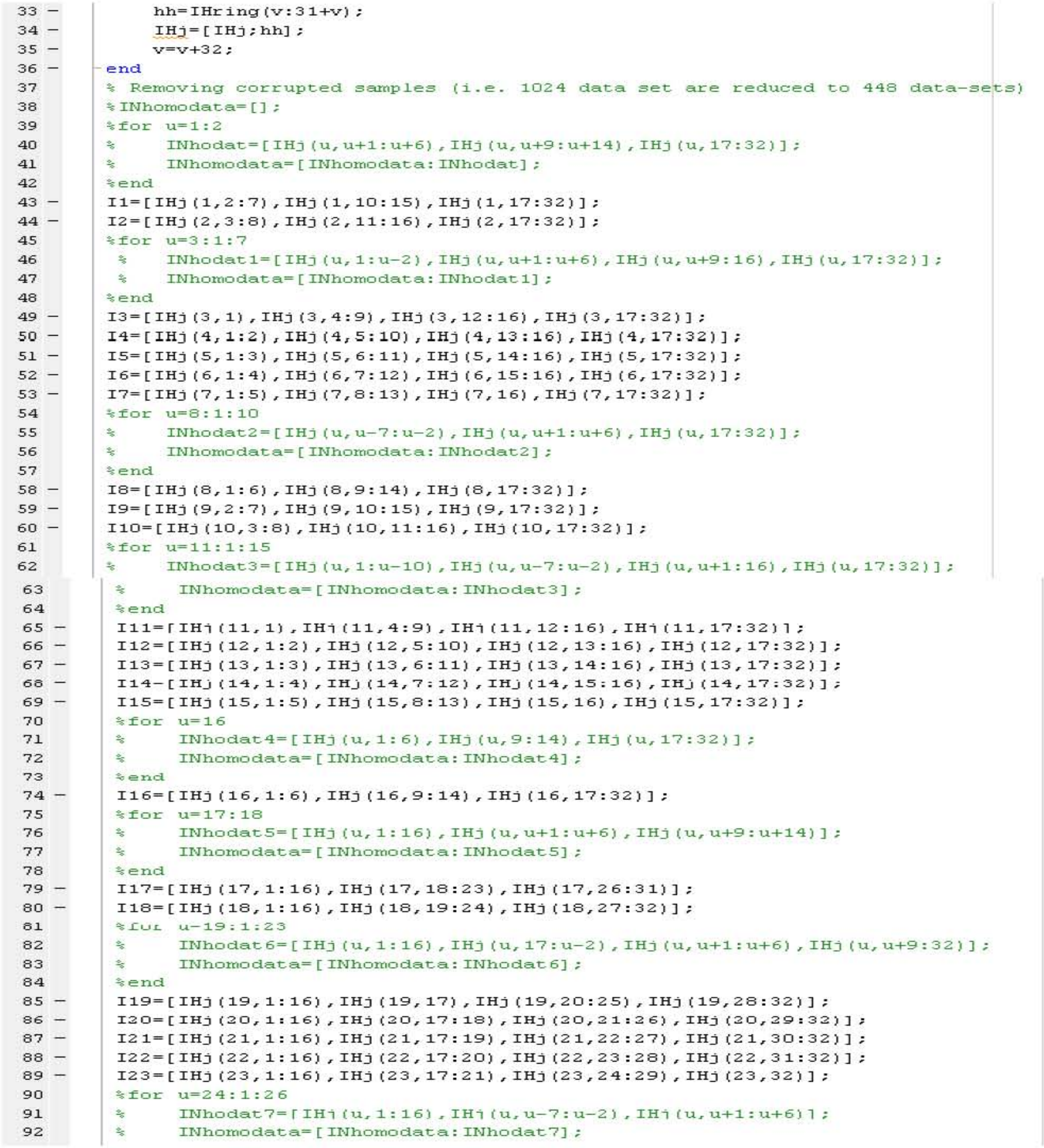

```
    hh=IHring(v:31+v);
    IHj=[IHj;hh];
    v=v+32;
end
% Removing corrupted samples (i.e. 1024 data set are reduced to 448 data-sets)
%INhomodata=[];
%for u=1:2
%     INhodat=[IHj(u,u+1:u+6),IHj(u,u+9:u+14),IHj(u,17:32)];
%     INhomodata=[INhomodata:INhodat];
%end
I1=[IHj(1,2:7),IHj(1,10:15),IHj(1,17:32)];
I2=[IHj(2,3:8),IHj(2,11:16),IHj(2,17:32)];
%for u=3:1:7
 %    INhodat1=[IHj(u,1:u-2),IHj(u,u+1:u+6),IHj(u,u+9:16),IHj(u,17:32)];
 %    INhomodata=[INhomodata:INhodat1];
%end
I3=[IHj(3,1),IHj(3,4:9),IHj(3,12:16),IHj(3,17:32)];
I4=[IHj(4,1:2),IHj(4,5:10),IHj(4,13:16),IHj(4,17:32)];
I5=[IHj(5,1:3),IHj(5,6:11),IHj(5,14:16),IHj(5,17:32)];
I6=[IHj(6,1:4),IHj(6,7:12),IHj(6,15:16),IHj(6,17:32)];
I7=[IHj(7,1:5),IHj(7,8:13),IHj(7,16),IHj(7,17:32)];
%for u=8:1:10
%     INhodat2=[IHj(u,u-7:u-2),IHj(u,u+1:u+6),IHj(u,17:32)];
%     INhomodata=[INhomodata:INhodat2];
%end
I8=[IHj(8,1:6),IHj(8,9:14),IHj(8,17:32)];
I9=[IHj(9,2:7),IHj(9,10:15),IHj(9,17:32)];
I10=[IHj(10,3:8),IHj(10,11:16),IHj(10,17:32)];
%for u=11:1:15
%     INhodat3=[IHj(u,1:u-10),IHj(u,u-7:u-2),IHj(u,u+1:16),IHj(u,17:32)];
%     INhomodata=[INhomodata:INhodat3];
%end
I11=[IHj(11,1),IHj(11,4:9),IHj(11,12:16),IHj(11,17:32)];
I12=[IHj(12,1:2),IHj(12,5:10),IHj(12,13:16),IHj(12,17:32)];
I13=[IHj(13,1:3),IHj(13,6:11),IHj(13,14:16),IHj(13,17:32)];
I14=[IHj(14,1:4),IHj(14,7:12),IHj(14,15:16),IHj(14,17:32)];
I15=[IHj(15,1:5),IHj(15,8:13),IHj(15,16),IHj(15,17:32)];
%for u=16
%     INhodat4=[IHj(u,1:6),IHj(u,9:14),IHj(u,17:32)];
%     INhomodata=[INhomodata:INhodat4];
%end
I16=[IHj(16,1:6),IHj(16,9:14),IHj(16,17:32)];
%for u=17:18
%     INhodat5=[IHj(u,1:16),IHj(u,u+1:u+6),IHj(u,u+9:u+14)];
%     INhomodata=[INhomodata:INhodat5];
%end
I17=[IHj(17,1:16),IHj(17,18:23),IHj(17,26:31)];
I18=[IHj(18,1:16),IHj(18,19:24),IHj(18,27:32)];
%for u=19:1:23
%     INhodat6=[IHj(u,1:16),IHj(u,17:u-2),IHj(u,u+1:u+6),IHj(u,u+9:32)];
%     INhomodata=[INhomodata:INhodat6];
%end
I19=[IHj(19,1:16),IHj(19,17),IHj(19,20:25),IHj(19,28:32)];
I20=[IHj(20,1:16),IHj(20,17:18),IHj(20,21:26),IHj(20,29:32)];
I21=[IHj(21,1:16),IHj(21,17:19),IHj(21,22:27),IHj(21,30:32)];
I22=[IHj(22,1:16),IHj(22,17:20),IHj(22,23:28),IHj(22,31:32)];
I23=[IHj(23,1:16),IHj(23,17:21),IHj(23,24:29),IHj(23,32)];
%for u=24:1:26
%     INhodat7=[IHj(u,1:16),IHj(u,u-7:u-2),IHj(u,u+1:u+6)];
%     INhomodata=[INhomodata:INhodat7];
```

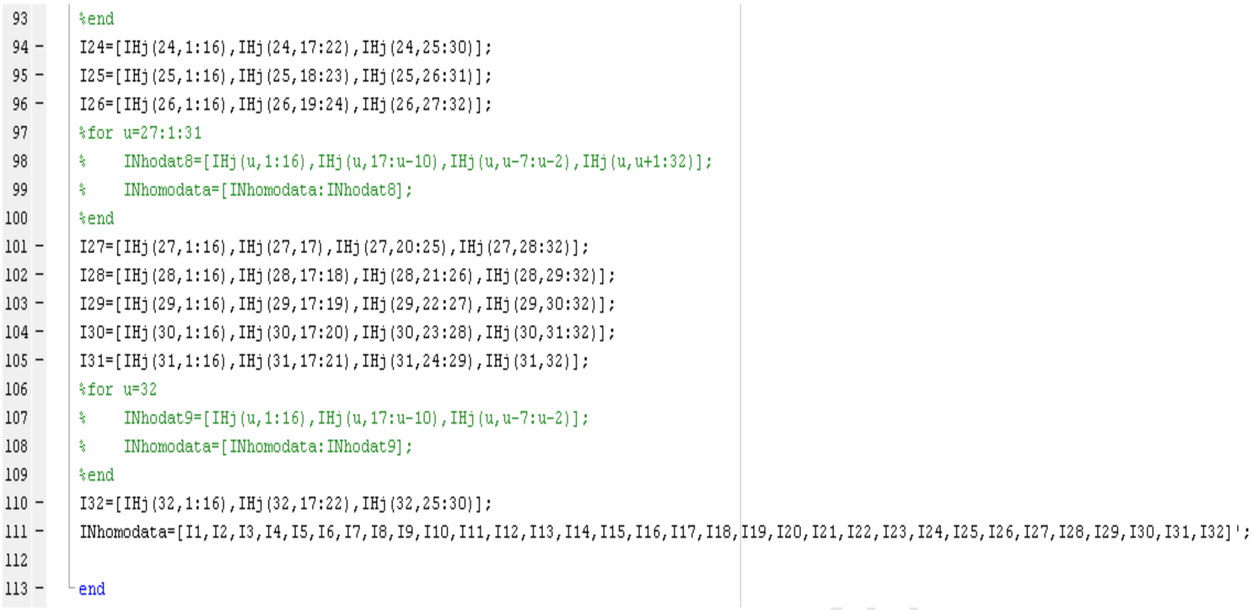

```
%end
I24=[IHj(24,1:16),IHj(24,17:22),IHj(24,25:30)];
I25=[IHj(25,1:16),IHj(25,18:23),IHj(25,26:31)];
I26=[IHj(26,1:16),IHj(26,19:24),IHj(26,27:32)];
%for u=27:1:31
%    INhodat8=[IHj(u,1:16),IHj(u,17:u-10),IHj(u,u-7:u-2),IHj(u,u+1:32)];
%    INhomodata=[INhomodata:INhodat8];
%end
I27=[IHj(27,1:16),IHj(27,17),IHj(27,20:25),IHj(27,28:32)];
I28=[IHj(28,1:16),IHj(28,17:18),IHj(28,21:26),IHj(28,29:32)];
I29=[IHj(29,1:16),IHj(29,17:19),IHj(29,22:27),IHj(29,30:32)];
I30=[IHj(30,1:16),IHj(30,17:20),IHj(30,23:28),IHj(30,31:32)];
I31=[IHj(31,1:16),IHj(31,17:21),IHj(31,24:29),IHj(31,32)];
%for u=32
%    INhodat9=[IHj(u,1:16),IHj(u,17:u-10),IHj(u,u-7:u-2)];
%    INhomodata=[INhomodata:INhodat9];
%end
I32=[IHj(32,1:16),IHj(32,17:22),IHj(32,25:30)];
INhomodata=[I1,I2,I3,I4,I5,I6,I7,I8,I9,I10,I11,I12,I13,I14,I15,I16,I17,I18,I19,I20,I21,I22,I23,I24,I25,I26,I27,I28,I29,I30,I31,I32]';

end
```

H2 : Loading Function for Adjacent Voltage Measurement Resulting from Stimulation through Adjacent Electrode Pairs in A Two Rings Electrode System (i.e. " `meas_inhomo2rg_adjacent`", "`getcalibrationdata2rg_adjacent_current`" and "`getcalibrationdata2rg_adjacent_nocurrent`" were written the same form)

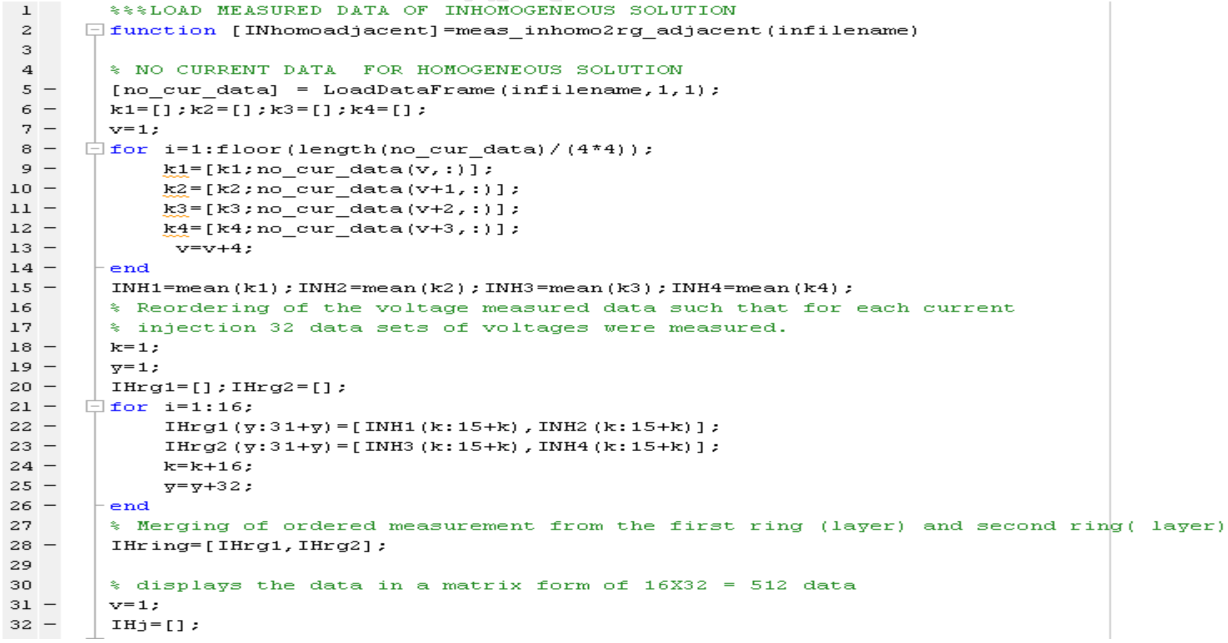

```
%%%LOAD MEASURED DATA OF INHOMOGENEOUS SOLUTION
function [INhomoadjacent]=meas_inhomo2rg_adjacent(infilename)

% NO CURRENT DATA  FOR HOMOGENEOUS SOLUTION
[no_cur_data] = LoadDataFrame(infilename,1,1);
k1=[];k2=[];k3=[];k4=[];
v=1;
for i=1:floor(length(no_cur_data)/(4*4));
    k1=[k1;no_cur_data(v,:)];
    k2=[k2;no_cur_data(v+1,:)];
    k3=[k3;no_cur_data(v+2,:)];
    k4=[k4;no_cur_data(v+3,:)];
     v=v+4;
end
INH1=mean(k1);INH2=mean(k2);INH3=mean(k3);INH4=mean(k4);
% Reordering of the voltage measured data such that for each current
% injection 32 data sets of voltages were measured.
k=1;
y=1;
IHrg1=[];IHrg2=[];
for i=1:16;
    IHrg1(y:31+y)=[INH1(k:15+k),INH2(k:15+k)];
    IHrg2(y:31+y)=[INH3(k:15+k),INH4(k:15+k)];
    k=k+16;
    y=y+32;
end
% Merging of ordered measurement from the first ring (layer) and second ring( layer)
IHring=[IHrg1,IHrg2];

% displays the data in a matrix form of 16X32 = 512 data
v=1;
IHj=[];
```

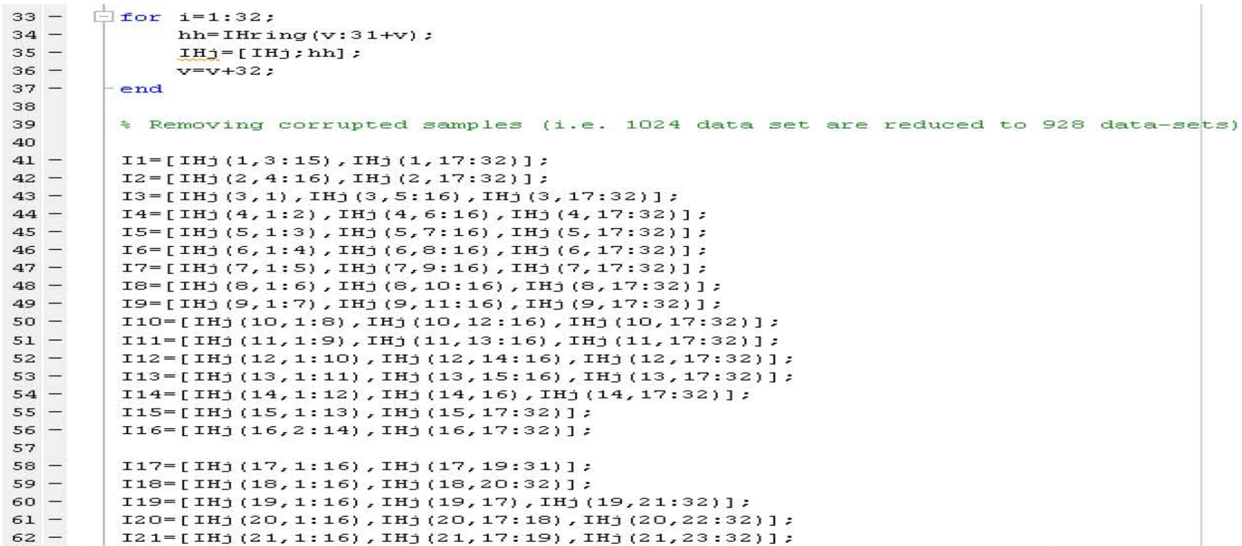

```
for i=1:32;
    hh=IHring(v:31+v);
    IHj=[IHj;hh];
    v=v+32;
end

% Removing corrupted samples (i.e. 1024 data set are reduced to 928 data-sets)

I1=[IHj(1,3:15),IHj(1,17:32)];
I2=[IHj(2,4:16),IHj(2,17:32)];
I3=[IHj(3,1),IHj(3,5:16),IHj(3,17:32)];
I4=[IHj(4,1:2),IHj(4,6:16),IHj(4,17:32)];
I5=[IHj(5,1:3),IHj(5,7:16),IHj(5,17:32)];
I6=[IHj(6,1:4),IHj(6,8:16),IHj(6,17:32)];
I7=[IHj(7,1:5),IHj(7,9:16),IHj(7,17:32)];
I8=[IHj(8,1:6),IHj(8,10:16),IHj(8,17:32)];
I9=[IHj(9,1:7),IHj(9,11:16),IHj(9,17:32)];
I10=[IHj(10,1:8),IHj(10,12:16),IHj(10,17:32)];
I11=[IHj(11,1:9),IHj(11,13:16),IHj(11,17:32)];
I12=[IHj(12,1:10),IHj(12,14:16),IHj(12,17:32)];
I13=[IHj(13,1:11),IHj(13,15:16),IHj(13,17:32)];
I14=[IHj(14,1:12),IHj(14,16),IHj(14,17:32)];
I15=[IHj(15,1:13),IHj(15,17:32)];
I16=[IHj(16,2:14),IHj(16,17:32)];

I17=[IHj(17,1:16),IHj(17,19:31)];
I18=[IHj(18,1:16),IHj(18,20:32)];
I19=[IHj(19,1:16),IHj(19,17),IHj(19,21:32)];
I20=[IHj(20,1:16),IHj(20,17:18),IHj(20,22:32)];
I21=[IHj(21,1:16),IHj(21,17:19),IHj(21,23:32)];
```

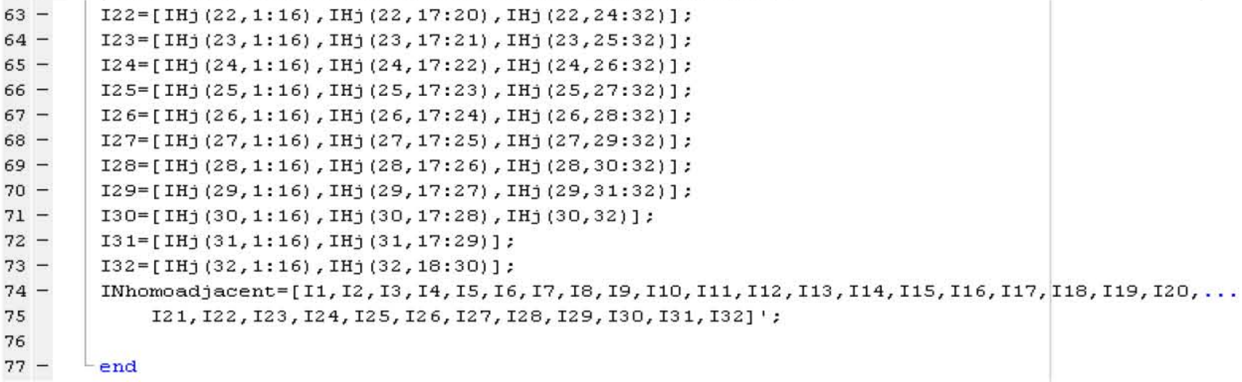

```
I22=[IHj(22,1:16),IHj(22,17:20),IHj(22,24:32)];
I23=[IHj(23,1:16),IHj(23,17:21),IHj(23,25:32)];
I24=[IHj(24,1:16),IHj(24,17:22),IHj(24,26:32)];
I25=[IHj(25,1:16),IHj(25,17:23),IHj(25,27:32)];
I26=[IHj(26,1:16),IHj(26,17:24),IHj(26,28:32)];
I27=[IHj(27,1:16),IHj(27,17:25),IHj(27,29:32)];
I28=[IHj(28,1:16),IHj(28,17:26),IHj(28,30:32)];
I29=[IHj(29,1:16),IHj(29,17:27),IHj(29,31:32)];
I30=[IHj(30,1:16),IHj(30,17:28),IHj(30,32)];
I31=[IHj(31,1:16),IHj(31,17:29)];
I32=[IHj(32,1:16),IHj(32,18:30)];
INhomoadjacent=[I1,I2,I3,I4,I5,I6,I7,I8,I9,I10,I11,I12,I13,I14,I15,I16,I17,I18,I19,I20,...
    I21,I22,I23,I24,I25,I26,I27,I28,I29,I30,I31,I32]';

end
```

H3 : Loading Function for Adjacent Voltage Measurement Resulting from Stimulation through Opposite Electrode Pairs in A Three Rings Electrode System (i.e. "meas_3rginhomo", " getcalibrationdata3rings_opp_currrent " and " getcalibrationdata3rings_opp_nocurrent " were written the same form)

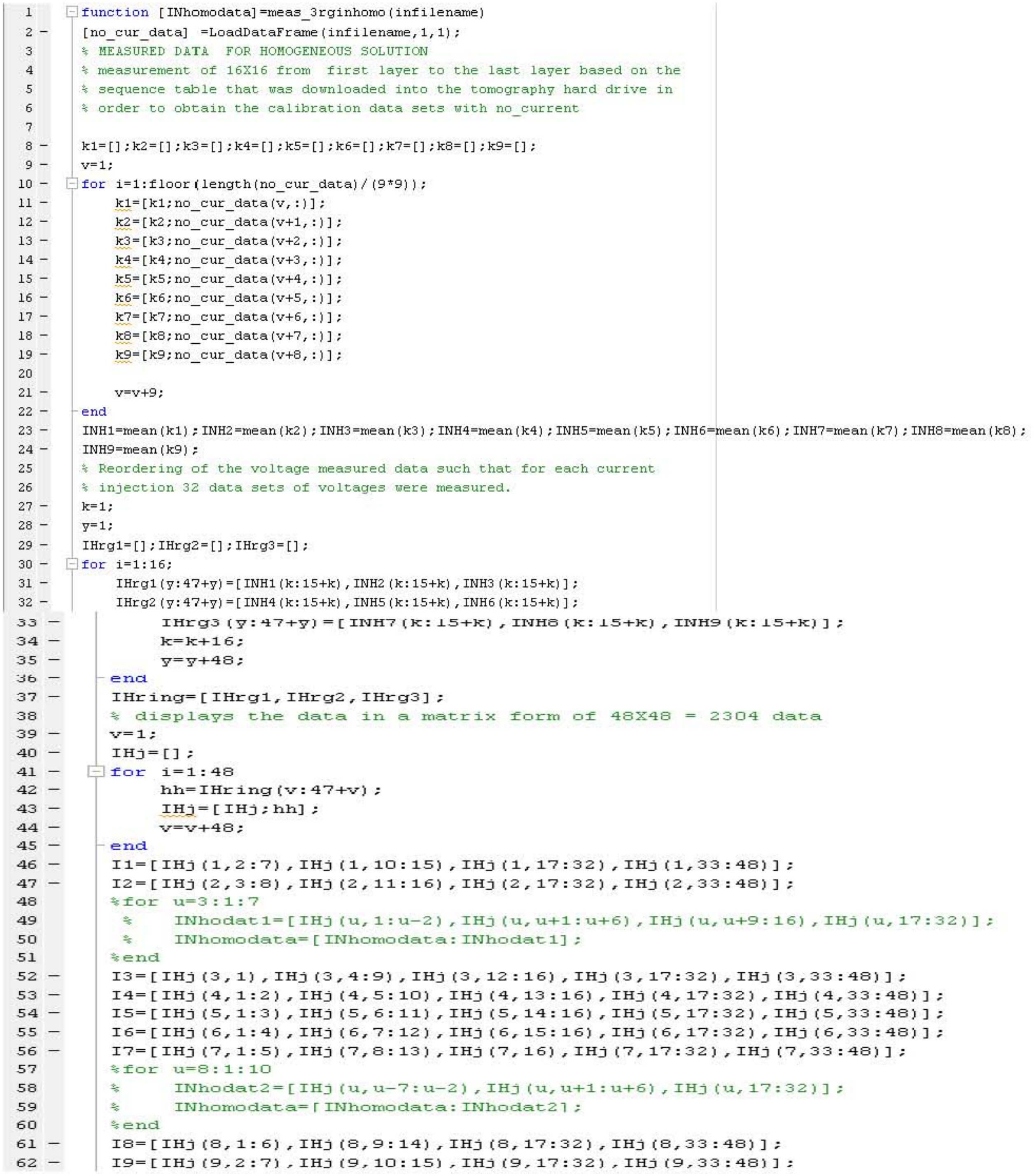

```
function [INhomodata]=meas_3rginhomo(infilename)
[no_cur_data] =LoadDataFrame(infilename,1,1);
% MEASURED DATA  FOR HOMOGENEOUS SOLUTION
% measurement of 16X16 from  first layer to the last layer based on the
% sequence table that was downloaded into the tomography hard drive in
% order to obtain the calibration data sets with no_current

k1=[];k2=[];k3=[];k4=[];k5=[];k6=[];k7=[];k8=[];k9=[];
v=1;
for i=1:floor(length(no_cur_data)/(9*9));
    k1=[k1;no_cur_data(v,:)];
    k2=[k2;no_cur_data(v+1,:)];
    k3=[k3;no_cur_data(v+2,:)];
    k4=[k4;no_cur_data(v+3,:)];
    k5=[k5;no_cur_data(v+4,:)];
    k6=[k6;no_cur_data(v+5,:)];
    k7=[k7;no_cur_data(v+6,:)];
    k8=[k8;no_cur_data(v+7,:)];
    k9=[k9;no_cur_data(v+8,:)];

    v=v+9;
end
INH1=mean(k1);INH2=mean(k2);INH3=mean(k3);INH4=mean(k4);INH5=mean(k5);INH6=mean(k6);INH7=mean(k7);INH8=mean(k8);
INH9=mean(k9);
% Reordering of the voltage measured data such that for each current
% injection 32 data sets of voltages were measured.
k=1;
y=1;
IHrg1=[];IHrg2=[];IHrg3=[];
for i=1:16;
    IHrg1(y:47+y)=[INH1(k:15+k),INH2(k:15+k),INH3(k:15+k)];
    IHrg2(y:47+y)=[INH4(k:15+k),INH5(k:15+k),INH6(k:15+k)];
    IHrg3(y:47+y)=[INH7(k:15+k),INH8(k:15+k),INH9(k:15+k)];
    k=k+16;
    y=y+48;
end
IHring=[IHrg1,IHrg2,IHrg3];
% displays the data in a matrix form of 48X48 = 2304 data
v=1;
IHj=[];
for i=1:48
    hh=IHring(v:47+v);
    IHj=[IHj;hh];
    v=v+48;
end
I1=[IHj(1,2:7),IHj(1,10:15),IHj(1,17:32),IHj(1,33:48)];
I2=[IHj(2,3:8),IHj(2,11:16),IHj(2,17:32),IHj(2,33:48)];
%for u=3:1:7
 %    INhodat1=[IHj(u,1:u-2),IHj(u,u+1:u+6),IHj(u,u+9:16),IHj(u,17:32)];
 %    INhomodata=[INhomodata:INhodat1];
%end
I3=[IHj(3,1),IHj(3,4:9),IHj(3,12:16),IHj(3,17:32),IHj(3,33:48)];
I4=[IHj(4,1:2),IHj(4,5:10),IHj(4,13:16),IHj(4,17:32),IHj(4,33:48)];
I5=[IHj(5,1:3),IHj(5,6:11),IHj(5,14:16),IHj(5,17:32),IHj(5,33:48)];
I6=[IHj(6,1:4),IHj(6,7:12),IHj(6,15:16),IHj(6,17:32),IHj(6,33:48)];
I7=[IHj(7,1:5),IHj(7,8:13),IHj(7,16),IHj(7,17:32),IHj(7,33:48)];
%for u=8:1:10
%     INhodat2=[IHj(u,u-7:u-2),IHj(u,u+1:u+6),IHj(u,17:32)];
%     INhomodata=[INhomodata:INhodat2];
%end
I8=[IHj(8,1:6),IHj(8,9:14),IHj(8,17:32),IHj(8,33:48)];
I9=[IHj(9,2:7),IHj(9,10:15),IHj(9,17:32),IHj(9,33:48)];
```

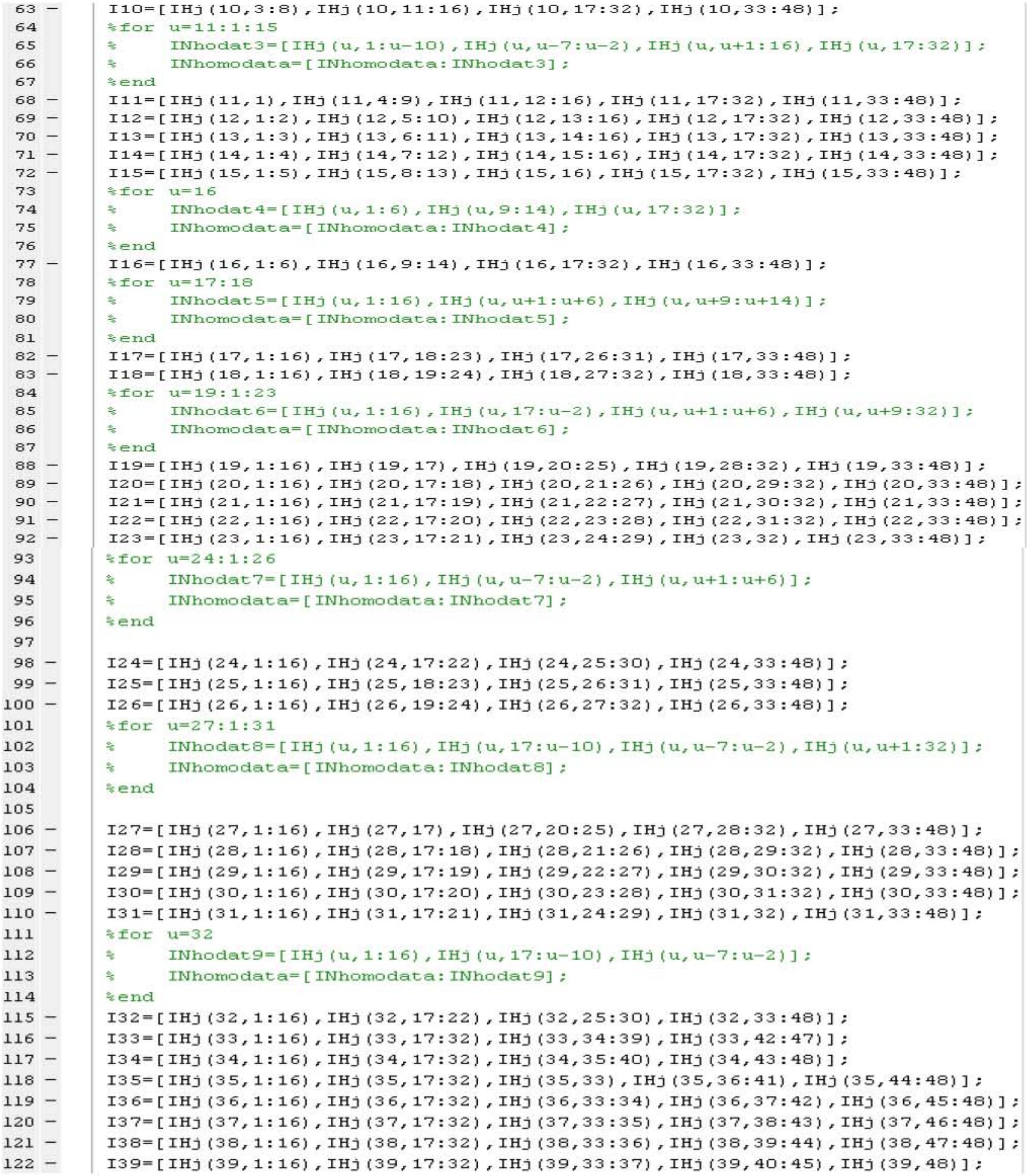

```
I10=[IHj(10,3:8),IHj(10,11:16),IHj(10,17:32),IHj(10,33:48)];
%for u=11:1:15
%     INhodat3=[IHj(u,1:u-10),IHj(u,u-7:u-2),IHj(u,u+1:16),IHj(u,17:32)];
%     INhomodata=[INhomodata:INhodat3];
%end
I11=[IHj(11,1),IHj(11,4:9),IHj(11,12:16),IHj(11,17:32),IHj(11,33:48)];
I12=[IHj(12,1:2),IHj(12,5:10),IHj(12,13:16),IHj(12,17:32),IHj(12,33:48)];
I13=[IHj(13,1:3),IHj(13,6:11),IHj(13,14:16),IHj(13,17:32),IHj(13,33:48)];
I14=[IHj(14,1:4),IHj(14,7:12),IHj(14,15:16),IHj(14,17:32),IHj(14,33:48)];
I15=[IHj(15,1:5),IHj(15,8:13),IHj(15,16),IHj(15,17:32),IHj(15,33:48)];
%for u=16
%     INhodat4=[IHj(u,1:6),IHj(u,9:14),IHj(u,17:32)];
%     INhomodata=[INhomodata:INhodat4];
%end
I16=[IHj(16,1:6),IHj(16,9:14),IHj(16,17:32),IHj(16,33:48)];
%for u=17:18
%     INhodat5=[IHj(u,1:16),IHj(u,u+1:u+6),IHj(u,u+9:u+14)];
%     INhomodata=[INhomodata:INhodat5];
%end
I17=[IHj(17,1:16),IHj(17,18:23),IHj(17,26:31),IHj(17,33:48)];
I18=[IHj(18,1:16),IHj(18,19:24),IHj(18,27:32),IHj(18,33:48)];
%for u=19:1:23
%     INhodat6=[IHj(u,1:16),IHj(u,17:u-2),IHj(u,u+1:u+6),IHj(u,u+9:32)];
%     INhomodata=[INhomodata:INhodat6];
%end
I19=[IHj(19,1:16),IHj(19,17),IHj(19,20:25),IHj(19,28:32),IHj(19,33:48)];
I20=[IHj(20,1:16),IHj(20,17:18),IHj(20,21:26),IHj(20,29:32),IHj(20,33:48)];
I21=[IHj(21,1:16),IHj(21,17:19),IHj(21,22:27),IHj(21,30:32),IHj(21,33:48)];
I22=[IHj(22,1:16),IHj(22,17:20),IHj(22,23:28),IHj(22,31:32),IHj(22,33:48)];
I23=[IHj(23,1:16),IHj(23,17:21),IHj(23,24:29),IHj(23,32),IHj(23,33:48)];
%for u=24:1:26
%     INhodat7=[IHj(u,1:16),IHj(u,u-7:u-2),IHj(u,u+1:u+6)];
%     INhomodata=[INhomodata:INhodat7];
%end

I24=[IHj(24,1:16),IHj(24,17:22),IHj(24,25:30),IHj(24,33:48)];
I25=[IHj(25,1:16),IHj(25,18:23),IHj(25,26:31),IHj(25,33:48)];
I26=[IHj(26,1:16),IHj(26,19:24),IHj(26,27:32),IHj(26,33:48)];
%for u=27:1:31
%     INhodat8=[IHj(u,1:16),IHj(u,17:u-10),IHj(u,u-7:u-2),IHj(u,u+1:32)];
%     INhomodata=[INhomodata:INhodat8];
%end

I27=[IHj(27,1:16),IHj(27,17),IHj(27,20:25),IHj(27,28:32),IHj(27,33:48)];
I28=[IHj(28,1:16),IHj(28,17:18),IHj(28,21:26),IHj(28,29:32),IHj(28,33:48)];
I29=[IHj(29,1:16),IHj(29,17:19),IHj(29,22:27),IHj(29,30:32),IHj(29,33:48)];
I30=[IHj(30,1:16),IHj(30,17:20),IHj(30,23:28),IHj(30,31:32),IHj(30,33:48)];
I31=[IHj(31,1:16),IHj(31,17:21),IHj(31,24:29),IHj(31,32),IHj(31,33:48)];
%for u=32
%     INhodat9=[IHj(u,1:16),IHj(u,17:u-10),IHj(u,u-7:u-2)];
%     INhomodata=[INhomodata:INhodat9];
%end
I32=[IHj(32,1:16),IHj(32,17:22),IHj(32,25:30),IHj(32,33:48)];
I33=[IHj(33,1:16),IHj(33,17:32),IHj(33,34:39),IHj(33,42:47)];
I34=[IHj(34,1:16),IHj(34,17:32),IHj(34,35:40),IHj(34,43:48)];
I35=[IHj(35,1:16),IHj(35,17:32),IHj(35,33),IHj(35,36:41),IHj(35,44:48)];
I36=[IHj(36,1:16),IHj(36,17:32),IHj(36,33:34),IHj(36,37:42),IHj(36,45:48)];
I37=[IHj(37,1:16),IHj(37,17:32),IHj(37,33:35),IHj(37,38:43),IHj(37,46:48)];
I38=[IHj(38,1:16),IHj(38,17:32),IHj(38,33:36),IHj(38,39:44),IHj(38,47:48)];
I39=[IHj(39,1:16),IHj(39,17:32),IHj(39,33:37),IHj(39,40:45),IHj(39,48)];
```

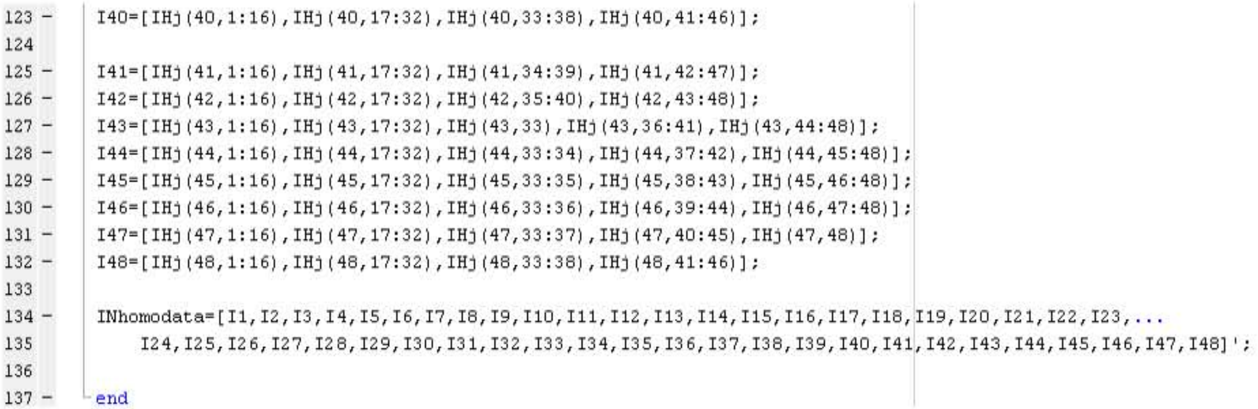

```
I40=[IHj(40,1:16),IHj(40,17:32),IHj(40,33:38),IHj(40,41:46)];

I41=[IHj(41,1:16),IHj(41,17:32),IHj(41,34:39),IHj(41,42:47)];
I42=[IHj(42,1:16),IHj(42,17:32),IHj(42,35:40),IHj(42,43:48)];
I43=[IHj(43,1:16),IHj(43,17:32),IHj(43,33),IHj(43,36:41),IHj(43,44:48)];
I44=[IHj(44,1:16),IHj(44,17:32),IHj(44,33:34),IHj(44,37:42),IHj(44,45:48)];
I45=[IHj(45,1:16),IHj(45,17:32),IHj(45,33:35),IHj(45,38:43),IHj(45,46:48)];
I46=[IHj(46,1:16),IHj(46,17:32),IHj(46,33:36),IHj(46,39:44),IHj(46,47:48)];
I47=[IHj(47,1:16),IHj(47,17:32),IHj(47,33:37),IHj(47,40:45),IHj(47,48)];
I48=[IHj(48,1:16),IHj(48,17:32),IHj(48,33:38),IHj(48,41:46)];

INhomodata=[I1,I2,I3,I4,I5,I6,I7,I8,I9,I10,I11,I12,I13,I14,I15,I16,I17,I18,I19,I20,I21,I22,I23,...
    I24,I25,I26,I27,I28,I29,I30,I31,I32,I33,I34,I35,I36,I37,I38,I39,I40,I41,I42,I43,I44,I45,I46,I47,I48]';

end
```

H4 : Loading Function for Adjacent Voltage Measurement Resulting from Stimulation through Adjacent Electrode Pairs in A Three Rings Electrode System (i.e. " `meas_inhomo_3rings_adjacent` ", " `getcalibrationdata3rings_adj_current`" and " `getcalibrationdata3rings_adj_no_current`" were written the same form)

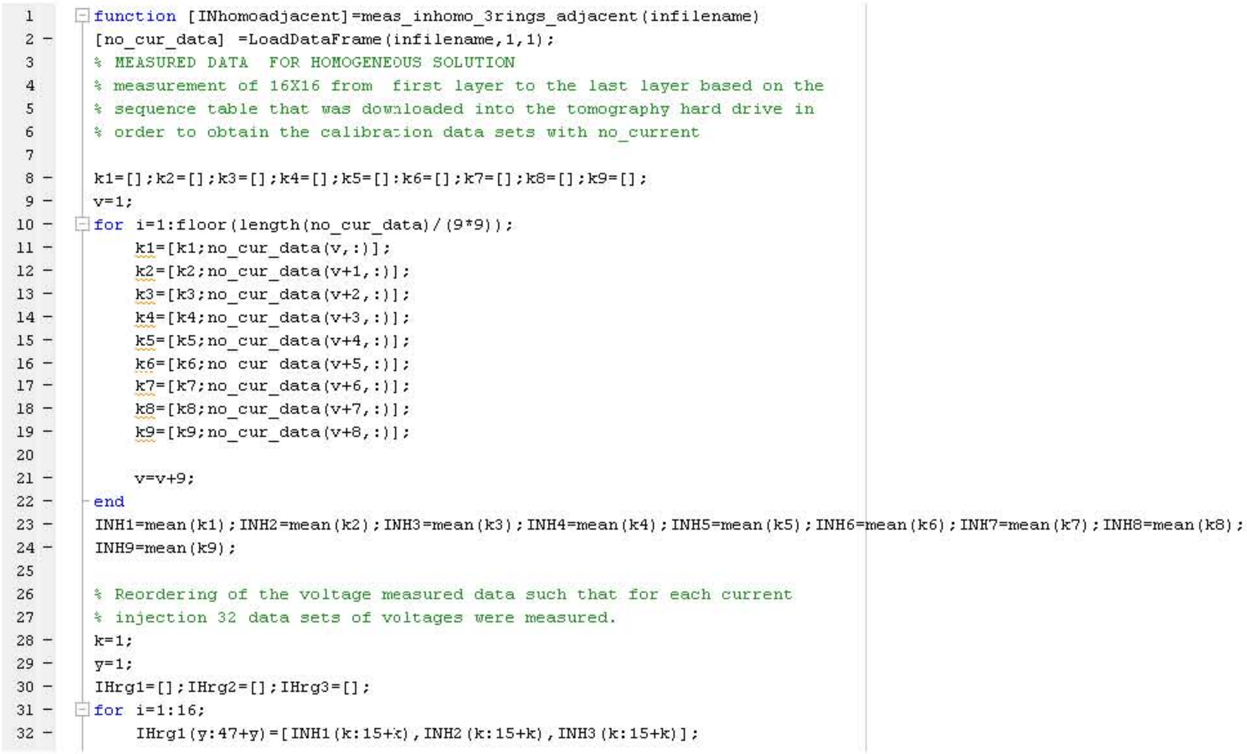

```matlab
function [INhomoadjacent]=meas_inhomo_3rings_adjacent(infilename)
[no_cur_data] =LoadDataFrame(infilename,1,1);
% MEASURED DATA  FOR HOMOGENEOUS SOLUTION
% measurement of 16X16 from  first layer to the last layer based on the
% sequence table that was downloaded into the tomography hard drive in
% order to obtain the calibration data sets with no_current

k1=[];k2=[];k3=[];k4=[];k5=[]:k6=[];k7=[];k8=[];k9=[];
v=1;
for i=1:floor(length(no_cur_data)/(9*9));
    k1=[k1;no_cur_data(v,:)];
    k2=[k2;no_cur_data(v+1,:)];
    k3=[k3;no_cur_data(v+2,:)];
    k4=[k4;no_cur_data(v+3,:)];
    k5=[k5;no_cur_data(v+4,:)];
    k6=[k6;no_cur_data(v+5,:)];
    k7=[k7;no_cur_data(v+6,:)];
    k8=[k8;no_cur_data(v+7,:)];
    k9=[k9;no_cur_data(v+8,:)];

    v=v+9;
end
INH1=mean(k1);INH2=mean(k2);INH3=mean(k3);INH4=mean(k4);INH5=mean(k5);INH6=mean(k6);INH7=mean(k7);INH8=mean(k8);
INH9=mean(k9);

% Reordering of the voltage measured data such that for each current
% injection 32 data sets of voltages were measured.
k=1;
y=1;
IHrg1=[];IHrg2=[];IHrg3=[];
for i=1:16;
    IHrg1(y:47+y)=[INH1(k:15+k),INH2(k:15+k),INH3(k:15+k)];
```

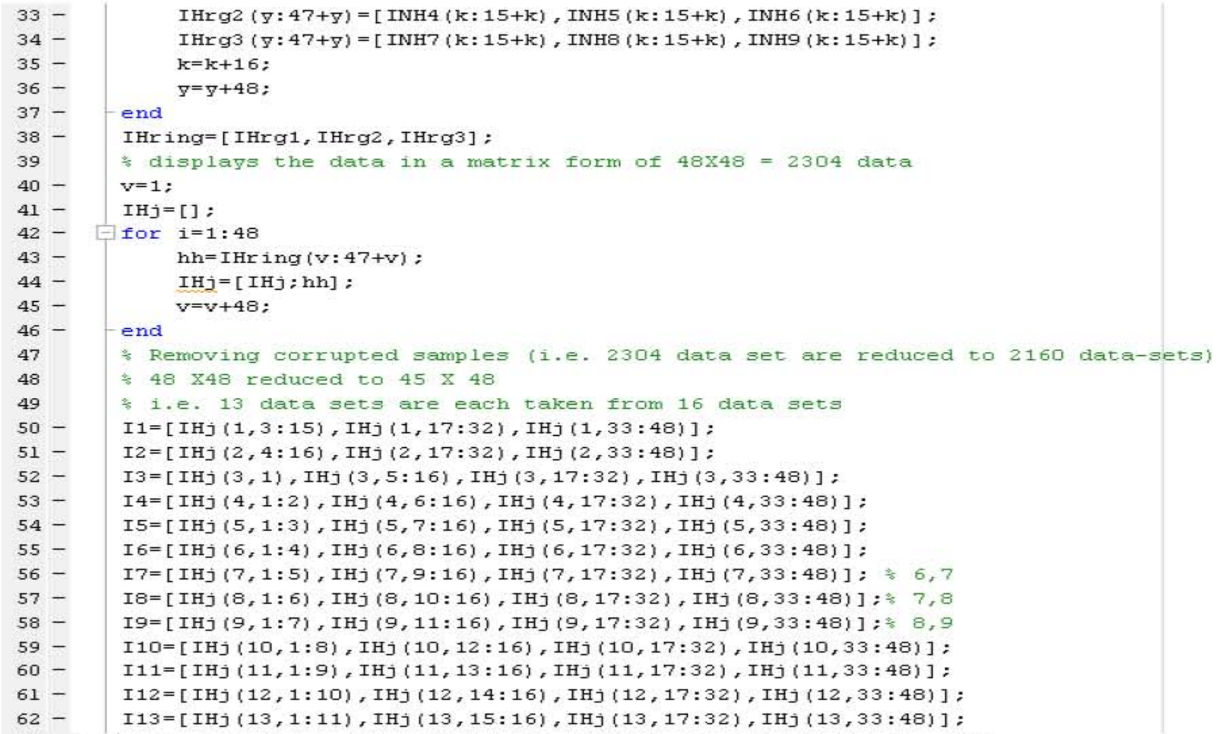

```
    IHrg2(y:47+y)=[INH4(k:15+k),INH5(k:15+k),INH6(k:15+k)];
    IHrg3(y:47+y)=[INH7(k:15+k),INH8(k:15+k),INH9(k:15+k)];
    k=k+16;
    y=y+48;
end
IHring=[IHrg1,IHrg2,IHrg3];
% displays the data in a matrix form of 48X48 = 2304 data
v=1;
IHj=[];
for i=1:48
    hh=IHring(v:47+v);
    IHj=[IHj;hh];
    v=v+48;
end
% Removing corrupted samples (i.e. 2304 data set are reduced to 2160 data-sets)
% 48 X48 reduced to 45 X 48
% i.e. 13 data sets are each taken from 16 data sets
I1=[IHj(1,3:15),IHj(1,17:32),IHj(1,33:48)];
I2=[IHj(2,4:16),IHj(2,17:32),IHj(2,33:48)];
I3=[IHj(3,1),IHj(3,5:16),IHj(3,17:32),IHj(3,33:48)];
I4=[IHj(4,1:2),IHj(4,6:16),IHj(4,17:32),IHj(4,33:48)];
I5=[IHj(5,1:3),IHj(5,7:16),IHj(5,17:32),IHj(5,33:48)];
I6=[IHj(6,1:4),IHj(6,8:16),IHj(6,17:32),IHj(6,33:48)];
I7=[IHj(7,1:5),IHj(7,9:16),IHj(7,17:32),IHj(7,33:48)]; % 6,7
I8=[IHj(8,1:6),IHj(8,10:16),IHj(8,17:32),IHj(8,33:48)];% 7,8
I9=[IHj(9,1:7),IHj(9,11:16),IHj(9,17:32),IHj(9,33:48)];% 8,9
I10=[IHj(10,1:8),IHj(10,12:16),IHj(10,17:32),IHj(10,33:48)];
I11=[IHj(11,1:9),IHj(11,13:16),IHj(11,17:32),IHj(11,33:48)];
I12=[IHj(12,1:10),IHj(12,14:16),IHj(12,17:32),IHj(12,33:48)];
I13=[IHj(13,1:11),IHj(13,15:16),IHj(13,17:32),IHj(13,33:48)];
```

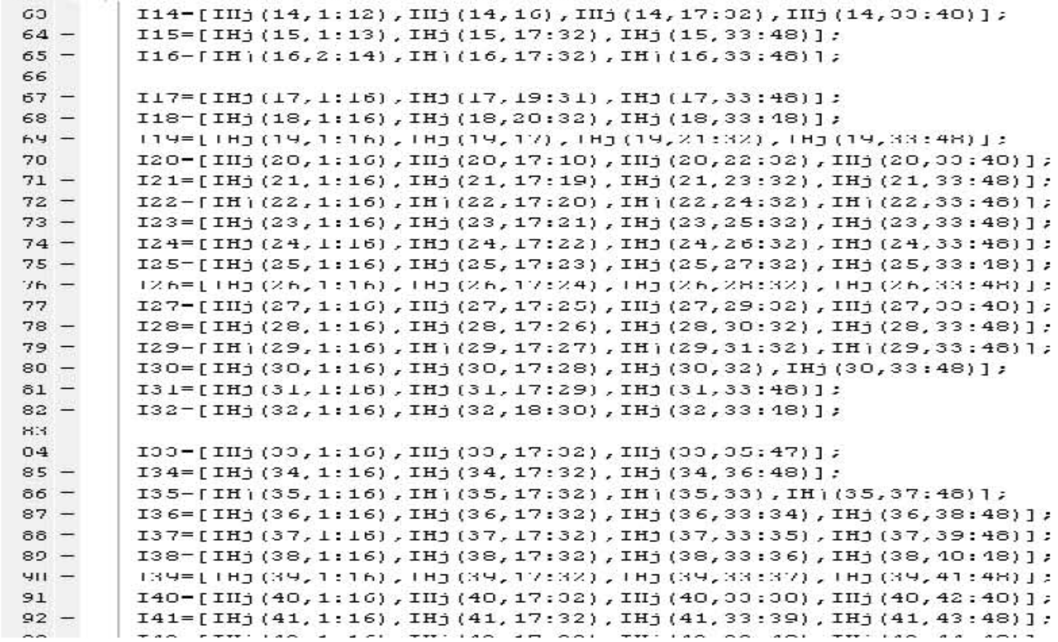

```
I14=[IHj(14,1:12),IHj(14,16),IHj(14,17:32),IHj(14,33:48)];
I15=[IHj(15,1:13),IHj(15,17:32),IHj(15,33:48)];
I16=[IHj(16,2:14),IHj(16,17:32),IHj(16,33:48)];

I17=[IHj(17,1:16),IHj(17,19:31),IHj(17,33:48)];
I18=[IHj(18,1:16),IHj(18,20:32),IHj(18,33:48)];
I19=[IHj(19,1:16),IHj(19,17),IHj(19,21:32),IHj(19,33:48)];
I20=[IHj(20,1:16),IHj(20,17:18),IHj(20,22:32),IHj(20,33:48)];
I21=[IHj(21,1:16),IHj(21,17:19),IHj(21,23:32),IHj(21,33:48)];
I22=[IHj(22,1:16),IHj(22,17:20),IHj(22,24:32),IHj(22,33:48)];
I23=[IHj(23,1:16),IHj(23,17:21),IHj(23,25:32),IHj(23,33:48)];
I24=[IHj(24,1:16),IHj(24,17:22),IHj(24,26:32),IHj(24,33:48)];
I25=[IHj(25,1:16),IHj(25,17:23),IHj(25,27:32),IHj(25,33:48)];
I26=[IHj(26,1:16),IHj(26,17:24),IHj(26,28:32),IHj(26,33:48)];
I27=[IHj(27,1:16),IHj(27,17:25),IHj(27,29:32),IHj(27,33:48)];
I28=[IHj(28,1:16),IHj(28,17:26),IHj(28,30:32),IHj(28,33:48)];
I29=[IHj(29,1:16),IHj(29,17:27),IHj(29,31:32),IHj(29,33:48)];
I30=[IHj(30,1:16),IHj(30,17:28),IHj(30,32),IHj(30,33:48)];
I31=[IHj(31,1:16),IHj(31,17:29),IHj(31,33:48)];
I32=[IHj(32,1:16),IHj(32,18:30),IHj(32,33:48)];

I33=[IHj(33,1:16),IHj(33,17:32),IHj(33,35:47)];
I34=[IHj(34,1:16),IHj(34,17:32),IHj(34,36:48)];
I35=[IHj(35,1:16),IHj(35,17:32),IHj(35,33),IHj(35,37:48)];
I36=[IHj(36,1:16),IHj(36,17:32),IHj(36,33:34),IHj(36,38:48)];
I37=[IHj(37,1:16),IHj(37,17:32),IHj(37,33:35),IHj(37,39:48)];
I38=[IHj(38,1:16),IHj(38,17:32),IHj(38,33:36),IHj(38,40:48)];
I39=[IHj(39,1:16),IHj(39,17:32),IHj(39,33:37),IHj(39,41:48)];
I40=[IHj(40,1:16),IHj(40,17:32),IHj(40,33:38),IHj(40,42:48)];
I41=[IHj(41,1:16),IHj(41,17:32),IHj(41,33:39),IHj(41,43:48)];
```

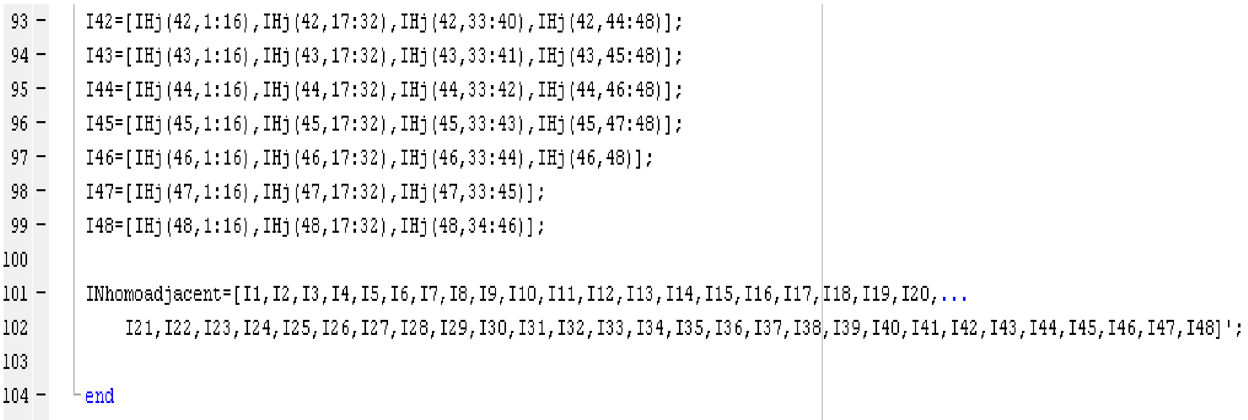

```
I42=[IHj(42,1:16),IHj(42,17:32),IHj(42,33:40),IHj(42,44:48)];
I43=[IHj(43,1:16),IHj(43,17:32),IHj(43,33:41),IHj(43,45:48)];
I44=[IHj(44,1:16),IHj(44,17:32),IHj(44,33:42),IHj(44,46:48)];
I45=[IHj(45,1:16),IHj(45,17:32),IHj(45,33:43),IHj(45,47:48)];
I46=[IHj(46,1:16),IHj(46,17:32),IHj(46,33:44),IHj(46,48)];
I47=[IHj(47,1:16),IHj(47,17:32),IHj(47,33:45)];
I48=[IHj(48,1:16),IHj(48,17:32),IHj(48,34:46)];

INhomoadjacent=[I1,I2,I3,I4,I5,I6,I7,I8,I9,I10,I11,I12,I13,I14,I15,I16,I17,I18,I19,I20,...
    I21,I22,I23,I24,I25,I26,I27,I28,I29,I30,I31,I32,I33,I34,I35,I36,I37,I38,I39,I40,I41,I42,I43,I44,I45,I46,I47,I48]';

end
```

H5 : Loading Function for Adjacent Voltage Measurement Resulting from Stimulation through Opposite Electrode Pairs in A Four Rings Electrode System (i.e. "`meas_4RINGShomo_OPP`", " `getcalibrationdata4rings_opp_no_current`" and " `getcalibrationdata4rings_opp_current`" were written the same form)

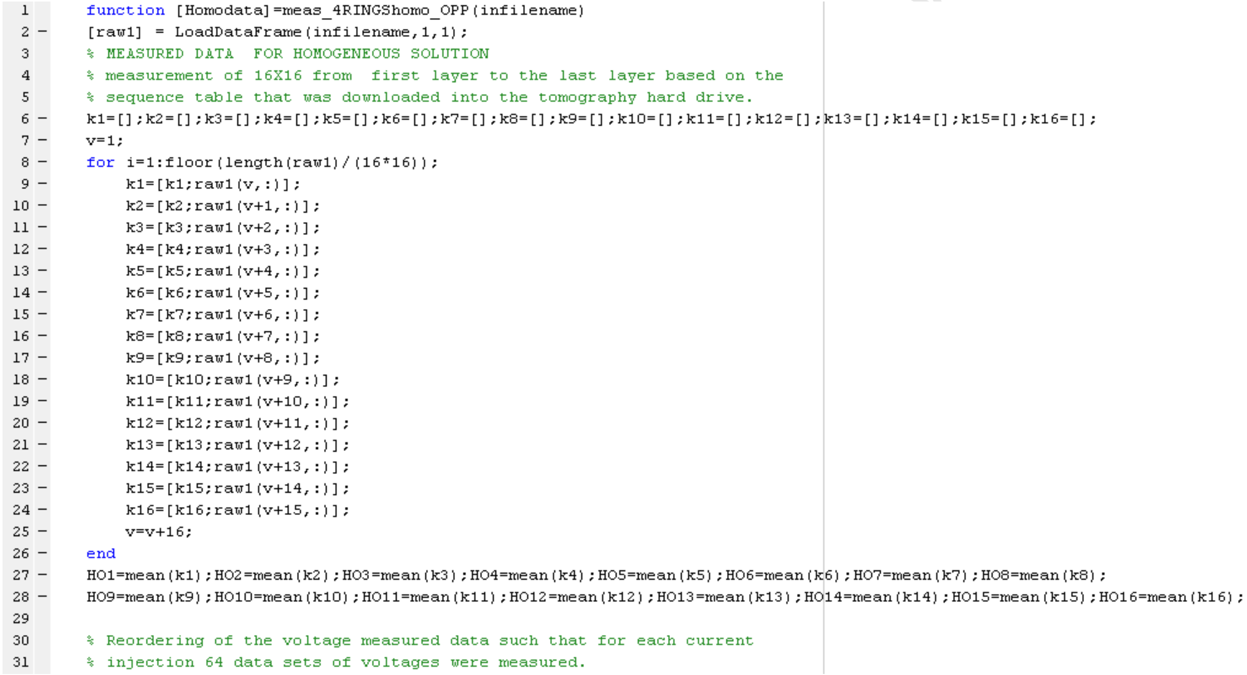

```
function [Homodata]=meas_4RINGShomo_OPP(infilename)
[raw1] = LoadDataFrame(infilename,1,1);
% MEASURED DATA  FOR HOMOGENEOUS SOLUTION
% measurement of 16X16 from  first layer to the last layer based on the
% sequence table that was downloaded into the tomography hard drive.
k1=[];k2=[];k3=[];k4=[];k5=[];k6=[];k7=[];k8=[];k9=[];k10=[];k11=[];k12=[];k13=[];k14=[];k15=[];k16=[];
v=1;
for i=1:floor(length(raw1)/(16*16));
    k1=[k1;raw1(v,:)];
    k2=[k2;raw1(v+1,:)];
    k3=[k3;raw1(v+2,:)];
    k4=[k4;raw1(v+3,:)];
    k5=[k5;raw1(v+4,:)];
    k6=[k6;raw1(v+5,:)];
    k7=[k7;raw1(v+6,:)];
    k8=[k8;raw1(v+7,:)];
    k9=[k9;raw1(v+8,:)];
    k10=[k10;raw1(v+9,:)];
    k11=[k11;raw1(v+10,:)];
    k12=[k12;raw1(v+11,:)];
    k13=[k13;raw1(v+12,:)];
    k14=[k14;raw1(v+13,:)];
    k15=[k15;raw1(v+14,:)];
    k16=[k16;raw1(v+15,:)];
    v=v+16;
end
HO1=mean(k1);HO2=mean(k2);HO3=mean(k3);HO4=mean(k4);HO5=mean(k5);HO6=mean(k6);HO7=mean(k7);HO8=mean(k8);
HO9=mean(k9);HO10=mean(k10);HO11=mean(k11);HO12=mean(k12);HO13=mean(k13);HO14=mean(k14);HO15=mean(k15);HO16=mean(k16);

% Reordering of the voltage measured data such that for each current
% injection 64 data sets of voltages were measured.
```

```
k=1;
y=1;
Hrg1=[];Hrg2=[];Hrg3=[];Hrg4=[];
for i=1:16;
    Hrg1(y:63+y)=[HO1(k:15+k),HO2(k:15+k),HO3(k:15+k),HO4(k:15+k)];
    Hrg2(y:63+y)=[HO5(k:15+k),HO6(k:15+k),HO7(k:15+k),HO8(k:15+k)];
    Hrg3(y:63+y)=[HO9(k:15+k),HO10(k:15+k),HO11(k:15+k),HO12(k:15+k)];
    Hrg4(y:63+y)=[HO13(k:15+k),HO14(k:15+k),HO15(k:15+k),HO16(k:15+k)];
    k=k+16;
    y=y+64;
end
Hring=[Hrg1,Hrg2,Hrg3,Hrg4];
v=1;
Hj=[];
for i=1:64
    hh=Hring(v:63+v);
    Hj=[Hj;hh];
    v=v+64;
end
I1=[Hj(1,2:7),Hj(1,10:15),Hj(1,17:32),Hj(1,33:48),Hj(1,49:64)];
I2=[Hj(2,3:8),Hj(2,11:16),Hj(2,17:32),Hj(2,33:48),Hj(2,49:64)];

I3=[Hj(3,1),Hj(3,4:9),Hj(3,12:16),Hj(3,17:32),Hj(3,33:48),Hj(3,49:64)];
I4=[Hj(4,1:2),Hj(4,5:10),Hj(4,13:16),Hj(4,17:32),Hj(4,33:48),Hj(4,49:64)];
I5=[Hj(5,1:3),Hj(5,6:11),Hj(5,14:16),Hj(5,17:32),Hj(5,33:48),Hj(5,49:64)];
I6=[Hj(6,1:4),Hj(6,7:12),Hj(6,15:16),Hj(6,17:32),Hj(6,33:48),Hj(6,49:64)];
I7=[Hj(7,1:5),Hj(7,8:13),Hj(7,16),Hj(7,17:32),Hj(7,33:48),Hj(7,49:64)];

I8=[Hj(8,1:6),Hj(8,9:14),Hj(8,17:32),Hj(8,33:48),Hj(8,49:64)];
I9=[Hj(9,2:7),Hj(9,10:15),Hj(9,17:32),Hj(9,33:48),Hj(9,49:64)];
I10=[Hj(10,3:8),Hj(10,11:16),Hj(10,17:32),Hj(10,33:48),Hj(10,49:64)];

I11=[Hj(11,1),Hj(11,4:9),Hj(11,12:16),Hj(11,17:32),Hj(11,33:48),Hj(11,49:64)];
I12=[Hj(12,1:2),Hj(12,5:10),Hj(12,13:16),Hj(12,17:32),Hj(12,33:48),Hj(12,49:64)];
I13=[Hj(13,1:3),Hj(13,6:11),Hj(13,14:16),Hj(13,17:32),Hj(13,33:48),Hj(13,49:64)];
I14=[Hj(14,1:4),Hj(14,7:12),Hj(14,15:16),Hj(14,17:32),Hj(14,33:48),Hj(14,49:64)];
I15=[Hj(15,1:5),Hj(15,8:13),Hj(15,16),Hj(15,17:32),Hj(15,33:48),Hj(15,49:64)];

I16=[Hj(16,1:6),Hj(16,9:14),Hj(16,17:32),Hj(16,33:48),Hj(16,49:64)];

I17=[Hj(17,1:16),Hj(17,18:23),Hj(17,26:31),Hj(17,33:48),Hj(17,49:64)];
I18=[Hj(18,1:16),Hj(18,19:24),Hj(18,27:32),Hj(18,33:48),Hj(18,49:64)];

I19=[Hj(19,1:16),Hj(19,17),Hj(19,20:25),Hj(19,28:32),Hj(19,33:48),Hj(19,49:64)];
I20=[Hj(20,1:16),Hj(20,17:18),Hj(20,21:26),Hj(20,29:32),Hj(20,33:48),Hj(20,49:64)];
I21=[Hj(21,1:16),Hj(21,17:19),Hj(21,22:27),Hj(21,30:32),Hj(21,33:48),Hj(21,49:64)];
I22=[Hj(22,1:16),Hj(22,17:20),Hj(22,23:28),Hj(22,31:32),Hj(22,33:48),Hj(22,49:64)];
I23=[Hj(23,1:16),Hj(23,17:21),Hj(23,24:29),Hj(23,32),Hj(23,33:48),Hj(23,49:64)];

I24=[Hj(24,1:16),Hj(24,17:22),Hj(24,25:30),Hj(24,33:48),Hj(24,49:64)];
I25=[Hj(25,1:16),Hj(25,18:23),Hj(25,26:31),Hj(25,33:48),Hj(25,49:64)];
I26=[Hj(26,1:16),Hj(26,19:24),Hj(26,27:32),Hj(26,33:48),Hj(26,49:64)];

I27=[Hj(27,1:16),Hj(27,17),Hj(27,20:25),Hj(27,28:32),Hj(27,33:48),Hj(27,49:64)];
I28=[Hj(28,1:16),Hj(28,17:18),Hj(28,21:26),Hj(28,29:32),Hj(28,33:48),Hj(28,49:64)];
I29=[Hj(29,1:16),Hj(29,17:19),Hj(29,22:27),Hj(29,30:32),Hj(29,33:48),Hj(29,49:64)];
I30=[Hj(30,1:16),Hj(30,17:20),Hj(30,23:28),Hj(30,31:32),Hj(30,33:48),Hj(30,49:64)];
I31=[Hj(31,1:16),Hj(31,17:21),Hj(31,24:29),Hj(31,32),Hj(31,33:48),Hj(31,49:64)];

I32=[Hj(32,1:16),Hj(32,17:22),Hj(32,25:30),Hj(32,33:48),Hj(32,49:64)];
```

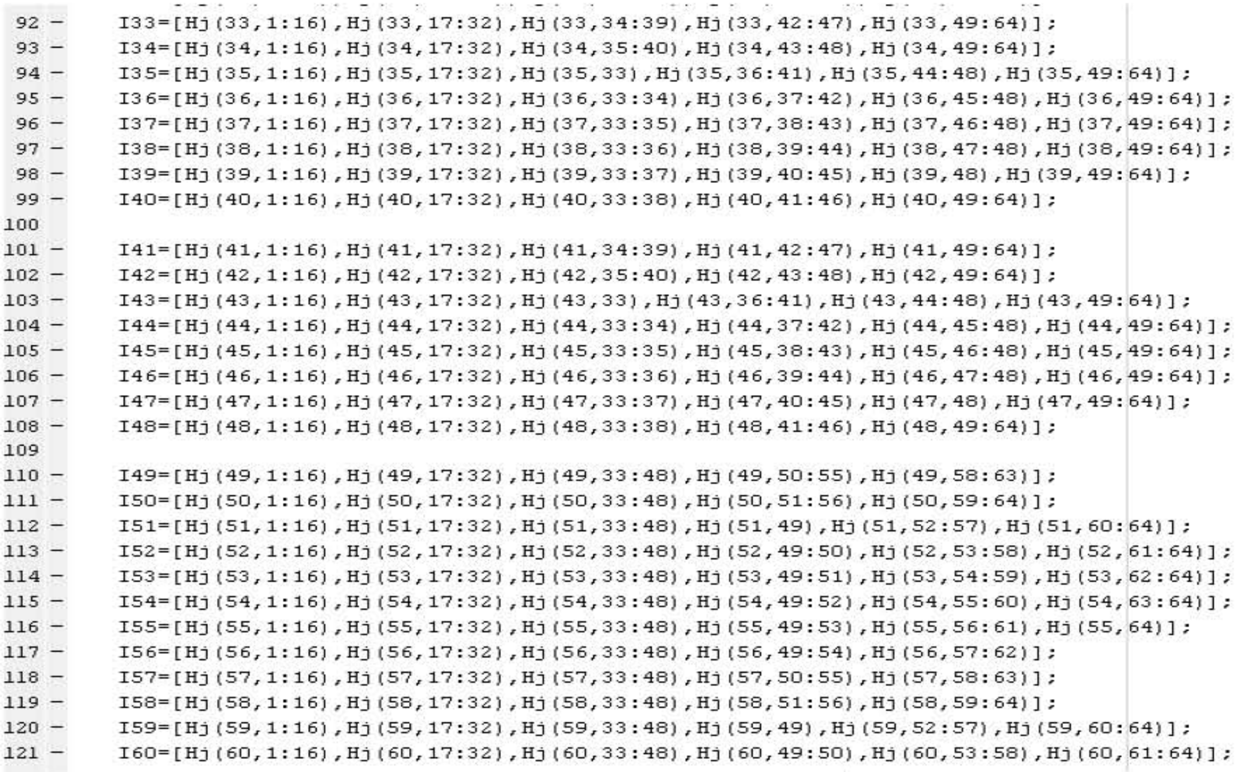

```
    I33=[Hj(33,1:16),Hj(33,17:32),Hj(33,34:39),Hj(33,42:47),Hj(33,49:64)];
    I34=[Hj(34,1:16),Hj(34,17:32),Hj(34,35:40),Hj(34,43:48),Hj(34,49:64)];
    I35=[Hj(35,1:16),Hj(35,17:32),Hj(35,33),Hj(35,36:41),Hj(35,44:48),Hj(35,49:64)];
    I36=[Hj(36,1:16),Hj(36,17:32),Hj(36,33:34),Hj(36,37:42),Hj(36,45:48),Hj(36,49:64)];
    I37=[Hj(37,1:16),Hj(37,17:32),Hj(37,33:35),Hj(37,38:43),Hj(37,46:48),Hj(37,49:64)];
    I38=[Hj(38,1:16),Hj(38,17:32),Hj(38,33:36),Hj(38,39:44),Hj(38,47:48),Hj(38,49:64)];
    I39=[Hj(39,1:16),Hj(39,17:32),Hj(39,33:37),Hj(39,40:45),Hj(39,48),Hj(39,49:64)];
    I40=[Hj(40,1:16),Hj(40,17:32),Hj(40,33:38),Hj(40,41:46),Hj(40,49:64)];

    I41=[Hj(41,1:16),Hj(41,17:32),Hj(41,34:39),Hj(41,42:47),Hj(41,49:64)];
    I42=[Hj(42,1:16),Hj(42,17:32),Hj(42,35:40),Hj(42,43:48),Hj(42,49:64)];
    I43=[Hj(43,1:16),Hj(43,17:32),Hj(43,33),Hj(43,36:41),Hj(43,44:48),Hj(43,49:64)];
    I44=[Hj(44,1:16),Hj(44,17:32),Hj(44,33:34),Hj(44,37:42),Hj(44,45:48),Hj(44,49:64)];
    I45=[Hj(45,1:16),Hj(45,17:32),Hj(45,33:35),Hj(45,38:43),Hj(45,46:48),Hj(45,49:64)];
    I46=[Hj(46,1:16),Hj(46,17:32),Hj(46,33:36),Hj(46,39:44),Hj(46,47:48),Hj(46,49:64)];
    I47=[Hj(47,1:16),Hj(47,17:32),Hj(47,33:37),Hj(47,40:45),Hj(47,48),Hj(47,49:64)];
    I48=[Hj(48,1:16),Hj(48,17:32),Hj(48,33:38),Hj(48,41:46),Hj(48,49:64)];

    I49=[Hj(49,1:16),Hj(49,17:32),Hj(49,33:48),Hj(49,50:55),Hj(49,58:63)];
    I50=[Hj(50,1:16),Hj(50,17:32),Hj(50,33:48),Hj(50,51:56),Hj(50,59:64)];
    I51=[Hj(51,1:16),Hj(51,17:32),Hj(51,33:48),Hj(51,49),Hj(51,52:57),Hj(51,60:64)];
    I52=[Hj(52,1:16),Hj(52,17:32),Hj(52,33:48),Hj(52,49:50),Hj(52,53:58),Hj(52,61:64)];
    I53=[Hj(53,1:16),Hj(53,17:32),Hj(53,33:48),Hj(53,49:51),Hj(53,54:59),Hj(53,62:64)];
    I54=[Hj(54,1:16),Hj(54,17:32),Hj(54,33:48),Hj(54,49:52),Hj(54,55:60),Hj(54,63:64)];
    I55=[Hj(55,1:16),Hj(55,17:32),Hj(55,33:48),Hj(55,49:53),Hj(55,56:61),Hj(55,64)];
    I56=[Hj(56,1:16),Hj(56,17:32),Hj(56,33:48),Hj(56,49:54),Hj(56,57:62)];
    I57=[Hj(57,1:16),Hj(57,17:32),Hj(57,33:48),Hj(57,50:55),Hj(57,58:63)];
    I58=[Hj(58,1:16),Hj(58,17:32),Hj(58,33:48),Hj(58,51:56),Hj(58,59:64)];
    I59=[Hj(59,1:16),Hj(59,17:32),Hj(59,33:48),Hj(59,49),Hj(59,52:57),Hj(59,60:64)];
    I60=[Hj(60,1:16),Hj(60,17:32),Hj(60,33:48),Hj(60,49:50),Hj(60,53:58),Hj(60,61:64)];
```

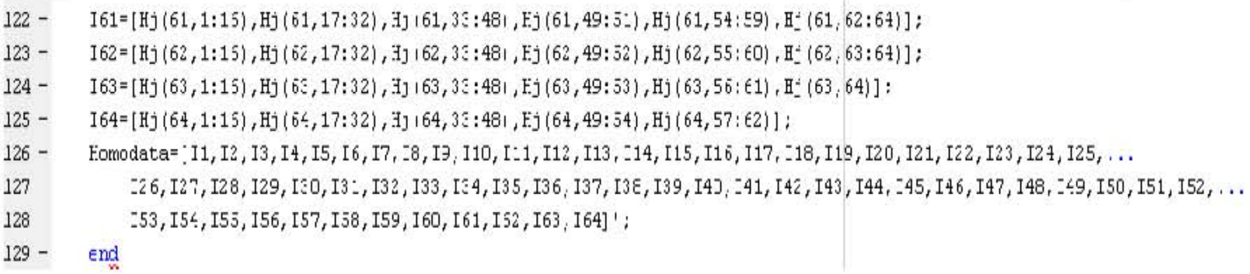

```
    I61=[Hj(61,1:16),Hj(61,17:32),Hj(61,33:48),Hj(61,49:53),Hj(61,54:59),Hj(61,62:64)];
    I62=[Hj(62,1:16),Hj(62,17:32),Hj(62,33:48),Hj(62,49:52),Hj(62,55:60),Hj(62,63:64)];
    I63=[Hj(63,1:16),Hj(63,17:32),Hj(63,33:48),Hj(63,49:53),Hj(63,56:61),Hj(63,64)];
    I64=[Hj(64,1:16),Hj(64,17:32),Hj(64,33:48),Hj(64,49:54),Hj(64,57:62)];
    Homodata=[I1,I2,I3,I4,I5,I6,I7,I8,I9,I10,I11,I12,I13,I14,I15,I16,I17,I18,I19,I20,I21,I22,I23,I24,I25,...
        I26,I27,I28,I29,I30,I31,I32,I33,I34,I35,I36,I37,I38,I39,I40,I41,I42,I43,I44,I45,I46,I47,I48,I49,I50,I51,I52,...
        I53,I54,I55,I56,I57,I58,I59,I60,I61,I62,I63,I64]';
end
```

H6 : Loading Function for Adjacent Voltage Measurement Resulting from Stimulation through Adjacent Electrode Pairs in A Four Rings Electrode System (i.e. "`meas_4RINGShomo_ADJ`", "`getcalibrationdata4rings_adj_no_current`" and "`getcalibrationdata4rings_adj_current`" were written the same form)

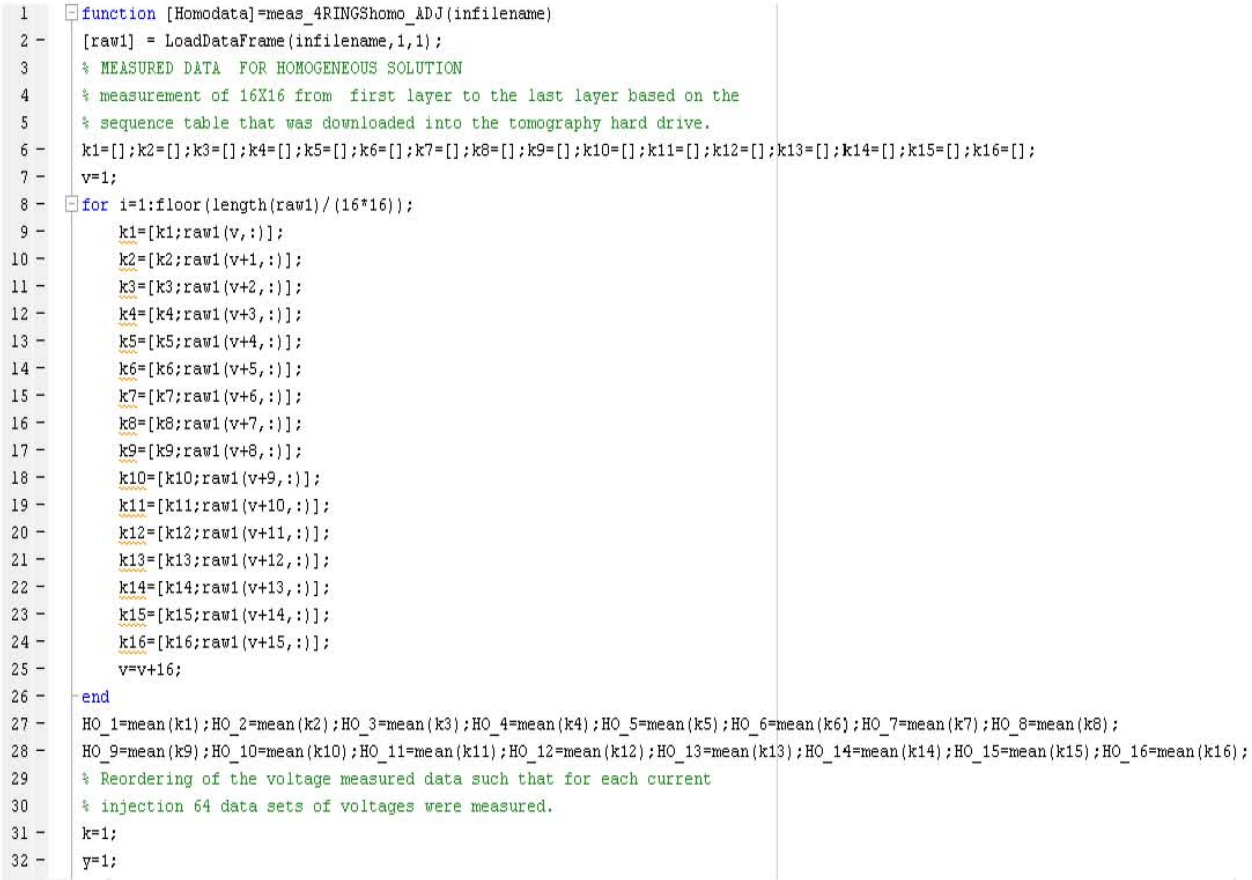

```
function [Homodata]=meas_4RINGShomo_ADJ(infilename)
[raw1] = LoadDataFrame(infilename,1,1);
% MEASURED DATA  FOR HOMOGENEOUS SOLUTION
% measurement of 16X16 from  first layer to the last layer based on the
% sequence table that was downloaded into the tomography hard drive.
k1=[];k2=[];k3=[];k4=[];k5=[];k6=[];k7=[];k8=[];k9=[];k10=[];k11=[];k12=[];k13=[];k14=[];k15=[];k16=[];
v=1;
for i=1:floor(length(raw1)/(16*16));
    k1=[k1;raw1(v,:)];
    k2=[k2;raw1(v+1,:)];
    k3=[k3;raw1(v+2,:)];
    k4=[k4;raw1(v+3,:)];
    k5=[k5;raw1(v+4,:)];
    k6=[k6;raw1(v+5,:)];
    k7=[k7;raw1(v+6,:)];
    k8=[k8;raw1(v+7,:)];
    k9=[k9;raw1(v+8,:)];
    k10=[k10;raw1(v+9,:)];
    k11=[k11;raw1(v+10,:)];
    k12=[k12;raw1(v+11,:)];
    k13=[k13;raw1(v+12,:)];
    k14=[k14;raw1(v+13,:)];
    k15=[k15;raw1(v+14,:)];
    k16=[k16;raw1(v+15,:)];
    v=v+16;
end
HO_1=mean(k1);HO_2=mean(k2);HO_3=mean(k3);HO_4=mean(k4);HO_5=mean(k5);HO_6=mean(k6);HO_7=mean(k7);HO_8=mean(k8);
HO_9=mean(k9);HO_10=mean(k10);HO_11=mean(k11);HO_12=mean(k12);HO_13=mean(k13);HO_14=mean(k14);HO_15=mean(k15);HO_16=mean(k16);
% Reordering of the voltage measured data such that for each current
% injection 64 data sets of voltages were measured.
k=1;
y=1;
```

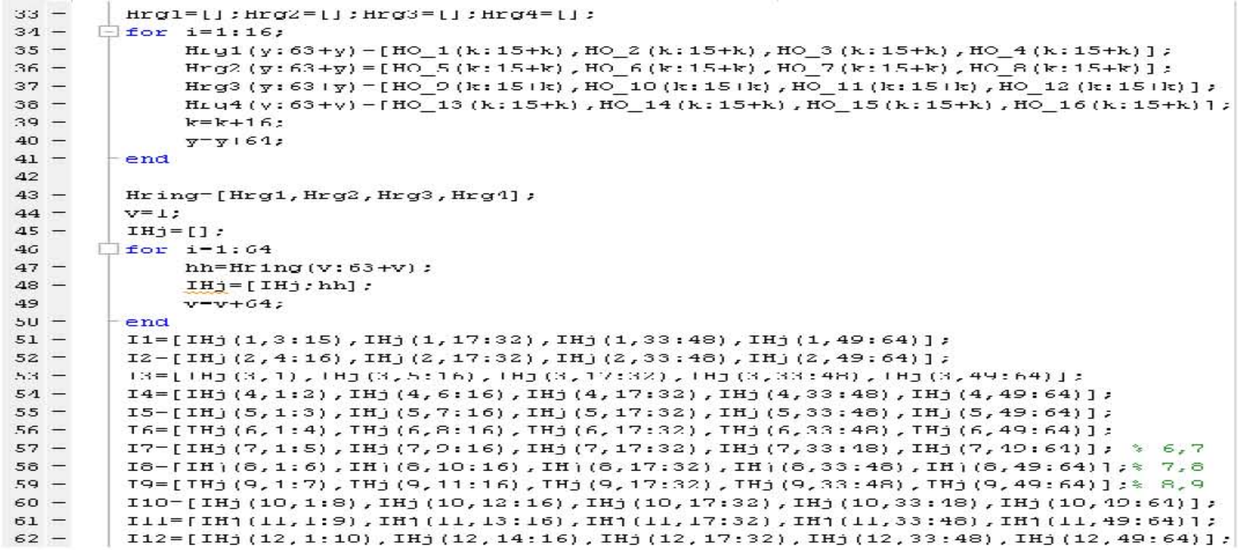

```
Hrg1=[];Hrg2=[];Hrg3=[];Hrg4=[];
for i=1:16;
    Hrg1(y:63+y)=[HO_1(k:15+k),HO_2(k:15+k),HO_3(k:15+k),HO_4(k:15+k)];
    Hrg2(y:63+y)=[HO_5(k:15+k),HO_6(k:15+k),HO_7(k:15+k),HO_8(k:15+k)];
    Hrg3(y:63+y)=[HO_9(k:15+k),HO_10(k:15+k),HO_11(k:15+k),HO_12(k:15+k)];
    Hrg4(y:63+y)=[HO_13(k:15+k),HO_14(k:15+k),HO_15(k:15+k),HO_16(k:15+k)];
    k=k+16;
    y=y+64;
end

Hring=[Hrg1,Hrg2,Hrg3,Hrg4];
v=1;
IHj=[];
for i=1:64
    hh=Hring(v:63+v);
    IHj=[IHj;hh];
    v=v+64;
end
I1=[IHj(1,3:15),IHj(1,17:32),IHj(1,33:48),IHj(1,49:64)];
I2=[IHj(2,4:16),IHj(2,17:32),IHj(2,33:48),IHj(2,49:64)];
I3=[IHj(3,1),IHj(3,5:16),IHj(3,17:32),IHj(3,33:48),IHj(3,49:64)];
I4=[IHj(4,1:2),IHj(4,6:16),IHj(4,17:32),IHj(4,33:48),IHj(4,49:64)];
I5=[IHj(5,1:3),IHj(5,7:16),IHj(5,17:32),IHj(5,33:48),IHj(5,49:64)];
I6=[IHj(6,1:4),IHj(6,8:16),IHj(6,17:32),IHj(6,33:48),IHj(6,49:64)];
I7=[IHj(7,1:5),IHj(7,9:16),IHj(7,17:32),IHj(7,33:48),IHj(7,49:64)]; % 6,7
I8=[IHj(8,1:6),IHj(8,10:16),IHj(8,17:32),IHj(8,33:48),IHj(8,49:64)];% 7,8
I9=[IHj(9,1:7),IHj(9,11:16),IHj(9,17:32),IHj(9,33:48),IHj(9,49:64)];% 8,9
I10=[IHj(10,1:8),IHj(10,12:16),IHj(10,17:32),IHj(10,33:48),IHj(10,49:64)];
I11=[IHj(11,1:9),IHj(11,13:16),IHj(11,17:32),IHj(11,33:48),IHj(11,49:64)];
I12=[IHj(12,1:10),IHj(12,14:16),IHj(12,17:32),IHj(12,33:48),IHj(12,49:64)];
```

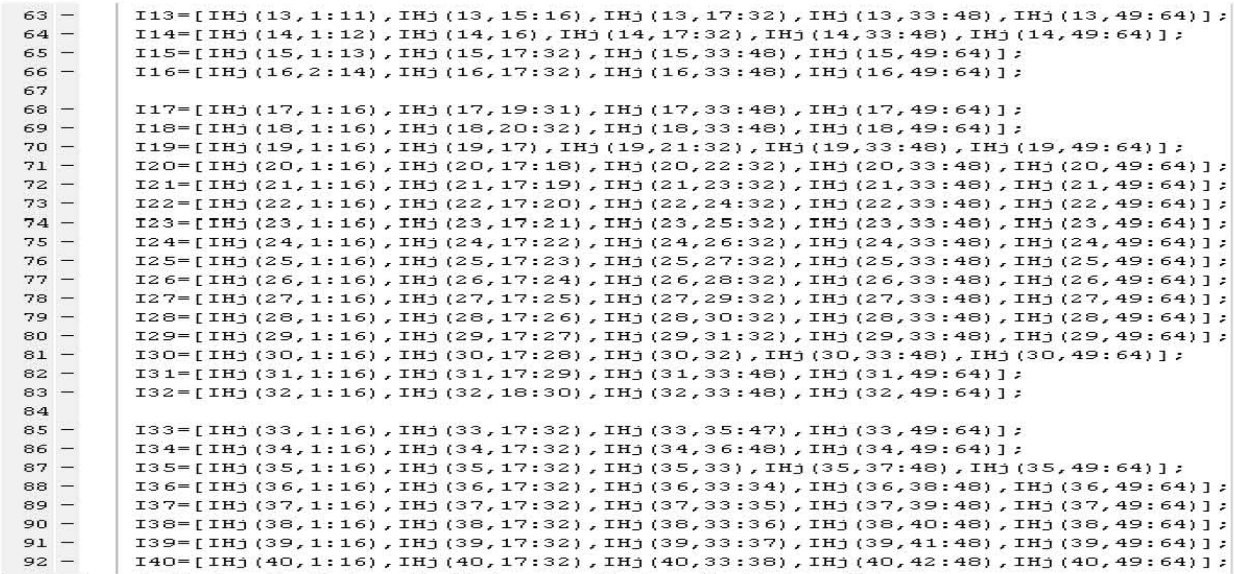

```
    I13=[IHj(13,1:11),IHj(13,15:16),IHj(13,17:32),IHj(13,33:48),IHj(13,49:64)];
    I14=[IHj(14,1:12),IHj(14,16),IHj(14,17:32),IHj(14,33:48),IHj(14,49:64)];
    I15=[IHj(15,1:13),IHj(15,17:32),IHj(15,33:48),IHj(15,49:64)];
    I16=[IHj(16,2:14),IHj(16,17:32),IHj(16,33:48),IHj(16,49:64)];

    I17=[IHj(17,1:16),IHj(17,19:31),IHj(17,33:48),IHj(17,49:64)];
    I18=[IHj(18,1:16),IHj(18,20:32),IHj(18,33:48),IHj(18,49:64)];
    I19=[IHj(19,1:16),IHj(19,17),IHj(19,21:32),IHj(19,33:48),IHj(19,49:64)];
    I20=[IHj(20,1:16),IHj(20,17:18),IHj(20,22:32),IHj(20,33:48),IHj(20,49:64)];
    I21=[IHj(21,1:16),IHj(21,17:19),IHj(21,23:32),IHj(21,33:48),IHj(21,49:64)];
    I22=[IHj(22,1:16),IHj(22,17:20),IHj(22,24:32),IHj(22,33:48),IHj(22,49:64)];
    I23=[IHj(23,1:16),IHj(23,17:21),IHj(23,25:32),IHj(23,33:48),IHj(23,49:64)];
    I24=[IHj(24,1:16),IHj(24,17:22),IHj(24,26:32),IHj(24,33:48),IHj(24,49:64)];
    I25=[IHj(25,1:16),IHj(25,17:23),IHj(25,27:32),IHj(25,33:48),IHj(25,49:64)];
    I26=[IHj(26,1:16),IHj(26,17:24),IHj(26,28:32),IHj(26,33:48),IHj(26,49:64)];
    I27=[IHj(27,1:16),IHj(27,17:25),IHj(27,29:32),IHj(27,33:48),IHj(27,49:64)];
    I28=[IHj(28,1:16),IHj(28,17:26),IHj(28,30:32),IHj(28,33:48),IHj(28,49:64)];
    I29=[IHj(29,1:16),IHj(29,17:27),IHj(29,31:32),IHj(29,33:48),IHj(29,49:64)];
    I30=[IHj(30,1:16),IHj(30,17:28),IHj(30,32),IHj(30,33:48),IHj(30,49:64)];
    I31=[IHj(31,1:16),IHj(31,17:29),IHj(31,33:48),IHj(31,49:64)];
    I32=[IHj(32,1:16),IHj(32,18:30),IHj(32,33:48),IHj(32,49:64)];

    I33=[IHj(33,1:16),IHj(33,17:32),IHj(33,35:47),IHj(33,49:64)];
    I34=[IHj(34,1:16),IHj(34,17:32),IHj(34,36:48),IHj(34,49:64)];
    I35=[IHj(35,1:16),IHj(35,17:32),IHj(35,33),IHj(35,37:48),IHj(35,49:64)];
    I36=[IHj(36,1:16),IHj(36,17:32),IHj(36,33:34),IHj(36,38:48),IHj(36,49:64)];
    I37=[IHj(37,1:16),IHj(37,17:32),IHj(37,33:35),IHj(37,39:48),IHj(37,49:64)];
    I38=[IHj(38,1:16),IHj(38,17:32),IHj(38,33:36),IHj(38,40:48),IHj(38,49:64)];
    I39=[IHj(39,1:16),IHj(39,17:32),IHj(39,33:37),IHj(39,41:48),IHj(39,49:64)];
    I40=[IHj(40,1:16),IHj(40,17:32),IHj(40,33:38),IHj(40,42:48),IHj(40,49:64)];
```

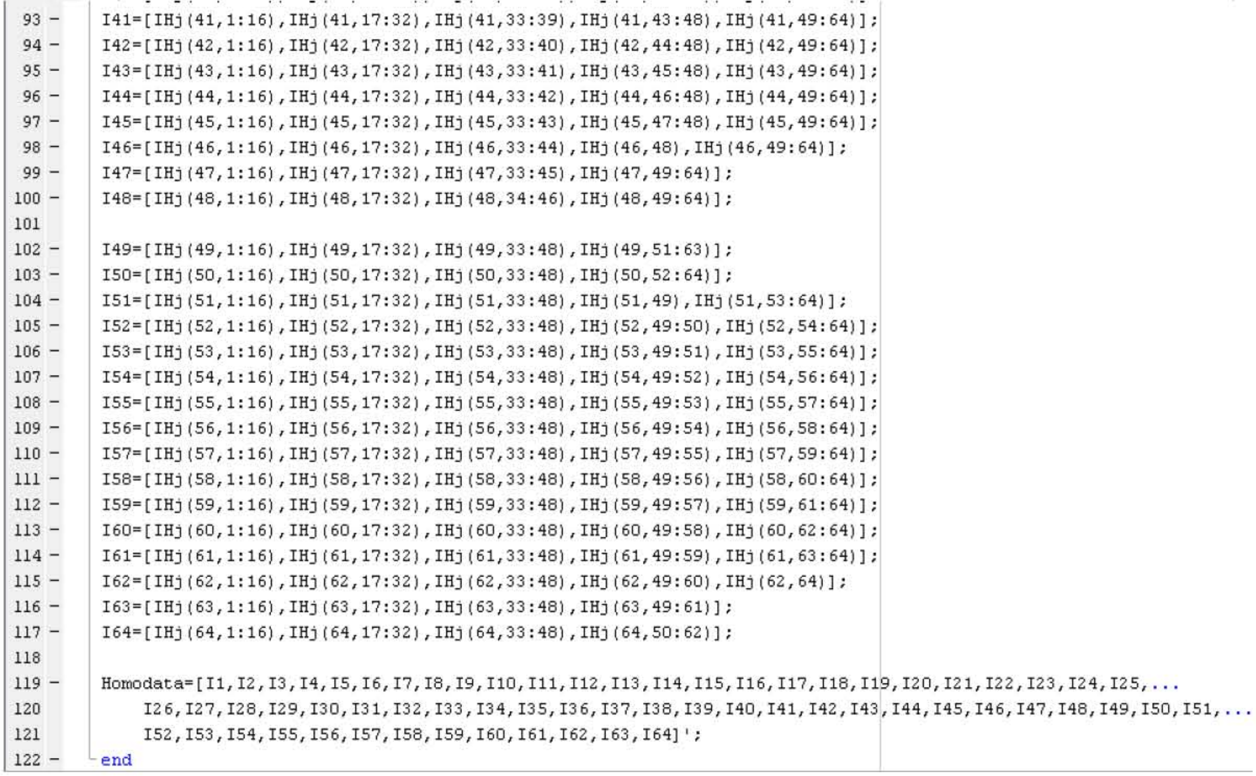

```
    I41=[IHj(41,1:16),IHj(41,17:32),IHj(41,33:39),IHj(41,43:48),IHj(41,49:64)];
    I42=[IHj(42,1:16),IHj(42,17:32),IHj(42,33:40),IHj(42,44:48),IHj(42,49:64)];
    I43=[IHj(43,1:16),IHj(43,17:32),IHj(43,33:41),IHj(43,45:48),IHj(43,49:64)];
    I44=[IHj(44,1:16),IHj(44,17:32),IHj(44,33:42),IHj(44,46:48),IHj(44,49:64)];
    I45=[IHj(45,1:16),IHj(45,17:32),IHj(45,33:43),IHj(45,47:48),IHj(45,49:64)];
    I46=[IHj(46,1:16),IHj(46,17:32),IHj(46,33:44),IHj(46,48),IHj(46,49:64)];
    I47=[IHj(47,1:16),IHj(47,17:32),IHj(47,33:45),IHj(47,49:64)];
    I48=[IHj(48,1:16),IHj(48,17:32),IHj(48,34:46),IHj(48,49:64)];

    I49=[IHj(49,1:16),IHj(49,17:32),IHj(49,33:48),IHj(49,51:63)];
    I50=[IHj(50,1:16),IHj(50,17:32),IHj(50,33:48),IHj(50,52:64)];
    I51=[IHj(51,1:16),IHj(51,17:32),IHj(51,33:48),IHj(51,49),IHj(51,53:64)];
    I52=[IHj(52,1:16),IHj(52,17:32),IHj(52,33:48),IHj(52,49:50),IHj(52,54:64)];
    I53=[IHj(53,1:16),IHj(53,17:32),IHj(53,33:48),IHj(53,49:51),IHj(53,55:64)];
    I54=[IHj(54,1:16),IHj(54,17:32),IHj(54,33:48),IHj(54,49:52),IHj(54,56:64)];
    I55=[IHj(55,1:16),IHj(55,17:32),IHj(55,33:48),IHj(55,49:53),IHj(55,57:64)];
    I56=[IHj(56,1:16),IHj(56,17:32),IHj(56,33:48),IHj(56,49:54),IHj(56,58:64)];
    I57=[IHj(57,1:16),IHj(57,17:32),IHj(57,33:48),IHj(57,49:55),IHj(57,59:64)];
    I58=[IHj(58,1:16),IHj(58,17:32),IHj(58,33:48),IHj(58,49:56),IHj(58,60:64)];
    I59=[IHj(59,1:16),IHj(59,17:32),IHj(59,33:48),IHj(59,49:57),IHj(59,61:64)];
    I60=[IHj(60,1:16),IHj(60,17:32),IHj(60,33:48),IHj(60,49:58),IHj(60,62:64)];
    I61=[IHj(61,1:16),IHj(61,17:32),IHj(61,33:48),IHj(61,49:59),IHj(61,63:64)];
    I62=[IHj(62,1:16),IHj(62,17:32),IHj(62,33:48),IHj(62,49:60),IHj(62,64)];
    I63=[IHj(63,1:16),IHj(63,17:32),IHj(63,33:48),IHj(63,49:61)];
    I64=[IHj(64,1:16),IHj(64,17:32),IHj(64,33:48),IHj(64,50:62)];

    Homodata=[I1,I2,I3,I4,I5,I6,I7,I8,I9,I10,I11,I12,I13,I14,I15,I16,I17,I18,I19,I20,I21,I22,I23,I24,I25,...
        I26,I27,I28,I29,I30,I31,I32,I33,I34,I35,I36,I37,I38,I39,I40,I41,I42,I43,I44,I45,I46,I47,I48,I49,I50,I51,...
        I52,I53,I54,I55,I56,I57,I58,I59,I60,I61,I62,I63,I64]';
end
```

APPENDIX I

Downloading and Installing EIDORS and NETGEN on a MATLAB platform

I1 : Downloading and Installing EIDORS on a MATLAB platform

EIDORS being a public domain software base can be downloaded and installed properly when the following steps are followed.

(a) User need type and enter 'http://eidors3d.sourceforge.net/index.shtml' on the address bar of winodow internet explorer.

(b) In the displayed page, user should click on 'eidors-v3.4.zip (7 July 2010)' under download latest released version in the Released versions section.

(c) Clicking on this opens the sourceforge page where 6.0MB of the software can be downloaded. It is recommended that the software should be extracted to the same directory where it was downloaded. Furthermore, the software is run on the MATLAB window prompt by entrying 'C:/users/bode/desktop/eidors3d/eidors3d/trunk/eidors/startup.m', had the software been downloaded into the directory ''C:/users/bode/desktop/'. This automatically loads all the functions and returns the statement below indicating that the software has been installed properly.

```
>> run C:/users/bode/desktop/eidors3d/eidors3d/trunk/eidors/startup.m
EIDORS:[Complete EIDORS (Ver: 3.3+ ($Date$))]
EIDORS:[Parameter: cache_size=100 MB]
EIDORS:[Parameter: mapped_colour=127]
EIDORS:[Default background colour: white]
EIDORS:[EIDORS mex folder: C:\users\bode\desktop\eidors3d\eidors3d\trunk\eidors/arch/matlab]
EIDORS:[New to EIDORS? Have a look at the Tutorials.]
```

I2 : Downloading and Installing NETGEN on a MATLAB Platform

Basic steps required to download NETGEN are as follows:

(a) The user types and enters 'http://www.hpfem.jku.at/netgen/' into the address bar of windows internet explorer.

(b) Under the News section, user should locate 'NETGEN/NGSolve 4.4 available!' and click on 'Get the complete NETGEN/NGSolve package here! ', the statement below it.

(c) Clicking on 'here' directs the user to a page where necessary details ought to be submitted before an access to downloading the software can be gained.

(d) With appropriate details successfully submitted, a page containing 'NETGEN/NGSolve 4.4 (17 November 2004) >> ngs44_rel.zip' should be displayed before the user. User need click on 'ngs44_rel.zip' to prompt a dialogue box through which the user specifies the directory the software should be downloaded to. It is recommended that the software should be downloaded into the one of the MATLAB search path or a directory that can be added to the MATLAB search path. When a MATLAB script of EIDORS containing NETGEN functions is run, MATLAB prompts the user to add the directory into its search paths should NETGEN be downloaded to a directory that is not one of its search path.

(e) NETGEN may require the MSVCR70.dll and some third party libraries such as tcl8.3.2.tar.gz and tk8.3.2.tar.gz file in order to optimise the computer's operation. tcl8.3.2.tar.gz and tk8.3.2.tar.gz can be downloaded from 'http://www.hpfem.jku.at/netgen/' while MSVCR70.dll may be downloaded from 'http://www.dll-files.com/pop.php?dll=msvcr70'. User need ensure that MSVCR70.dll is downloaded into the directory of the programme requesting it or it should be extracted into the system directory. By default system directory for windows xp, vista 7, windows 95/98/mac and windows NT/ 2008 are respectively C:\windows\system 32, C:\windows\system32 and C:\wiNNT\system 32.

APPENDIX J

Implemented Functions in EIDORS Developed from MATLAB Libraries

J1 : FEM by EIDORS: Step-wise Approach to Solving the Forward Problem (CONTINUE)

(b) The function, *mk_stim_patterns,* was used for the stimulation pattern specifying the sequence of current injection into the domain and the sequence of 3-D voltage measurement over the entire domain.

(c) The function, *np_calc_system_mat,* was used for setting up the global system matrix developed from each tetrahedral element.

(d) In order to Set the Jacobian matrix computation function, the function *np_calc_jacobian* was employed

(e) To setting the forward solver function of the forward problem, the function *np_fwd_solve* was used

(f) Creating an EIDORS-object with appropriate input variables required the use of function *eidors_obj*

(g) Specifying the conductivity of each element to be homogeneous in the NETGEN mesh, say fixing the value of conductivity to be 1 for all element in the mesh was made with the function *ones*

(h) Creating a function that relates the homogeneous property of all element in the NETGEN mesh to the created EIDORS object;

(g) The function *fwd_solve* was used to call the set forward solver function to solve for the boundary voltages arising from injecting current into a homogeneous solution.

J2 : Solving the Forward Problem Using EIDORS

J2.1 Three-dimensional Mesh Generation with NETGEN

The first step in addressing the forward problem requires generating a three-dimensional cylindrical mesh using the NETGEN function $ng\_mk\_cyl\_models$ on line 4 of the code below.

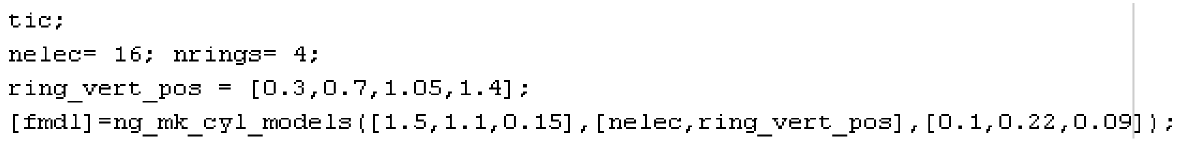

```
tic;
nelec= 16; nrings= 4;
ring_vert_pos = [0.3,0.7,1.05,1.4];
[fmdl]=ng_mk_cyl_models([1.5,1.1,0.15],[nelec,ring_vert_pos],[0.1,0.22,0.09]);
```

Line 1: The statement tic is used to start the time counter in seconds.

Line 2: $nelec$ and $nrings$ are variables specifying the modelled rig to be four rings of sixteen equally spaced electrodes system in a ring.

Line 3: $ring\_vert\_pos$ is an array indicating the position of the four rings of electrode begining from the base, i.e., the first, second, third and fourth ring were placed at 3.0, 7.0, 10.5 and 14.0 centimeters respectively from the base.

Line 4: $ng\_mk\_cyl\_models$ is the NETGEN function that was called by specifying the array [1.5, 1.1, 0.15] to define the height, radius and maximum size of mesh element, [nelec, ring_vert_pos] to define the number of electrodes in a ring and the respective position of each ring and [0.1, 0.22, 0.09] to define the electrode shape as in width, height and maximum mesh density on each electrode area.

J2.2 Defining the Stimulation Pattern of Sequence of Current Injections and Voltage Measurement on the Periphery Electrode

Since the sensitivity of the electric field distribution by the electrode system off the plane through which the current was injected is far from being negligible, voltage measurement by the boundary electrode for every injection ought to be carried out in a three dimensional manner, that is around the perimeter of the domain of the cylindrical vessel. Using EIDORS free library of MATLAB functions, the $mk\_stim\_patterns$ function was used to explore various current injection sequences and voltage measurement sequences to obtain an optimal measurement sequence as in line 6 below.

```
6 -    stim = mk_stim_patterns(nelec,nrings,[0,nelec/2],[0,1],{'no_meas_current','do_redundant'},2.5);
```

The function requires as input the following notations with the specified definitions as illustrated in the table J2.2

Table J2.2.1. Input variables for the current stimulation and voltage measurement pattern function.

Function	**Notation of Input Variables**	**Definition of Input Variables**
$mk\_stim\_patterns$	$nelec$	Number of electrodes in each ring
	$nrings$	Number of rings for the modelled vessel
	$[0, nelec/2]$	Opposite current injection pattern
	$[0, 1]$	Adjacent current injection pattern
	$[0, nelec/2]$	Opposite voltage measurement pattern
	$[0, 1]$	Adjacent voltage measurement pattern
	$no\_meas\_current$	A specification for sequences of voltage measurement across all periphery electrodes on all rings for every current injection excluding measurement across electrodes through which current is injected
	$do\_redundant$	A specification of sequence of voltage measurement across all periphery electrodes on all rings with polarity of injected current swopped over current injection electrode pairs
	$stim\_amplitude$	Denotes the magnitude of injected current

The function needs a specification of whether or not the voltage on electrodes, through which current was injected, should be measured. Entering $no\_meas\_current$ or $meas\_current$ informs the function not to measure voltage on the injection electrode or to measure voltage on injection electrode, respectively. Similarly, the function needs to be informed if it is to do a redundant measurement, involving voltage measurement across electrodes 1 and 2 not being counted independently from voltage measurement across electrodes 2 and 1. Entering $do\_redundant$ or $no\_redundant$ enables the detail of the measurement pattern to be specified. The magnitude of the constant current injected through boundary electrodes to stimulating the medium is defined as 2.5. In the case of two rings, the input variables for the $mk\_stim\_patterns$ function for adjacent current injection and adjacent voltage measurement sequence with no measurement on injection electrodes and with redundant measurement were specified as in line 8 below.

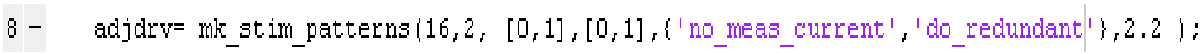

```
8 -    adjdrv= mk_stim_patterns(16,2, [0,1],[0,1],{'no_meas_current','do_redundant'},2.2 );
```

For the two rings opposite current injection and other input kept the same, the input variables are specified as in line 10 below.

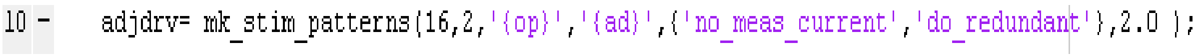

```
10 -    adjdrv= mk_stim_patterns(16,2,'{op}','{ad}',{'no_meas_current','do_redundant'},2.0 );
```

Similarly, for three rings, the input variables for the stimulation function for adjacent current injection and adjacent voltage measurement sequence were specified as in line 7,

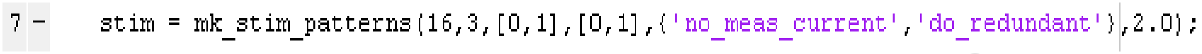

```
7 -    stim = mk_stim_patterns(16,3,[0,1],[0,1],{'no_meas_current','do_redundant'},2.0);
```

and opposite current injection and adjacent voltage measurement sequences were specified with

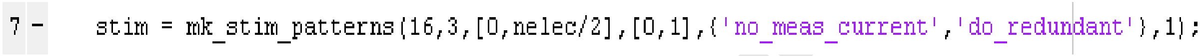

```
7 -    stim = mk_stim_patterns(16,3,[0,nelec/2],[0,1],{'no_meas_current','do_redundant'},1);
```

In the case of four rings, the input variables for the stimulation function for adjacent current injection and adjacent voltage measurement sequence were assigned as in the line below

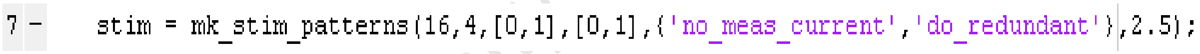

```
7 -    stim = mk_stim_patterns(16,4,[0,1],[0,1],{'no_meas_current','do_redundant'},2.5);
```

while for opposite current injection with other input kept the same, the input variables of the stimulation function were specified with the function

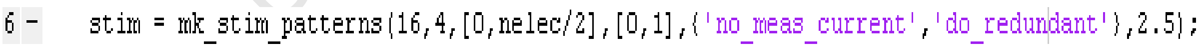

```
6 -    stim = mk_stim_patterns(16,4,[0,nelec/2],[0,1],{'no_meas_current','do_redundant'},2.5);
```

The modelled vessel denoted by $fmdl$ is linked to the designed stimulation pattern assigned to $stim$ in this form

```
fmdl.stimulation=stim;
```

With respect to the UCT tomography hardware, a measurement sequence was written for two rings such that a sequence of sixteen (16) current stimulations was made on the first ring and measurement of 256 data sets were made on the same ring, followed by a sequence of sixteen (16) stimulations on the first ring and measurement of 256 data on the second ring. Subsequently, a sequence of sixteen (16) stimulations was made on the second ring and measurement of 256 data sets on the first ring, followed by a sequence of sixteen (16) stimulations on the second ring and measurement of 256 data on the same ring as depicted in the figure D2 (a – d) of appendix D. The measurement sequence tables loaded into the c++ programme, controlling the data acquisition unit, are written in appendix C1 and C2 for current stimulation through adjacent and opposite electrode pairs, respectively.

The electrode system, consisting of 16 equally spaced electrodes, formed a ring around the UCT tomography vessel and produces 256 measured voltage data sets (a frame) for a stimulation through sixteen adjacent electrodes. That is, for every stimulation through adjacent electrodes, sixteen voltage measurements were taken. Similarly, for stimulation of current through opposite placed electrodes involving a redundant stimulation pattern, such as electrode 1 and 9, electrode 2 and 10, electrode 3 and 11, etc. and electrode 11 and 3, electrode 10 and 2, electrode 9 and 1, etc., 256 voltage data sets were measured for each ring. Three dimensional voltage measurement requires voltage measurements between adjacent electrode pairs in the two or three or four ring electrodes system for every stimulation through either adjacently or oppositely placed electrodes in each of these systems, respectively. In loading the measured data to a reconstruction code, the voltage measurements need to be sorted for any specified number of rings over which a three dimensional measurement strategy is to be made. The sorting is such that for every stimulation through any electrode pair, measurements were taken in all remaining adjacent pairs while excluding some measurements to avoid interference of current with sensed signals. The selection of 208 measured voltage data sets from a total of 256 sets is carried out to remove measurement across electrodes through which current was stimulated. Considering adjacent current injection sequences, for every stimulation through adjacent electrodes in a ring, thirteen measurement were selected from the sixteen measurements in the same ring. Thus, for sixteen current stimulation sequences in a ring, 208 (16 times 13) voltage measurements were measured in the same ring, while all measurements through adjacent electrodes were measured in the remaining rings. Table E1 in the appendix gives an indication of the selection of thirteen (13) measurements in a ring for every stimulation in the same ring, yielding 208 measurements from an injection ring. An illustration of the selection of twelve (12) measurement in a ring for every stimulation yielding 192 measurements from an injection ring by opposite current injection is presented in table E2 in the appendix. In this way, for a three-dimensional measurement using the two or three or four rings electrode system, a total of 256 measurement were made in each of the other rings for sixteen injections in one ring as no selection of measurement was made beacuse current was not injected in any of the electrode pair.

Table J.2.2.2. Total data selected from the total measured data for various current injections

S/N	**Number of rings**	**Total data selected for various injection sequences**		**Total data measured (Adjacent measurement)**
		Opposite	Adjacent	
1	2 rings	896 (28 x 32)	928 (29 x 32)	1024
2	3 rings	2112 (44 x 48)	2160 (45 x 48)	2304
3	4 rings	3840 (60 x 64)	3904 (61 x 64)	4096

From table 3.2, for every stimulation of the 32 stimulations through adjacent electrode pairs in a two rings system, 29 measurement were made yielding 928 data sets using adjacent measurement sequences. For every stimulation of the 32 stimulations through opposite electrode pairs, 28 measurements were made yielding 896 data sets using adjacent measurement sequences in a two rings system.

In the three rings system, for every stimulation of the 48 stimulations through adjacent eletrode pairs, 45 measurements were made using adjacent measurement sequences to obtain 2160 data sets. For every stimulation of the 48 stimualtions through opposite electrode pair, 44 measurment were made using adjacent measurement sequences to obtain 2112 data sets.

In the four rings system, for each of the 64 stimulations through adjacent electrode pairs, 61 measurements were made through adjacent electrode pairs, yielding 3904 data sets while for each of the 64 stimulations through opposite electrode pairs, 60 measurements through adjacent electrode pairs were made yielding 3840 data sets.

Sequence tables were written based on the architecture of figure D1 (appendix) in order to synchronise the output of the stimulation pattern (the simulated data sets) with that of the actual measured data sets from the UCT tomography rig. The sequence table contains details such as position of electrodes in a ring through which current should be injected and across which voltage should be measured. The plane of current injection and voltage measurement are also specified in the sequence tables which are displayed in section C1 to C6 of the appendix.

J2.3 Setting up the Global System Matrix

In calculating the global sensitivity matrix, Nick Polidorides' function (Polidorides 2002) was explored in developing the global system matrix from the local matrix system of each tetrahedral for the written programme in the form of

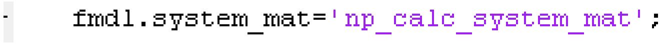

```
fmdl.system_mat='np_calc_system_mat';
```

J2.4 Setting up the function for the Computation of the Jacobian Matrix

In the reconstruction programme from the developed algorithm, Nick Poldoride's function (Polidorides 2002) for computing the Jacobian matrix, matrix of the derivative of the measured voltage with respect to the conductivity distribution, was explored. The Jacobian matrix was computed by linking it to the modelled vessel in the following form

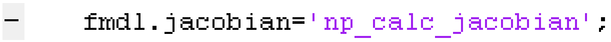

```
fmdl.jacobian='np_calc_jacobian';
```

J2.5 Setting the Forward Solver Function of the Forward Problem

Nick Polidorides' function (Polidorides 2002) was again explored in the development of the forward solver function. Here, the Cholesky method or preconjugate gradient method was employed if the conductivity values are real and LU or biconjugate gradient method if the conductivity values lies in the set of complex numbers. The forward solver was set as follows

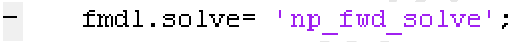

```
fmdl.solve= 'np_fwd_solve';
```

J2.6 Creating an EIDORS-object with Appropriate Input Variables

The forward solver function requires an EIDORS object with well-defined properties as an input variable. Creating an EIDORS object requires the type ($image$), name ($homogeneous\ image$), matrix of conductivity of finite elements (mat) with name $elem\_data$ and the forward modelling mesh associated with the object ($fmdl$) with the name fwd_model. In the written code, the EIDORS object was developed using the lines of code below.

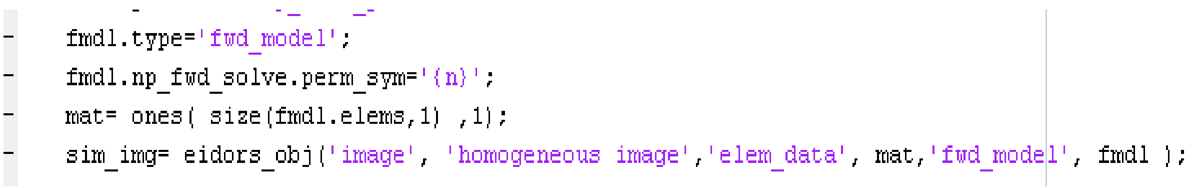

```
fmdl.type='fwd_model';
fmdl.np_fwd_solve.perm_sym='{n}';
mat= ones( size(fmdl.elems,1) ,1);
sim_img= eidors_obj('image', 'homogeneous image','elem_data', mat,'fwd_model', fmdl );
```

J2.7 Specifying the Conductivity of Each Element to be Homogeneous in the NETGEN Mesh such as Fixing the Value of Conductivity to be One for All Element in the Mesh

Data collection to visualise the perturbation within a conductivity domain requires voltage measurement for homogeneous distribution of conductivity as well as inhomogeneous distribution of conductivity. Introduction of insulating materials or hyper-saline solution into regions of the entire domain produces less conductive medium or more conductive medium that perturbs the uniform distribution of the flux lines detected by the periphery sensor electrodes. Matrix of homogeneous distribution of conductivity is specified to be one as in

```
mat= ones( size(fmdl.elems,1) ,1);
```

J2.8 Relating the Homogeneous Property of All Elements in the NETGEN Mesh to the Created EIDORS Object

The created EIDORS object, denoted by sim_img is linked to the associated forward modelling mesh, and the conductivity of each element in the mesh, by the following code

```
sim_img.fwd_solve.get_all_meas = 1;
sim_img.fwd_model= fmdl;
sim_img.elem_data(mat) = 1;
```

J2.9 Calling the Forward Solver Function to Solve for the Boundary Voltages Arising from Injecting Current into a Homogeneous Solution

The forward solver, np_fwd_solve, is called with the function fwd_solve. This requires the EIDORS forward modelling object and mesh as input variable as shown in the function

```
vh = fwd_solve(fmdl,sim_img);
```

J2.10 Loading the Measured Data from the UCT Tomography Rig into the Written Code

The calibrated data sets of measured voltages were contaminated with 25 decibel of Gaussian noise when the conductivity distribution within the tomography vessel is inhomogeneous. The simulated data sets of voltages for homogeneous distribution of conductivity was obtained using the forward solver function of EIDORS. Both the calibrated data sets and the simulated data sets are needed as input data for the inverse solver function of EIDORS. To compute the calibrated data sets for inhomogeneous solution, the following data sets are required

(1) the raw tomography data sets for homogeneous solution with no current stimulated into the medium (offset voltage datasets),

(2) for homogeneous solution with certain magnitude of constant current (2.5mA), and

(3) for inhomogeneous solution with the same magnitude of current applied as in raw data for homogeneous solution.

From these data, the processed tomography data sets for the homogeneous solution were computed from the difference between the raw tomography data sets for homogeneous solution and the offset data sets. Similarly, the processed tomography data sets for the inhomogeneous solution were computed from the difference between the raw tomography data sets for inhomogeneous solution and the offset data sets. Furthermore, the scaling factor data sets were computed from the ratio of simulated data sets for homogeneous solution with the same magnitude of current applied to the processed tomography data for the homogeneous solution. Thereafter, the calibrated data sets of measured voltages were computed from the product of the processed tomography data sets for inhomogeneous solution and the scaling factor data sets. Therefore, the calibrated data sets were derived such that the ratio of the simulated voltage data sets for inhomogeneous solution to the processed data sets of measured voltages for inhomogeneous solution was the same as the ratio of the simulated voltage data sets for homogeneous solution to processed data sets of measured voltages for homogeneous solution about each data point. That is

$$Calibrated\ \ data\ for\ inhomo = (processed\ data\ for\ inhomo) \times \frac{(simulated\ data\ for\ homo)}{(processed\ data\ for\ homo)}.$$

With reference to one of the six written codes with file name $RECONSTRUCT\_4RINGS\_ALGOR\_OPP.m$, $meas\_4RINGShomo\_OPP$ is a written MATLAB function required to load the raw tomography data sets for inhomogeneous solution. Then, the function $getcalibrationdata4rings\_opp\_no\_current$ loads the raw tomography data sets with no current applied for homogeneous solution while $getcalibrationdata4rings\_opp\_current$ function loads the raw tomography data sets with current applied for homogeneous solution. Similarly, $Meas\_HOMOdata$, and

Meas_INHOMOdata denote the processed tomography data for homogeneous and inhomogeneous solution respectively while *Calib_Inhomo* denotes the calibrated tomography voltage data sets as detailed in the few lines of code below.

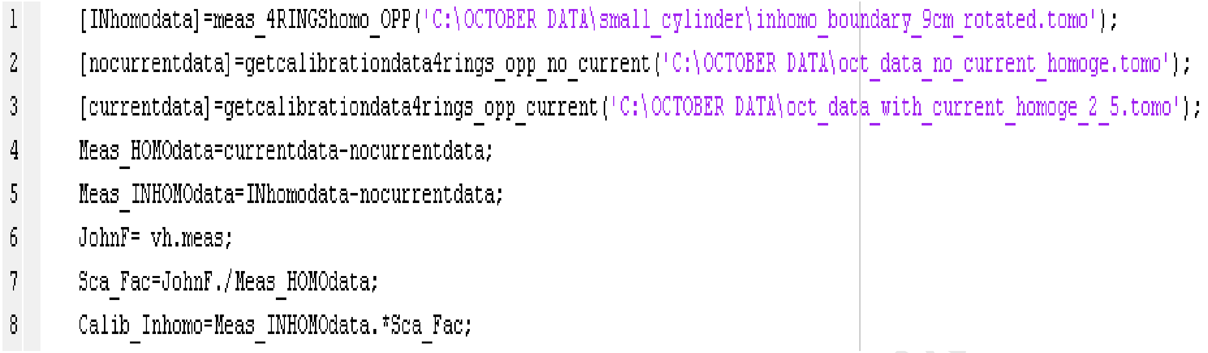

```
[INhomodata]=meas_4RINGShomo_OPP('C:\OCTOBER DATA\small_cylinder\inhomo_boundary_9cm_rotated.tomo');
[nocurrentdata]=getcalibrationdata4rings_opp_no_current('C:\OCTOBER DATA\oct_data_no_current_homoge.tomo');
[currentdata]=getcalibrationdata4rings_opp_current('C:\OCTOBER DATA\oct_data_with_current_homoge_2_5.tomo');
Meas_HOMOdata=currentdata-nocurrentdata;
Meas_INHOMOdata=INhomodata-nocurrentdata;
JohnF= vh.meas;
Sca_Fac=JohnF./Meas_HOMOdata;
Calib_Inhomo=Meas_INHOMOdata.*Sca_Fac;
```

Since the EIDORS inverse solver function was explored to solve for the conductivity distribution (inverse of resistivity) using the *difference* voltage approach, the calibrated tomography voltage data sets for inhomogeneous solution had to be defined as the simulated voltage data sets for the inhomogeneous solution with the following lines of code

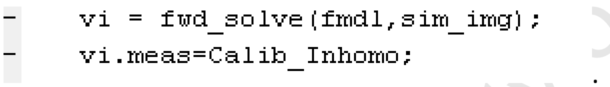

```
vi = fwd_solve(fmdl,sim_img);
vi.meas=Calib_Inhomo;
```

The MATLAB script for loading voltage data sets obtained by a sequence of measurement through adjacent electrode pairs for a sequence of current stimulation through opposite electrode pairs in a two, three and four electrode systems are illustrated in section H1, H3 and H5 of the appendix respectively. Similarly, the MATLAB script for loading voltage data sets considering a sequence of current injection through adjacent electrode pairs and voltage measurement through adjacent electrode pairs in a two, three and four rings of electrode tank are highlighted in section H2, H4 and H6 of the appendix respectively.

J3 : Computational operations to addressing the inverse problem of computing the conductivity distribution given the boundary voltages for a sequence of current stimulation pattern

(a) Writing a MATLAB function for loading the measured offset voltage data set, raw voltage with current for homogeneous and raw voltage with current for inhomogeneous from the UCT tomography equipment;

(b) Computation of the processed measured voltage data sets for the homogeneous solution;

(c) Computation of the scaling factor data sets from the ratio of the simulated voltages for homogeneous solution using EIDORS library of MATLAB function to processed measured voltage data sets for homogeneous solution;

(d) Computation of the processed measured voltages for inhomogeneous solution;

(e) Computation of the calibrated tomography voltages for inhomogeneous solution by multiplying the scaling factor with processed measured voltages for inhomogeneous solution about each data point;

(f) Defining the calibrated tomography voltages for inhomogeneous solution as the solved simulated voltages for inhomogeneous solution using EIDORS forward solver;

(g) Computation of the white Gaussian noise to be added to the calibrated tomography voltages required for the inverse problem in order to improve the signal to noise ratio in the reconstructed image (computed with the function *std* and *rand*);

(h) Adding the noise to the calibrated tomography voltages for inhomogeneous solution;

(i) Creating an EIDORS object for the inverse solver function (using the function *eidors_obj*);

(j) Specifying the forward model property, method of reconstruction, jacobian background value, the hyperparameter value, number of maximum iteration and the inverse solver function of EIDORS (the functions *fwd_model, reconst_type, jacobian_bkgnd_value, hyperparameter.value, parameters.max_iterations* and *@np_inv_solve* were used respectively);

(k) Specifying the image-prior data sets (the function *@np_calc_image_prior* was used);

(l) Calling the inverse solver function, plotting of the reconstructed image in 3-D and 2-D plot of slices through the images parallel to x, y, and z axis and displaying the jpeg picture of the UCT tomography rig with an immersed object (*show_fem* and *show_3d_slices* functions were used respectively).

J4: Solving the Inverse problem Using EIDORS

J4.1 Computation of the White Gaussian Noise to be Added to the Calibrated Tomography Voltages

The probabilistic idea described in section 4.5 indicates that the regularisation matrix was constructed with a prior knowledge that the calibrated voltage data sets was contaminated with low level noise. A distribution of white Gaussian noise signals (of 25 decibel signal to noise ratio) with an expectation value of approximately zero and variance v was used to contaminate the calibrated voltage data sets so as to synchronise the noise in the measured data with that adopted in the regularisation technique. The noise added to the calibrated data sets ($vi.meas$) was computed with the following lines of code

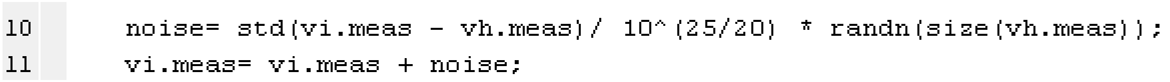

```
10      noise= std(vi.meas - vh.meas)/ 10^(25/20) * randn(size(vh.meas));
11      vi.meas= vi.meas + noise;
```

J4.2 Creating an EIDORS Object for the Inverse Solver Function

Similar to the forward solver function of EIDORS, an inverse solver function requires an EIDORS object with specified properties as input variables. The reconstruction type was selected to be $difference$ instead of $static$ to indicate that the reconstruction was based on the difference between two data objects as compared to an image being reconstructed from a single data object. In line 21 below, Nick Polidorides' computed $image\ prior$ was explored in solving the inverse problem as it yields a more accurate solution of the inverse problem than both the Tikhonov prior, $@tikhonov\_image\_prior$, and Andrea Borsic's image prior, $@ab\_calc\_tv\_prior$, when the measured voltage data from the UCT tomography rig was loaded to the reconstruction codes. Line 18 signifies hyperparameter values and the number of iterations to obtaining approximate solution of the exact solution was specified on line 23. The lines of code below show how $eidors\_obj$ function was used to create an object linking the object's properties to the object.

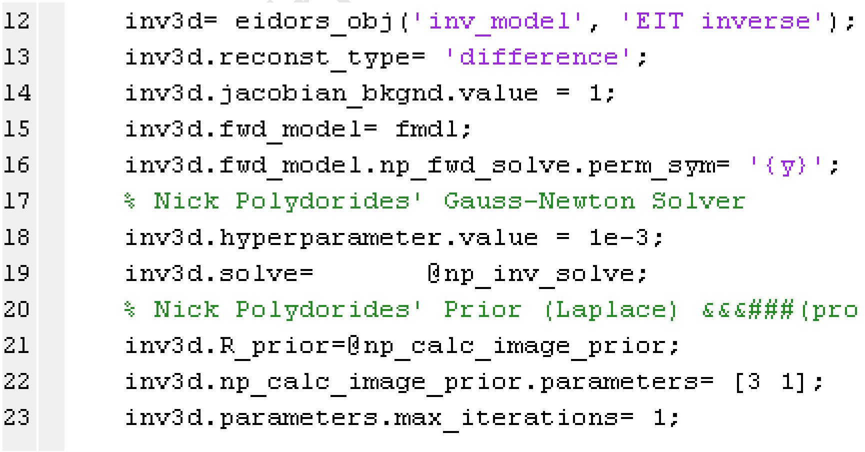

```
12      inv3d= eidors_obj('inv_model', 'EIT inverse');
13      inv3d.reconst_type= 'difference';
14      inv3d.jacobian_bkgnd.value = 1;
15      inv3d.fwd_model= fmdl;
16      inv3d.fwd_model.np_fwd_solve.perm_sym= '{y}';
17      % Nick Polydorides' Gauss-Newton Solver
18      inv3d.hyperparameter.value = 1e-3;
19      inv3d.solve=        @np_inv_solve;
20      % Nick Polydorides' Prior (Laplace) &&&###(pro
21      inv3d.R_prior=@np_calc_image_prior;
22      inv3d.np_calc_image_prior.parameters= [3 1];
23      inv3d.parameters.max_iterations= 1;
```

J4.3 Calling the Inverse Solver Function and Plotting the Reconstructed Images in 3-D and 2-D

The inverse solver function, inv_solve, solves the inverse problem when the EIDORS object ($inv3d$), simulated voltage data sets for homogeneous solution (vh) and calibrated data sets for inhomogeneous solution (vi) are set as input variables as in line 26. The $show\_fem$ function in line 39 displays the solution of the inv_solve (img) in three dimensions while $show\_3d\_slices$ in line 30, 35 and 43 displays the slices through the reconstructed image on a two-dimensional plane parallel to the z-axis, y-axis and x-axis respectively. The $imread$ function in line 48 attaches the $.jpeg$ file of the tomography rig on the same page of the plots.

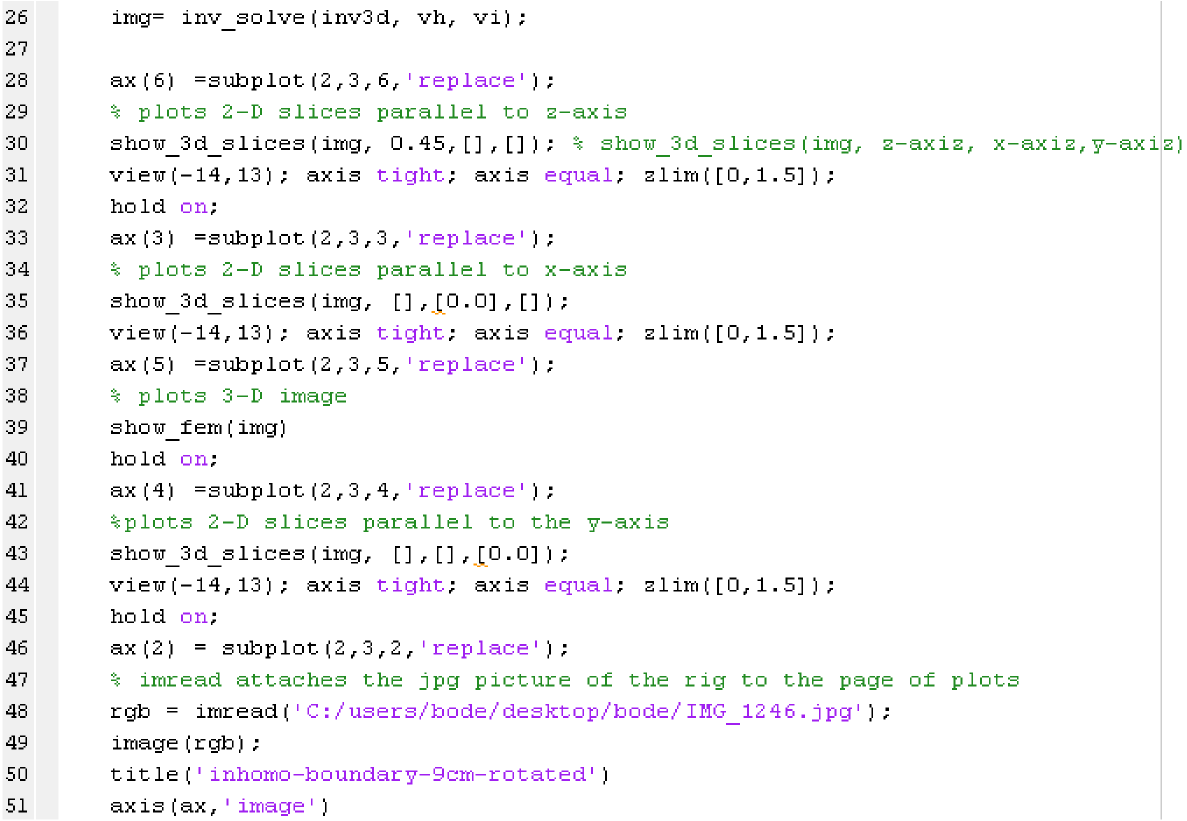

```
26      img= inv_solve(inv3d, vh, vi);
27
28      ax(6) =subplot(2,3,6,'replace');
29      % plots 2-D slices parallel to z-axis
30      show_3d_slices(img, 0.45,[],[]); % show_3d_slices(img, z-axiz, x-axiz,y-axiz)
31      view(-14,13); axis tight; axis equal; zlim([0,1.5]);
32      hold on;
33      ax(3) =subplot(2,3,3,'replace');
34      % plots 2-D slices parallel to x-axis
35      show_3d_slices(img, [],[0.0],[]);
36      view(-14,13); axis tight; axis equal; zlim([0,1.5]);
37      ax(5) =subplot(2,3,5,'replace');
38      % plots 3-D image
39      show_fem(img)
40      hold on;
41      ax(4) =subplot(2,3,4,'replace');
42      %plots 2-D slices parallel to the y-axis
43      show_3d_slices(img, [],[],[0.0]);
44      view(-14,13); axis tight; axis equal; zlim([0,1.5]);
45      hold on;
46      ax(2) = subplot(2,3,2,'replace');
47      % imread attaches the jpg picture of the rig to the page of plots
48      rgb = imread('C:/users/bode/desktop/bode/IMG_1246.jpg');
49      image(rgb);
50      title('inhomo-boundary-9cm-rotated')
51      axis(ax,'image')
```

APPENDIX K

Computation of Volume of Region Discretised into Finite Number of Tetrahedra with Resistivity Values lying within a Specified Range

K1 : The code below was used for the computation of volume of region of high resistivity values

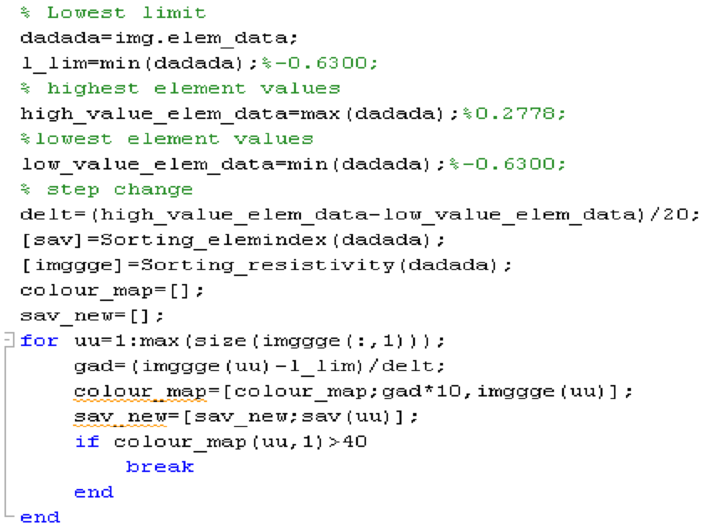

```
% Lowest limit
dadada=img.elem_data;
l_lim=min(dadada);%-0.6300;
% highest element values
high_value_elem_data=max(dadada);%0.2778;
%lowest element values
low_value_elem_data=min(dadada);%-0.6300;
% step change
delt=(high_value_elem_data-low_value_elem_data)/20;
[sav]=Sorting_elemindex(dadada);
[imggge]=Sorting_resistivity(dadada);
colour_map=[];
sav_new=[];
for uu=1:max(size(imggge(:,1)));
    gad=(imggge(uu)-l_lim)/delt;
    colour_map=[colour_map;gad*10,imggge(uu)];
    sav_new=[sav_new;sav(uu)];
    if colour_map(uu,1)>40
        break
    end
end
```

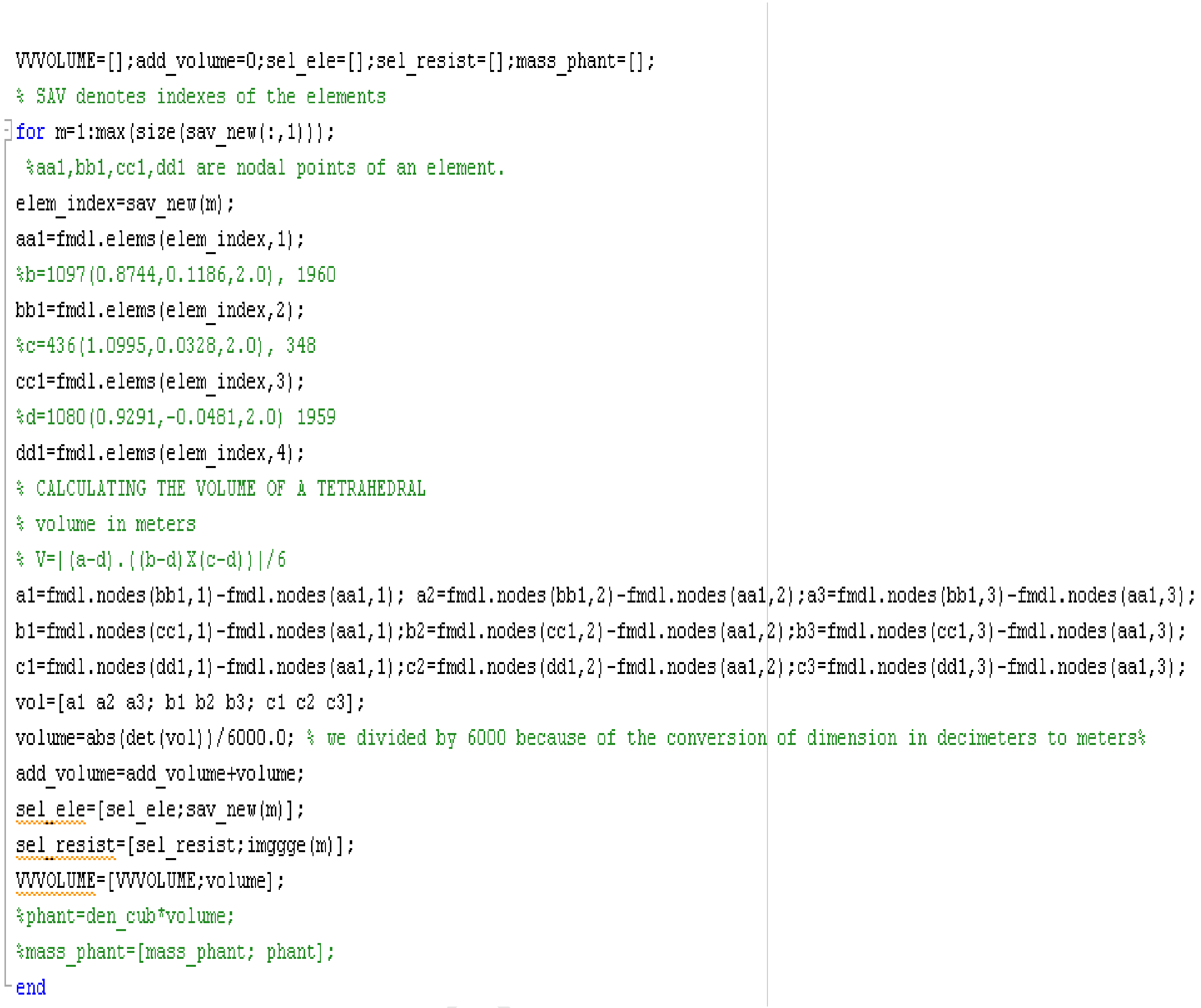

```
VVVOLUME=[];add_volume=0;sel_ele=[];sel_resist=[];mass_phant=[];
% SAV denotes indexes of the elements
for m=1:max(size(sav_new(:,1)));
 %aa1,bb1,cc1,dd1 are nodal points of an element.
elem_index=sav_new(m);
aa1=fmdl.elems(elem_index,1);
%b=1097(0.8744,0.1186,2.0), 1960
bb1=fmdl.elems(elem_index,2);
%c=436(1.0995,0.0328,2.0), 348
cc1=fmdl.elems(elem_index,3);
%d=1080(0.9291,-0.0481,2.0) 1959
dd1=fmdl.elems(elem_index,4);
% CALCULATING THE VOLUME OF A TETRAHEDRAL
% volume in meters
% V=|(a-d).((b-d)X(c-d))|/6
a1=fmdl.nodes(bb1,1)-fmdl.nodes(aa1,1); a2=fmdl.nodes(bb1,2)-fmdl.nodes(aa1,2);a3=fmdl.nodes(bb1,3)-fmdl.nodes(aa1,3);
b1=fmdl.nodes(cc1,1)-fmdl.nodes(aa1,1);b2=fmdl.nodes(cc1,2)-fmdl.nodes(aa1,2);b3=fmdl.nodes(cc1,3)-fmdl.nodes(aa1,3);
c1=fmdl.nodes(dd1,1)-fmdl.nodes(aa1,1);c2=fmdl.nodes(dd1,2)-fmdl.nodes(aa1,2);c3=fmdl.nodes(dd1,3)-fmdl.nodes(aa1,3);
vol=[a1 a2 a3; b1 b2 b3; c1 c2 c3];
volume=abs(det(vol))/6000.0; % we divided by 6000 because of the conversion of dimension in decimeters to meters%
add_volume=add_volume+volume;
sel_ele=[sel_ele;sav_new(m)];
sel_resist=[sel_resist;imggge(m)];
VVVOLUME=[VVVOLUME;volume];
%phant=den_cub*volume;
%mass_phant=[mass_phant; phant];
end
```

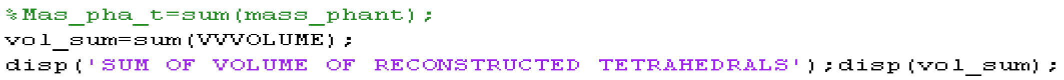

```
%Mas_pha_t=sum(mass_phant);
vol_sum=sum(VVVOLUME);
disp('SUM OF VOLUME OF RECONSTRUCTED TETRAHEDRALS');disp(vol_sum);
```

K2 : Computation of coordinates of the centre of mass of Region Discretised into Finite Number of Tetrahedrals with Resistivity Values lying within a Specified Range

PAS values, computed using the code below, were compared to that of the actual suspended phantom for various position along the diameter of the tomography rig. The code for computing the coordinate of the center of mass is shown below.

```
weighted_pos_mass=[];coordinates=[];
for tt=1:max(size(sav_new(:,1)));
    elem_index=sav_new(tt);
    aa1=fmdl.elems(elem_index,1);
%b=1097(0.8744,0.1186,2.0), 1960
    bb1=fmdl.elems(elem_index,2);
%c=436(1.0995,0.0328,2.0), 348
    cc1=fmdl.elems(elem_index,3);
%d=1080(0.9291,-0.0481,2.0) 1959
    dd1=fmdl.elems(elem_index,4);
    x_val=(fmdl.nodes(aa1,1)+fmdl.nodes(bb1,1)+fmdl.nodes(cc1,1)+fmdl.nodes(dd1,1))/4;
    y_val=(fmdl.nodes(aa1,2)+fmdl.nodes(bb1,2)+fmdl.nodes(cc1,2)+fmdl.nodes(dd1,2))/4;
    z_val=(fmdl.nodes(aa1,3)+fmdl.nodes(bb1,3)+fmdl.nodes(cc1,3)+fmdl.nodes(dd1,3))/4;
    a1=fmdl.nodes(bb1,1)-fmdl.nodes(aa1,1); a2=fmdl.nodes(bb1,2)-fmdl.nodes(aa1,2);a3=fmdl.nodes(bb1,3)-fmdl.nodes(aa1,3);
    b1=fmdl.nodes(cc1,1)-fmdl.nodes(aa1,1);b2=fmdl.nodes(cc1,2)-fmdl.nodes(aa1,2);b3=fmdl.nodes(cc1,3)-fmdl.nodes(aa1,3);
    c1=fmdl.nodes(dd1,1)-fmdl.nodes(aa1,1);c2=fmdl.nodes(dd1,2)-fmdl.nodes(aa1,2);c3=fmdl.nodes(dd1,3)-fmdl.nodes(aa1,3);
    vol=[a1 a2 a3; b1 b2 b3; c1 c2 c3];
    volume=abs(det(vol))/6000.0;
    weighted_pos_mass=[weighted_pos_mass; x_val*volume,y_val*volume,z_val*volume];

end
X_CM= sum(weighted_pos_mass(:,1))/vol_sum; Y_CM=sum(weighted_pos_mass(:,2))/vol_sum; Z_CM=sum(weighted_pos_mass(:,3))/vol_sum;
disp('X_CM');disp(X_CM);disp('Y_CM');disp(Y_CM);disp('Z_CM');disp(Z_CM);
```